CISM International Centre for Mechanical Sciences 563
Courses and Lectures

Oskar Paris
Editor

Structure and Multiscale Mechanics of Carbon Nanomaterials

International Centre for Mechanical Sciences

Springer

CISM Courses and Lectures

Series Editors:

The Rectors
Friedrich Pfeiffer - Munich
Franz G. Rammerstorfer - Vienna
Elisabeth Guazzelli - Marseille

The Secretary General
Bernhard Schrefler - Padua

Executive Editor
Paolo Serafini - Udine

The series presents lecture notes, monographs, edited works and proceedings in the field of Mechanics, Engineering, Computer Science and Applied Mathematics.
Purpose of the series is to make known in the international scientific and technical community results obtained in some of the activities organized by CISM, the International Centre for Mechanical Sciences.

International Centre for Mechanical Sciences

Courses and Lectures Vol. 563

For further volumes:
www.springer.com/series/76

Oskar Paris
Editor

Structure and Multiscale Mechanics of Carbon Nanomaterials

Springer

Editor

Oskar Paris
Montanuniversitaet Leoben
Leoben, Austria

ISSN 0254-1971
ISBN 978-3-7091-1885-6 ISBN 978-3-7091-1887-0 (eBook)
DOI 10.1007/ 978-3-7091-1887-0
Springer Wien Heidelberg New York Dordrecht London

All contributions have been typeset by the authors

Printed in Italy

Printed on acid-free paper

Springer is part of Springer Science+Business Media (www.springer.com)

PREFACE

Carbon is often designated as The Material of the 21st century. Graphene, carbon nanotubes, fullerenes and other highly organized carbon nanostructures are under investigation worldwide for advanced functional materials in diverse fields. Among the numerous applications, they will likely play a key role in modern energy storage devices such as Li-ion batteries, supercapacitors, or fuel cells; they are thought to have the potential to revolutionize electronics by at least partly replacing silicon technology by carbon technology; and most importantly in the present context, they have extraordinary mechanical properties, making them attractive for light-weight structural applications. Graphene is the strongest material ever tested, with a tensile strength 200 times greater than that of steel and a tensile modulus beyond 1000 GPa. Some few applications were realized with this unique material already and numerous others are envisaged. Similar prospects hold also true for the rolled-up graphene versions in 1D (nanotubes) and 2D (fullerenes). Beside these "modern", highly ordered carbon nanomaterials, there exist a broad variety of more disordered carbons. A whole continuum of partly disordered, defect rich materials such as carbon fibres, carbon black, activated carbons, etc., are widely applied in diverse fields and their properties are continuously improved. It is important to note that the outstanding mechanical properties of carbon materials are not only useful for structural applications (e.g. in composites), they are also of critical importance for the mechanical integrity of essentially all functional devices based on them.

There have been numerous conferences, workshops, and schools on the functional properties of carbon nanomaterials in the past, and a number of monographs and edited books, as well as many dedicated conference proceedings have been published. Nevertheless, seldom the main focus was laid on mechanical properties with the emphasis on engineering aspects. The aim of the CISM advanced course on "Structure and Multiscale Mechanics of Carbon Nanomaterials" held in Udine 21.-25.07.2014 was to close this gap by bringing together scientists from diverse fields related to the mechanics of carbon nanomaterials. It was considered important to have a balance between state-of-the-art experimental work combined with theoreti-

cal modelling and simulations, the latter covering all scales from ab-initio DFT and atomistic modelling up to continuum mechanical approaches. Among the topics presented carbon nanotubes were dominant, but also graphene as well as classical carbon fibres were covered. An overall focus was set on highly sophisticated in-situ experimental techniques such as micro Raman spectroscopy or micro X-ray diffraction applied during mechanical testing or the application of high pressure. A further focus was on the composite mechanics of carbon nanomaterial reinforced polymers and on the collective mechanical behaviour of aligned carbon nanotubes. The lectures have been given by:

Claudia Draxl, Humboldt Universitaet Berlin, Germany
David J. Dunstan, Queen Mary University of London, UK
Markus A. Hartmann, Montanuniversitaet Leoben, Austria
Oskar Paris, Montanuniversitaet Leoben, Austria
Siddhartha Pathak, Los Alamos National Laboratory,USA
Robert J. Young, University of Manchester, UK

This volume was prepared based on the lecture notes by the lecturers and in some cases by additional co-authors, and covers most of the topics discussed in the advanced course. First of all, I wish to warmly thank all contributors to this volume for their excellent work. My thanks also go to the CISM directors Franz G. Rammerstorfer for the initiation of this advanced course and Frederic Pfeiffer for the smooth monitoring of the course, and to all the CISM staff in Udine.

Oskar Paris

CONTENTS

1 Single Carbon Fibres: Structure from X-ray Diffraction and Nanomechanical Properties

Oskar Paris[*] and Herwig Peterlik[†]

[*]Institute of Physics, Montanuniversitaet Leoben, Leoben AUSTRIA
[†]Faculty of Physics, University of Vienna, Vienna AUSTRIA

1.1. Introduction

High performance carbon fibres are mainly used as reinforcement in fibre-reinforced structural components in aerospace-, automotive-, sports-, and energy applications. For example, many of the lightweight and stiff structural parts of bicycles, sport cars or wind turbine blades are nowadays made of carbon fibre reinforced plastics (CFRP), and the demand for such materials is continuously increasing. The dominant part (more than 90%) of carbon fibres are produced from polyacrylonitrile (PAN) precursor fibres with intermediate moduli of a few 100 GPa, but very high tensile strength up to 8 GPa. The second important class are fibres produced from mesophase pitches (MPP), leading to fibres with extremely high moduli (almost 1000 GPa) as well as good thermal and electrical conductivity. Together with their low weight, chemical resistance, biocompatibility, temperature tolerance and low thermal expansion, carbon fibres may only be beaten by other carbons such as carbon nanotubes (chapter 3) or graphene (chapter 4) as reinforcing materials. Although being much cheaper than those "modern" carbon nanomaterials, still carbon fibres are relatively expensive as compared to, e.g., glass fibres. Nonetheless, the world-wide carbon fibre production is steadily increasing and is expected to double from 68.000 tons in 2015 to 130.000 tons in 2020 (Holmes 2013). This demonstrates that carbon fibres are - and will further remain - the absolutely dominating carbon nanomaterials for light weight structural parts.

Basic fibre production routes have been refined and up-scaled over the last 50 years. They are described in many textbooks, e.g., (Fitzer and Manocha 1998; Paris and Peterlik 2009; Peterlik 2015), and review articles (Liu and Kumar 2012) and are not considered here in any detail. We just mention the most important processing step common to all carbon fibres, which is the final high-temperature treatment (HTT) in inert atmosphere at temperatures ranging from 1500°C – 3000°C. This final treatment determines decisively the desired mechanical properties. As a general rule, the tensile modulus increases with HTT, while the tensile strength is rather unaffected. It increases for PAN-based fibres for a HTT up to about 1500°C and is

O. Paris (Ed.), *Structure and Multiscale Mechanics of Carbon Nanomaterials*,
CISM International Centre for Mechanical Sciences
DOI 10.1007/ 978-3-7091-1887-0_1

then rather constant up to a HTT of more than 2500°C (Fitzer et al. 1986; Fitzer 1989; Fitzer and Frohs 1990). A slight hot stretching during HTT might further increase the tensile strength to some extend (Ozbek and Isaac 2000). Many light-weight structural components do not only require high strength but they are also stiffness-limited due to Euler buckling. Therefore, the high tensile modulus together with the high strength is the main reason for the incredible success and the increasing demand for carbon fibres in composites, since they outperform in this respect practically all other materials given the restriction that they must be available in sufficient quantities. Weak points remain the mechanical properties of carbon fibres under compression and/or shear, which are a consequence of the extreme anisotropy of the in-plane and inter-plane bond structure of sp^2-bonded graphene sheets. There is considerable progress in recent years on the role of defects that determine local curvature of the sheets (Meyer et al. 2008) and critically influence inter-plane bond strength (Telling et al. 2003; Kis et al. 2004). This research was also strongly triggered by the hype around carbon nanotubes, and more recently, graphene, particularly by theoretical work and atomistic modelling (Yazyev and Louie 2010; Kotakoski and Meyer 2012) (see also chapter 6). Since carbon fibres can be seen as a form of defective multilayer graphene composites, graphene research has also contributed to a better fundamental understanding of the structure – mechanics relationships in carbon fibres.

In this chapter, we show how X-ray diffraction, in particular in combination with in-situ mechanical testing of single carbon fibres has contributed to this progress from the experimental point of view. This field is quite recent, since only the availability of X-ray micro- and nanobeams at third generation synchrotron radiation sources allowed performing such experiments starting at around the beginning of the new millennium. For an introduction into X-ray diffraction we refer to one of the many textbooks available, e.g. by Klug and Alexander (1974) or Zolotoyabko (2013), and with respect to synchrotron radiation, the most classic introductory textbook is probably the one by Als-Nielsen and McMorrow (2011).

1.2. X-ray diffraction from carbon fibres

1.2.1. Structural parameters from X-ray diffraction (XRD)

The basic structural unit of all carbon fibres is the (defective and finite size) graphene sheet. Stacks of graphene sheets form crystallites, which can be wrinkled and folded and which at their edges are connected to other crystallites at different angles, forming elongated and wedged pores (Figure 1.2a). The most important difference between these crystallites and graphite is that two adjacent sheets are typically fully out of registry, having neither orientational nor positional correla-

tions. This so-called turbostratic structure is common to most carbon fibres and leads to characteristic X-ray powder patterns[1] (Figure 1.1). Since a turbostratic crystallite is in fact a one-dimensional (1D) stack of 2D graphene sheets, only reflections of the type *hk0* and *00l* are present in the diffractogramm. Only very few carbon fibre types are graphitisable at very high temperatures, exhibiting also mixed reflections *hkl*. Due to the non-perfect packing, the layer distance between two carbon planes, denoted $d_{002}=2\pi/q_{002}$, is larger than the corresponding distance in graphite. However, the criterion whether a carbon fibre (or any other soft carbon) is graphitic should not be the sharpness of the reflections or a "degree of graphitization" (which measures the deviation from the graphite value, d_{002}=0.335 nm), but exclusively the appearance of mixed reflections with *l* and (*h* or *k*) being different from zero. To make this important difference more clear we stress this in the present chapter by using the nomenclature *00l* for the layer stacking peaks and *hk* for the in-plane peaks of the 2D graphene structure.

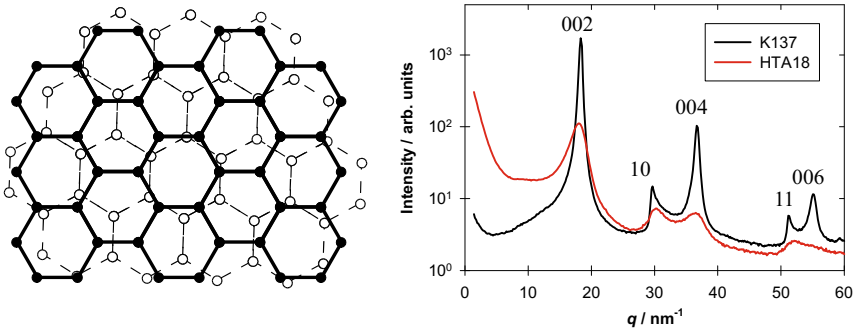

Figure 1.1. Left: Sketch of the turbostratic structure. Right: corresponding powder XRD pattern for two typical carbon fibres (see Table 1.1).

An additional apparent feature in the powder patterns of carbon fibres is the strong anisotropy of the *hk* reflections, being very steep at the low-*q* side and quite shallow at the high-*q* side. This feature is a direct consequence of the 2D crystal nature of stacked graphene sheets, which give each rise to layer-lines in reciprocal space. As a major difference to most other disordered carbons, the graphene sheets in carbon fibres are preferentially arranged parallel to the fibre axis (see Fig. 1.2a). The layers are turbostratically stacked, and in most cases (for exceptions see section 1.2.3) the resulting crystallites are arranged either randomly or rotationally sym-

[1] In this chapter we present X-ray diffraction patterns by the scattering intensity versus the scattering vector $\boldsymbol{q}$, or its length *q* where $q=|\boldsymbol{q}|=(4\pi/\lambda)\sin(\theta)$, 2θ being the scattering angle and λ the X-ray wavelength.

metric with respect to the fibre axis. Thus, the *hk* layer-lines from single graphene sheets are smeared into "disks" in reciprocal space leading to the characteristic shape of these reflections in a 2D X-ray fibre diffraction pattern[2] (see Fig. 1.2b). After averaging over all orientations this gives rise of the characteristic *hk* peak shape discussed above for X-ray powder profiles of carbon fibres. These so called random-layer line profiles are described in more detail in Paris and Peterlik (2009), and have been treated mathematically already by Warren (1941) and later by Ruland (1967a), and Ruland and Tompa (1968).

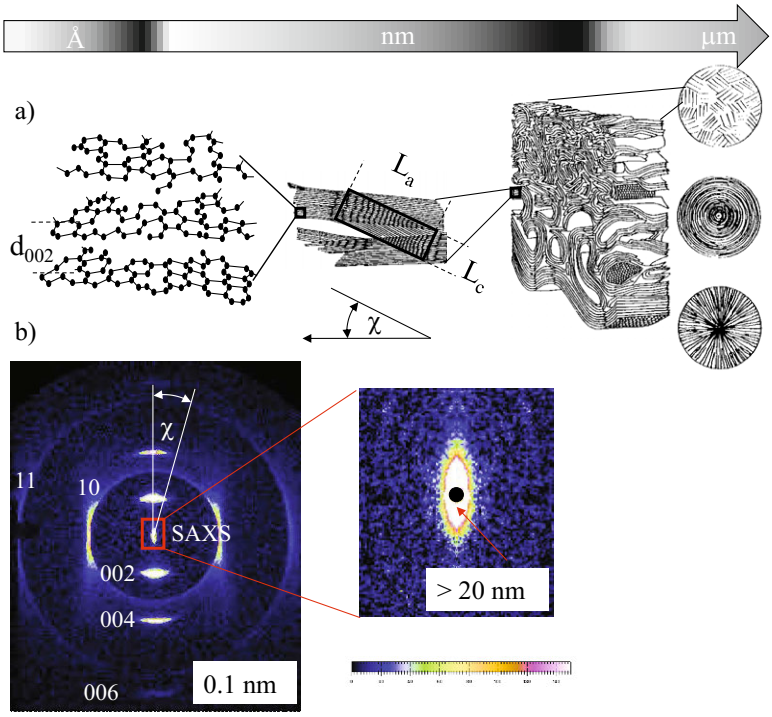

Figure 1.2. (a) Hierarchical structure of carbon fibres and (b) corresponding 2D X-ray fibre diffraction pattern from a single carbon fibre. The fibre axis is horizontal except for the rightmost panel in a), where the fibre cross section with three different cross-sectional texture patterns is sketched.

[2] A fibre diffraction pattern is measured with a 2D position-sensitive detector in transmission geometry with the fibre axis perpendicular to the primary X-ray beam. Since the structure is rotationally symmetric around the fibre axis, a single 2D detector image contains the entire accessible information.

In addition to the *hk* reflections on the meridian, a fibre diffraction pattern contains the equatorial *00l* reflections from which not only the layer spacing d_{002} is readily obtained. Also the main mis-orientation of the crystallites with respect to the fibre axis (indicated by the angle χ in Fig. 1.2) can be deduced. A simple way of defining a preferred orientation parameter f_C is to use

$$f_C = 1 - \frac{w_{002}}{\pi} \qquad (1.1),$$

where w_{002} is a measure for the azimuthal peak broadening (e.g. the full width at half maximum, *FWHM*). More sophisticated measures of f_C were proposed in the literature by taking the azimuthal orientation distribution $p(\chi)$ of crystallites explicitly into account (Ruland 1967b). Frequently, such parameters are defined by the even cosine moments of the orientation distribution (Northolt et al. 1991; Shioya et al. 1996)

$$Z_n = \left\langle \cos^n \chi \right\rangle = \frac{\int_0^{\pi/2} p(\chi) \cos^n \chi \sin \chi \, d\chi}{\int_0^{\pi/2} p(\chi) \sin \chi \, d\chi} \qquad (1.2).$$

For instance, the Herman's orientation function ($f = (3Z_2 - 1) / 2$) is widely used in polymer science and was also sometimes applied to carbon fibres (Zussman et al. 2005). The axial preferred orientation of crystallites is the key to understand and quantitatively describe the tensile modulus of carbon fibres (see section 1.3). Hence, when comparing absolute values from literature, it is important to consider the different measures of preferred orientation. Eq. 1.1 for instance gives $f_C = 1$ for crystallites perfectly aligned with respect to the fibre axis and $f_C = 0$ for fully randomly aligned crystallites, while Eq. 1.2 (for $n = 2$) gives $Z_2 = 0$ for perfectly aligned, and $Z_2 = 1/3$ for fully randomly oriented crystallites.

Beside of their preferred orientation with respect to the fibre axis the crystallites sketched in Fig. 1.2a are characterized by two characteristic length scales, named the stacking height L_C, and the in-plane crystallite size L_a. These parameters are most often determined from X-ray diffraction by applying the Scherrer Equation

$$L = K \frac{2\pi}{\Delta q} \qquad (1.3),$$

where Δq is the radial peak width and the parameter K depends on the detailed geometry of the crystallites. For the stacking height L_C in carbon fibres, K is usually taken to be $K \approx 0.9$ which is very close to the original calculation by Scherrer (1918). For L_a, the corresponding value $K \approx 1.84$ was calculated by Warren (1941). In practice, mostly the *FWHM* is taken for Δq, although several authors claim that the integral breath (i.e. the width of a rectangle having the same area and the same height as the actual peak) should be taken (Langford and Wilson 1978). While the difference is small (only 6.4%) for a Gaussian peak shape, for other peak shapes such as Cauchy peaks the difference may be considerably larger. Therefore, most of the data from literature should be seen as "apparent" length scales which should be taken with some caution when comparing them. The stacking height L_C, can also be estimated from lattice fringe images in the transmission electron microscope (TEM), and was found to be in good agreement with X-ray data (Bennett et al. 1976; Guigon et al. 1984a; Guigon et al. 1984b). However, L_a values from TEM and X-ray diffraction can differ considerably and should not be directly compared. Comparison with more elaborate models for L_a determined from X-ray diffraction (Ruland and Smarsly 2002) has shown that the classical Scherrer evaluation gives acceptable values for a broad range of carbon fibres (Zickler et al. 2006). A frequently used method to conveniently determine L_a for single fibres is Raman spectroscopy. Tuinstra and Koenig (1970) found that the intensity ratio of the Raman D and G bands (see chapter 2) can be used to determine L_a, which was found to hold reliably for carbon fibres if the crystallite size is > 2nm (Zickler et al. 2006). It should also be mentioned here that the peak broadening of a Bragg reflection may be caused also by other contributions (e.g. microstrains of the crystal lattice), and thus the straightforward Scherrer size gives only a crude estimate of the crystallite size. Using the different q-dependence of size and strain, these contributions can be separated by using standard approaches such as the Williamson-Hall Method (Zolotoyabko 2013), or more sophisticated structural modelling of the structure of carbon fibres (Perret and Ruland 1968a; Shioya and Takaku 1988; Ruland and Smarsly 2002). For completeness, we also note here that some authors evaluate two values for L_a, one parallel ($L_{a\parallel}$) and one perpendicular ($L_{a^\perp}$) to the fibre axis.

Table 1.1 summarizes some important X-ray structural parameters for several commercial carbon fibres. There is a clear correlation of all these parameters with the Young's modulus E of the fibres, i.e. d_{002} decreases, and L_C, L_a and f_C increase monotonically with increasing E. It is seen that for the PAN-based fibres with known HTT in Table 1.1, this trend is also clearly related to the final heat treatment temperature. This demonstrates that HTT is indeed one of the most important processing steps to influence fibre stiffness. While generally there is also a correlation of the fibre density with the X-ray parameters, there is a clear difference between PAN and MPP-based fibres, suggesting generally a higher porosity in PAN based fibres. The issue of porosity will be discussed in the next subsection.

Table 1.1. Structural parameters of several commercial carbon fibres. The fibres were characterized as received (AR), and in addition the PAN fibres were heat-treated at 1800°C, 2100°C, and 2400°C. Data taken from Loidl et al. (2005).

Fibre-HTT (precursor)	ρ (g/cm^3)	E (GPa)	d_{002} (nm)	L_C (nm)	L_a (nm)	f_C ( )
HTA7-AR (PAN)	1.77	198	0.354	1.47	2.83	0.89
HTA7-1800 (PAN)	1.77	273	0.350	2.18	3.60	0.91
HTA7-2100 (PAN)	1.71	332	0.346	3.78	6.30	0.93
HTA7-2400 (PAN)	1.91	349	0.344	5.11	7.61	0.95
FT500-AR (MPP)	2.11	380	0.343	10.06	10.22	0.96
K137-AR (MPP)	2.12	500	0.343	13.38	11.61	0.98

1.2.2. What can we learn from small-angle X-ray scattering (SAXS)?

As already discussed in section 1.2.1, a carbon fibre is built from crystalline domains of turbostratically stacked graphene sheets with distance d_{002}, which are characterized by the average dimensions L_C and L_a and by an average preferred orientation parameter f_C with respect to the fibre axis. How these crystalline domains are connected at their edges to form a 3D network separated by slit-like or needle-like pores has been in the focus of research for many years. While it is generally true that all three parameters L_C, L_a and f_C tend to increase with HTT (Table 1.1), there are crucial differences in particular between different types of carbon fibres which are not expressed by these simple average structural parameters. In MPP-based fibres, the crystallites can be seen as quite well defined geometrical entities or grains, separated by grain boundaries and pores. This is a consequence of the disk-shaped liquid-crystalline molecules which form the precursor phase of these crystallites which eventually grow and coalesce upon HTT. In contrast, fibres from polymeric precursors such as PAN-based carbon fibres form rather ribbon like structures of undulating graphene sheets forming fibrillar pore structures (see Fig. 1.2a).

With respect to the porosity of carbon fibres, again X-ray methods, in this case small-angle X-ray scattering (SAXS), play an important role. Fig. 1.2b displays the SAXS pattern close to the direct X-rays beam, which contains information on the shape, size and orientation of pores within the fibre. Already the shape of the 2D SAXS pattern indicates that the pores are elongated and preferentially aligned along the fibre axis. When a 2-phase system of pores in a carbon matrix with homogeneous electron density (at length scales considerably larger than atomic distances) can be assumed, more quantitative information on porosity, specific surface area, and geometrical aspects of the pores can be deduced. SAXS allows in particular

obtaining a general correlation length from integral parameters of the spherically averaged SAXS intensity, i.e., the mean chord length (Glatter and Kratky 1983)

$$T = \frac{4}{\pi}\frac{\tilde{I}}{P} = 4\Phi(1-\Phi)\frac{V}{S} \qquad (1.4),$$

where $\tilde{I}$ is the "invariant" obtained from the integrated SAXS intensity, P is the Porod constant, Φ is the pore volume fraction, and S/V is the total pore surface area per unit volume. T is different from the above mentioned crystallite dimensions and is related to the chord length of the pores l_p by $l_p=T(1-\Phi)$ and to the chord length of carbon $l_C=T\Phi$. (Smarsly et al. 2002). For slit- or needle like pores (pore width << pore length) and $L_C << L_a$, one can assume $l_C \approx L_C$, i.e., the chord length of carbon corresponds to the crystallite stacking height from XRD. Then, the pore volume fraction $\Phi = L_C / T$ and volume specific surface $S / V=4\Phi(1-\Phi) / T$ can be determined from X-ray diffraction and SAXS without any additional information. This can be of great practical value, since most of the pores in carbon fibres are typically closed and these parameters are therefore not accessible by the usual nitrogen sorption method.

Interpretation of details of SAXS curves from carbon fibres has been considered by Ruland and coworkers (Perret and Ruland 1968b; Perret and Ruland 1969; Perret and Ruland 1970) and others (Shioya and Takaku 1985; Gupta et al. 1994; Peterlik et al. 1994). With the availability of 2D detectors, also the shape of 2D SAXS became of interest, due to the rather straight forward interpretation of orientational correlations. Perret and Ruland (1969) pioneered the theoretical considerations by deriving a transformation equation from the angular intensity distribution in reciprocal space to the orientation distribution of needle-like pores. Even simpler, the orientation distribution of large slit-like pores corresponds directly to the intensity distribution extracted from 2D SAXS. It has to be considered however that there is also a broadening of the SAXS intensity in fibre-axis direction due to the finite length h of slit-like pores. Figure 1.3 sketches the basic strategy how to separate these contributions in order to derive both, a measure for the large dimension of pores h and the width of the orientation distribution w_p of pores (Paris et al. 1997)

$$w_{SAXS}(q_\perp) \approx \frac{2\pi}{h} + w_p q_\perp \qquad (1.5).$$

In the case of slit like pores separating the multilayer graphene stacks, this width should correspond essentially to the azimuthal width of the *00l* reflections *w* obtained from XRD in Eq. 1.1.

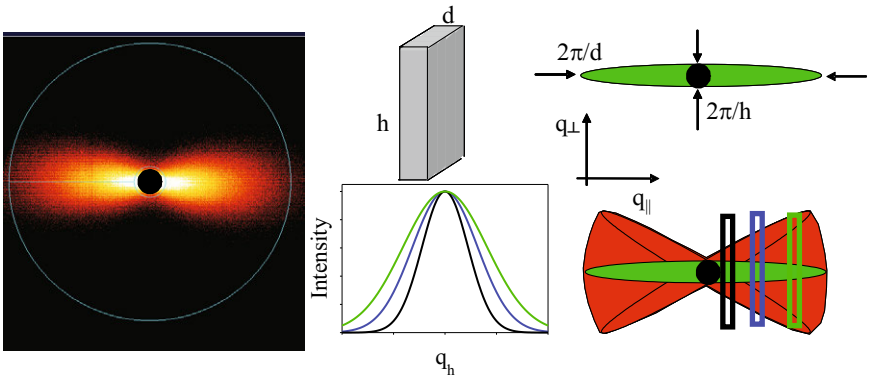

Figure 1.3. 2D SAXS pattern of HTA7-1800 (left) and sketch of the procedure to determine the pore length *h* and the orientation distribution of pores w_p.

1.2.3. What additionally can we get by using X-ray microbeams?

Since the graphene sheets in carbon fibres are mainly oriented parallel to the fibre axis, they can be viewed edge-on in the TEM when the electron beam is parallel to the fibre axis. Fig. 1.4 shows a lattice fringe image from a PAN-based fibre. This image confirms the picture of crystallites of different orientation viewed edge-on, although the boundaries between these crystallites are not so well defined. The corresponding electron diffraction pattern suggests that the orientation distribution is fully random. The sketch of the fibre cross-sections in Fig. 1.2a indicates however that the graphene layers must not necessarily be randomly oriented within the fibre cross section. Such cross-sectional textures are readily seen in scanning electron microscopy (SEM) images of fractured fibres (Kobets and Deev 1997; Qin et al. 2012; Peterlik 2015). The most frequent patterns are radial or onion-type of orientations, but also other more complex patterns are found (Edie 1998). Often, these textures are also not homogeneous within the fibre cross-section. In particular in PAN based carbon fibres the fibre core exhibits frequently a random texture with a thin onion-type skin layer (Bennett and Johnson 1979). Such cross-sectional textures are believed to be particularly important for fibre strength (Endo 1988), and it is therefore an important detail in carbon fibre research to quantitatively determine the cross-sectional orientation distribution.

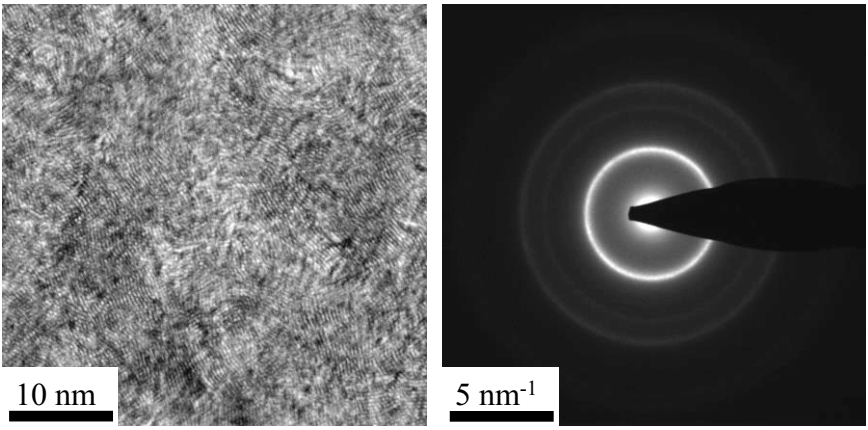

Figure 1.4. TEM lattice fringe image (left) and corresponding electron diffraction pattern (right) from the cross section of the PAN-based fibre HTA7-2400.

TEM is an excellent tool to characterize such textures quantitatively, see e.g. Qin et al. (2012). However, beside the tedious and time-consuming sample preparation, issues of statistical significance and preparation artefacts are serious. X-ray diffraction and/or SAXS can help in this respect, although the experimental effort becomes similar to TEM since thin fibre cross-sections of a few microns have to be prepared and scanned within an X-ray microbeam at a synchrotron radiation source with beam size considerably smaller than the fibre diameter. The advantage of 2D scanning is the potential of directly imaging the cross-sectional crystallite orientation by making use of the anisotropy of the 2D SAXS/XRD patterns. While this works quite well for SAXS (Paris et al. 2000), the interpretation of XRD patterns becomes rather difficult due to subtle geometric aspects related to Ewald sphere curvature and local sample tilt (Paris and Muller 2003). Experimentally much simpler is the scanning of a microbeam across a single carbon fibre in fibre geometry, i.e., measuring fibre diffraction patterns as a function of (linear) scan position across the fibre. For rotationally symmetric textures such as radial or onion-type orientation, a detailed modelling of the position dependent intensity of the different diffraction peaks allows to obtain quantitative parameters describing the degree of orientational order within the fibre cross-section (Paris et al. 2001). If the X-ray beam is not considerably smaller than the fibre diameter, additional convolution of the model calculations with the beam profile is necessary as shown in Fig. 1.5.

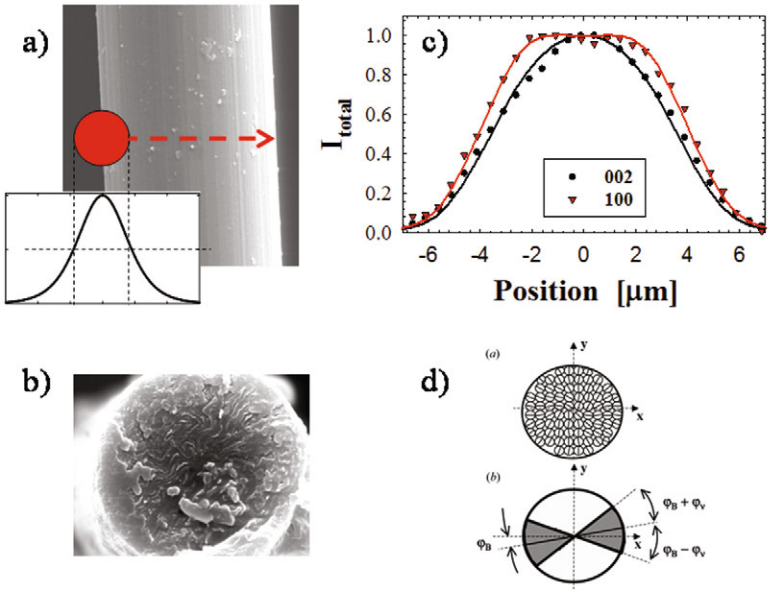

Figure 1.5. Cross-sectional texture in the MPP-based fibre FT500-AR: a) SEM image of the fibre with X-ray beam and beam profile; b) SEM image of fibre cross-section; c) Model fit of the position dependent *002* and *10* peak intensities with the model shown in d). Reproduced from Paris et al. (2001) with permission from the International Union of Crystallography.

Measuring single fibres with a microbeam in fibre geometry does not only allow determining the "real" axial preferred orientation by avoiding the artefacts due to fibre tilt in fibre bundle experiments. Scanning gives also information on the local axial preferred orientation and thus, gradients due to a skin-core structure in PAN-based fibres can be quantitatively resolved (Paris et al. 2002). Detailed analysis of such data allows even to distinguish different "phases" of carbon in some MPP-based fibres, i.e., a cross-sectional randomly oriented phase and a radial folded phase, the two phases exhibiting different axial preferred orientation. Hence, the concept of some fibres being "carbon/carbon composites" can be proven by microbeam X-ray diffraction (Paris et al. 2002).

Although modern synchrotron radiation sources provide nowadays micron- and even sub-micron sized beams almost routinely, the characterization of carbon fibres by these techniques has remained limited due to the quite high experimental effort (Kobayashi et al. 2011). Some recent work shows however impressively to which detail scanning XRD can provide local structural parameters (Baimpas et al. 2014), with the advantage over TEM of still covering the whole fibre. Several new techniques, which are based either on an extension of microbeam scanning to

tomographic principles (Stribeck et al. 2008), or the use of coherent X-ray diffraction imaging to get 3D real-space images from carbon fibres with sub-100nm resolution (Diaz et al. 2014) are very promising for future carbon fibre research.

The real success of microbeam X-ray diffraction techniques for carbon fibres is however connected to the possibility of performing mechanical tests of single fibres while monitoring structural changes in-situ. This has opened fascinating new opportunities for a better understanding of structure – mechanics relationships in carbon fibres and will therefore be discussed in more detail in the next section.

1.3. In-situ mechanical testing of single carbon fibres

1.3.1. Stiffness of carbon fibres

The tensile modulus of carbon fibres is one of the highest of all materials known Table 1.1), reaching for high modulus MPP-based fibres almost the value of 1 TPa (Edie 1998). One peculiar feature of stress-strain curves of single carbon fibres, depicted in Fig. 1.6, is the apparent non-linearity with the clear tendency of the fibres to stiffen with increasing stress (Reder et al. 2003). It is clear that this non-linearity must be related to changes in the nanostructure of the fibres, in particular to the orientation of single crystallites with respect to the fibre axis.

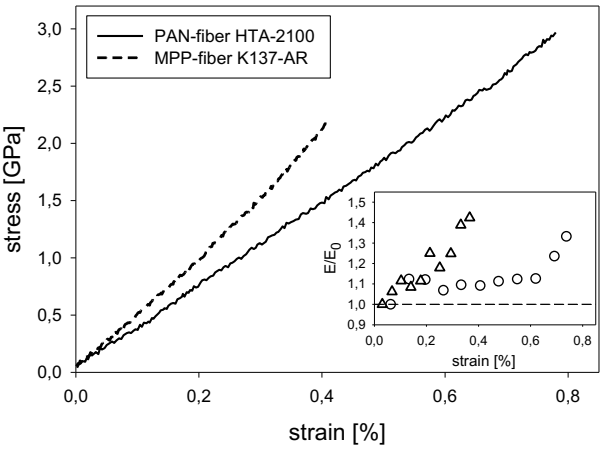

Figure 1.6. Stress-strain curves of a PAN- and MPP based carbon fibre. The inset shows the increase in the Young's modulus normalized to its initial value. Adapted from Reder et al. (2003) with permission from Elsevier.

Carbon fibre tensile tests are frequently performed on fibre bundles. This has the advantage that with one single test a complete strength distribution of thousands of fibres is obtained. However, the method has some serious drawbacks, starting already from the non-identical fibre cross sections. While this problem can be overcome by carefully determining an average fibre diameter with the help of SEM, when performing X-ray in-situ tensile tests on fibre bundles to obtain nanomechanical properties additional problems arise. For instance, the inevitable fibre tilt with respect to the tensile direction makes it difficult to relate mechanical response to axial preferred orientation of the crystallites. Moreover, the stress distribution may be quite different within different fibres, which will smear out changes of structural parameters measured by in-situ XRD. This is the reason why single fibre mechanical experiments with accompanying structural investigations are urgently needed. Micromechanical models for the measured effective (i.e., corrected for porosity) Young's modulus of a single fibre typically need information on crystallite elastic properties, such as their Young's modulus and their shear modulus. An early model was Ruland's elastic unwrinkling model under the assumption of uniform stress (Fischer and Ruland 1980), which was later extended and refined by several groups (Northolt et al. 1991; Shioya et al. 1996; Loidl et al. 2003; Sauder and Lamon 2005).

$$\frac{1}{E_{eff}} = \frac{1}{e_{eff}} + \frac{1}{g_{eff}}\left(Z_2 - Z_4\right) \qquad (1.6).$$

Here e_{eff} and g_{eff} are effective (or apparent) crystallite Young's and shear moduli, respectively, and Z_{i} are crystallite orientation parameters calculated with Eq. 1.2. The term effective means here that when plotting the fibre modulus versus (Z_2-Z_4), a linear behaviour is observed. Fig. 1.7 indicates that this is indeed the case for a series of MPP- and PAN-based fibres, respectively. While the effective Young's moduli $e_{\mathrm{eff}} \approx 700$ GPa are similar for both, MPP- and PAN-based fibres, the effective shear modulus is $g_{\mathrm{eff}} \approx 12$ GPa for MPP-based fibres, and is roughly twice as large for PAN-based fibres. To test the validity of such micromechanical models, the direct measurement of the crystallite moduli is highly desirable.

1.3.2. In-situ XRD during tensile testing of single carbon fibres

In-situ XRD single fibre tensile testing using a microbeam with a similar size as the fibre diameter allows directly obtaining an apparent crystallite Young's modulus e_{cr} (Loidl et al. 2003; Kobayashi et al. 2012). This is achieved by measuring the change in the *10* lattice spacing with applied stress in the direction of the fibre axis in a fibre diffraction pattern (see Fig. 1.2b) and assuming that the same stress is acting on all crystallites (uniform stress model). Fig. 1.8 shows these

crystallite moduli for several carbon fibres versus the orientation parameter $Z_2 - Z_4$. For almost perfect crystallite orientation ($Z_2 - Z_4 < 0.02$), the crystallite modulus was found above 1.0 TPa, which is in the same range as experimental values reported for graphite, carbon nanotubes, or graphene[3]. However, for larger crystallite mis-orientations the crystallite modulus is not constant as would be suggested by Eq. 1.6 (i.e., $e_{cr} \neq e_{eff}$ in Eq. 1.6). This needs to be considered when discussing micromechanical deformation models of carbon fibres such as the uniform stress model.

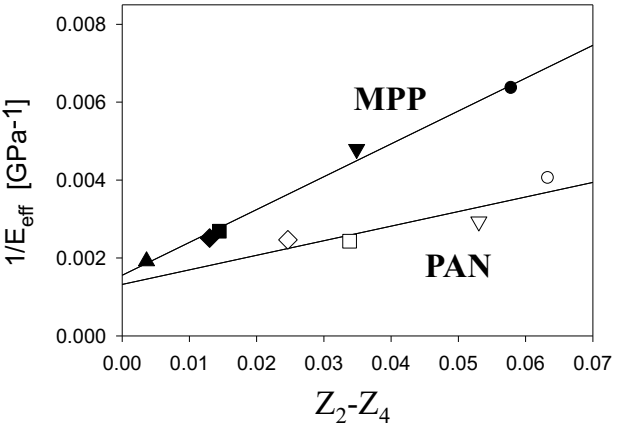

Figure 1.7. Effective Young's modulus of different MPP-based (black symbols) and PAN-based carbon fibres (open symbols) versus the orientation parameter Z_2-Z_4. Reproduced from Loidl et al. (2003) with permission from Elsevier.

Information about the crystallite shear modulus can also be obtained from the in-situ XRD single fibre tensile tests by evaluating the stress dependent change of the crystallite orientation determined from the azimuthal orientation distribution $p(\chi) = I(\chi)$. Northolt et al. (1991) derived a simple analytical expression

$$\tan \chi_m(\sigma) \approx \tan \chi_m(0) \exp\left(-\frac{\sigma}{2g_{cr}}\right) \qquad (1.7)$$

[3] In reality the concept of a Young's modulus should not be used for single-layer graphene since this requires knowledge of the layer thickness which is obviously not defined for a true 2D material.

where $\chi_m(\sigma)$ is a measure of the mean mis-orientation angle derived from the orientation distribution.

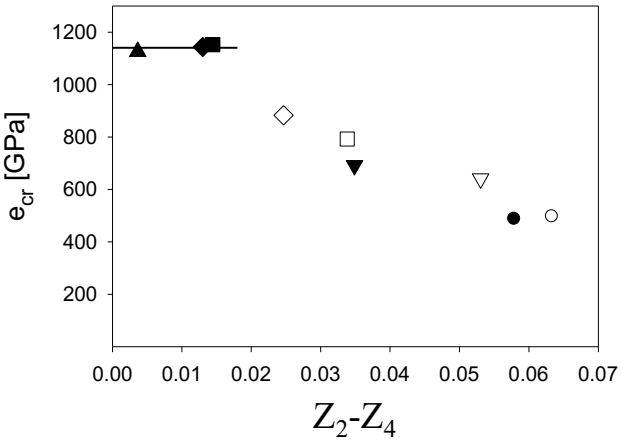

Figure 1.8. Crystallite Young's moduli from X-ray diffraction for several MPP-based (black symbols) and PAN-based carbon fibres. Reproduced from Loidl et al. (2003) with permission from Elsevier.

Fig. 1.9 displays $\chi_m(\sigma)$ for a series of PAN- and MPP-based fibres. In contrast to the crystallite Young's modulus, there seems to be one single crystallite shear modulus for all investigated PAN based fibres, and the same is true when considering the limit of low stress values for MPP-based fibres. However, for both fibre types $g_{cr} \approx g_{eff}/2$, with the absolute value for MPP-based fibres being very close to the bulk shear modulus of graphite ($G \approx 4$ GPa). Hence, even though Eq. 1.6 seems to work for a wide range of fibres from the same type (Fig. 1.7), the effective crystallite moduli g_{eff} and e_{eff} do not coincide with the crystallite moduli g_{cr} and e_{cr} determined from X-ray diffraction under the assumption of uniform stress. This shows that the simple uniform stress model is not able to describe all details of the complex tensile behaviour of carbon fibres. Though the increase of the stress-strain curve and thus the increase in the Young's modulus is predicted from the unwrinkling model, the above mentioned differences suggest that this is not the only structural change of carbon fibres during loading. Nevertheless, it is clear that PAN based fibres exhibit generally better shear properties than MPP based fibres, which points to a fundamentally different inter-plane bonding of these two types of fibres.

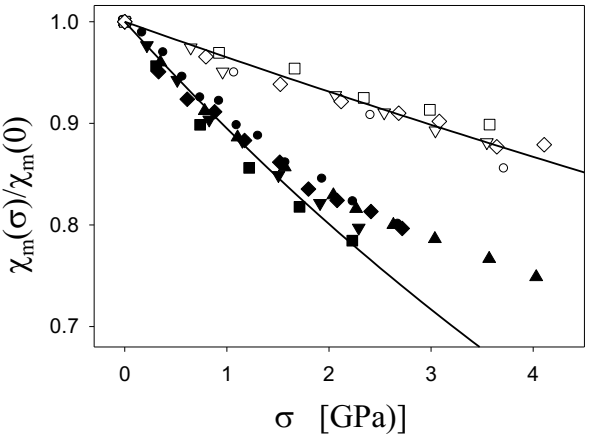

Figure 1.9. Crystallite shear moduli for different PAN-based (open symbols) and MPP-based carbon fibres (black symbols). Solid lines are fits with Eq. 1.7 giving g_{cr} = 13.6 GPa for the PAN-based and g_{cr} = 4.5 GPa for the MPP-based fibres. Reproduced from Loidl et al. (2003) with permission from Elsevier.

A more recent approach to describe the complex deformation of carbon fibres was a skin-core model, which combined amorphous and crystalline regions in the fibre core with a skin layer exhibiting a higher degree of orientation, and thus, a higher modulus (Kobayashi et al. 2011). The authors combined tensile testing of single fibres with in-situ microbeam XRD to obtain information from the fibre centre and in-situ Raman scattering to determine the deformation on the surface of the fibre. The latter method is a powerful tool to probe single fibre mechanical properties (see also Chapter 2). A heterogeneous stress distribution within the fibres was also observed experimentally (Kobayashi et al. 2012; Kobayashi et al. 2013). Unfortunately, the model is restricted to a linear stress-strain behaviour and is not able to describe the non-linear stress-strain curve (Fig. 1.6) and thus the real elastic behaviour of fibres. However, it opens the discussion on the tensile strength of carbon fibres and the origin of failure. It is not clear, whether a skin-core structure is favourable or unfavourable for the mechanical properties of carbon fibres. If there is a considerable difference in the strains within skin and core, this might lead to failure from shear in the interface region. It is clear that inhomogeneities and surface structure will certainly have an effect. For instance, a thin coating - which is used in practice to improve the processability of carbon fibres – is known to improve the tensile strength, while thick coatings show the opposite effect (Helmer et al. 1995). It was also frequently observed that large defects are not the

origin of failure of fibres, in contradiction to the theory of brittle fracture. Thus, in an early and fundamental work it was stated that interlinking and misalignment of crystallites are responsible for failure (Reynolds and Sharp 1974). In a recent work failure was attributed to continuous defective graphene nanoribbons arranged as stacks (Emmerich 2014). Hence, even after 40 years of research, the structural origin of the failure of carbon fibres is still a matter of scientific discussion.

1.3.3. Compressive properties from in-situ X-ray diffraction

Mechanical stability under bending load is critical for carbon fibres, since essentially all fibre weave pattern in composites induce some amount of bending. Failure occurs mostly due to Euler buckling on the compression side of the fibres, making detailed analysis of compressive properties at a local scale necessary. In particular the compressive Young's modulus of single fibres is not easy to determine.

In-situ compression combined with in-situ microbeam XRD/SAXS have recently been demonstrated for single carbon fibres (Sugimoto et al. 2013). In their work, the change of X-ray structural parameters such as d_{002}, L_C and axial preferred orientation of crystallites f_C (Eq. 1.1) from XRD, as well as measures for the pore length h and pore orientation fp (derived from an equation similar to Eq. 1.5) and a measure for the pore cross sectional dimension assuming needle like pores from SAXS were followed as a function of compressive stress. The structural changes were found in agreement with the picture of buckling of carbon layer stacks as the source of fracture, but also reversibility of the structural changes up to 90% of the compression strength was found.

Another way of probing compressive properties is single fibre bending. Fig. 1.10 shows the sketch of a microbeam bending experiment were a single fibre loop is created by threading the fibre ends through a hollow needle. The bending radius, determining the stress in the fibre is easily adjusted by pulling down the ends of the fibre. The fibre was scanned with an X-ray nanobeam (roughly 100 nm beam width in scanning direction) from the tensile to the compression side of the bent fibre, and the experiments were repeated for different bending radii. The axial fibre strain was determined as a function of position from the shift of the *10* reflection, and the change of the axial preferred orientation f_C was derived from the change of the azimuthal width of the *002* reflection. While the data for the PAN-based fibre showed a symmetric change of f_C on the tension and compression side, these changes were strongly asymmetric for MPP-based fibres. Here, the increase in f_C on the compression side was much larger than its corresponding decrease at the tensile side, giving a clear indication of extensive crystallite buckling. A further result of this study was a clear shift of the neutral zone of the fibre from the fibre centre towards the tension region as a consequence of the

different Young's moduli of the fibres in tension (E_T) and compression (E_C). Simple force balance together with the quantitative shift of the neutral zone allows calculating the ratio between compressive and tensile moduli E_C/E_T. Fig. 1.10b demonstrates that beside a general decrease of this ratio with the in-plane crystallite size L_a, it is considerably smaller for MPP based fibres. This difference was attributed to covalent cross-links between crystallites in PAN fibres, while in MPP fibres these cross-links are largely absent. A recent attempt to model this in a simple scenario by a finite element (FEM) mechanical model by Todt et al. (2010) revealed that the distribution of such cross-links critically influences the buckling behaviour (see also chapter 6). Experimentally, these cross-links and in particular their distribution are extremely difficult to grasp, and an experimental verification is therefore still missing.

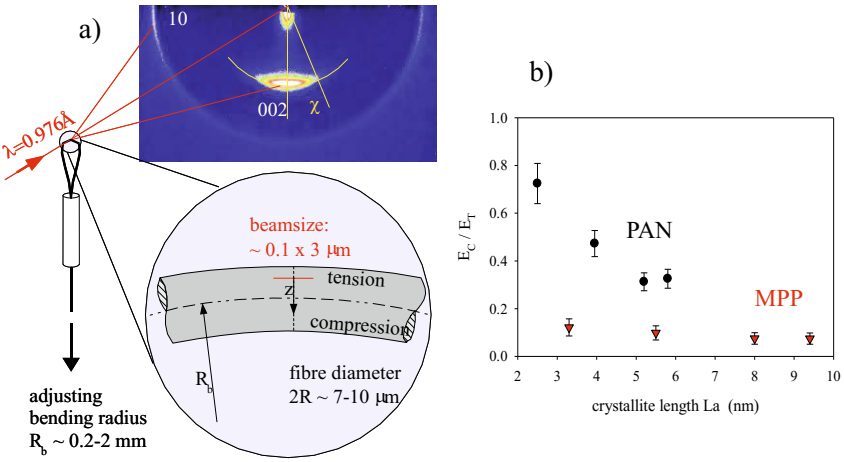

Figure 1.10. Scheme of an in-situ bending experiment with X-ray nanobeam diffraction (a), and the resulting ratio of the compressive and tensile Young's moduli for a series of PAN-based (black symbols) and MPP-based carbon fibres (red symbols). Reproduced from Loidl et al. (2005) with permission from the American Physical Society.

1.3.4. High-temperature in-situ creep

The high-temperature mechanical properties of carbon fibres are unrivalled. The tensile strength of PAN-based fibres is constant up to more than 2500 °C. It may even increase in the regime between 2000 °C and 2500 °C due to a plastification process, which leads to a higher orientation of the graphene planes (Fitzer and Hyem 1978). For pitch-based carbon fibres, also a constant tensile strength up to 1300 °C in nitrogen atmosphere was reported (Tanabe et al. 1991).

In-situ high-temperature experiments on carbon fibre bundles date back to the seventies of the last millennium (Fitzer and Weisenburger 1974). High temperature testing of fibres with a diameter in the micron range faces two main problems. One is the homogeneity of the temperature distribution within the fibre, and the other the accurate temperature measurement. Concerning the first point, carbon fibres exhibit an extremely high strength and clamping is in general not sufficient to ensure that the fibres do not slip during the experiment. One solution is keeping the fibres in a hot zone and fixing them with cold grips outside of the furnace. Then, an epoxy glue can be used, which guarantees a good contact to the fibres. Unfortunately, this procedure leads to a strong temperature inhomogeneity along the fibres. To avoid this, a more suitable approach is the application of hot grips (Villeneuve et al. 1993). This requires the attachment of fibres to a holder with a high-temperature stable ceramics-based cement. The disadvantage is that not for all test materials suitable cements are available which are harmless to the fibres themselves. In addition, the temperature of ceramic-based cements is limited to about 1500 °C (Sauder et al. 2002). For carbon fibres, graphite grips with carbon based cement were successfully applied by Sauder et al. (2004). In their work no furnace was used, but the fibres were directly heated. For carbon fibre bundles, a temperature gradient was observed in the case of direct heating, as inner fibres were shielded by outer ones. Heating single fibres leads to a more uniform temperature distribution, where a temperature gradient appears only in a small region towards the grips (Rennhofer et al. 2010; Rennhofer et al. 2014).

While direct heating is appealing due to its simplicity, the main difficulty which arises is the accurate temperature measurement of the fibres. Whereas for fibre bundles a bichromatic pyrometer can be used, for single fibres the most promising method is using the relationship between fibre temperature and the supplied electrical power. The fibre temperature has to be cross-calibrated with a pyrometer or thermocouples (Sauder et al. 2002; Rennhofer et al. 2014). This method is insensitive to a change of the resistivity of the sample as a consequence of the structural change at high temperatures, as long as the geometrical diameter of the fibre is not affected.

The tensile strength of some carbon fibres is known to increase in a range up to more than 2000 °C (Fitzer 1985). This rather unexpected effect was followed in detail by Sauder et al. (2004). It was attributed to the viscoelastic behaviour of carbon fibres at temperatures above 1400 °C, and even to viscoplastic behaviour above 1800 °C. Molecular-like deformations are activated by temperature and contribute to the shear strain, leading to viscoelasticity, whereas above a critical shear stress, the deformation becomes inelastic. This was the starting point for *in-situ* XRD of carbon fibre bundles (Rennhofer et al. 2010) and single carbon fibres (Rennhofer et al. 2014) under load at high temperatures. Three different mechanisms were proposed in these papers: Crystallite size L_a and L_C grow by a rearrangement of crystallites with graphene layers facing either their edges (in-

crease of L_a), or with graphene layers facing the planes (increase of L_C). The third possibility is a process similar to dislocation gliding, which leads to a simultaneous increase of both, L_a and L_C (Rennhofer et al. 2010). *In-situ* XRD of single carbon fibres could quantitatively show the influence of HTT on the structure of carbon fibres. As depicted in Fig. 1.11, both the pore orientation (determined from SAXS) and the crystallite orientation (determined from XRD) are unaffected up to a temperature of about 1400 °C (Rennhofer et al. 2014). Above this temperature, likewise PAN- and MPP-fibres without heat treatment exhibit a structural change, i.e., an increasingly higher orientation with increasing temperature.

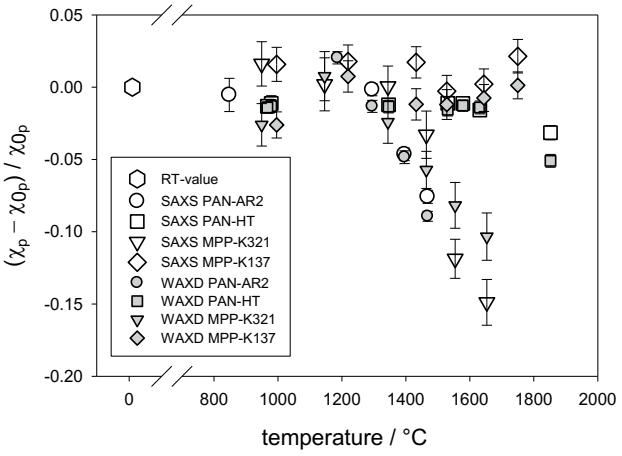

Figure 1.11. Change of pore orientation (SAXS data, open symbols) and orientation of graphene planes (XRD data, grey symbols) of different PAN-based and MPP-based fibres. All values are normalized to their initial value. Adapted from from Rennhofer et al. (2014) with permission from Elsevier.

An important observation was that a heat treatment without load leads to a complete stabilization of the structure. This concerns mechanical behaviour (the absence of creep, see (Rennhofer et al. 2006)) as well as structural parameters (no change in orientation for the fibres with a high temperature treatment as shown by Rennhofer et al. (2014) (Fig. 1.11). The same effect was observed for the size of structural features in carbon fibres. Neither the pore size (characterized by the radius of gyration from SAXS) nor the crystallite size (from the out-of-plane stacking height of graphene planes L_C) changed up to 1400 °C. However, at higher temperatures a pore and crystallite growth is observed, which can be supressed by a heat treatment without load (Fig. 1.12).

For the Young's modulus the situation is different: Although it is generally accepted that a thermal treatment leads to an increase of the Young's modulus of PAN-based fibres, the Young's modulus decreases, if stress-strain curves at different test temperatures are evaluated (Sauder et al. 2004). However, this is no contradiction. Referring to the results in Fig. 1.11 and Fig. 1.12 it can be concluded that the structure of carbon fibres is unstable, but can be stabilized by a suitable heat treatment without load. In this case, the Young's modulus increases due to the increase of orientation of the graphene planes, as shown in the sections 1.2 and 1.3. A prerequisite is of course the stability of the structure.

As carbon fibres are very sensitive to the application of temperature and strain, combining these two parameters has a strong influence on density, Young's modulus and crystallite orientation (Ozbek and Isaac 2000). This treatment of carbon fibres is named hot stretching graphitisation (Li et al. 2007). It leads to an increase of the Young's modulus and the tensile strength of rayon-based carbon fibres up to a factor of 2.5 and 1.8, respectively (Zhang et al. 2014). Certainly, this method is also limited, as for very high stresses and temperatures the fibres will disintegrate and fail.

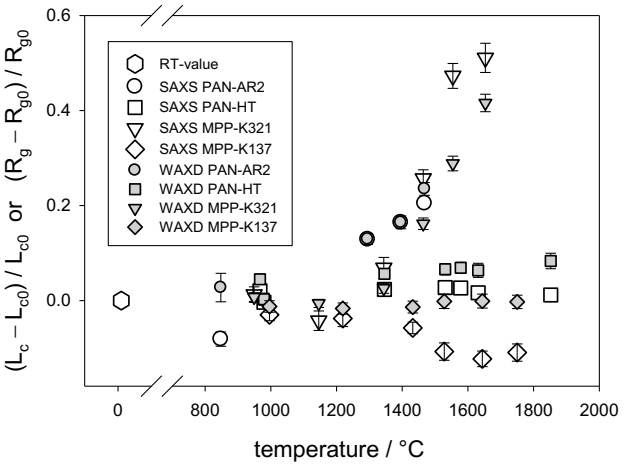

Figure 1.12. Change of pore size (radius of gyration from SAXS, open symbols) and crystallite size (stacking height of planes L_C from WAXD, grey symbols). All values are normalized to their initial value. Adapted from Rennhofer et al. (2014) with permission from Elsevier.

1.4. Conclusions

Carbon fibres are probably the best reinforcing material for stiff and strong light-weight components when larger scale structural parts are needed. Although the properties of single layer graphene or carbon nanotubes might be even superior for some applications, they are currently not available in the quantities needed. Amongst the most fascinating properties of carbon fibres are values for the Young's modulus of more than 900 GPa (Naito et al. 2008), or a tensile strength of more than 5 GPa (Naito et al. 2010). When relating to their specific values (i.e. normalised to density) these values outperform other engineering materials (e.g. steels) by typically an order of magnitude. Moreover, also the excellent thermal conductivity and biocompatibility make these materials attractive for many applications.

There is obviously a huge demand for carbon fibres for an increasing number of applications. For instance, carbon fibre reinforced composites as structural parts in aeroplanes increased from about 10 % in the Boeing 777 to more than 20 % in the Airbus A380 and to almost 50 % for the Airbus A350 and the Boeing Dreamliner. The worldwide request for sustainable and energy-saving products together with the need for a low carbon footprint will probably bring carbon fibre reinforced composites increasingly stronger into the automotive market. Cars with up to 50% weight safe due to the consequent application of carbon fibre reinforced composites for structural parts are already on the market today. It can be expected that the massive entering into this marked will drastically influence the production costs, enabling mass applications of carbon fibres and other carbon products based on "multilayer graphene".

Although intense application-driven research on carbon fibres was conducted for roughly 50 years now, there remain still some fundamental open questions. These include in particular the understanding and control of the defect structure at the atomic scale, notably covalent cross-links between graphene sheets. It is still open to discussion whether these out-of-plane bonds are located within the graphene sheets or at the boundaries of the crystallites, or whether highly crystalline regions are interlinked with more amorphous regions. In addition it is still a matter of debate how non-carbon impurities – in particular nitrogen - influence structure and mechanical properties of carbon fibres.

References

Als-Nielsen, J. and D. McMorrow (2011). *Elements of modern X-ray physics*. UK, John Wiley & Sons Ltd.

Baimpas, N., A. J. G. Lunt, I. P. Dolbnya, J. Dluhos and A. M. Korsunsky (2014). Nano-scale mapping of lattice strain and orientation inside carbon core SIC fibres by synchrotron X-ray diffraction. *Carbon* 79: 85-92.

Bennett, S. C. and D. J. Johnson (1979). Electron-Microscope Studies of Structural Heterogeneity in Pan-Based Carbon-Fibers. *Carbon* 17(1): 25-39.

Bennett, S. C., D. J. Johnson and R. Murray (1976). Structural Characterization of a High-Modulus Carbon-Fiber by High-Resolution Electron-Microscopy and Electron-Diffraction. *Carbon* 14(2): 117-122.

Diaz, A., M. Guizar-Sicairos, A. Poeppel, A. Menzel and O. Bunk (2014). Characterization of carbon fibers using X-ray phase nanotomography. *Carbon* 67: 98-103.

Edie, D. D. (1998). The effect of processing on the structure and properties of carbon fibers. *Carbon* 36(4): 345-362.

Emmerich, F. G. (2014). Young's modulus, thermal conductivity, electrical resistivity and coefficient of thermal expansion of mesophase pitch-based carbon fibers. *Carbon* 79: 274-293.

Endo, M. (1988). Structure of Mesophase Pitch-Based Carbon-Fibers. *Journal of Materials Science* 23(2): 598-605.

Fischer, L. and W. Ruland (1980). The Influence of Graphitization on the Mechanical-Properties of Carbon-Fibers. *Colloid and Polymer Science* 258(8): 917-922.

Fitzer, E. (1985). Carbon- fibres – the miracle material for temperatures between 5 and 3000 K. *High Temperature-High Pressure* 18: 479-508.

Fitzer, E. (1989). Pan-Based Carbon-Fibers Present State and Trend of the Technology from the Viewpoint of Possibilities and Limits to Influence and to Control the Fiber Properties by the Process Parameters. *Carbon* 27(5): 621-645.

Fitzer, E. and W. Frohs (1990). Modern carbon fibres from polyacrylonitrile (PAN)-polyheteroaromatics with preferred orientation. *Chemical Engineering Technology* 13: 41-49.

Fitzer, E., W. Frohs and M. Heine (1986). Optimization of Stabilization and Carbonization Treatment of Pan Fibers and Structural Characterization of the Resulting Carbon-Fibers. *Carbon* 24(4): 387-395.

Fitzer, E. and M. Heym (1978). High-temperature mechanical properties of carbon and graphite (a review). *High Temp High Pressures* 10(1): 29-66.

Fitzer, E. and L. M. Manocha (1998). *Carbon Reinforcements and Carbon/Carbon Composites*. Berlin-Heidelberg, Springer.

Fitzer, E. and S. Weisenburger (1974). Graphitization studies by in-situ X-ray technique. *Carbon* 12: 657-666.

Glatter, O. and O. Kratky (1983). *Small-angle X-ray scattering*. New York, Academic Press.

Guigon, M., A. Oberlin and G. Desarmot (1984a). Microtexture and Structure of Some High-Modulus, Pan-Base Carbon-Fibers. *Fibre Science & Technology* 20(3): 177-198.

Guigon, M., A. Oberlin and G. Desarmot (1984b). Microtexture and Structure of Some High-Tensile Strength, Pan-Base Carbon-Fibers. *Fibre Science & Technology* 20(1): 55-72.

Gupta, A., I. R. Harrison and J. Lahijani (1994). Small-Angle X-Ray-Scattering in Carbon-Fibers. *Journal of Applied Crystallography* 27: 627-636.

Helmer, T., H. Peterlik and K. Kromp (1995). Coating of Carbon-Fibers - the Strength of the Fibers. *Journal of the American Ceramic Society* 78(1): 133-136.

Holmes, M. (2013). Carbon fibre reinforced plastics market continues growth path. *Reinforced Plastics* 57(6): 24-29.

Kis, A., G. Csanyi, J. P. Salvetat, T. N. Lee, E. Couteau, A. J. Kulik, W. Benoit, J. Brugger and L. Forro (2004). Reinforcement of single-walled carbon nanotube bundles by intertube bridging. *Nature Materials* 3(3): 153-157.

Klug, H. P. and L. E. Alexander (1974). *X-ray diffraction procedures*. New York, John Wiley & Sons.

Kobayashi, T., K. Sumiya, Y. Fujii, M. Fujie, T. Takahagi and K. Tashiro (2012). Stress-induced microstructural changes and crystallite modulus of carbon fiber as measured by X-ray scattering. *Carbon* 50(3): 1163-1169.

Kobayashi, T., K. Sumiya, Y. Fujii, M. Fujie, T. Takahagi and K. Tashiro (2013). Stress concentration in carbon fiber revealed by the quantitative analysis of X-ray crystallite modulus and Raman peak shift evaluated for the variously-treated monofilaments under constant tensile forces. *Carbon* 53: 29-37.

Kobayashi, T., K. Sumiya, Y. Fukuba, M. Fujie, T. Takahagi and K. Tashiro (2011). Structural heterogeneity and stress distribution in carbon fiber monofilament as revealed by synchrotron micro-beam X-ray scattering and micro-Raman spectral measurements. *Carbon* 49(5): 1646-1652.

Kobets, L. P. and I. S. Deev (1997). Carbon fibres: Structure and mechanical properties. *Composites Science and Technology* 57(12): 1571-1580.

Kotakoski, J. and J. C. Meyer (2012). Mechanical properties of polycrystalline graphene based on a realistic atomistic model. *Physical Review B* 85(19).

Langford, J. I. and A. J. C. Wilson (1978). Scherrer after 60 Years - Survey and Some New Results in Determination of Crystallite Size. *Journal of Applied Crystallography* 11(Apr): 102-113.

Li, D. F., H. J. Wang and X. K. Wang (2007). Effect of microstructure on the modulus of PAN-based carbon fibers during high temperature treatment and hot stretching graphitization. *Journal of Materials Science* 42(12): 4642-4649.

Liu, Y. D. and S. Kumar (2012). Recent Progress in Fabrication, Structure, and Properties of Carbon Fibers. *Polymer Reviews* 52(3-4): 234-258.

Loidl, D., O. Paris, M. Burghammer, C. Riekel and H. Peterlik (2005). Direct observation of nanocrystallite buckling in carbon fibers under bending load. *Physical Review Letters* 95(22): 225501.

Loidl, D., H. Peterlik, M. Muller, C. Riekel and O. Paris (2003). Elastic moduli of nanocrystallites in carbon fibers measured by in-situ X-ray microbeam diffraction. *Carbon* 41(3): 563-570.

Meyer, J. C., C. Kisielowski, R. Erni, M. D. Rossell, M. F. Crommie and A. Zettl (2008). Direct Imaging of Lattice Atoms and Topological Defects in Graphene Membranes. *Nano Letters* 8(11): 3582-3586.

Naito, K., Y. Tanaka, J. M. Yang and Y. Kayawa (2008). Tensile properties of ultrahigh strength PAN-based, ultrahigh modulus pitch-based and high ductility pitch-based carbon fibers. *Carbon* 46(2): 189-195.

Naito, K., J. M. Yang, Y. B. Xu and Y. Kagawa (2010). Enhancing the thermal conductivity of polyacrylonitrile- and pitch-based carbon fibers by grafting carbon nanotubes on them. *Carbon* 48(6): 1849-1857.

Northolt, M. G., L. H. Veldhuizen and H. Jansen (1991). Tensile Deformation of Carbon-Fibers and the Relationship with the Modulus for Shear between the Basal Planes. *Carbon* 29(8): 1267-1279.

Ozbek, S. and D. H. Isaac (2000). Strain-induced density changes in PAN-based carbon fibres. *Carbon* 38(14): 2007-2016.

Paris, O., M. Fahrmann, E. Fahrmann, T. M. Pollock and P. Fratzl (1997). Early stages of precipitate rafting in a single crystal Ni-Al-Mo model alloy investigated by small-angle X-ray scattering and TEM. *Acta Materialia* 45(3): 1085-1097.

Paris, O., D. Loidl, M. Mueller, H. Lichtenegger and H. Peterlik (2001). Cross-sectional texture of carbon fibres analysed by scanning microbeam X-ray diffraction. *Journal of Applied Crystallography* 34: 473-479.

Paris, O., D. Loidl and H. Peterlik (2002). Texture of PAN- and pitch-based carbon fibers. *Carbon* 40(4): 551-555.

Paris, O., D. Loidl, H. Peterlik, M. Muller, H. Lichtenegger and P. Fratzl (2000). The internal structure of single carbon fibers determined by simultaneous small- and wide-angle X-ray scattering. *Journal of Applied Crystallography* 33(1): 695-699.

Paris, O. and M. Muller (2003). Scanning X-ray microdiffraction of complex materials: Diffraction geometry considerations. *Nuclear Instruments & Methods in Physics Research Section B-Beam Interactions with Materials and Atoms* 200: 390-396.

Paris, O. and H. Peterlik (2009). Carbon fibers. *Handbook of textile fibre structure*. S. J. Eichhorn, J. W. S. Hearle, M. Jaffe and T. Kikutani. Oxford, Woodhead Publishing Ltd. **2:** 353-377.

Perret, R. and W. Ruland (1968a). Profile Analysis of Random-Layer Lines. *Journal of Applied Crystallography* 1: 257-262.

Perret, R. and W. Ruland (1968b). X-Ray Small-Angle Scattering of Non-Graphitizable Carbons. *Journal of Applied Crystallography* 1: 308-313.

Perret, R. and W. Ruland (1969). Single and Multiple X-Ray Small-Angle Scattering of Carbon Fibres. *Journal of Applied Crystallography* 2: 209-218.

Perret, R. and W. Ruland (1970). Microstructure of Pan-Base Carbon Fibres. *Journal of Applied Crystallography* 3(DEC1): 525-532.

Peterlik, H. (2015). Carbon Fibers. *Ceramic Matrix Composites: Materials, Modeling and Technology*. N. P. Bansal and J. Lamon. New Jersey, John Wiley & Sons**:** 27-39.

Peterlik, H., P. Fratzl and K. Kromp (1994). Pore Structure of Carbon-Carbon Composites Studied by Small-Angle X-Ray-Scattering. *Carbon* 32(5): 939-945.

Qin, X. Y., Y. G. Lu, H. Xiao, Y. Wen and T. Yu (2012). A comparison of the effect of graphitization on microstructures and properties of polyacrylonitrile and mesophase pitch-based carbon fibers. *Carbon* 50(12): 4459-4469.

Reder, C., D. Loidl, S. Puchegger, D. Gitschthaler, H. Peterlik, K. Kromp, G. Khatibi, A. Betzwar-Kotas, P. Zimprich and B. Weiss (2003). Non-contacting strain measurements of ceramic and carbon single fibres by using the laser-speckle method. *Composites Part a-Applied Science and Manufacturing* 34(11): 1029-1033.

Rennhofer, H., D. Loidl, J. Brandstetter, K. Kromp, R. Weiss and H. Peterlik (2006). Structural change of carbon-fibres at high temperatures under load. *Fatigue & Fracture of Engineering Materials & Structures* 29(2): 167-172.

Rennhofer, H., D. Loidl, S. Puchegger and H. Peterlik (2010). Structural development of PAN-based carbon fibers studied by in situ X-ray scattering at high temperatures under load. *Carbon* 48(4): 964-971.

Rennhofer, H., S. Puchegger, S. Pabisch, C. Rentenberger, C. H. Li, S. Siegel, A. Steiger-Thirsfeld, O. Paris and H. Peterlik (2014). The structural evolution of multi-layer graphene stacks in carbon fibers under load at high temperature - A synchrotron radiation study. *Carbon* 80: 373-381.

Reynolds, W. N. and J. V. Sharp (1974). Crystal Shear Limit to Carbon-Fiber Strength. *Carbon* 12(2): 103-110.

Ruland, W. (1967a). Fourier Transform Methods for Random-Layer Line Profiles. *Acta Crystallographica* 22: 615-623.

Ruland, W. (1967b). X-Ray Studies on Preferred Orientation in Carbon Fibers. *Journal of Applied Physics* 38(9): 3585-3589.

Ruland, W. and B. Smarsly (2002). X-ray scattering of non-graphitic carbon: an improved method of evaluation. *Journal of Applied Crystallography* 35: 624-633.

Ruland, W. and H. Tompa (1968). Effect of Preferred Orientation on Intensity Distribution of (Hk) Interferences. *Carbon* 6(2): 231-236.

Sauder, C. and J. Lamon (2005). Prediction of elastic properties of carbon fibers and CVI matrices. *Carbon* 43(10): 2044-2053.

Sauder, C., J. Lamon and R. Pailler (2002). Thermomechanical properties of carbon fibers at high temoeratures up to 2000°C. *Composites Science and Technology* 62: 499-504.

Sauder, C., J. Lamon and R. Pailler (2004). The tensile behavior of carbon fibers at high temperatures up to 2400 degrees C. *Carbon* 42(4): 715-725.

Scherrer, P. (1918). Bestimmung der Größe und der inneren Struktur von Kolloidteilchen mittels Röntgenstrahlen. *Nachr. Ges. Wiss. Goettingen*: 98-100.

Shioya, M., E. Hayakawa and A. Takaku (1996). Non-hookean stress-strain response and changes in crystallite orientation of carbon fibres. *Journal of Materials Science* 31(17): 4521-4532.

Shioya, M. and A. Takaku (1985). Characterization of Microvoids in Carbon-Fibers by Absolute Small-Angle X-Ray Measurements on a Fiber Bundle. *Journal of Applied Physics* 58(11): 4074-4082.

Shioya, M. and A. Takaku (1988). Wide-Angle X-Ray-Diffraction of Materials Comprising Layer-Type Molecules. *Acta Crystallographica Section A* 44: 150-157.

Smarsly, B., M. Antonietti and T. Wolff (2002). Evaluation of the small-angle scattering of carbons using parametrization methods. *Journal of Chemical Physics* 116(6): 2618-2627.

Stribeck, N., U. Nochel and A. A. Camarillo (2008). Scanning Microbeam X-Ray Scattering of Fibers Analyzed by One-Dimensional Tomography. *Macromolecular Chemistry and Physics* 209(19): 1976-1982.

Sugimoto, Y., T. Kato, M. Shioya, T. Kobayashi, K. Sumiya and M. Fujie (2013). Structure change of carbon fibers during axial compression. *Carbon* 57: 416-424.

Tanabe, Y., E. Yasuda, A. R. Bunsell, Y. Favry, M. Inagaki and M. Sakai (1991). The Strength of Pitch-Based Carbon-Fiber at High-Temperature. *Journal of Materials Science* 26(6): 1601-1604.

Telling, R. H., C. P. Ewels, A. A. El-Barbary and M. I. Heggie (2003). Wigner defects bridge the graphite gap. *Nature Materials* 2: 333-337.

Todt, M., F. G. Rammerstorfer, O. Paris and F. D. Fischer (2010). Nanomechanical studies of the compressive behavior of carbon fibers. *Journal of Materials Science* 45(24): 6845-6848.

Tuinstra, F. and J. L. Koenig (1970). Raman Spectrum of Graphite. *Journal of Chemical Physics* 53(3): 1126-1130.

Villeneuve, J. F., D. Mocaer, R. Pailler, R. Naslain and P. Olry (1993). Tensile Testing at High-Temperatures of Ex-Pcs Si-C-O and Ex-Pcsz Si-C-N Single Filaments. *Journal of Materials Science* 28(5): 1227-1236.

Warren, B. E. (1941). X-ray diffraction from random layer lattices. *Physical Review* 59(9): 693-698.

Yazyev, O. V. and S. G. Louie (2010). Topological defects in graphene: Dislocations and grain boundaries. *Physical Review B* 81(19).

Zhang, X., Y. G. Lu, H. Xiao and H. Peterlik (2014). Effect of hot stretching graphitization on the structure and mechanical properties of rayon-based carbon fibers. *Journal of Materials Science* 49(2): 673-684.

Zickler, G. A., B. Smarsly, B. Gierlinger, H. Peterlik and O. Paris (2006). A reconsideration of the relationship between the crystallite size La of carbons determined by X-ray diffraction and Raman spectroscopy. *Carbon* 44: 3239-3246.

Zolotoyabko, E. (2013). *Basic concepts of X-ray diffraction*. Weinheim, Wiley-VCH.

Zussman, E., X. Chen, W. Ding, L. Calabri, D. A. Dikin, J. P. Quintana and R. S. Ruoff (2005). Mechanical and structural characterization of electrospun PAN-derived carbon nanofibers. *Carbon* 43(10): 2175-2185.

2 Carbon Fibre Composites: Deformation Micromechanics Analysed using Raman Spectroscopy

Robert J Young

School of Materials, University of Manchester, Manchester, M13 9PL, UK

2.1. Introduction

In the quest to understand reinforcement by high performance fibres, such as carbon fibres, the development of the subject of composite micromechanics is traced from its earliest roots. It is shown first how, employing concepts introduced by Kelly, it is possible through the use of shear-lag theory to predict the distribution of stress and strain in a single discontinuous fibre in a low-modulus matrix. For a number of years the shear-lag approach could only be used theoretically as there were no techniques available to monitor the stresses within a fibre in a resin. It is then shown that the advent of Raman spectroscopy and the discovery of stress-induced Raman bands shifts in reinforcing fibres, has enabled us to map out the stresses in individual fibres in a transparent resin matrix, and thereby both test and develop Kelly's pioneering analytical approach.

2.2. Fibre Reinforcement – Theory

2.2.1. Composite micromechanics

Interest in the mechanics of fibre reinforcement can be traced back to the first uses of high-modulus fibres to reinforce a low modulus matrix. A useful relationship developed to describe this reinforcement is the so-called 'rule of mixtures' in which, for stress parallel to the fibre direction, the Young's modulus of a composite E_c consisting of infinitely-long aligned fibres is given by an equation of the form

$$E_c = E_f V_f + E_m V_m \tag{2.1}$$

where E_f and E_m are the Young's modulus of the fibre and matrix and V_f and V_m are the volume fraction of the fibre and matrix respectively (Young and Lovell, 2011). This equation captures the essence of fibre reinforcement and is found to work well in the specific conditions outlined above when high modulus fibres are incorporated into low modulus matrix materials. Since the strain in the fibre and matrix are the same, the stress in the fibres is much higher than that in the matrix - hence the fibres take most of the load and so reinforce the polymer matrix.

O. Paris (Ed.), *Structure and Multiscale Mechanics of Carbon Nanomaterials*,
CISM International Centre for Mechanical Sciences
DOI 10.1007/ 978-3-7091-1887-0_2

In reality, however, composites do not consist of infinitely-long aligned fibres and are not always stressed parallel to the fibre direction. The full analysis of the situation in reality is the subject of many composites textbooks (Hull and Clyne, 1996; Gibson, 2012). The deformation of composites containing fibres of finite length deformed axially has been considered by a number of authors including Krenchel (1964). In addition he also analysed the situation with fibres aligned randomly in plane and also randomly in three dimensions (Krenchel, 1964).

The problem of transfer of stress from the matrix to a fibre and the subsequent variation of stress along a fibre of finite length in a matrix was first tackled properly by Kelly (1966) in his classical text, 'Strong Solids'. This ground breaking work involved both the revival of the shear lag concept of Cox (1952) and considerable intuition on his part. Indeed, in the introductory text to Chapter V of Strong Solids (Kelly, 1966) he makes the following statement. "*In this chapter we will discuss firstly how stress can be transferred between the matrix and fibre. This will be done in a semi-intuitive fashion since it is a difficult problem to solve exactly*".

Kelly's analysis became the foundation of a new research field known as 'composite micromechanics'. It will be shown how it gave us the framework for the study of fibre reinforcement at both a theoretical and practical level, also enabling us to use the approach to tailor the properties of fibre-matrix interfaces in composites.

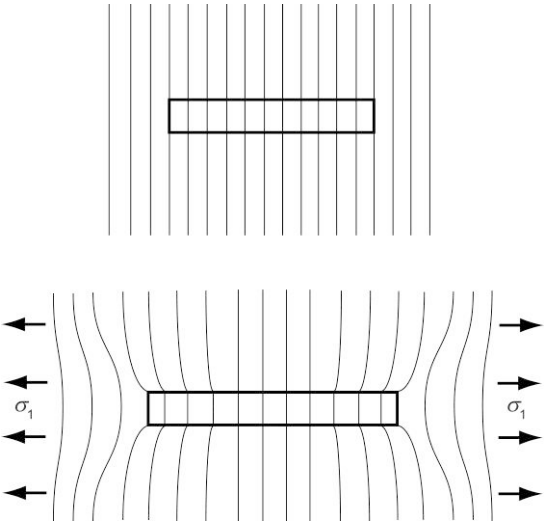

Figure 2.1. Deformation patterns for a discontinuous high-modulus fibre in a low-modulus polymer matrix. The top diagram shows the situation before deformation and the bottom diagram shows the effect of the application of a tensile stress, σ_1, parallel to the fibre. (Adapted from Young and Lovell, 2011 with permission from CRC Press).

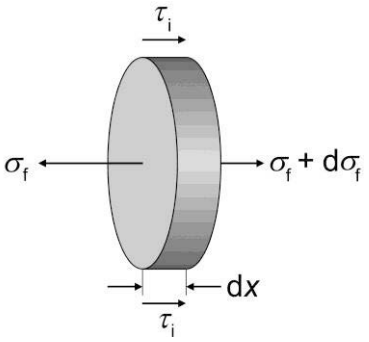

Figure 2.2. Balance of stresses acting on an element of the fibre of thickness d*x* in the composite. (Adapted from Young and Lovell, 2011 with permission from CRC Press).

2.2.2. Discontinuous Fibres

In the case of discontinuous fibres reinforcing a composite matrix, stress transfer from the matrix to the fibre takes place through a shear stress at the fibre-matrix interface as shown in Figure 2.1. It is envisaged that parallel lines perpendicular to the fibre can be drawn from the matrix through the fibre before deformation. When the system is subjected to an axial stress σ_l parallel to the fibre axis, the lines become distorted since the Young's modulus of the matrix is much lower than that of the fibre. This induces a shear stress at the fibre/matrix interface and the axial stress in the fibre builds up from zero at the fibre ends to a maximum value in the middle of the fibre. The assumption of uniform strain means that in the middle of the fibre the strain in the fibre equals that in the matrix, if the fibre is long enough. Since the fibres generally have a much higher Young's modulus than the matrix, the fibres then carry most of the stress (and hence load) in the composite – this is essentially how composites work (Kelly and Macmillan, 1986).

It is now necessary to introduce the concept of interfacial shear stress (Kelly, 1966). The relationship between the interfacial shear stress τ_i near the fibre ends and the fibre stress σ_f can be determined by using a balance of the shear forces at the interface and the tensile forces in a fibre element, as shown in Figure 2.2. The main assumption is that the force due to the shear stress τ_i at the interface is balanced by the force due to the variation of axial stress $d\sigma_f$ in the fibre such that

$$2\pi r \tau_i dx = -\pi r^2 d\sigma_f \tag{2.2}$$

and so

$$\frac{d\sigma_f}{dx} = -\frac{2\tau_i}{r} \tag{2.3}$$

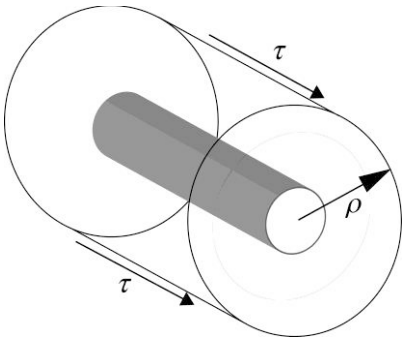

Figure 2.3. Model of a fibre undergoing deformation within a resin used in shear-lag theory. The shear stress τ acts at a radius ρ from the fibre centre. (Adapted from Young and Lovell, 2011 with permission from CRC Press).

2.2.3. Elastic Stress Transfer

The behaviour of a discontinuous fibre in a matrix can be modelled using shear lag theory, developed initially by Cox (1952) to model the mechanical properties of paper. It is assumed in the theory that the fibre is surrounded by a cylinder of resin extending to a radius ρ from the fibre centre, as show in Figure 2.3. In this model it is assumed that both the fibre and matrix deform elastically and that the fibre-matrix interface remains intact. If u is the displacement of the matrix in the fibre axial direction at a radius ρ then the shear strain γ at that position is be given by

$$\gamma = \frac{\mathrm{d}u}{\mathrm{d}\rho} \tag{2.4}$$

The shear modulus of the matrix is defined as $G_\mathrm{m} = \tau/\gamma$, hence it follows that

$$\frac{\mathrm{d}u}{\mathrm{d}\rho} = \frac{\tau}{G_\mathrm{m}} \tag{2.5}$$

The shear force per unit length carried by the matrix cylinder surface is $2\pi\rho\tau$ and is transmitted to the fibre surface though the layers of resin and so the shear stress at radius ρ is given by

$$2\pi\rho\tau = 2\pi r\tau_\mathrm{i} \tag{2.6}$$

and so

$$\tau = \left(\frac{r}{\rho}\right)\tau_\mathrm{i} \tag{2.7}$$

It follows using Equation (2.5), that

$$\frac{\mathrm{d}u}{\mathrm{d}\rho} = \left(\frac{r}{\rho}\right)\frac{\tau_\mathrm{i}}{G_\mathrm{m}} \tag{2.8}$$

It is possible to integrate this equation using the limits of the displacement at the fibre surface ($\rho = r$) of $u = u_\mathrm{f}$ and the displacement at $\rho = R$ of $u = u_\mathrm{R}$

$$\int_{u_\mathrm{f}}^{u_\mathrm{R}} \mathrm{d}u = \left(\frac{r\tau_\mathrm{i}}{G_\mathrm{m}}\right)\int_{r}^{R}\frac{\mathrm{d}\rho}{\rho} \tag{2.9}$$

hence

$$u_\mathrm{R} - u_\mathrm{f} = \left(\frac{r\tau_\mathrm{i}}{G_\mathrm{m}}\right)\ln\left(\frac{R}{r}\right) \tag{2.10}$$

These displacements can be converted into strain since the fibre strain e_f and matrix strain e_m can be approximated as $e_\mathrm{f} \approx \mathrm{d}u_\mathrm{f}/\mathrm{d}x$ and $e_\mathrm{m} \approx \mathrm{d}u_\mathrm{R}/\mathrm{d}x$. It should be noted that this shear-lag analysis is not rigorous, as shown by Nairn (1997), but it serves as a simple illustration of the process of stress transfer from the matrix to a fibre in a short-fibre composite. In addition, τ_i is given by Equation (2.3) and so differentiating Equation (2.10) with respect to x leads to

$$e_\mathrm{f} - e_\mathrm{m} = -\frac{r^2}{2G_\mathrm{m}}\left(\frac{\mathrm{d}^2\sigma_\mathrm{f}}{\mathrm{d}x^2}\right)\ln\left(\frac{R}{r}\right) \tag{2.11}$$

Furthermore, multiplying through by E_f gives

$$\frac{\mathrm{d}^2\sigma_f}{\mathrm{d}x^2} = -\frac{n^2}{r^2}\left(\sigma_\mathrm{f} - e_\mathrm{m}E_\mathrm{f}\right) \tag{2.12}$$

where

$$n = \sqrt{\frac{2G_\mathrm{m}}{E_f\ln(R/r)}}$$

This differential equation has the general solution

$$\sigma_\mathrm{f} = E_\mathrm{f}e_\mathrm{m} + C\sinh\left(\frac{nx}{r}\right) + D\cosh\left(\frac{nx}{r}\right)$$

where C and D are constants of integration. Now, equation (2.12) can be simplified and solved by double differentiation of the general solution, if it is assumed that the boundary conditions are that there is no stress transmitted across the fibre ends, i.e. if

$x = 0$ in the middle of the fibre where $\sigma_f = E_f e_m$ then $\sigma_f = 0$ at $x = \pm l/2$ where l is the length of the fibre. This leads to $C = 0$ and comparing terms gives

$$D = -\frac{E_f e_m}{\cosh(nl/2r)}$$

Finally, the equation for the distribution of fibre stress as a function of distance, x along the fibre is

$$\sigma_f = E_f e_m \left[1 - \frac{\cosh(nx/r)}{\cosh(nl/2r)}\right] \tag{2.13}$$

2.2.4. Interfacial shear stress

It is possible, now, to determine the distribution of interfacial shear stress along the fibre using Equation (2.3) which by differentiation of Equation (2.13) leads to

$$\tau_i = \frac{n}{2} E_f e_m \frac{\sinh(nx/r)}{\cosh(nl/2r)} \tag{2.14}$$

It is convenient to introduce the concept of fibre aspect ratio s (= $l/2r$) which is dimensionless so that the two above equations can be rewritten as

$$\sigma_f = E_f e_m \left[1 - \frac{\cosh\left(ns\frac{2x}{l}\right)}{\cosh(ns)}\right] \tag{2.15}$$

for the axial fibre stress and as

$$\tau_i = \frac{n}{2} E_f e_m \frac{\sinh\left(ns\frac{2x}{l}\right)}{\cosh(ns)} \tag{2.16}$$

for the interfacial shear stress. The effect of the different parameters upon the variation of stress in a fibre is demonstrated in Figure 2.4 for different values of the product ns. It can be seen from this figure that the fibre is most highly stressed, i.e. the most efficient fibre reinforcement is obtained, when the product ns is high. This therefore implies that a high aspect ratio s is desirable along with a high value of n, for the best reinforcement.

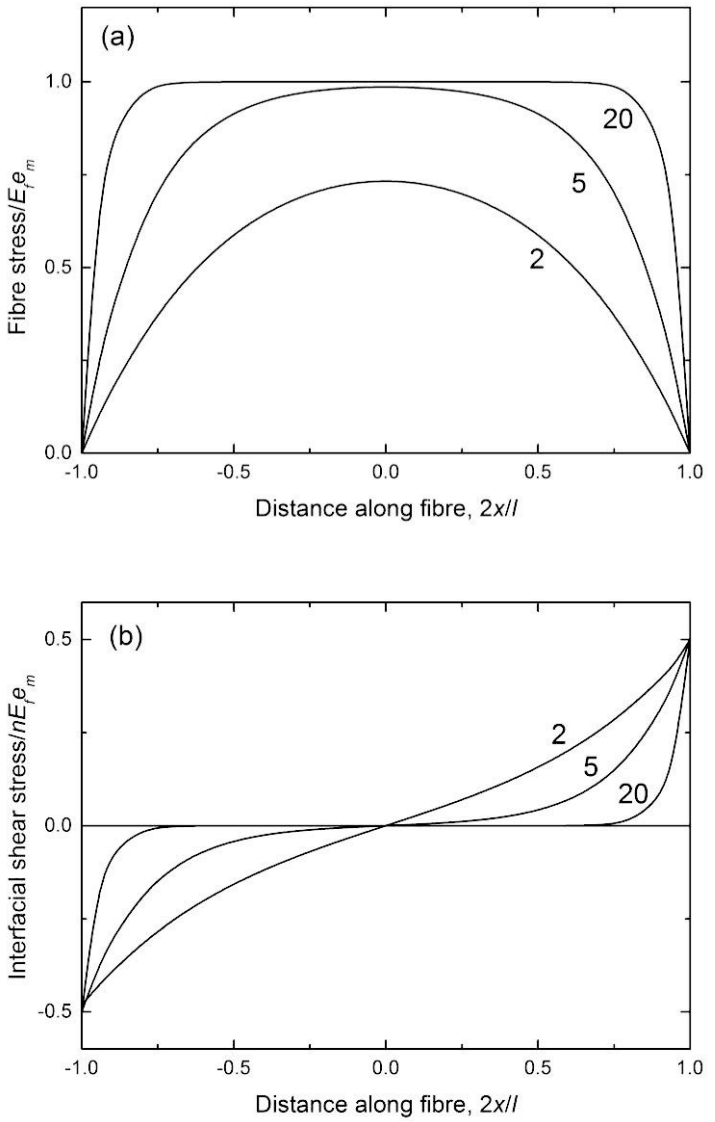

Figure 2.4. (a) Predicted variation of fibre stress with distance along the fibre for a short fibre in matrix. (b) Predicted variation of interfacial shear stress with distance along the fibre for a short fibre. The values of the product *ns* are indicated in each case. (Adapted from Young and Lovell, 2011 with permission from CRC Press).

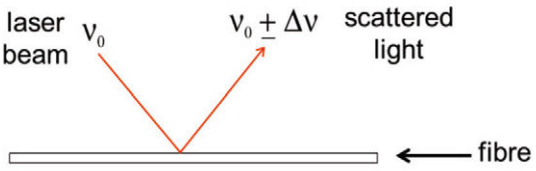

Figure 2.5. Schematic diagram of the Raman scattering from a single fibre.

2.3. Fibre Reinforcement – Experiment

2.3.1. Raman Spectra of Carbon Fibres

Following this original theoretical determination of stresses in discontinuous fibres, researchers had to rely upon it for the analysis of the micromechanics of composites, since there were initially no experimental methods available to measure local fibre stress or strain. Experimental measurement of the fibre stress and strain in discontinuous fibres in a composite under stress has now become available through the use of Raman spectroscopy (Huang and Young, 1994). This is shown schematically in Figure 2.5 where a sample such as a carbon fibre is irradiated with a laser beam of frequency, ν_0. Most of the light is scattered at the same frequency (or energy) with a small amount scattered at different frequencies of $\pm \Delta\nu$. This is the Raman scattered light and many high-performance fibres have well-defined Raman spectra (Young, 1995). Moreover when the fibres are deformed in a Raman spectrometer large stress-induced band shifts are obtained as the result of the externally applied stress distorting the covalent bond in the fibre backbone. This type of behaviour has been found for fibres such as Kevlar, polyethylene and PBO (Young, 1995). This is not so surprising since the excellent mechanical properties of high performance fibres are the result to the covalent bond in the backbone taking the load during deformation. Indeed, carbon fibres are found to behave in a similar manner.

Raman spectra are shown in Figure 2.6 for PAN- and pitch-based carbon fibres. In all cases the spectra exhibit the same appearance, that is, four well-resolved bands, namely D (~1330 cm^{-1}), G (~1580 cm^{-1}), D' (~1620 cm^{-1}) and 2D (~2660 cm^{-1}) along with additional weaker features. Figure 2.6 shows spectra for the fibres both untreated and treated with oxygen plasma to improve fibre-matrix adhesion (Montes-Morán and Young, 2002a). No differences were observed in Raman band positions and widths after the plasma treatment of the fibres but the intensity ratio of the two first-order bands D and G is always higher after the plasma treatment, showing that this treatment introduces defects and functionality into the fibre surface which we will see results in better fibre-matrix adhesion.

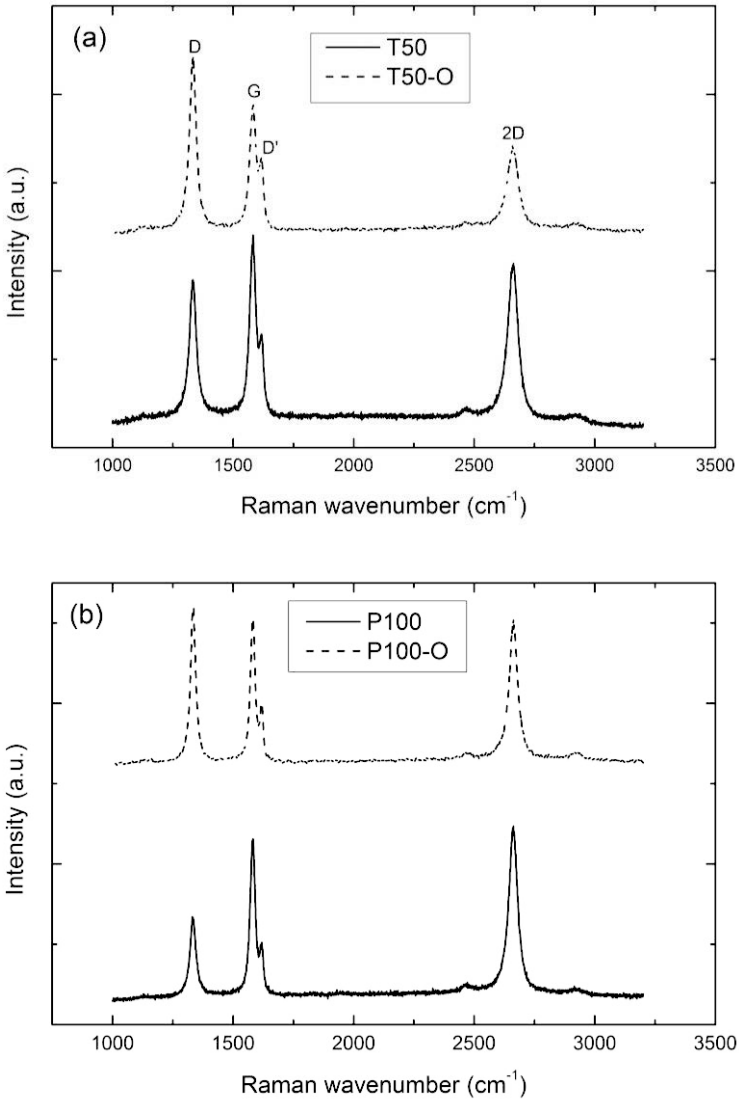

Figure 2.6. Raman spectra of (a) a T50 PAN-based carbon fibres and (b) a P100 pitch-based carbon fibres (untreated (top) and plasma treated (bottom)). (Adapted from Montes-Morán and Young, 2002b with permission from Elsevier).

2.3.2. Stress-induced Raman Band Shifts

The positions of all the Raman bands are found to shift when the carbon fibres are subjected to tensile deformation and this phenomenon can be employed to follow the deformation micromechanics.

Figure 2.7 compares the 2D band of a P100 fibre in the undeformed state and two levels of tensile and compressive strain (0.6% and 0.2% respectively). The band moves towards lower wavenumbers (red shift) when the fibre is in tension, the shift is in the opposite direction (blue shift) when in compression. A significant broadening of the Raman band when the fibre is deformed can be also seen from Figure 2.7. Similar stress-induced Raman band shift behaviour is also found for PAN-based carbon fibres such as T50.

It is found that there is an approximately linear shift of the band position with tensile strain as shown in Figure 2.8 for the 2D band of both the T50 and P100 fibres. Since the fibres deform in an approximately linearly elastic manner there is also a linear shift with stress. It will be shown that Figure 2.8 can be used as a simple calibration to determine the distribution of stress along a fibre using a Raman laser beam focused onto individual fibres inside the matrix resin.

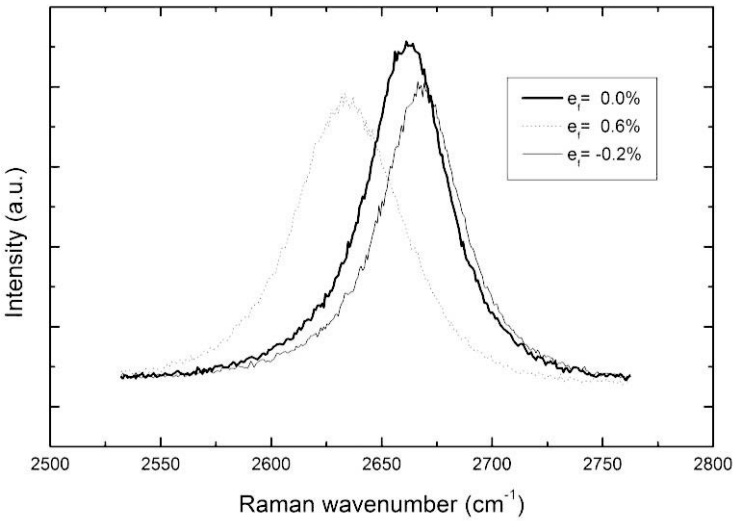

Figure 2.7. Shift of the 2D band peak on the application of tensile and compressive strain to a P100 carbon fibre. (Adapted from Montes-Morán and Young, 2002b with permission from Elsevier).

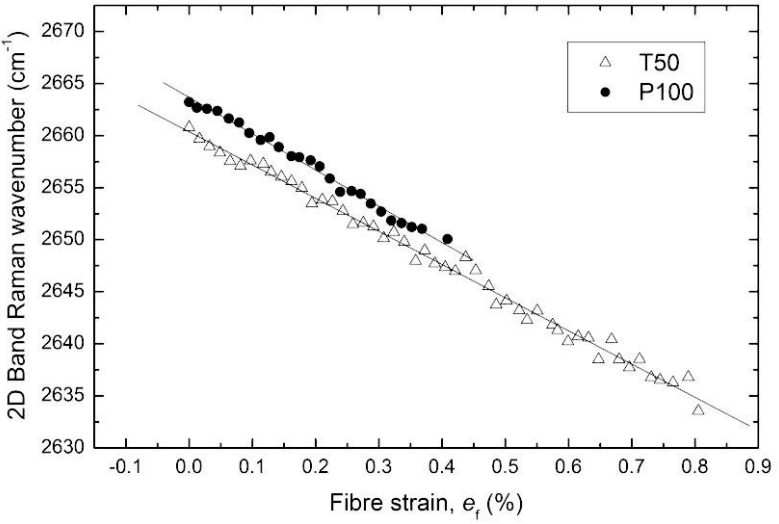

Figure 2.8. Variation of the 2D Raman band peak position with strain in as-received T50 and P100 carbon fibres. (Adapted from Cooper et al. 2001 with permission from Elsevier).

It is also important to point out that it is found that the slope of the lines in Figure 2.8 is found to depend upon the Young's modulus of the carbon fibres (Cooper et al, 2001). This is shown in Figure 2.9 for a number of pitch-based carbon fibres. The measured Raman band shifts of PAN-based carbon fibres are found to fall upon the same line (Young, 1995)

It can be seen that there is an approximately linear dependence of the band shift rate upon the fibre Young's modulus and the slope of the dashed line is of the order of -50 to -60 cm^{-1}/TPa. It is found that this is a universal relationship for the 2D band applicable to all different forms of graphitic carbon materials (Cooper et al, 2001). It is now used widely to follow the deformation behaviour of other types of sp^2 carbon materials such as carbon nanotubes (Deng et al, 2011) and graphene (Young et al, 2012). The rates of Raman band shift (per unit strain) for such materials in nano-composites are found to be proportional to the effective values of their Young's moduli.

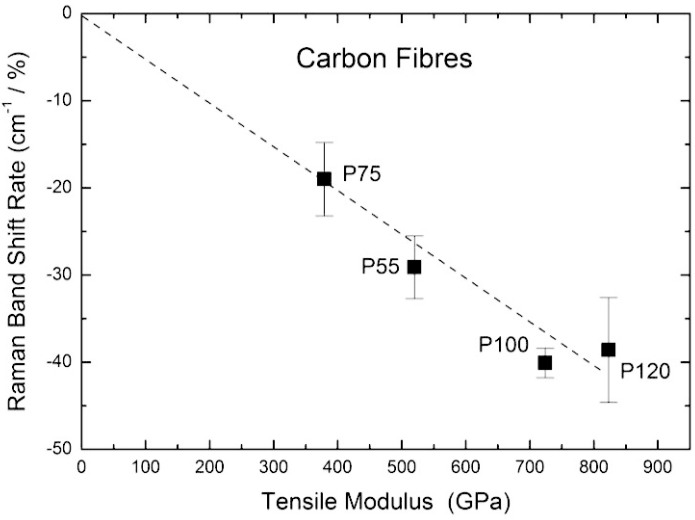

Figure 2.9. Shift rate of the 2D Raman band per unit strain as a function of the tensile Young's modulus for a number of different pitch-based carbon fibres.

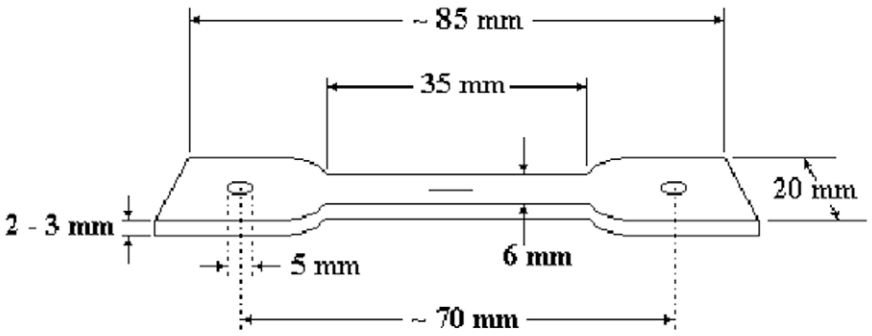

Figure 2.10. Schematic diagram of a model composite specimen containing a single fibre embedded within a transparent polymer resin. The matrix strain is determined by the resistance strain gauge and fibre strain by obtaining Raman spectra along the length of the fibre. (Adapted from Montes-Morán and Young, 2002b with permission from Elsevier).

2.3.3. Analysis of Micromechanics

The fibre stress or strain can be determined from the stress-induced shift of the Raman bands obtained from the fibre using a laser beam focused onto an individual fibre inside the matrix resin as shown in Figure 2.10. The laser beam diameter in a typical modern microscope-based Raman spectrometer is typically ~1 μm. This is significantly smaller than the usual fibre diameter (5-10 μm) which means that fibre stress and strain mapping can now be undertaken at high precision along individual fibres (Montes-Morán and Young, 2002b).

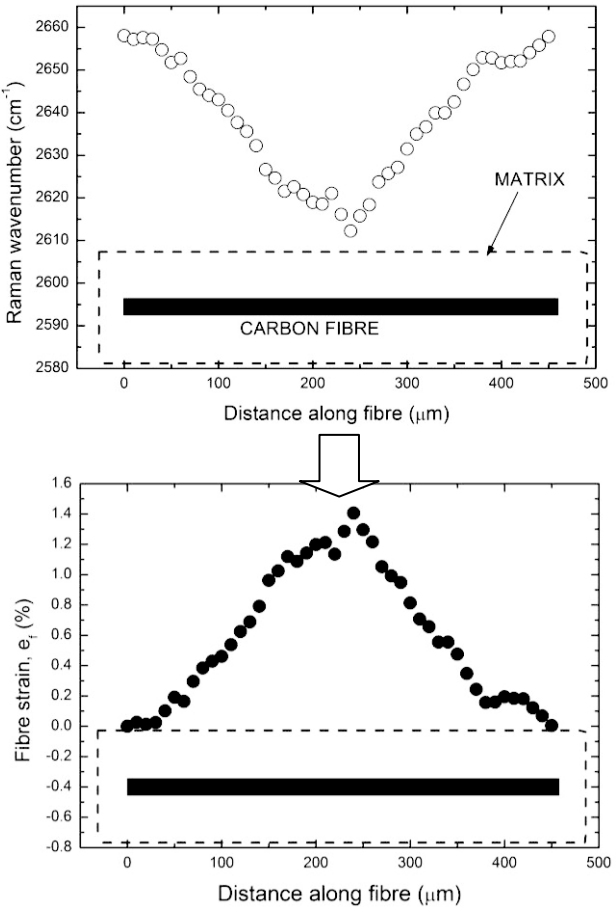

Figure 2.11. Determination of strain from Raman spectra obtained along a carbon fibre. (Adapted from Montes-Morán and Young, 2002b with permission from Elsevier).

Figure 2.11 shows how the strain along a carbon fibre within a matrix can be determined from the local positions of the 2D band in the Raman spectra obtained from the fibre. Well-defined Raman bands can be obtained from the fibres since the Raman scattering from the fibres is generally much stronger than that of the resin matrix. The band shift need to be calibrated first of all by deforming single fibres in air producing data such as those shown in Figure 2.8. The fibre strain can then be readily determined since the bands tend to shift approximately linear with strain.

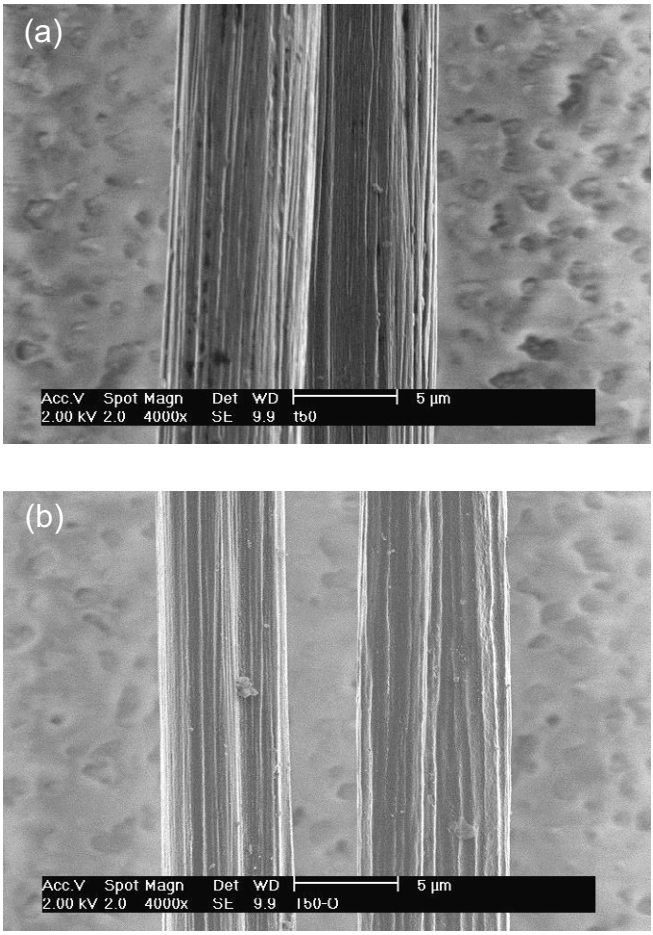

Figure 2.12. Scanning electron micrographs of (a) untreated and (b) plasma-treated T50 carbon fibres. (Adapted from Montes-Morán and Young, 2002a with permission from Elsevier).

2.3.4. Effect of Fibre Surface Treatment

The carbonaceous nature of the surface of carbon fibres leads to low levels of stress transfer from the matrix to the fibres. This lack of fibre/matrix adhesion has been partially overcome with the development of surface treatments that nowadays are implemented fully in the carbon fibre fabrication process. The conventional surface treatment used by carbon fibre manufacturers is an electrochemical oxidation. Apart from the relative success they achieve in the improvement of the interfacial properties of composites, increasing concern about environmental pollution problems has limited wide industrial application of such chemical surface treatments. The development of alternative environmental-friendly methods is an attractive prospect, from both scientific and technological points of view. Among these new methods, the surface modification of fibres by cold plasma is becoming popular and it is now an important branch of plasma technology

High modulus (HM) carbon fibres are possibly one of the most impressive reinforcements of composites in terms of specific tensile properties. These properties are related to the high degree of orientation of the crystallites and this highly graphitic character is also responsible for high level of thermal and electric conductivity. All these properties confer upon HM carbon fibres an unquestionable role in the aerospace industry. On the other hand, the enhanced crystallinity of this type of fibre is often reflected in a lower efficiency of industrial methods for increasing the carbon surface activity, in comparison with the high strength (HT) carbon fibres in that HM carbon fibres are more resistant to electrochemical oxidation than HT ones

The behaviour of untreated and unsized T50 PAN-based HM carbon fibres has been studied by Montes-Morán and Young (2002b). Plasma-treated samples were obtained (-O series) from the as-received fibres. Microwave (2.45 GHz) plasma treatments were carried out in a cylindrical chamber where the fibres were placed during 3 min of residence at 75 W. Yarns of fibres (2k, 20 cm long) were attached to a glass rack, running parallel to the cylinder axis. Oxygen (99.999%) was employed as the activation gas with a chamber pressure of 1.0 ± 0.1 mbar during the treatment time. Such a configuration gave rise to a very homogeneous treatment confirmed by several fibre surface characterisation techniques. Scanning electron micrographs of the two types of fibres are shown in Figure 2.12.

Figure 2.13(a) shows the variation of fibre strain e_f ($= \sigma_f/E_f$) along a T50-O plasma-treated carbon fibre in an epoxy resin subjected to different levels of matrix strain, e_m. The data have been fitted to Equation (2.15) using the aspect ratio of the fibre, s and by choosing appropriate values of n and it can be seen that there is a close correlation between the theoretical curves and experimental data points. Moreover, it can be seen that the strain in the fibre is that same as the matrix strain in the middle of the fibres as was assumed in the theoretical analysis earlier.

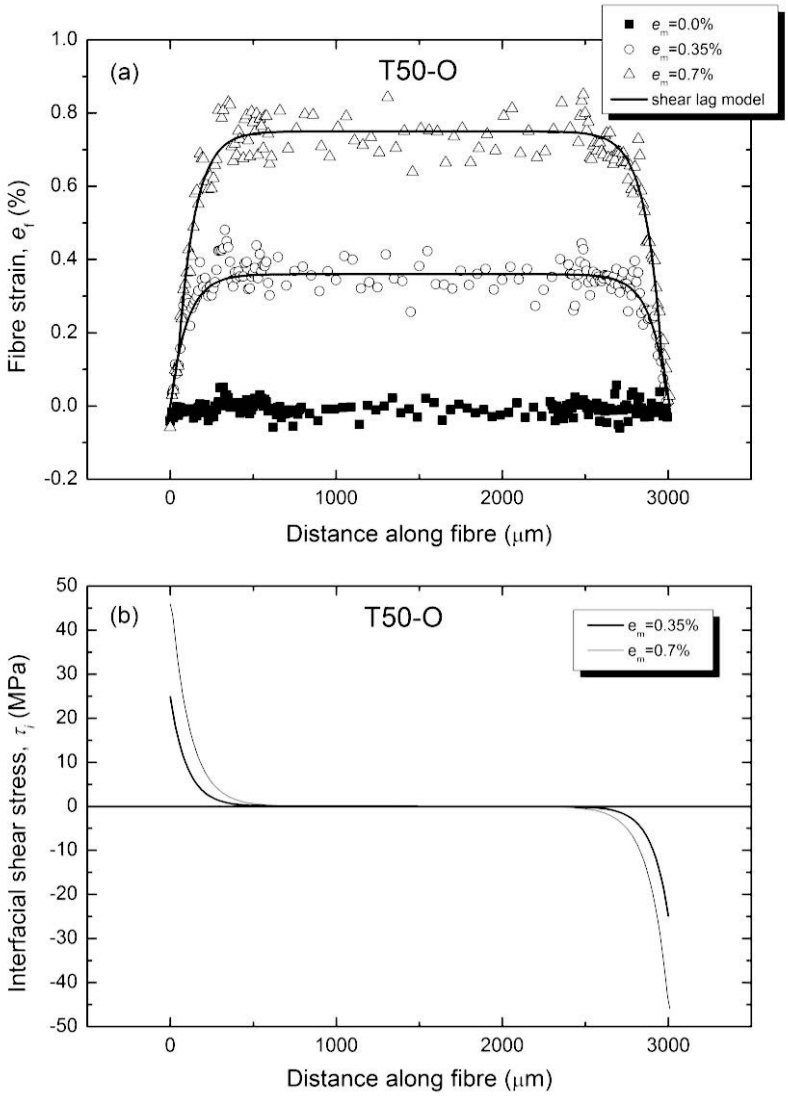

Figure 2.13. (a) Fibre strain distributions determined from strain-induced Raman band shifts at different levels of matrix strain in an epoxy resin for a plasma treated T50-O fibre up to 0.7% strain. (b) Derived distribution of interfacial shear stress along the fibre. (Adapted from Montes-Morán and Young, 2002b with permission from Elsevier).

It should be noted, however, that Equation (2.15) cannot be used to determine n since the value of $\ln(R/r)$ is essentially indeterminate. It is more appropriate to think of n as a fitting parameter that characterises the efficiency of stress transfer between the matrix and fibre (Young and Lovell, 2011). It is possible, however, to determine the distribution of interfacial shear stress τ_i along the fibre as shown in Figure 2.13(b). It can be seen that the interfacial shear stress is highest at the fibre ends (where there is a gradient of fibre strain or stress). For a matrix strain of 0.7% the value increases to around 45 MPa which is approaching the shear yield stress of the resin.

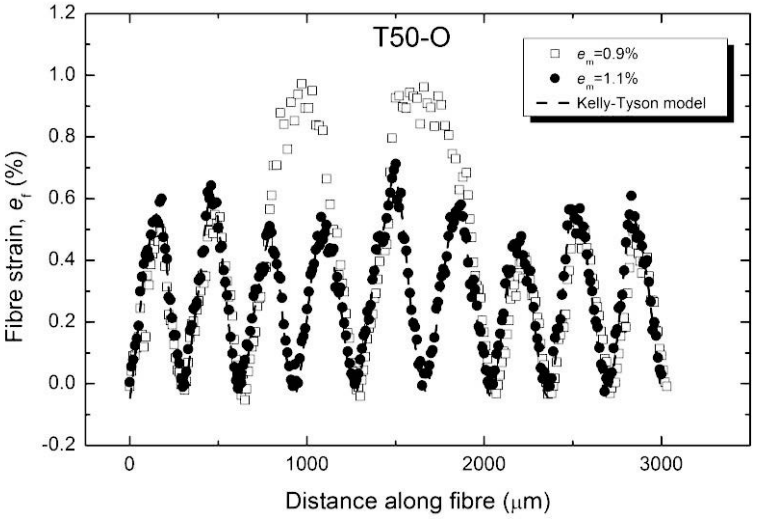

Figure 2.14. Fibre strain distributions determined from strain-induced Raman band shifts at different levels of matrix strain (up to 1.1%) in an epoxy resin for a plasma-treated T50-O fibre showing the effect of fibre fragmentation. (Adapted from Montes-Morán and Young, 2002b with permission from Elsevier).

The effect of increasing the matrix strain to 0.9% is shown in Figure 2.14. At this matrix strain level the T50-O fibre undergoes fragmentation (the strain falls to zero at the fibre breaks) which saturates at a matrix strain of 1.1%. In this case the interfacial adhesion has been lost and stress transfer at the interface is essentially frictional so that there is an approximately triangular variation along the length of each fragment (Kelly and Tyson, 1965). Moreover, it can be seen that the peak fragment strain are well below the matrix strain, indicating that once the fibres have undergone fragmentation reinforcement is diminished.

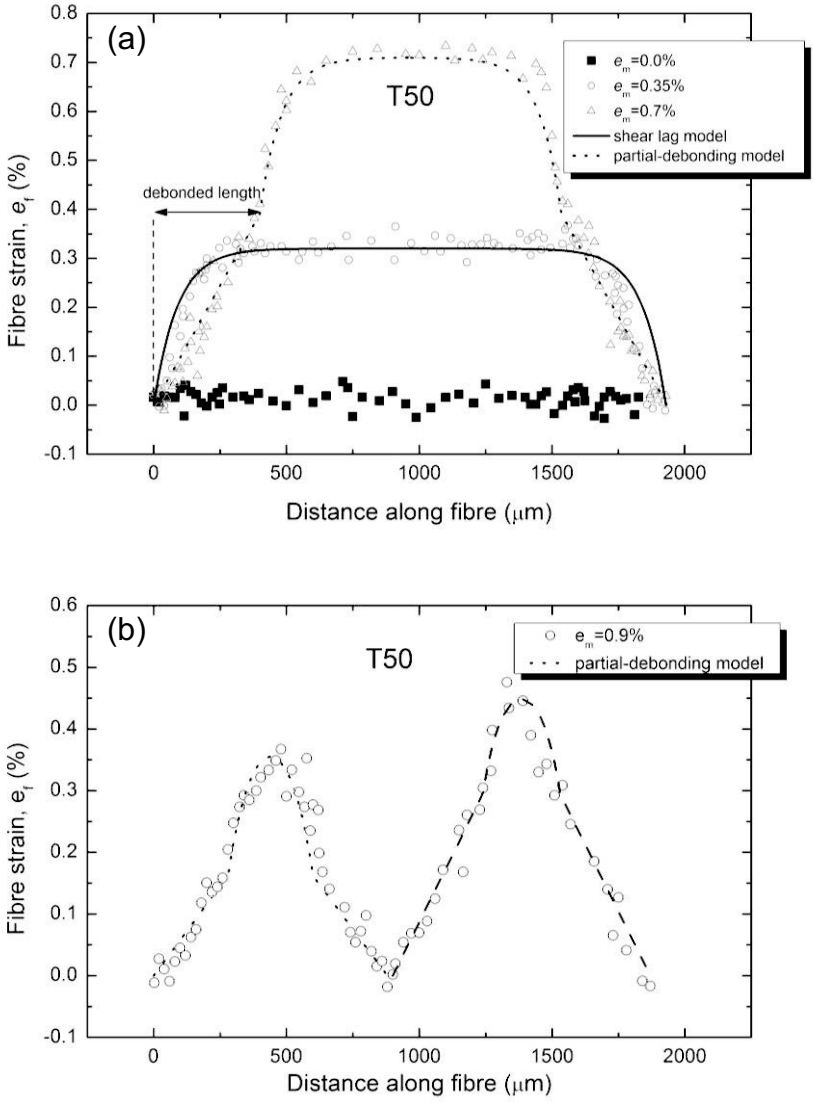

Figure 2.15. Fibre strain distributions determined from strain-induced Raman band shifts at different levels of matrix strain in an epoxy resin for an untreated T50 fibre, showing the effect of debonding at the fibre matrix interface at the higher strain level. (a) Low strain region and (b) high strain region. (Adapted from Montes-Morán and Young, 2002b with permission from Elsevier).

The behaviour of a T50 fibre that had not been modified by plasma treatment is shown in Figure 2.15. The distribution of strain in the fibre at 0.35% matrix strain follows the shear-lag model defined by Equation (2.15). When the matrix strain is increased to 0.7%, however, the distribution of strain is somewhat different with approximately linear behaviour at the two ends. This is an indication that the fibre has undergone debonding that starts at the fibre ends and progresses along the fibre as the level of matrix strain is increased (Montes-Morán and Young, 2002b). This can be compared with the behaviour shown in Figure 2.12(a) for the T50-O fibre at 0.7% strain.

At high strain Figure 2.15(b) shows that the fibre-matrix interface has failed completely and the fibre has broken into two fragments with approximately triangular strain distributions. The length of the two fragments is around 1000 μm (around 1 mm). This is significantly longer than that of the fragments of the T50-O fibre shown in Figure 2.14 which are only around 300 μm long. This is a clear demonstration of the effect of fibre surface treatment upon the micromechanics of deformation.

2.3.5. Interfacial Shear Stress

So far the ability of Raman spectroscopy has been demonstrated for the assessment, in a qualitative manner, of the changes on fibre/matrix adhesion after the plasma treatment of the T-50 HM carbon fibres. It is necessary, however, to quantify such an adhesion enhancement. For a given matrix strain level, the interfacial shear stress, τ_i, at any point along the fibre can be derived from a consideration of the balance of forces at the interface. Equation (2.3) can be recast to give

$$\tau_i(x) = \frac{E_f r}{2} \frac{de_f}{dx} \tag{2.17}$$

where E_f and r are the fibre modulus and radius, respectively, e_f is the fibre strain, and x is the position along the fibre. Since Raman spectroscopic studies of single-fibre composites provide the fibre strain distribution, it makes it also possible to determine the point-to-point variation of the interfacial shear stress using either analytical models or directly from the measured fibre strain distribution.

The maximum value of the interfacial shear stress, $\tau_{i,\,max}$, can be determined directly from plots of the variation of $\tau_i(x)$ with distance along the fibre (e.g. Figure 2.13(b)). Figure 2.16 compares the evolution of $\tau_{i,\,max}$ with applied matrix strain for a T50-O single-fibre/epoxy composite. It can be seen that τ_{max} initially increases with increasing matrix strain and reaches a maximum value of 45 MPa at 0.9% matrix strain. There are basically two possible routes to interface failure in fibre-reinforced composites. Firstly interface failure occurs when $\tau_{i,\,max}$ reaches the interfacial shear strength (IFSS), i.e., the parameter used conventionally to quantify the degree of adhesion between fibre and matrix. Secondly, the interface failure can also occur

when $\tau_{i,\,max}$ reaches the shear yield stress of the matrix, τ_y. The shear yield stress of the matrix used in this study was thought to be around 45 MPa as indicated in Figure 2.16. Hence it appears that the strength of the fibre-matrix interface in the case of the T50-O plasma-treated fibre was limited by the shear yield stress of the matrix. This should be contrasted with similar measurements upon the untreated T50 fibre where $\tau_{i,\,max}$ was found to be only around 20 MPa and its value is controlled by cohesive failure of the fibre-matrix interface (Montes-Morán and Young, 2002b).

In conclusion it is found that the fibre surface treatment increases the value of $\tau_{i,max}$ significantly compared with the untreated fibre but the strength of the interface is eventually limited by shear yielding of the epoxy resin matrix.

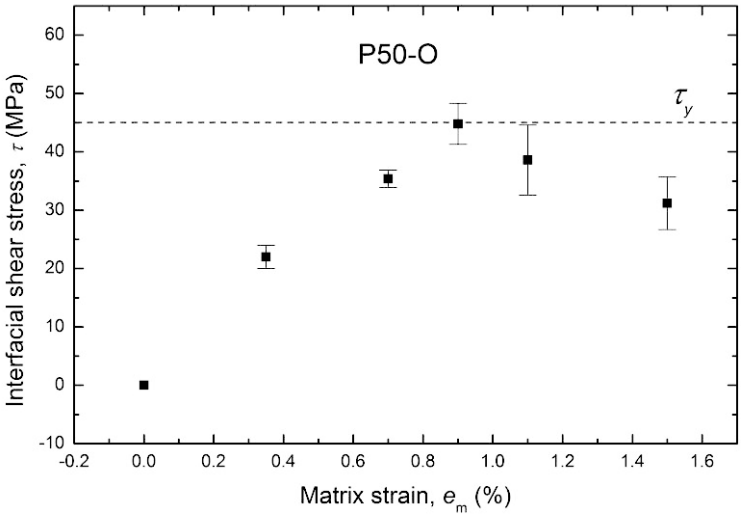

Figure 2.16. Variation of maximum interfacial shear stress $\tau_{i,\,max}$ with applied matrix strain for T50-O fibre/epoxy composite. (Adapted from Montes-Morán and Young, 2002b with permission from Elsevier).

2.4. Conclusions

It has been shown that a relatively simple theoretical analysis can be used to predict the local distribution of stress and strain in a fibre in a composite. Moreover, it has been demonstrated that the local stress or strain distribution can be determined experimentally using Raman spectroscopy and that there is a good correlation between the theoretical and experimental approaches.

It is clear that the issue of reinforcement by a single discontinuous fibre is now well understood but there are still challenges to be addressed in terms of the fundamental mechanics such as developing better analytical methods that do not suffer from some of the issues that arise using the shear-lag approach. There continue to be developments in numerical methods such as finite element analysis and the increasing power of computer systems offers scope for solving even more complex problems.

There are, however, a number of unsolved problems in the field of composite micromechanics that include:

- Fibre compression – the extent to which failure occurs through geometrical instabilities or internal compressive failure processes is still not resolved.
- Effect of fibre orientation and waviness – it is still not fully understood how fibre waviness affects properties especially when a composite is subjected to axial compression.
- Reinforcement with nanofibres and nanotubes – there is no clear indication as yet as to the extent to which the deformation of nanofibres and nanotubes within a composite can be modelled using continuum mechanics. Experience with graphene (Gong et al, 2010) now indicates that it may also be applicable in this case.

There is no doubt that future developments of the theoretical and experimental approaches outlined in this review will enable further significant advances to be made.

References

Cooper C. A., Young R. J., and Halsall M. (2001). Investigation into the deformation of carbon nanotubes and their composites through the use of Raman spectroscopy. *Composites A: Applied Science and Manufacturing*, 32:401-411.

Cox H. L. (1952). The elasticity and strength of paper and other fibrous materials. *British Journal of Applied Physics*, 3:72-79.

Deng L. B., Eichhorn S. J., Kao C. C., and Young R. J. (2011). The effective Young's modulus of carbon nanotubes in composites. *ACS Applied Materials & Interfaces*, 3:433-440.

Gong L., Kinloch I. A., Young R. J., Riaz I., Jalil R., and Novoselov K. S. (2010). Interfacial stress transfer in a graphene monolayer nanocomposite. *Advanced Materials*, 22:2694-2697.

Gibson R. F. (2012). *Principles of Composite Material Mechanics*, 3rd Edition, CRC Press, Boca Raton.

Huang Y., and Young R. J. (1994). Analysis of the fragmentation test for carbon fibre/epoxy model composites using Raman spectroscopy. *Composites Science and Technology*, 52:505-517.

Hull D., and Clyne T. W., (1996). *An Introduction to Composites Materials*, Cambridge University Press, Cambridge.

Kelly A., and Macmillan N. H. (1986). *Strong Solids*, 3rd Edition, Clarendon Press, Oxford.

Kelly A., and Tyson W. R. (1965). Tensile properties of fibre-reinforced metals - copper/tungsten and copper/molybdenum. *Journal of the Mechanics and Physics of Solids*, 13:329-350.

Kelly A. (1966). *Strong Solids*, Clarendon Press, Oxford.

Krenchel H. (1964). *Fibre Reinforcement*, Akademisk Forlag, Copenhagen.

Montes-Morán M. A., and Young R. J. (2002a). Raman spectroscopy study of HM carbon fibres: effect of plasma treatment on the interfacial properties of single fibre/epoxy composites, Part I: Fibre characterization. *Carbon*, 40:845-855.

Montes-Morán M. A., and Young R. J. (2002b). Raman spectroscopy study of HM carbon fibres: effect of plasma treatment on the interfacial properties of single fibre/epoxy composites, Part II: Characterisation of the fibre/matrix interface. *Carbon*, 40:857-875.

Nairn J. A. (1997). On the use of shear-lag methods for analysis of stress transfer unidirectional composites. *Mechanics of Materials*, 26:63-80.

Young R. J. (1995). Monitoring deformation processes in high-performance fibres using Raman spectroscopy. *Journal of the Textile Institute*, 86:360-381.

Young R. J., Kinloch I. A., Gong L., and Novoselov K. S. (2012). The mechanics of graphene nanocomposites: A review', *Composites Science and Technology*, 72:1459–1476.

Young R. J., and Lovell P. A. (2011). *Introduction to Polymers*, CRC Press, Boca Raton. Chapter 24

3 Carbon Nanotubes and Nanotube-Based Composites: Deformation Micromechanics

Robert J Young and Libo Deng

School of Materials, University of Manchester, Manchester, M13 9PL, UK

3.1. Introduction

The pioneering work upon the two-dimensional graphene, a one-atom thick planar sheet of sp^2-bonded carbon atoms, was awarded the Nobel Prize in Physics in 2010. Carbon nanotubes (CNTs) are related nanostructures that can be envisaged as being made by rolling the two-dimensional graphene sheets into cylinders. This gives rise to fascinating materials, which have been attracting great deal of research interest in the last two decades, due to their impressive properties and wide range of potential applications. Their applications in mechanical reinforcement and electronic device are particularly promising. The excellent mechanical properties of nanotubes are related to the strong sp^2 hybridized carbon-carbon bonds and the perfect hexagonal structure in the graphene sheet from which they are built up, while the unique electronic properties are due largely to the one-dimensional confinement of electronic and phonon states which results in van Hove singularities in the density of states (DOS) of nanotubes (Dresselhaus et al., 2005).

Raman spectroscopy has become an important technique to both characterise the electronic structure and follow the deformation behaviour of CNTs. This technique provides insight into their intrinsic properties and the interaction of nanotubes with the surrounding environment, as well as the mechanical reinforcing efficiency of nanotubes in composites.

This chapter aims to give a brief introduction to the structure, preparation and properties of carbon nanotubes, and to review the background and main properties of nanotube Raman bands, with an emphasis on the effect of deformation upon the Raman bands. More comprehensive reviews on the physical properties and Raman spectroscopy of CNTs can be found elsewhere (Dresselhaus et al., 2002 and Dresselhaus et al., 2005).

3.2. The Preparation, Structure and Properties of CNTs

3.2.1. Preparation

Three methods are employed widely to prepare nanotubes: arc-discharge, laser ablation, and chemical vapour deposition (CVD) (Moniruzzaman and Winey, 2006).

O. Paris (Ed.), *Structure and Multiscale Mechanics of Carbon Nanomaterials*,
CISM International Centre for Mechanical Sciences
DOI 10.1007/ 978-3-7091-1887-0_3

The first two methods involve the condensation of hot gaseous carbon atoms generated from the evaporation of solid carbon, while in the CVD process, a gaseous carbon source is decomposed catalytically and the nanotubes are deposited on a substrate or grown from a substrate. Catalytic-grown nanotubes have fewer impurities but have more defects than the arc-grown nanotubes. The arc-grown CNTs are therefore mechanically stronger than the CVD-CNTs, but the latter will almost certainly find more applications. This is because the length and structure are more controllable in a CVD process, and this process is also more amenable to being scaled-up for industrial production (Moniruzzaman and Winey, 2006).

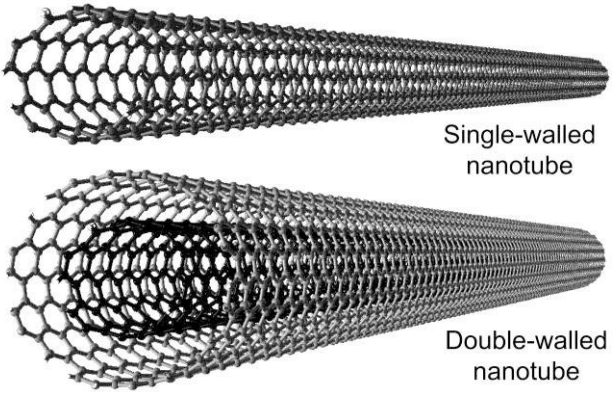

Figure 3.1. Schematic representations of single- and double-walled carbon nanotubes. Multi-walled nanotubes can have up to 20 layers of nested tubes. (Courtesy of Dr F. Ding, Hong Kong Polytechnic University). (Adapted from Young and Lovell, 2011 with permission from CRC Press).

3.2.2. Structure

CNTs are long cylinders of covalently bonded carbon atoms. The carbon atoms are arranged on a hexagonal network and each of them has three neighbours with which they form strong sp^2 hybridized carbon-carbon bonds. There are basically two main types of carbon nanotubes according to the numbers of graphene cylinder in their structure as shown in Figure 3.1: single-wall nanotubes (SWNTs) and multi-wall nanotubes (MWNTs); double-wall nanotubes (DWNTs) are a special case of MWNTs (Saito et al., 1998).

An SWNT can be considered as a seamless roll of a single graphene sheet. The nanotube is one atom in thickness (which is 0.34 nm), tens of atoms in circumference, and up to a few millimetres in length. The different ways of rolling graphene into

tubes are described by the chirality as defined by the circumferential vector (Saito et al., 1998; Moniruzzaman and Winey, 2006)

$$\vec{C}_h = n\vec{a}_1 + m\vec{a}_2 \tag{3.1}$$

where n and m is the length along the unit vectors of the two lattice vectors, respectively, as shown in Figure 3.2. MWNTs are made of many coaxial single-wall nanotubes with an interlayer separation of 0.34 nm, and each of the walls may possess different chiralities.

The diameter and chiral angle are two important parameters that define the nanotube structure, which can be derived from the chirality indices (n, m). The diameter d_t is given by:

$$d_t = a_0\sqrt{(n^2 + nm + m^2)}/\pi \tag{3.2}$$

where a_0 is the length of lattice vector and has a value of 0.249 nm. The chiral angle Φ is defined as the angle between the chiral vector and the zigzag direction x (Figure 3.2). It varies in the range of 0 - 30º and is given by:

$$\Phi = \tan^{-1}\frac{\sqrt{3}n}{2m+n} \tag{3.3}$$

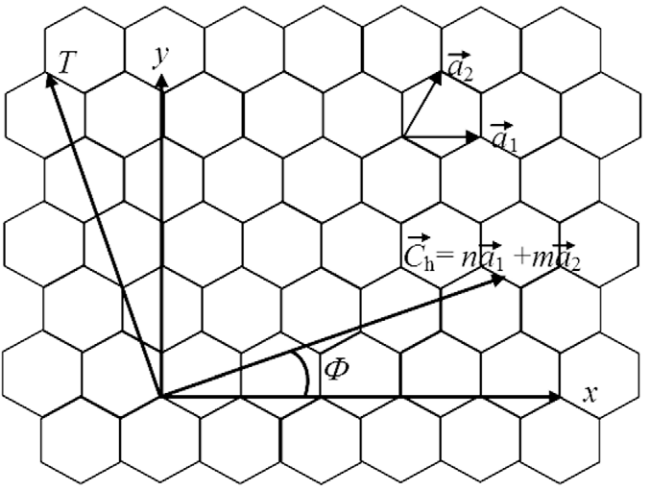

Figure 3.2. Schematic diagram of a graphene sheet showing the chiral vectors.

3.2.3. Properties

The high aspect ratio, the strong sp^2 carbon-carbon bonds, and the one-dimensional confinement of electronic states, confer CNTs with a range of interesting physical properties such as unique electronic properties, excellent mechanical properties, and good thermal conductivity and electrical conductivity.

SWNTs behave as either semiconductors or metals, depending on the remainder of (n-m) divided by 3: those with n-m = 3k are metallic nanotubes while those with n-m = 3k±1 are semiconducting nanotubes (where k is integer) (Moniruzzaman and Winey, 2006). Therefore, approximately one third of SWNTs are metallic and the rest are semiconducting. For semiconducting nanotubes, the band gap decreases as the diameter increases.

Deformation has a significant effect on electronic structure of nanotubes. The effect of strain on the electronic structure depends on the deformation mode (i.e. uniaxial strain, torsional strain or radial deformation) and nanotube chirality. For example, uniaxial strain opens the band gap of non-armchair metallic nanotubes but has no effect on armchair nanotubes. Torsional strain can change the electronic structure of armchair nanotubes but does not affect zigzag nanotubes.

Nanotubes and graphite share the same hexagonal network of sp^2 carbons in their structure. Mechanical properties of nanotubes are therefore expected to be comparable with graphene which has in-plane Young's modulus of 1.06 TPa and strength of 130 GPa (Coleman et al., 2006a, 2006b). In fact, some computer simulation work soon after the discovery of nanotubes did predict similar mechanical properties to those of graphene (Lu, 1997). The first actual mechanical measurement on nanotubes was performed using transmission electron microscopy (TEM) (Treacy et al, 1996). Since then, bending tests using an atomic force microscopy (AFM) tip have been developed and used widely (Wong et al., 1997). A Young's modulus for SWNTs of 1.0 TPa and 0.3 - 0.9 TPa for MWNTs, and tensile strength of 50 - 150 GPa for SWNTs and 10 - 50 GPa for MWNTs are generally quoted by the scientific community. The actual values vary from nanotube to nanotube, cover a wide range, and depend on many factors such as the nanotube type, preparation method, purity and diameter.

Theoretical work has predicted a very high thermal conductivity for CNTs, of approximately 6000 W m^{-1} K^{-1}, while experimental work has recorded a value of 3000 W m^{-1} K^{-1}. MWNTs have been found to also exhibit good electrical conductivity, which is in the range of 10^6 - 10^7 S/m (As a comparison, the copper has a thermal conductivity of 400 W m^{-1} K^{-1} and electrical conductivity of 6×10^7 S/m). The physical properties of CNTs and a comparison with typical engineering materials are summarized in Table 3.1.

Table 3.1. Physical properties of CNTs compared with other engineering materials

Material	Mechanical properties		Thermal conductivity ($W\ m^{-1}\ K^{-1}$)	Electrical conductivity (S/m)
	Modulus (GPa)	Strength (GPa)		
Carbon nanotubes	1000	30 - 100	>3000	10^6 - 10^7
Carbon fibre (Pitch)	300 - 700	5 - 7	1000	2 - 8.5×10^6
Copper	110 - 128		400	6×10^7

3.3. Raman spectroscopy of SWNTs

The Raman spectroscopy of CNTs has becoming an important research topic since the first work was published in 1997. This technique is particularly useful for investigation of the properties of SWNTs due to the resonance effects and the discussion in the following section is confined to SWNTs only.

Four characteristic Raman bands, namely the radial breathing modes (RBMs), G-band, D-band and 2D -band (also called the G'-band) carry a large amount of structural information and have been studied in most detail, although several other weaker and broader features have also been observed in the nanotube spectra. A typical Raman spectrum of SWNTs is shown in Figure 3.3.

3.3.1. Radial Breathing Modes

The RBM features appear between 100 and 500 cm^{-1}, and are vibrational modes in which all the carbon atoms move radially, perpendicular to the nanotube axis, as if the nanotube was breathing. The lineshape of the RBM peak for a single nanotube is a simple Lorentzian line and the natural linewidth is 3 cm^{-1}. The RBM peak is quite often broadened to exhibit a linewidth of 4 - 10 cm^{-1} due to the interaction of nanotubes with the environment (Dresselhaus et al., 2005).

The RBM frequency ω_{RBM} is independent of the chiral angle Φ but depends linearly on the reciprocal nanotube diameter d_t through the relation (Dresselhaus et al., 2002 and Dresselhaus et al., 2005):

$$\omega_{\mathrm{RBM}} = \frac{A}{d_t} + B \tag{3.4}$$

where the parameters A and B (B is associated with the effect of environment on the ω_{RBM}) are determined experimentally. Although the form of the relation is well established, a variety of values for the parameters A and B have been found by different groups with different samples. The interaction with the different environments leads to each sample having its own set of parameters to determine d_t from ω_{RBM}. Table 3.2 summarizes the values for the ω_{RBM}/d_t relation reported in the literature.

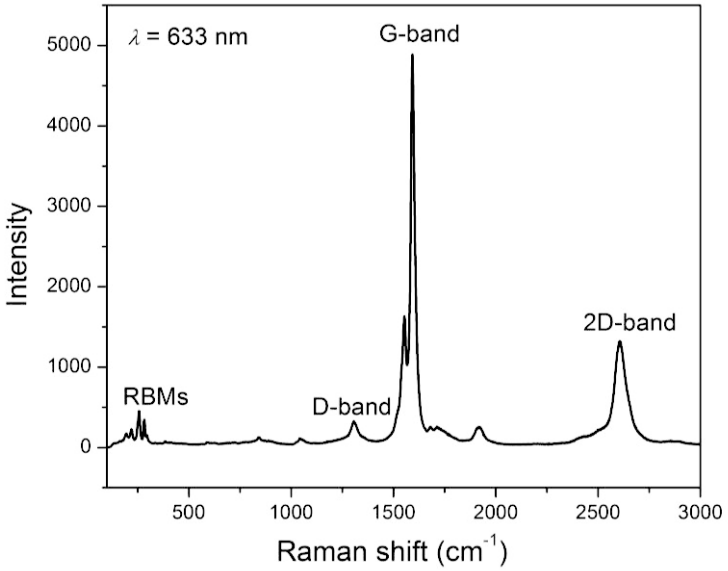

Figure 3.3. A typical Raman spectrum of SWNTs showing the four characteristic bands.

Table 3.2. A and B values for Equation (3.4) reported in the literature.

Sample	A	B	Reference
SWNTs on a silicon substrate	248	0	Jorio et al., 2001
SDS-dispersed HiPco SWNTs	223.5	12.5	Bachilo et al., 2002
SDS-dispersed HiPco SWNTs	218	17	Fantini et al., 2004
Alcohol-assisted CVD-SWNTs	217	15	Araujo et al., 2007
Laser ablation bundled SWNTs	232	0	Milnera et al., 2000

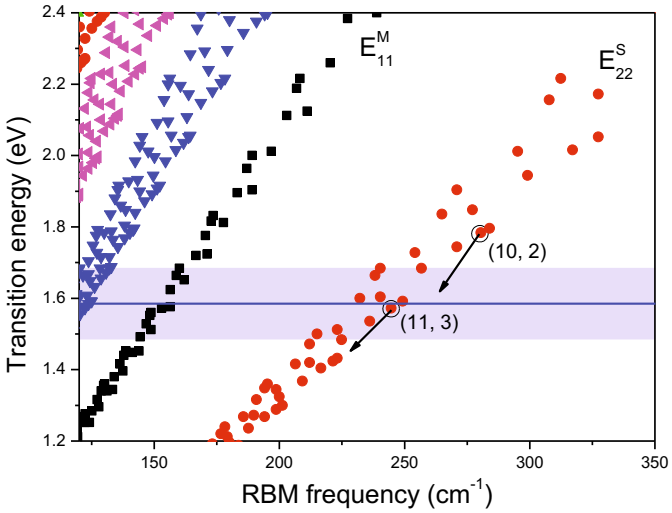

Figure 3.4. A theoretical Kataura plot for individual SWNTs. The blue box indicates a resonance window for an excitation laser with energy of 1.58 eV. The arrows indicate the down-shift of E_{22}^{S} for two individual nanotubes when they aggregate into bundles, showing the roping effect on RBMs. All E_{ii} values were calculated using a nearest-tight binding model.

The most important information one can determine from the RBMs is the nanotube chirality, which is given by the (n, m) indices. The identification of the (n, m) indices is based on resonance theory which gives rise to the so-called Kataura plot which is a plot of interband transition energy E_{ii} versus nanotube diameter (or ω_{RBM}) (Kataura et al., 1999). The diameter can be determined from ω_{RBM} using Equation (3.4). The interband transition energy E_{ii} for the Kataura plot can be determined using resonance Raman spectroscopy equipped with a tunable laser (this method gives a precision of 3 meV for each E_{ii}), photoluminescence spectroscopy (with the precision of 20 - 30 meV) and theoretical approaches (Bachilo et al., 2002 and Fantini et al., 2004).

The value of E_{ii} is influenced by many factors such as whether the nanotubes are in bundles or isolated, whether they are wrapped by surfactants, the type of solvent in which nanotubes are dispersed, the type of substrate and the temperature. As for the influence of intertube interaction, the E_{ii} value shifts to lower energies and RBM peaks shift to lower frequencies by 1 - 10 cm^{-1} when isolated individual nanotubes aggregate into bundles. Theoretical studies predicted that the value of E_{ii} can shift as much as 0.25 eV upon bundling (O'Connell et al., 2004), and they determined ex-

experimentally an average value of 86 meV for the down-shift. The down-shift of the E_{ii} may lead to the so-called "roping effect" on RBM peaks, that is, some RBMs that are seen in the isolated state disappear when in bundles (there is an opposite case: some RBMs that are absent for isolated nanotubes appear when they are in bundles) (Doorn et al., 2003 and Heller et al., 2005). Figure 3.4 illustrates the roping effect upon two nanotubes: the (10, 2) and (11, 3) nanotubes that are off resonance and in resonance with a 785 nm laser, respectively, when isolated, are brought into and outside the resonance window when in bundles due to the changes of E_{ii}.

The uncertainties in E_{ii} values and $\omega_{\mathrm{RBM}}/d_{\mathrm{t}}$ relation bring difficulty in identifying nanotube chirality. Additional information for identification of nanotube chirality can be provided by deforming nanotubes which affects the electronic structure and consequently the Raman bands. Lucas and Young (2007) managed to assign a unique nanotube structure to each RBM separated by just 1 - 2 cm^{-1} by studying the effect of deformation upon the RBM intensity.

3.3.2. G-band

The G-band originates from the vibrations of neighbouring carbon atoms in opposite direction along the nanotube axis and its circumference and is observed in the 1500 - 1605 cm^{-1} region for SWNTs. In most cases, the G-band can be fitted with two most intense peaks labeled by G^+, for atomic vibration along the tube axis; and G^-, for modes with atomic vibration along the circumferential direction (Dresselhaus et al., 2002). ω_{G^+} is independent of the diameter while ω_{G^-} decreases with the decreasing diameter. The dependence of ω_{G} on nanotube diameter is given by:

$$\omega_{\mathrm{G}^-} = \omega_{\mathrm{G}^+} - \xi / d_{\mathrm{t}}^2 \tag{3.5}$$

where ξ has a value of 47.7 nm^2 cm^{-1} and 79.5 nm^2 cm^{-1} for semiconducting and metallic nanotubes, respectively (Dresselhaus et al., 2005). This equation allows the determination of nanotube diameter when the RBM is absent, although the information is less accurate than direct RBM measurement.

The lineshape of the G-band of semiconducting SWNTs is quite different from that of metallic nanotubes. Specifically, the difference in G^- lineshape allows one to readily distinguish between semiconducting and metallic nanotubes (Dresselhaus et al., 2002). For semiconducting nanotubes both the G^+ and G^- peaks are of a Lorentzian profile with linewidths of 6 - 15 cm^{-1}, whereas for metallic nanotubes, the G^+ peak has a Lorentzian lineshape similar to the semiconducting tubes, but the G^- peak is a broad and asymmetry peak and is usually fitted using a Breit-Wigner-Fano (BWF) function (Dresselhaus et al., 2002). The BWF broadening is related to free electrons in nanotubes with metallic character. There are however conflicting reports in the G^- lineshape of metallic nanotubes. Paillet et al. (2005) demonstrated

BWF line is an intrinsic feature of metallic nanotube bundles but the BWF component vanishes in isolated metallic nanotubes. In contrast, Bose et al. (2005) predicted the BWF lineshape to be intrinsic in single metallic nanotubes.

Interacting with the environment can also influence the G-band of nanotubes significantly. Important environmental factors include the aggregation state (i.e. isolated nanotube or bundles), the charge transfer arising from doping a SWNT and the substrate. For SWNTs debundled with the assistance of dispersant, the dispersant molecules wrapping the nanotube can suppress the vibration in the circumferential direction, giving rise to a weak G^- peak (Kawamoto et al., 2006). In addition, the G^+ linewidth is lower for individual nanotube than for nanotube bundles. As for the influence of charge transfer, removing charge from a SWNT (i.e. p-doping or oxidizing) leads to an up-shift of the G^+ peak around 1592 cm^{-1}, while adding charge (i.e. n-doping or reducing) to a SWNT results in a down-shift (Wise et al., 2004).

3.3.3. D-band and 2D-band

The D-band and its second order overtone 2D-band (also called 2D band) are observed in the 1250 - 1450 cm^{-1} and 2500 - 2900 cm^{-1} regions, respectively. The D-band scattering involves one-phonon emission while the 2D-band scattering involves emission of two phonons. The causes of these two bands both involve a double resonance Raman process as shown in Figure 3.5. The D-band scattering consists of one-elastic and one-inelastic scattering process, in which the elastic scattering arises from defects (such as vacancies, impurities and hetero-atoms) in the crystal. On the other hand, the 2D-band is due to two-inelastic scattering process, in which the two emitted phonons possess vectors of $+\boldsymbol{q}$ and $-\boldsymbol{q}$, respectively. The momentum constant is therefore automatically preserved and no defect is required to observe the 2D-band.

The D- and 2D- bands are known as dispersive bands because they change their frequencies when the laser excitation energy changes. For example, a function $\omega_{2D}=2420+106E_{laser}$ has been found for the dependence of 2D-band position upon E_{laser} (Dresselhaus et al., 2002). The dependence of ω_D and ω_{2D} on E_{laser} is due to the dependence of phonon energy on E_{laser}.

Both the ω_D and ω_{2D} are found to be dependent also on both the nanotube diameter d_t and the chiral angle Φ, a property unique to nanotubes. The diameter dependence is a more complex issue. When considering the ω_{2D}/d_t dependence in a broad range of d_t where different E_{ii} interband transitions are involved in resonance, the value of the ω_{2D} decreases as the d_t decreases and follows the relation: $\omega_{2D}=2708.1-35.4/d_t$. On the other hand, when analysing the data within the same interband transition where the d_t varies over a small range, ω_{2D} decreases with increasing d_t through the dependence: $\omega_{2D}=\omega_0+C_i/d_t$, where the parameter C_i has a value of 34 nm cm^{-1} for E_{33}^S and 182 nm cm^{-1} for E_{44}^S (Filho et al., 2003).

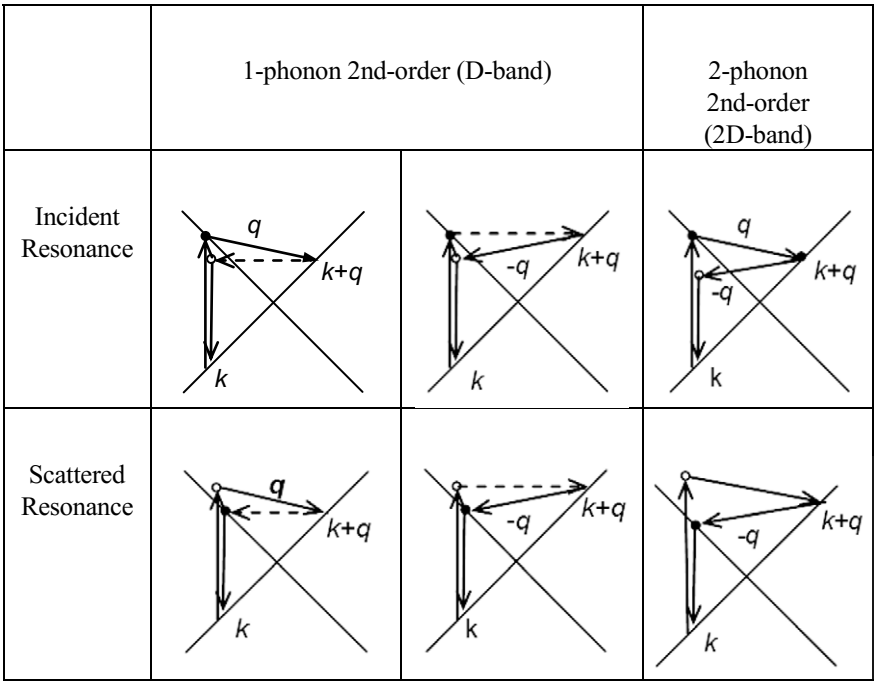

Figure 3.5. Second-order resonance Raman spectral processes for D-band and 2D-band. The dashed lines indicate elastic scattering. Resonance points are shown as solid circles.

In most cases, the 2D-band shows a single Lorentzian peak, but a two-peak 2D-band has also been observed from individual SWNTs. The two-peak structure of 2D-band is observed when two independent double resonance processes are involved. Specifically, for semiconducting SWNTs this occurs when one level of the E_{ii} transition is in resonance with the incident laser while a lower level of interband transition is in resonance with the scattered photon; while for metallic SWNTs, each E_{ii} transition is split into an upper and lower subbands, and both the upper and lower subbands can be involved simultaneously in the two independent resonance processes (Filho et al., 2002a and Filho et al., 2002b). There are 16 (n, m) nanotubes that exhibits a two-peak 2D-band when excited with a 514 nm laser.

For individual SWNTs, the linewidth ranges from 7 to 40 cm^{-1} for the D-band and from 30 to 35 cm^{-1} for the 2D-band. The 2D-band linewidth is a measure of the dispersion state as its value decreases with the decrease of bundle size (Cardenas and Gromov, 2009). The 2D-band position is most sensitive to stress and is usually

employed to follow the deformation of nanotubes. The effect of both the dispersion state and deformation on nanotube Raman bands are important topics in this study and will be discussed next.

3.4. Carbon Nanotube Composites

In view of the impressive mechanical properties of carbon nanotubes, one obvious application of the materials is in the reinforcement of polymer matrices. Examples will now be given of different systems in which SWNTs have been used to produce polymer-based composites (Deng et al., 2011).

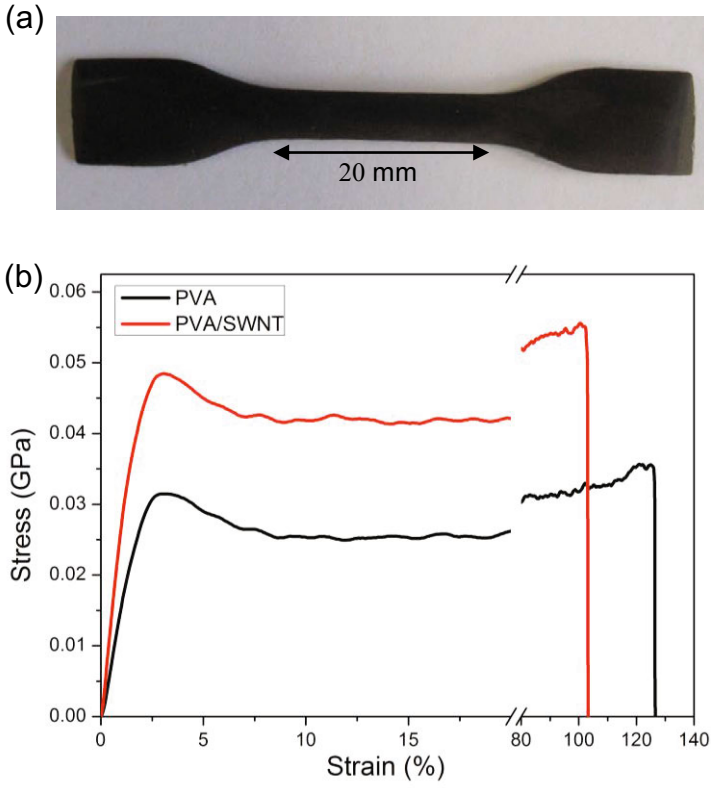

Figure 3.6. Tensile testing of PVT/SWNT nanocomposites. (a) Tensile specimen and (b) stress-strain curves. (Adapted from Deng et al., 2011 with permission from the American Chemical Society).

Table 3.3. Mechanical properties of PVA and PVA/SWNT films (Deng et al., 2011).

Material	Modulus (GPa)	Strength (MPa)	Elongation (%)
PVA	1.9	36	130
PVA/SWNT	2.3	42	110

3.4.1. Bulk SWNT nanocomposites

Bulk composites were prepared consisting of 0.2% by weight of HiPco single-walled carbon nanotubes in a poly(vinyl alcohol) matrix. Tensile specimens were cut out from the as-cast nanocomposite film as shown in Figure 3.6(a). Mechanical testing was carried out with the film samples using an Instron testing machine, and typical stress-strain curves are shown in Figure 3.6(b). For both neat the PVA and PVA/SWNT films, the stress increased linearly with the strain in the low strain range (< 2.5% strain) and the polymers yielded at around 3% strain. The films fractured when the strain exceeds 100%, showing good ductility of the sample. The moduli of the films were calculated in the strain range of 0.5 - 2.5% where good linearity was found. It was found the modulus increase from 1.9 GPa for neat PVA film to 2.3 GPa for PVA/SWNT composite film (see Table 3.3) and the ultimate tensile strength increased from 36 MPa to 42 MPa with just 0.2% of SWNTs in the composite film.

It is also possible to use Raman spectroscopy to follow the deformation of the nanotubes with in the composites. Figure 3.7(a) shows the Raman spectra of the PVA/SWNT composite film and HiPco SWNTs. It can be seen that the spectrum of the nanocomposite is very similar to that to that of the pure nanotubes, even though the nanocomposite only contains 0.2% of SWNTs by weight. This is because the nanotubes undergo very strong resonance Raman scattering (Dresselhaus et al., 2002; Dresselhaus et al., 2005), whereas the PVA matrix only shows weak scattering. It also means that Raman spectroscopy is a very useful technique to analyse many aspects of the structure and properties of nanotube composites.

The PVA/SWNT films were deformed using a four-point bending rig and Figure 3.7(b) shows the 2D-band position as a function of the strain applied to the composites. Good linearity between 2D peak position and strain can be seen over the strain range. The nanotube 2D-band shift per unit strain, observed in the elastic deformation region in PVA/SWNT film, of -23 cm^{-1}/% strain, is the highest found in isotropic polymer/nanotube films. The Raman band shift rate can be converted to the nanotube modulus using a universal calibration of -5 $cm^{-1}\%^{-1}$/GPa. This calibration was established by Cooper et al. (2001) by in-situ Raman spectroscopic study of a number of different carbon fibres. The high band shift rate measured for the PVA/SWNT film implies that the effective Young's modulus of the SWNTs in the nanocomposites is 600 GPa (Deng et al., 2011). It is also similar to the effective modulus of the SWNTs in the film determined from the data in Figure 3.6.

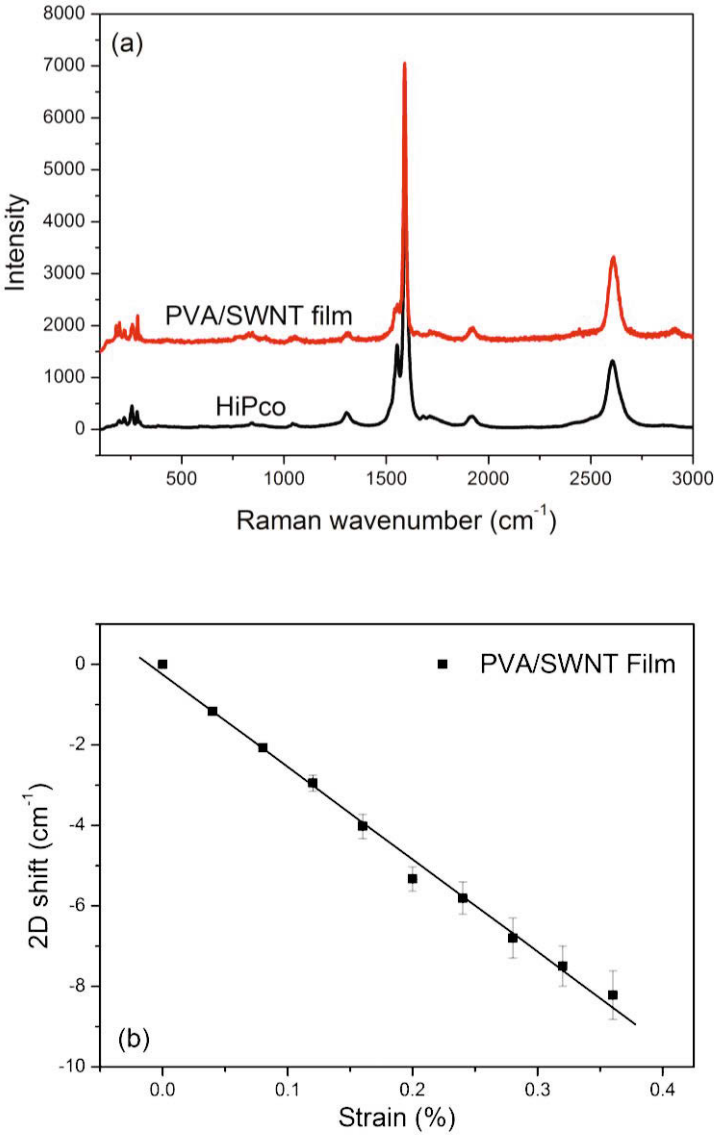

Figure 3.7. (a) Raman spectra of HiPco SWNTs and the PVA/SWNT film. (b) Variation of 2D-band position for nanotube in PVA/SWNT film as a function of strain. (Adapted from Deng et al., 2011 with permission from the American Chemical Society).

3.4.2. SWNT nanocomposites fibres

PVA/SWNT composite fibres containing 0.2% by weight (relative to the polymer) of HiPco SWNTs were prepared by electrospinning (Deng et al., 2011). The spinning conditions were: voltage, 20 kV; flow rate, 0.01 mL/min; and needle tip-to-collector distance, 8 cm. The fibres were collected using either 1) a grounded stationary stage or 2) for deformation studies a rotating disk on which a PMMA beam was attached. The angular velocity of the disk was 1500 rpm.

Narrow-diameter electrospun nanocomposite fibres, an example of which is shown in Figure 3.8, were collected after being aligned macroscopically using the rotating disk. The fibre diameter was controlled by varying the processing conditions such as the concentration of polymer solution, the flow rate and the speed of disk rotation. A range of different fibre diameters were obtained. The average diameter decreased from 700 nm for fibres collected at 0 rpm (a grounded stationary stage) to 590 nm for those collected with a disk rotating at an angular velocity of 1500 rpm. The macroscopic orientation of the fibres collected on the PMMA beam could be controlled by changing the position of the beam on the rotating disk relative to the direction of disc rotation (Deng et al., 2011).

Figure 3.9 shows the Raman spectra of a single PVA/SWNT fibre. Because of the resonantly-enhanced signal from the nanotubes, well-defined Raman bands such as the RBMs, G-band and 2D-band from nanotubes can be seen even at the low loadings of nanotubes employed (0.2%). The strong G band was used to characterize the orientation of the SWNTs in the nanocomposites and the highly stress-sensitive 2D band was employed to follow their deformation.

The 2D-band position in the electrospun fibres collected at 0 rpm was 2 cm^{-1} higher than in the film while the 2D-band position in fibres collected with 1500 rpm was 2 cm^{-1} lower than in the films. This suggests that the electrospinning process alone induces a small residual compression of the nanotubes in the fibres, possibly due to shrinkage as the solvent evaporates. In contrast, in fibres collected with a high-speed rotating disk the nanotubes are pre-stretched and had a slight residual tension that is not relaxed by solvent evaporation. Weak but resolvable Raman bands in the 600-1200 cm^{-1} region corresponding to PVA polymer are shown in the inset. They also enable the orientation of the polymer to be followed through the use of Raman spectroscopy (Deng et al., 2011).

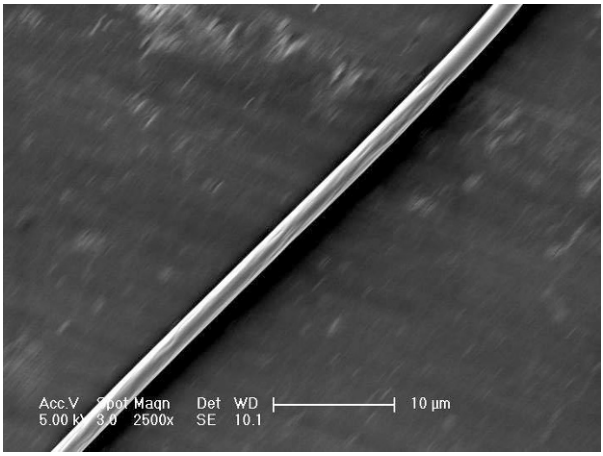

Figure 3.8. SEM micrograph of a single electrospun nancomposite fibre. (Adapted from Deng et al., 2011 with permission from the American Chemical Society).

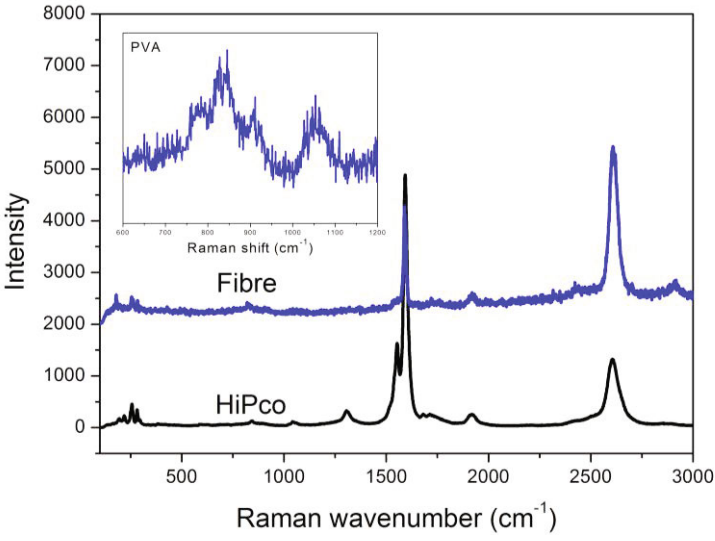

Figure 3.9. Raman spectra obtained from a single electrospun PVA/SWNT fibre and the HiPco nanotubes. The spectra have been offset for clarity and the region of the spectrum showing the PVA bands is inset. (Adapted from Deng et al., 2011 with permission from the American Chemical Society).

The orientation of the nanotubes in the nanofibres was characterized using polarized Raman spectroscopy using VV laser polarization with the incident laser beam and analyser both polarized parallel to the fibre axis (Deng et al., 2011). Figure 3.10 shows the normalized intensity of the nanotube G-band of a single nanocomposite fibre oriented at different angles φ between fibre axis and the laser polarization direction. It can be seen the intensity decreases dramatically as the angle φ increases, indicating a high degree of alignment of the nanotubes in the fibre. The solid line is generated for a relationship of $I \propto \cos^4\varphi$ which is expected to apply for perfect orientation of the nanotubes in the fibre (Liu and Kumar, 2003). The data follow the curve very closely until $\varphi > 60°$ but deviate a little from the theoretical line above this angle, showing some slight misorientation. The strong drawing force exerted by electrical field results in a high draw ratio in electrospinning jets and a high degree of nanotube alignment.

Along with the high degree of orientation of nanotubes achieved in the electrospun fibre, the polymer molecules can also be oriented under the strong electrical forces together with the drawing force exerted by the rotating disk. The ~2 μm diameter laser spot is significantly larger than both the nanotubes and fibre diameter. Hence these measurements determine only the average orientation of the SWNTs – there may be significant local variations of both of these parameters within the nanofibres (Deng et al., 2011).

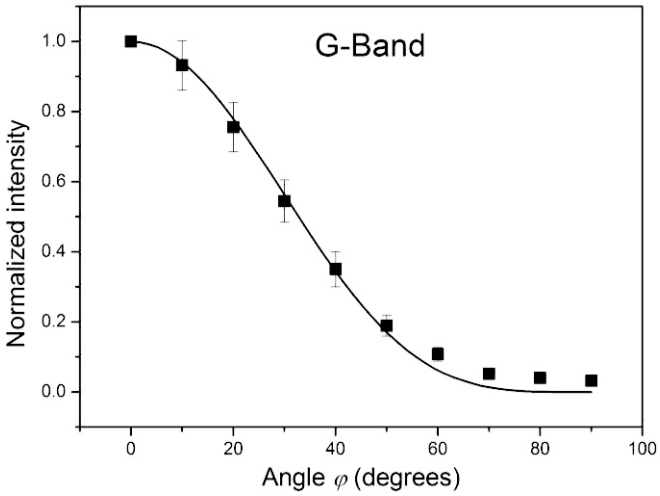

Figure 3.10. Variation of nanotube G-band intensity recorded using the VV configuration, as a function of the angle φ between the fibre axis and the laser polarization direction for an electrospun PVA/SWNT fibre. (Adapted from Deng et al., 2011 with permission from the American Chemical Society).

Figure 3.11 shows the stress induced shift of the G'-band for an electrospun nanofibre. The electrospun fibre exhibited a Raman band shift rate of -35 cm^{-1}/% strain which is higher than that shown for the film in Figure 3.7(b) as a consequence of the better orientation of both the nanotubes and polymer molecules in the nanofibres (Deng et al., 2011). Cooper et al. (2001) measured the Raman band shift rate for the 2D band for a number of different carbon fibres and showed that there was a universal calibration of -5 $cm^{-1}\%^{-1}$/GPa. Assuming that the calibration was also valid for the stress-induced shift of the same 2D band in carbon nanotubes, they used it to determine the effective Young's modulus of both single- and multi-walled carbon nanotubes in epoxy-matrix composites.

The 2D Raman band shift rate can be used to determine the effective modulus of the SWNTs in the electrospun nanofibres and it is again found to be of the order of 600 GPa, i.e. about 60% of the accepted value of around 1000 GPa. The slightly lower value for the nanocomposite films determined from Figure 3.7(b) may be due to all of the nanotubes not lying exactly in the plane of the films. The discrepancy with the accepted value can further be accounted for by factors such as SWNT bundling and finite length effects (Deng et al., 2011).

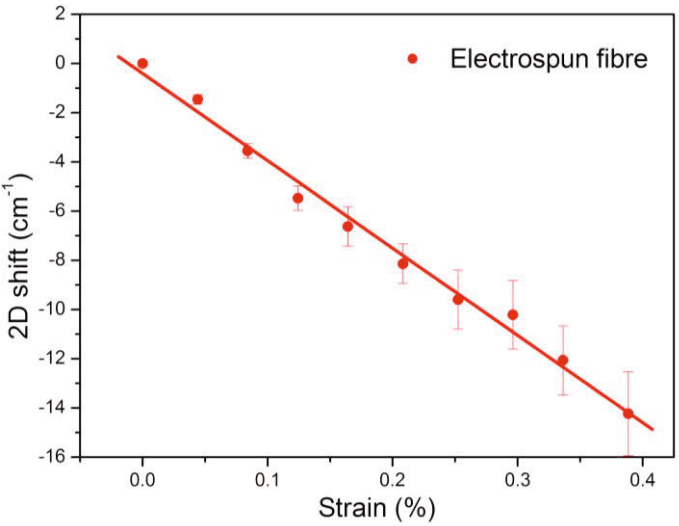

Figure 3.11. Variation of 2D-band position for nanotubes in the PVA/SWNT electrospun fibre as a function of strain. (Adapted from Deng et al., 2011 with permission from the American Chemical Society).

3.4.3. Aramid/nanotube fibres

Poly(p-phenylene terephthalamide)/single-walled carbon (PPTA/SWNT) composite fibres with different draw ratios (DR) were spun using a dry-jet wet spinning process and their structure and deformation behaviour has been analysed using Raman spectroscopy (Deng et al., 2010).

Figure 3.12 shows the Raman spectrum of a neat PPTA fibre, the original carbon nanotubes and a PPTA/SWNT composite fibre. Characteristic bands of both nanotubes and PPTA polymers can be seen from the composite fibres, and this enables the use of Raman spectroscopy for further characterization. Two features have been found by comparing the spectrum of composite and the original SWNTs: 1) The 2D-band from the composite fibre is higher in wavenumber than that from the original SWNTs in air, and fibres with higher DRs show a higher peak position, indicating residual compressive stress in the fibre upon drawing; and 2) The multiple peaks observed in the low-frequency region (radial breathing mode, RBM), together with the peak position and bandwidth of G'-band suggest the nanotubes were still in bundles even the processing condition were optimized to exfoliate nanotubes (Deng et al., 2010).

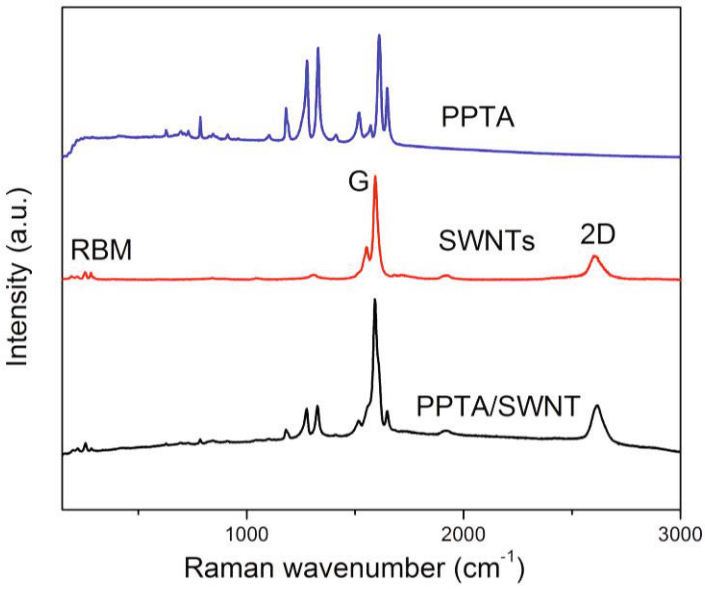

Figure 3.12. Raman spectrum of neat PPTA, SWNTs and PPTA/SWNT composite fibres. (Adapted from Deng et al., 2010 with permission from Elsevier).

The mechanical properties were determined for both the neat PPTA and PPTA/SWNT fibres and typical stress-strain curves are shown in Figure 3.13 for the composite fibres. It can be seen the slope in these curves decreases when the strain exceeds 0.5% and increases after 1%. The variation in modulus is thought to be due to change of the molecular configuration under strain and the variation becomes less pronounced as the DR of fibres increases (Deng et al., 2010).

It was found that the Young's modulus of reinforced fibres was improved by 15% for composite fibres relative to the neat fibres for a DR of 2. For fibres with higher DRs, the mechanical properties were degraded, an effect that has been observed for other high performance polymer/nanotube composites as well. It should be noted that mechanical reinforcement of polymers by nanotubes has been mostly on relatively low modulus polymers such as PVA (Deng et al., 2011). It appears that attempts to reinforce high-performance fibres such as PPTA have been less successful. Mechanical degradation by pristine nanotubes has also been reported where poor dispersion of nanotubes and weak interfacial interactions occur. The use of Raman spectroscopy to follow the mechanisms of stress transfer in the PPTA/SWNT fibres will now be presented.

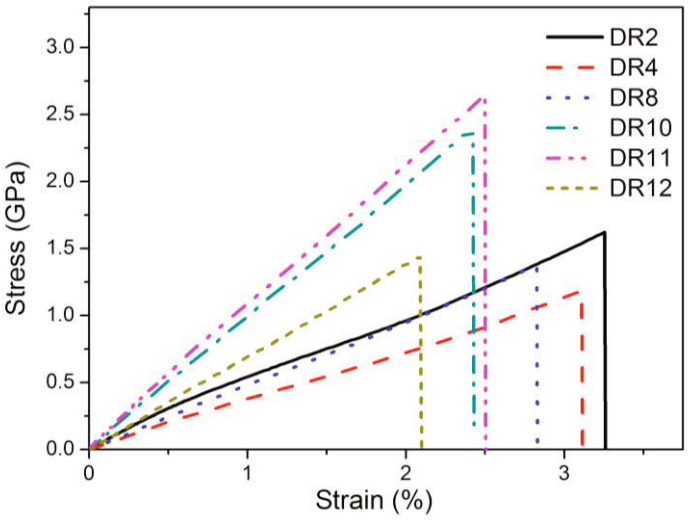

Figure 3.13. Typical stress-strain curves of PPTA/SWNT fibres. (Adapted from Deng et al., 2010 with permission from Elsevier).

In-situ Raman spectroscopy was employed to follow the deformation behaviour of the composite fibres by Deng et al. (2010). Figure 3.14 shows the variation of Raman band positions during tensile deformation. The PPTA 1610 cm^{-1} peak shifted to lower wavenumber linearly with increasing strain up to fibre fracture. On the other hand, the nanotube 2D-band and G-band wavenumbers were found to decrease as the strain increased until it reached 0.35%, and the downshift for both bands ceased when the strain exceeded 0.6%. This indicates breakdown of the interface in the strain range of 0.35-0.6%, which can be a result of interfacial sliding at SWNT-SWNT interface and/or SWNT-polymer interface.

The Raman shift rate increases with the DR of the fibre, and is found to scale with the modulus of the composite fibre. The large band shift rate of nanotube 2D-band within small strain range is clearly an indication of stress transfer from the matrix to the nanotubes. Molecular dynamics simulation carried out by Yang et al. (2005) has demonstrated that strong interfacial adhesion exists between nanotubes and polymers that contain aromatic rings in their backbone, as is the case for PPTA molecules. This strong interfacial interaction should give rise to mechanical reinforcing on PPTA fibres, but is not the case for PPTA/SWNT fibres except for the fibre with a DR of 2. Chang et al. (2006) have also observed the phenomenon that high efficiency of stress transfer results in very limited reinforcement and the reason remained unclear in their work. In the work of Deng et al. (2010), the matrix became degraded compared to the neat PPTA due to the orientation deterioration, which consequently resulted in the negative reinforcing effect in the composite even when good stress transfer was observed.

The overall downshift of nanotube 2D-band in the fibre deformation process reflects the strength of the interface. For fibres with a DR of 11 in which the nanotubes are highly aligned, a maximum down shift of 8 cm^{-1} has been observed. This level of band shift is significantly less than that observed for the PVA/SWNT materials described above. It is difficult to compare the shift rate for different composites system as it depends on the orientation and type (preparation method) of nanotubes, as well as the properties of polymer matrix. Nevertheless, it is clear that the poor level of reinforcement in the case of PPTA/SWNT fibres shows why the material has inferior properties to the PPTA fibres without the nanotubes.

The examples given above show the use of employing stress-induced Raman band shift to characterize stress transfer from polymer matrices to carbon nanotubes in a variety of different composite systems.

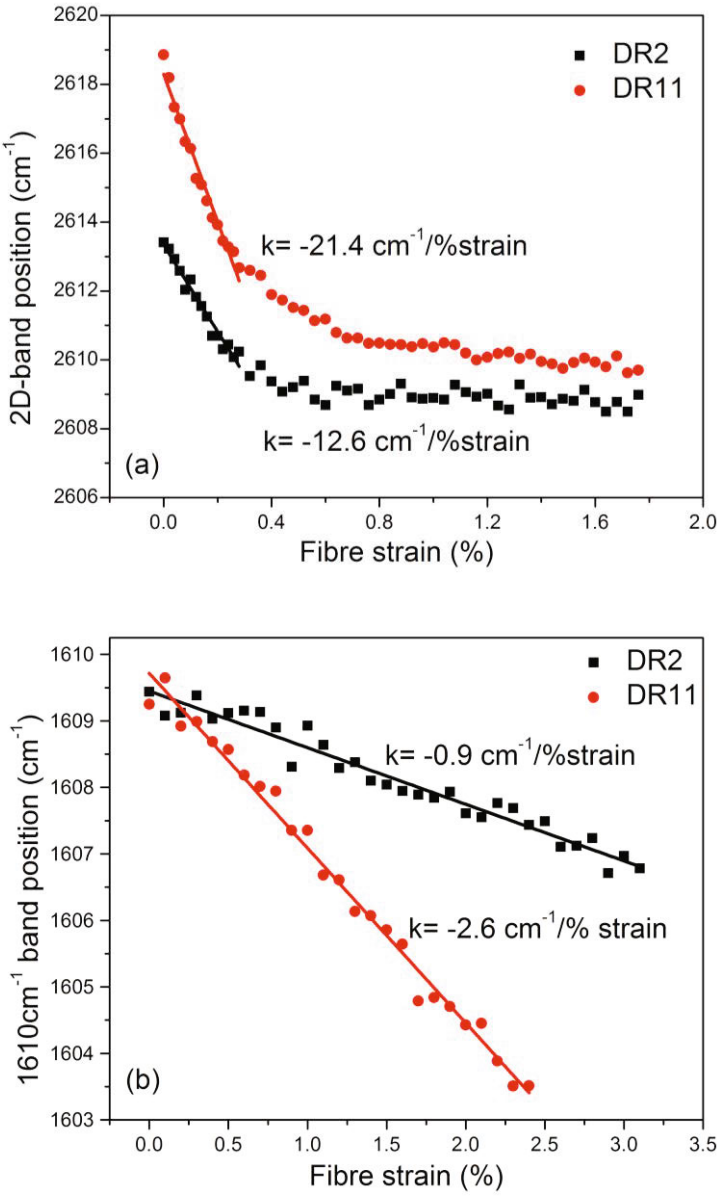

Figure 3.14. Variation of Raman band peak position for composite fibre with different DRs under tensile deformation: a) nanotube 2D-band and b) PPTA 1610 cm^{-1} peak. (Adapted from Deng et al., 2010 with permission from Elsevier).

3.5. Conclusions

It has been shown that carbon nanotubes have a range of different well-defined nanostructures that control their electronic and mechanical properties. Moreover, it has been demonstrated that Raman spectroscopy is a powerful technique to characterize the nanotubes and the origin of the different Raman bands found in nanotubes has been discussed in detail.

The deformation behaviour of the nanotubes in both PVA/SWNT composite films produced by solution casting and composite fibres fabricated by electrospinning and coagulation spinning has been discussed. Significant levels of reinforcement were shown to be found upon the addition of carbon nanotubes, even at loading levels as low as 0.2% by weight.

Raman spectroscopy has again been demonstrated to be extremely powerful in characterizing the deformation of these PVA/SWNT composite materials. Large Raman band shift rates were observed in the composite film and electrospun fibres corresponding to high levels of stress transfer between the polymer matrix and the nanotubes. This good stress transfer was shown to the consistent with the bulk mechanical properties of the PVA/SWNT composite materials.

The modification of aramid fibres with the addition of carbon nanotubes has also been described. Although it is demonstrated that through the use of Raman spectroscopy, reasonable levels of stress transfer are found between the aramid matrix and the nanotubes, it is found that there is generally poor reinforcement in this system due to slippage of the nanotubes at high strain levels.

Overall it has been shown that Raman spectroscopy is a powerful technique to characterize a range of important aspects of the structure and properties of carbon nanotubes.

References

Araujo P. T., Doorn S. K., Kilina S., Tretiak S., Einarsson E., Maruyama S., Chacham H., Pimenta M. A., and Jorio A. (2007) Third and fourth optical transitions in semiconducting carbon nanotubes. *Physical Review Letters*, 98:067401 1-4.

Bachilo S., Strano M., Kittrell C., Hauge R., Smalley R., and Weisman R. (2002). Structure-Assigned Optical Spectra of Single-Walled Carbon Nanotubes. *Science*, 298:2361-2366.

Bose S. M., Gayen S., and Behera S. N. (2005). Theory of the tangential G-band feature in the Raman spectra of metallic carbon nanotubes. *Physical Review B*, 72:153402 1-4.

Cardenas J., and Gromov A. (2009). The effect of bundling on the G' Raman band of single-walled carbon nanotubes. *Nanotechnology*, 20:465703 1-8.

Chang T. E., Kisliuk A., Rhodes S. M., Brittain W. J. and Sokolov A. P. (2006). Conductivity and mechanical properties of well-dispersed single-wall carbon nanotube/polystyrene composite. *Polymer*, 47:7740-7746.

Coleman J., Khan U., Blau W., and Gun'Ko Y. (2006a). Small but strong: A review of the mechanical properties of carbon nanotube–polymer composites. *Carbon*, 44:1624-1652.

Coleman J., Khan U., Blau W., and Gun'Ko Y. (2006b). Mechanical reinforcement of polymers using carbon nanotubes, *Advanced Materials*, 18:689-706.

Cooper C. A., Young R. J., and Halsall M. (2001). Investigation into the deformation of carbon nanotubes and their composites through the use of Raman spectroscopy. *Composites A: Applied Science and Manufacturing*, 32:401-411.

Deng L. B., Young R. J., van der Zwaag S., and Picken S. (2010). Characterization of the adhesion of single-walled carbon nanotubes in poly (*p*-phenylene terephthalamide) composite fibres, *Polymer*, 51:2033-2039.

Deng L. B., Eichhorn S. J., Kao C. C., and Young R. J. (2011). The effective Young's modulus of carbon nanotubes in composites, *ACS Applied Materials & Interfaces*, 3:433-440.

Doorn S. K., Strano M. S., Haroz E. H., Rialon K. L., Hauge R. H., and Smalley R. E. (2003). Capillary electrophoresis separations of bundled and individual carbon nanotubes. *Journal of Physical Chemistry B*, 107:6063-6069.

Dresselhaus M, Dresselhaus G, Jorio A, Souza A and Saito R (2002), Raman spectroscopy on isolated single wall carbon nanotubes, *Carbon*, 40, 2043-2061.

Dresselhaus M., Dresselhaus G., Saito R., and Jorio A. (2005). Raman spectroscopy of carbon nanotubes, *Physics Reports*, 409:47-99.

Fantini C., Jorio A., Souza M., Strano M. S., Dresselhaus M. S., and Pimenta M. A. (2004). Optical transition energies for carbon nanotubes from resonant Raman spectroscopy: Environment and temperature effects. *Physical Review Letters*, 93:147406 1-4.

Filho A. G. S., Jorio A., Dresselhaus M. S., Hafner J. H., Lieber C. M., and Pimenta M. A. (2002a). Probing the electronic trigonal warping effect in individual single-wall carbon nanotubes using phonon spectra. *Chemical Physics Letters*, 354:62-68.

Filho A. G. S., Jorio A., Swan A. K., Ünlü M. S., Goldberg B. B., Saito R., Hafner J. H., Lieber C. M., Pimenta M. A., Dresselhaus G., and Dresselhaus M. S. (2002b), Anomalous two-peak G-band Raman effect in one isolated single-wall carbon nanotube. *Physical Review B*, 65:085417 1-6.

Filho A. G. S., Jorio A., Samsonidze G., Dresselhaus G., Pimenta M. A., Dresselhaus M. S., Swan A. K., Ünlü M., Goldberg B. B., and Saito R. (2003). Competing spring constant versus double resonance effects on the properties of dispersive modes in isolated single-wall carbon nanotubes. *Physical Review B*, 67:035427 1-7.

Heller D. A., Barone P. W., Swanson J. P., Mayrhofer R. M., and Strano M. S. (2005). Using Raman spectroscopy to elucidate the aggregation state of single-walled carbon nanotubes. *Journal of Physical Chemistry B*, 108:6905-6909.

Jorio A., Saito R., Hafner J. H., Lieber C. M., Hunter M., McClure T., Dresselhaus G., and Dresselhaus M. S. (2001). Structural (*n, m*) determination of isolated single-wall carbon nanotubes by resonant Raman scattering. *Physical Review Letters*, 86:1118-1121.

Kataura H., Kumazawa Y., Maniwa Y., Umezu I., Suzuki S., Ohtsuka Y., and Achiba Y. (1999). Optical properties of single-wall carbon nanotubes. *Synthetic Metals*, 103:2555-2558.

Kawamoto H., Uchida H., Kojima T., and Tachibana M. (2006). G band Raman features of DNA-wrapped single-wall carbon nanotubes in aqueous solution and air. *Chemical Physics Letters*, 432:172-176.

Liu T. and Kumar S. (2003). Quantitative characterization of SWNT orientation by polarized Raman spectroscopy. *Chemical Physics Letters*, *378*:257-262

Lu J. P. (1997). Elastic properties of single and multilayered nanotubes. *Journal of the Physical Chemistry of Solids*, 58:1649-1652.

Lucas M., and Young R. J. (2007). Unique identification of single-walled carbon nanotubes in composites. *Composites Science and Technology*, 67:2135–2149.

Milnera M., Kurti J., Hulman M., and Kuzmany H. (2000). Periodic resonance excitation and intertube interaction from quasicontinuous distributed helicities in single-wall carbon nanotubes. *Physical Review Letters*, 84:1324-1327.

Moniruzzaman M., and Winey K. (2006). Polymer nanocomposites containing carbon nanotubes. *Macromolecules*, 39:5194-5205.

O'Connell M. J., Sivaram S., and Doorn S. K. (2004). Near-infrared resonance Raman excitation profile studies of single-walled carbon nanotube intertube interactions: A direct comparison of bundled and individually dispersed HiPco nanotubes, *Physical Review B*, 69:235415 1-15.

Paillet M., Poncharal P., Zahab A., and Sauvajol J. L. (2005). Vanishing of the Breit-Wigner-Fano component in individual single-wall carbon nanotubes. *Physical Review Letters*, 94:237401 1-4.

Saito R., Dresslhaus G., and Dressihaus M. (1998). *Physical properties of carbon nanotubes*, London: Imperial College Press.

Treacy M. M., Ebbesen T. W., and Gibson T. M. (1996). Exceptionally high Young's modulus observed for individual carbon nanotubes. *Nature*, 381:680-687.

Wise K. E., Park C., Siochi E. J., and Harrison J. S. (2004). Stable dispersion of single wall carbon nanotubes in polyimide: the role of noncovalent interactions. *Chemical Physics Letters*, 391:207-211.

Wong E. W., Sheehan P. E., and Lieber C. M. (1997). Nanobeam mechanics: Elasticity, strength, and toughness of nanorods and nanotubes. *Science*, 277:1971-1975.

Yang M. J., Koutsos V., and Zaiser M. (2005). Interactions between polymers and carbon nanotubes: A molecular dynamics study. *Journal of Physical Chemistry B*, 109:10009 – 10014.

4 Graphene and Graphene-Based Nanocomposites

Robert J Young

School of Materials, University of Manchester, Manchester, M13 9PL, UK

4.1. Introduction

The study of graphene is one of the most exciting topics in materials science and condensed matter physics (Geim and Novoselov, 2007) and graphene has good prospects for applications in a number of different fields (Novoselov, 2011; Geim, 2011). There has been a rapid rise of interest in the study of the structure and properties of graphene following the first report in 2004 of the preparation and isolation of single graphene layers in Manchester (Novoselov et al, 2004). It had previously been thought that the isolation of single-layer graphene would not be possible since such 2D crystals would be unstable thermodynamically and/or might roll up into scrolls if prepared as single atomic layers (Young et al, 2012). A large number of studies since 2004 have shown that this is certainly not the case. There was excitement about graphene initially because of its electronic properties, with its charge carriers exhibiting very high intrinsic mobility, having zero effective mass and being able to travel distances of microns at room temperature without being scattered (Geim and Novoselov, 2007). Thus the majority of the original research upon graphene had concentrated upon electronic properties, aimed at applications such as using graphene in electronic devices (Avouris, 2010).

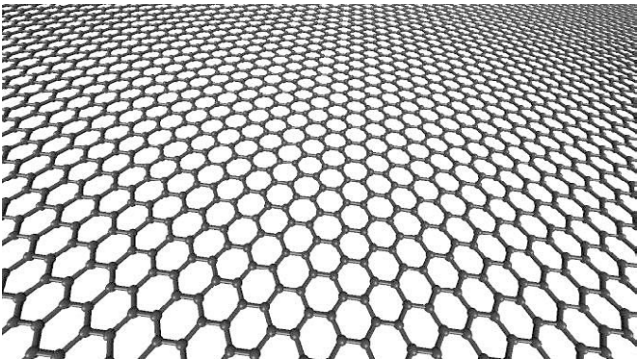

Figure 4.1. A molecular model of a single layer of graphene. (Courtesy of F. Ding, Hong Kong Polytechnic University). (Adapted from Young and Lovell, 2011 with permission from CRC Press).

O. Paris (Ed.), *Structure and Multiscale Mechanics of Carbon Nanomaterials*,
CISM International Centre for Mechanical Sciences
DOI 10.1007/ 978-3-7091-1887-0_4 © CISM Udine 2016

Graphene is the basic building block of all graphitic forms of carbon. It consists of a single atomic layer of sp^2 hybridized carbon atoms arranged in a honeycomb structure as shown in Figure 4.1. Research upon the material has now broadened considerably as it was soon realised that graphene might have other interesting and exciting physical properties such as high levels of stiffness and strength, and thermal conductivity, combined with an impermeability to gases. One obvious application of graphene is in the field of nanocomposites (Young et al, 2012) and researchers working upon other forms of nanocomposites, such as those reinforced by nanotubes or nanoclays, have now refocused their efforts towards graphene nanocomposites. Additionally there was pre-existing expertise in the exfoliation of graphite (e.g. expanded graphite) and in the preparation of graphene oxide (originally termed "graphite oxide"). The advantages and disadvantages of using graphene oxide in composite materials in comparison with pristine graphene has been discussed elsewhere (Young et al, 2012).

4.2. Graphene

4.2.1. Preparation

There has already been considerable effort put into the development of ways of preparing high-quality graphene in large quantities for both research purposes and with a view to possible applications (Rao et al, 2009). Since it was first isolated in 2004 several approaches have been employed to prepare the material. One is to break graphite down into graphene by techniques such as a mechanical cleavage or liquid phase exfoliation (sometimes termed "top-down"). The other methods is to synthesize graphene using techniques such as chemical vapour deposition (CVD) (often known as "bottom-up"), epitaxial growth on silicon carbide, molecular beam epitaxy, etc (Young et al, 2012).

Expanded graphite was developed more than 100 years as a filler for the polymer resins that were being developed at the same time and investigated extensively over the intervening period. More recently there have been developments in the preparation of thinner forms of graphite, known as graphite nanoplatelets (GNPs) (Kalaitzidou et al, 2007). They can be produced by a number of techniques that include the exposure of acid-intercalated graphite to microwave radiation, ball-milling and ultrasonication. The addition of GNPs to polymers has been found to lead to substantial improvements in mechanical and electrical properties at lower loadings than are needed with expanded graphite. The definition of GNPs covers all types of graphitic material from 100 nm thick platelets down to single layer graphene (Kalaitzidou et al, 2007). It is, however, the availability of single- or few-layer graphene that has caused the most excitement in recent times.

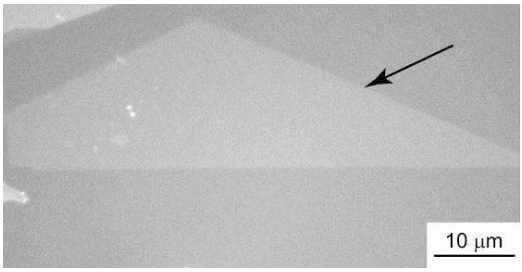

Figure 4.2. Optical micrograph of a graphene monolayer (indicated by an arrow) prepared by mechanical cleavage and deposited on a polymer substrate. (Adapted from Young and Lovell, 2011 with permission from CRC Press).

The simplest way of preparing small samples of single- or few-layer graphene is by the mechanical cleavage (i.e. the repeated peeling of graphene layers with adhesive tape) from either highly-oriented pyrolytic graphite or good-quality natural graphite (Novoselov et al, 2004). Figure 4.2 shows an optical micrograph of a sample of monolayer graphene prepared by mechanical cleavage and then deposited upon a polymer substrate. Typically, this method produces a mixture of one-, two- and many-layer graphene flakes that have dimensions of the order of tens of microns.

The rapid rise of interest in graphene for use in applications that require high volumes of material, such as in composites, led to investigations into methods of undertaking large-scale exfoliation. One of the first successful methods was the exfoliation and dispersion of graphite in organic solvents such as dimethylformamide or N-methylpyrrolidone (Hernandez et al, 2008). Depending on the levels of agitation and purification suspensions with large (>50%) fractions of graphene monolayers could be prepared. The material produced by this method is relatively free of defects and is not oxidised but the lateral dimensions of the graphene layers are typically no more than a few microns.

An important breakthrough has been the growth graphene films with macroscopic dimensions on the surfaces of metals. In the case of copper, growth takes place upon Cu foils via a surface-catalyzed process and thin metal films do not have to be employed (Suk et al, 2011). For both metals, it was found that the graphene films could be transferred to other substrates. This process has now been scaled-up to a roll-to-roll production process in which the graphene is grown by CVD on copper-coated rolls. It can then be transferred to a thin polymer film backed with an adhesive layer to produce transparent conducting films (Bae et al, 2010). It has been found that such films have a low electrical sheet resistance and optical transmittance of the order of 97.7%. They are found to be predominantly covered with a monolayer graphene film but also have some bilayer and multilayer islands.

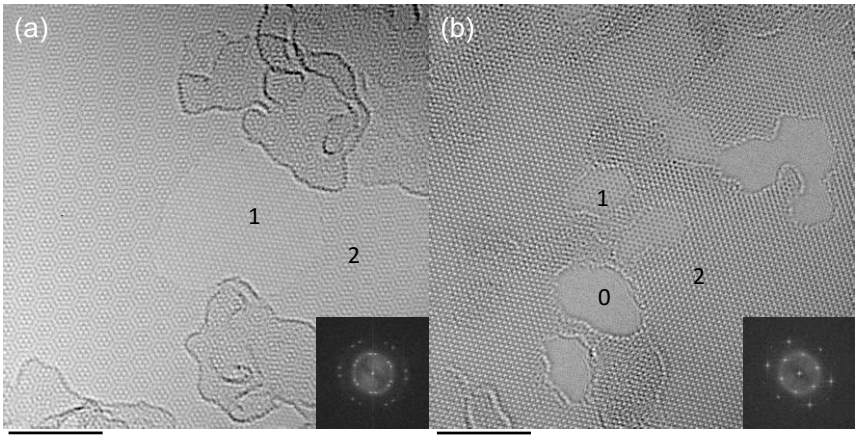

Figure 4.3. High resolution TEM image from CVD graphene showing regions of (a) non-Bernal stacking and (b) Bernal stacking (Scale bars = 5 nm). The selected area diffraction patterns are given and number of layers in the different areas is indicated (Courtesy of Jamie Warner and Sarah Haigh)

4.2.2. Characterisation

A single atomic layer of graphene absorbs ~2.3 % of visible light and its absorption is virtually independent of wavelength (Nair et al, 2008). Thus, being significantly optically active, graphene can be observed on certain substrates by simple methods, Figure 4.2. In fact, it is possible to distinguish between flakes of graphene with different numbers of layers relatively easily in a transmission optical microscope.

The atomic structure of graphene can be observed directly using transmission electron microscopy (TEM) (Meyer et al, 2007) as shown in Figure 4.3. It is relatively easy to resolve individual carbon atoms by TEM and the differences between Bernal-stacked and irregularly stacked material can be seen.

It is found that both an image of the graphene lattice and well-defined electron diffraction patterns can be obtained from suspended graphene sheets in the TEM (Meyer et al, 2007). The sheets, however, are not exactly flat but have static ripples out of plane on a scale of the order of 1 nm (Bangert et al, 2009). It was also found that there was no tendency for the graphene sheets to scroll or fold in contradiction to one of the preconceptions of its behaviour. Moreover, it was found that a sliver of graphene could extend nearly 10 μm from the edge of a metal TEM grid without any external support. This was taken as an indication that the graphene monolayers have a very high level of stiffness (Booth et al, 2008).

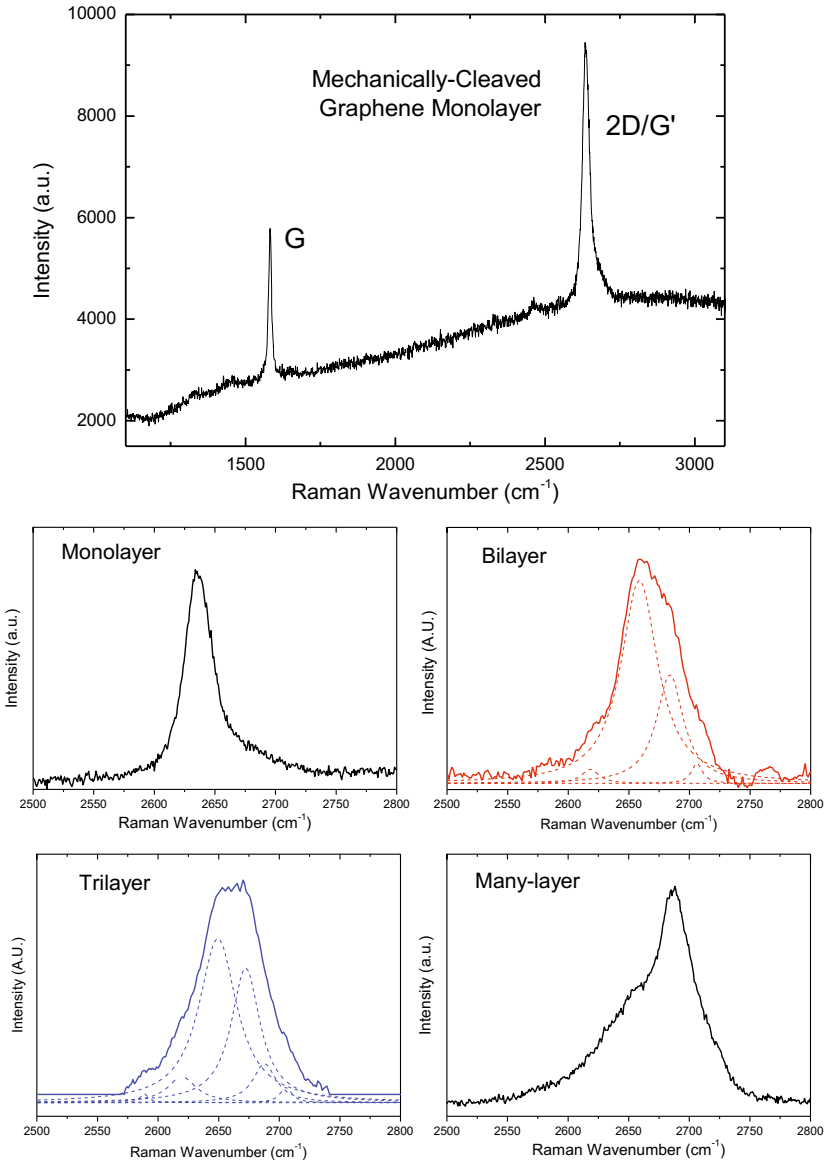

Figure 4.4. Raman spectra of monolayer graphene showing full spectrum with the G and 2D/G' bands (top). Details of the 2D/G' band for monolayer, bilayer, trilayer and many-layer materials (bottom).

Raman spectroscopy is a particularly useful technique to characterize graphene monolayers, bilayers and trilayers since, quite remarkably, Raman spectra can even be obtained from a single layer of carbon atoms (due to strong resonance Raman scattering in this material (Ferrari et al, 2006)). Moreover, graphene samples with different numbers of layers show significant differences in their Raman spectra as can be seen in Figure 4.4. In the case of single layer graphene, the G' (or 2D) Raman band is twice the intensity of the G band whereas in the two-layer material the G band is stronger than the 2D band. In addition, the 2D band is shifted to higher wavenumber in the two-layer graphene and has a different shape, consisting of 4 separate bands due to the resonance effects in the electronic structure of the 2-layer material (Ferrari et al, 2006). In fact it is possible to use Raman spectroscopy to determine the stacking order in several layers of graphene (for instance to distinguish between two separate single layers overlapping and a graphene bilayer in which the original Bernal crystallographic stacking is retained (Young et al, 2012)). As the number of layers is increased the 2D band moves to higher wavenumber and becomes broader and more asymmetric in shape for more than around 5 layers very similar to the 2D band of graphite. It should also be noted that in the Raman spectra shown in Figure 4.4 the D band, which is normally found in different forms of graphitic carbon due the presence of defects, is not present indicating that the mechanically-exfoliated graphene used to obtain the spectra in Figure 4.4 has a very high degree of perfection (Ferrari et al, 2006). More prominent D bands are found in samples of imperfect or damaged graphene such as some CVD material or in the vicinity of edges of small exfoliated fragments.

4.2.3. Mechanical properties

Lee et al (2009) undertook the direct determination of the mechanical properties of monolayer graphene through the nanoindentation of graphene membranes, suspended over holes of 1.0 - 1.5 μm in diameter on a silicon substrate, in an atomic force microscope (AFM). They isolated the monolayers through the use of optical microscopy and identified them with Raman spectroscopy. They determined the variation of force with indentation depth and derived stress-strain curves by assuming that the graphene behaved mechanically as a 2D membrane of thickness 0.335 nm. It was found that failure of the graphene took place by the bursting of the single molecular layer membrane at large displacements with failure initiating at the indentation point. The stress-strain curve for the graphene derived from the analysis of the indentation experiments is shown in Figure 4.5. It can be seen that the stress-strain curve becomes non-linear with increasing strain and that fracture occurs at a strain of well over 20%.

Using density functional theory, Liu, Ming and Li (2007) had earlier undertaken an ab initio calculation of the stress-strain curve of a graphene single layer. This is

also plotted in Figure 4.5 and it can be seen that there is extremely good agreement between the theoretical analysis and the experimentally-derived curve. The value of Young's modulus determined from the indentation experiment (Lee et al, 2009) is 1000 ± 100 GPa and this compares very well with the theoretical estimate (Liu, Ming and Li, 2007) of 1050 GPa. It is also similar to the value of 1020 GPa determined many years ago for the Young's modulus of bulk graphite In addition, the strength of the graphene monolayer was determined experimentally to be up to 130 ± 10 GPa. This is the order of $E/8$, where E is the Young's modulus, and so is close to the theoretically-predicted value of the strength of a defect-free material (Kelly and Macmillan, 1986).

The theoretical failure stress can also be determined from the maximum stress in the calculated stress-strain curve in Figure 4.5. Liu, Ming and Li (2007) found that the behaviour of the graphene at high-strains should differ slightly depending upon the crystallographic direction in which the graphene is deformed. They predicted the strength to be in the range 107 - 121 GPa, which is again in very good agreement with the range of values measured experimentally.

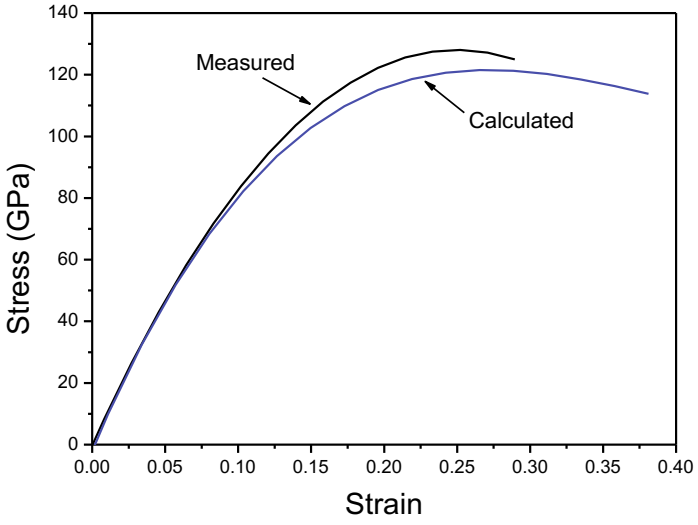

Figure 4.5. Measured (Lee et al, 2009) and calculated (Liu, Ming and Li, 2007) stress-strain curve for the deformation of a graphene monolayer.

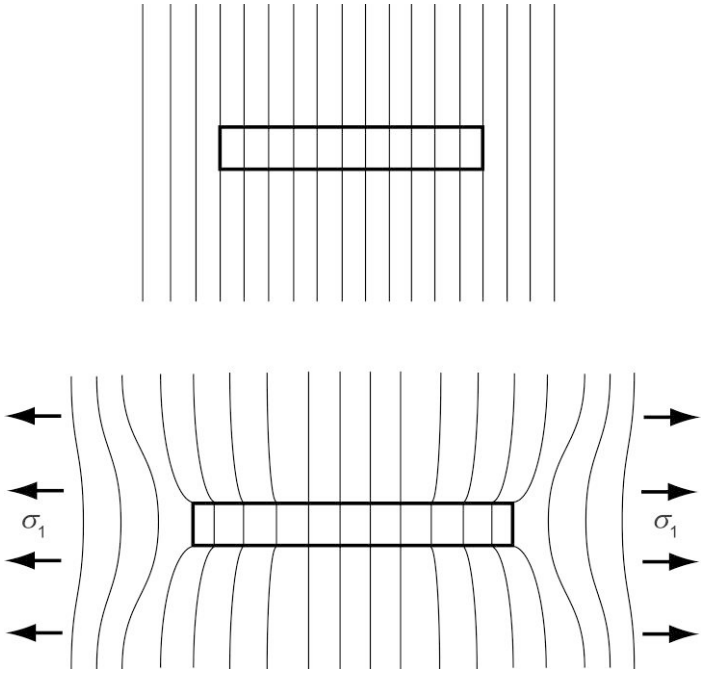

Figure 4.6. Deformation patterns for a discontinuous graphene flake in a low-modulus polymer matrix. The top diagram shows the situation before deformation and the bottom diagram shows the effect of the application of a tensile stress, σ_1, parallel to the flake. (Adapted from Gong et al., 2010 with permission from Wiley-VCH).

4.3. Nanoplatelet Reinforcement – Theory

In view of the growing interest in the study of polymer-based nanocomposites, it will be shown how the shear-lag methodology can be modified to predict the distribution of stress and strain in nanoplatelets reinforcing a polymer matrix and an analogous set of relationships is obtained for nanoplatelet reinforcement to those obtained for fibre reinforcement. Because of the very strong resonance Raman scattering, it will be shown that well-defined Raman spectra can be obtained from graphene monolayers. Large stress-induced band shifts can be obtained from these sheets when embedded in a polymer matrix which has enabled the prediction of the shear lag model to be validated. It will be shown further how the shear-lag model (Cox, 1952; Kelly, 1966; Kelly and Macmillan, 1986) can be used to model reinforcement by few-layer graphene.

4.3.1. Micromechanics

It is of interest to see if the reinforcement of composites with nanoplatelets can also be analyzed using continuum mechanics. In the case of nanoplatelets such as a discontinuous graphene flake reinforcing a composite matrix, stress transfer from the matrix to the flake will also be assumed to take place through a shear stress at the flake/matrix interface (Gong et al., 2010). This can also be represented diagrammatically by Figure 4.6 where the rectangle in this case represents the two-dimensional section through a nanoplatelet in a matrix rather than along the middle of a fibre. Before deformation parallel lines perpendicular to the flake can again be drawn from the matrix through the flake before deformation. When the system is subjected to axial stress, σ_l, parallel to the flake axis, the lines become distorted since the Young's modulus of the matrix is much less than that of the flake. This induces a shear stress at the flake/matrix interface. The axial stress in the flake will build up from zero at the flake ends to a maximum value in the middle of the flake. The uniform strain assumption means that, if the flake is long enough, in the middle of the flake the strain in the flake equals that in the matrix. Since the nanoplatelets have a much higher Young's modulus it means that the nanoplatelets carry most of the stress, and therefore load, in the composite.

The relationship between the interfacial shear stress, τ_i, near the flake ends and the flake stress, σ_f, can be determined by using a force balance of the shear forces at the interface and the tensile forces in a flake element as shown in Figure 4.7. The main assumption is that the forces due to the shear stress at the interface, τ_i, is balanced by the force due to the variation of axial stress in the flake, $d\sigma_f$, such that if the element shown in Figure 4.7 is of unit width

$$\tau_i dx = t d\sigma_f \tag{4.1}$$

and so

$$\frac{d\sigma_f}{dx} = \frac{\tau_i}{t} \tag{4.2}$$

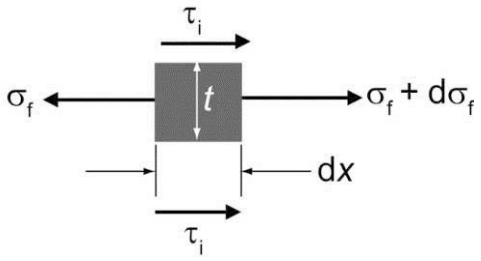

Figure 4.7. Balance of stresses acting on an element of length, d*x*, of the flake of thickness, *t*, in the composite. (Adapted from Gong et al., 2010 with permission from Wiley-VCH).

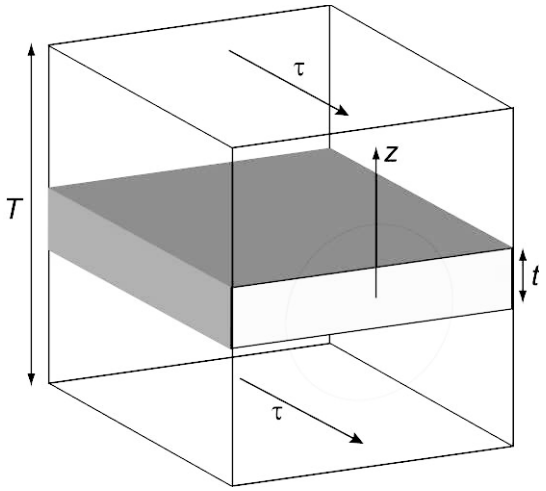

Figure 4.8. Model of a flake within a resin used in shear-lag theory. The shear stress τ acts at a distance z from the flake centre. (Adapted from Gong et al., 2010 with permission from Wiley-VCH).

The behaviour of a discontinuous flake in a matrix can be modelled using shear lag theory in which it is assumed that the flake is surrounded by a layer of resin at a distance, z, from the flake centre as shown in Figure 4.8. The resin has an overall thickness of T. It is assumed that both the flake and matrix deform elastically and the flake-matrix interface remains intact. If u is the displacement of the matrix in the flake axial direction at a distance, z, then the shear strain, γ, at that position is be given by

$$\gamma = \frac{\mathrm{d}u}{\mathrm{d}z} \tag{4.3}$$

The shear force per unit length carried by the matrix is transmitted to the flake surface though the layers of resin and so the shear strain at any distance z is given by

$$\frac{\mathrm{d}u}{\mathrm{d}z} = \frac{\tau_\mathrm{i}}{G_\mathrm{m}} \tag{4.4}$$

This equation can be integrated using the limits of the displacement at the flake surface ($z = t/2$) of $u = u_\mathrm{f}$ and the displacement at $z = T/2$ of $u = u_\mathrm{T}$

$$\int_{u_f}^{u_T} \mathrm{d}u = \frac{\tau_i}{G_m} \int_{t/2}^{T/2} \mathrm{d}z \tag{4.5}$$

hence $$u_T - u_f = \left(\frac{\tau_i}{2G_m}\right)(T - t) \tag{4.6}$$

It is possible to convert these displacements into strain since the flake strain, e_f and matrix strain, e_m, can be approximated as $e_f \approx \mathrm{d}u_f/\mathrm{d}x$ and $e_m \approx \mathrm{d}u_T/\mathrm{d}x$. It should be noted again that this shear-lag analysis is not rigorous but it serves as a simple illustration of the process of stress transfer from the matrix to a flake in a graphene-flake composite. In addition, τ_i is given by Equation (4.2) and so differentiating Equation (4.6) with respect to x leads to

$$e_f - e_m = \frac{tT}{2G_m} \frac{\mathrm{d}^2\sigma_f}{\mathrm{d}x^2} \tag{4.7}$$

since $T >> t$. Multiplying through by E_f gives

$$\frac{\mathrm{d}^2\sigma_f}{\mathrm{d}x^2} = \frac{n^2}{t^2}\left(\sigma_f - e_m E_f\right) \tag{4.8}$$

where $$n = \sqrt{\frac{2G_m}{E_f} \frac{t}{T}}$$

This differential equation has the general solution

$$\sigma_f = E_f e_m + C\sinh\left(\frac{nx}{t}\right) + D\cosh\left(\frac{nx}{t}\right)$$

where C and D are constants of integration. This equation can be simplified and solved if it is assumed that the boundary conditions are that there is no stress transmitted across the flake ends, i.e. if $x = 0$ in the middle of the flake where $\sigma_f = E_f e_m$ then $\sigma_f = 0$ at $x = \pm l/2$. This leads to $C = 0$ and

$$D = \frac{E_f e_m}{\cosh(nl/2t)}$$

The final equation for the distribution of flake stress as a function of distance, x along the flake is then

$$\sigma_f = E_f e_m \left(1 - \frac{\cosh(nx/t)}{\cosh(nl/2t)}\right) \tag{4.9}$$

4.3.2. Interfacial Shear Stress

Finally it is possible to determine the distribution of interfacial shear stress along the flake using Equation (4.2) which leads to

$$\tau_i = nE_f e_m \frac{\sinh(nx/t)}{\cosh(nl/2t)} \tag{4.10}$$

It is convenient at this stage to reintroduce the concept of flake aspect ratio, defined in this case as $s = l/t$ so that the two equations above can be rewritten as

$$\sigma_f = E_f e_m \left[1 - \frac{\cosh\left(ns\frac{x}{l}\right)}{\cosh(ns/2)}\right] \tag{4.11}$$

for the axial flake stress and as

$$\tau_i = nE_f e_m \left[\frac{\sinh\left(ns\frac{x}{l}\right)}{\cosh(ns/2)}\right] \tag{4.12}$$

for the interfacial shear stress.

It can be seen that the nanoplatelet is most highly stressed, i.e. the most efficient flake reinforcement is obtained, when the product ns is high. This implies that a high aspect ratio, s, is desirable along with a high value of n. The similarity of this analysis for the nanoplatelet to the shear lag analysis for a fibre and of the equations derived is remarkable. The reason for this is that the shear-lag analysis considers only axial stresses and the shear-lag model represented by Figure 4.6 is applicable to both situations.

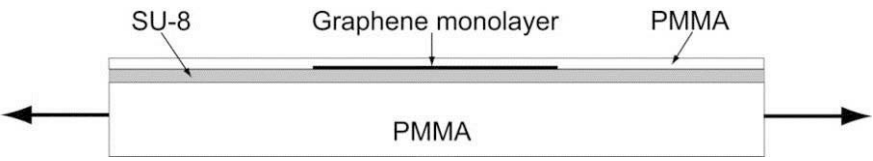

Figure 4.9 Schematic diagram (not to scale) of a section through a single monolayer graphene composite. (Adapted from Gong et al., 2010 with permission from Wiley-VCH).

4.4. Nanoplatelet Reinforcement – Experiment

As in the case of carbon fibres (Montes-Morán and Young, 2002), Raman spectroscopy can be employed to follow the micromechanics of reinforcement by graphene nanoplatelets in nanocomposites (Gong et al, 2010). Figure 4.9 shows a schematic diagram of a model composite specimen consisting of a single graphene monolayer sandwiched between two polymer layers. The SU-8 epoxy was spin-coated onto a poly(methyl methacrylate) (PMMA) beam and allowed to cure. The graphene monolayer was produced by repeated cleavage of a graphite crystal with adhesive tape and pressed onto the beam. The PMMA top coat was spin coated to seal the monolayer on the beam. Deformation was applied by bending the PMMA beam and monitoring the matrix strain using a resistance strain gauge (Gong et al, 2010).

4.4.1. Monolayer graphene

Graphene undergoes very strong resonance Raman scattering (Malard et al, 2009) which means that it is possible to obtain a spectrum from a single-atom thick monolayer embedded in several microns of PMMA (Gong et al, 2010). Figure 4.4 shows a Raman spectrum obtained from a single graphene monolayer. It can be seem that it consists of two sharp bands with the 2D band being characteristically stronger than the G band for the monolayer (Ferrari et al, 2006). The absence of a D band also shows that the graphene is relatively free of defects.

The 2D band is found to shift to lower wavenumber with tensile deformation as shown in Figure 4.10. It can be seen that there is a large, approximately linear shift of the band, with a shift rate of the order of -60 cm^{-1}/% strain. Cooper et al (2001) found that there was a simple linear relationship between the 2D band position for carbon fibres. Assuming that the relationship for carbon fibres between band shift rate and Young's modulus determined by Cooper et al (2001) is also applicable to monolayer graphene, this would imply that the graphene has a Young's modulus in excess of 1000 GPa, which is similar to the value determined by direct measurement (Lee et al, 2008).

As with carbon fibres (Montes-Morán and Young, 2002), the relationship shown in Figure 4.10(b) can also be used in a number of different situations to determine stress or strains distributions in graphene nanoplatelets in nanocomposites (Young et al, 2012). Examples of this approach will now be presented.

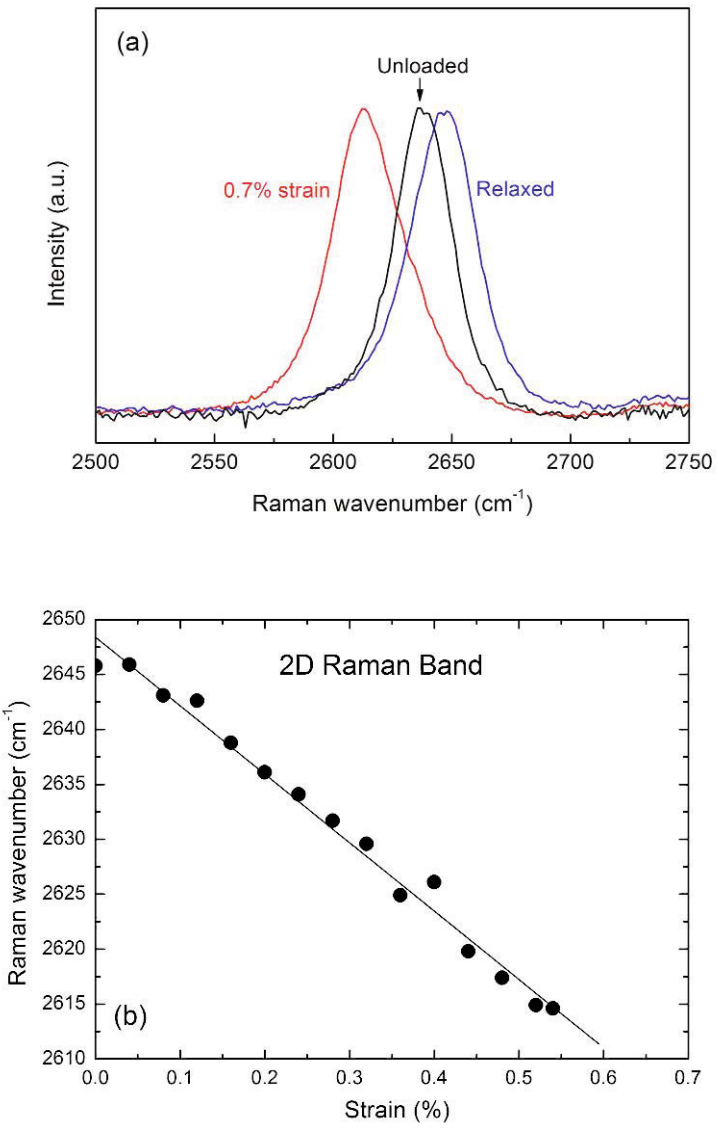

Figure 4.10. Effect of tensile deformation upon the position of the 2D Raman band for a graphene monolayer. (a) Shift of the band with a strain of 0.7%. (b) Shift of the band as a function of strain. (Adapted from Gong et al., 2010 with permission from Wiley-VCH).

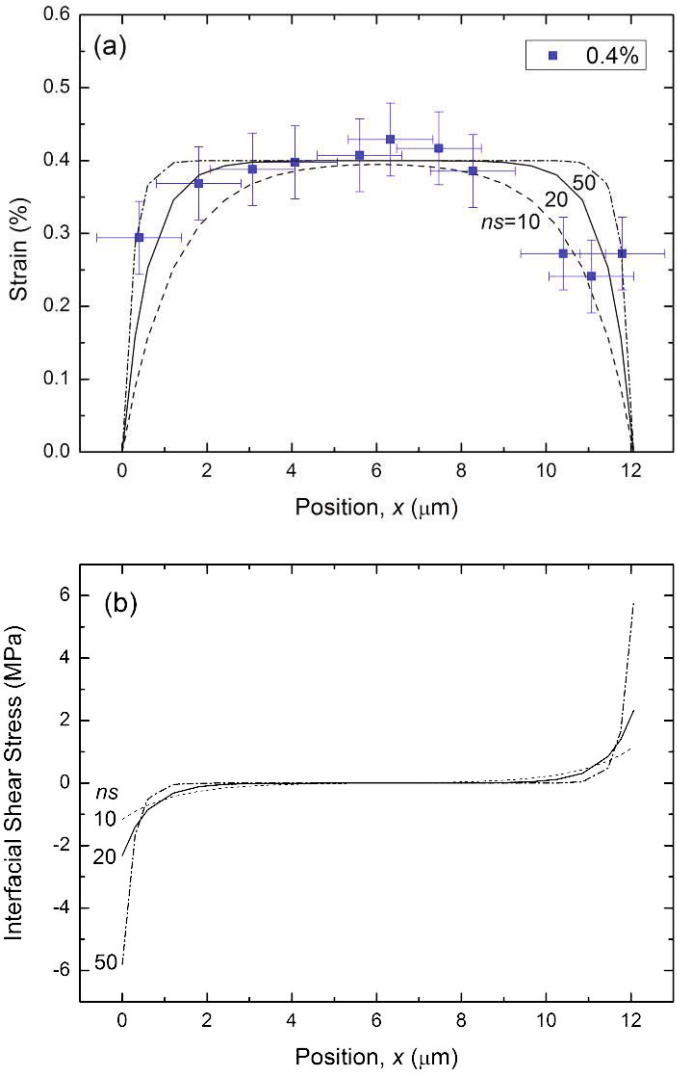

Figure 4.11. (a) Distribution of strain at 0.4% matrix strain in direction of the tensile axis across a graphene monolayer. The curves are fits of Equations (4.11) (b) Variation of interfacial shear stress with position determined from Equation (4.12). (Adapted from Gong et al., 2010 with permission from Wiley-VCH).

The experimental data on the variation of graphene strain across the middle of a monolayer flake are shown in Figure 4.11(a). The data were fitted to Equation (4.11) from the shear lag analysis derived above (Gong et al, 2010). It can be seen that the fits of the theoretical shear-lag curves to the strain distribution are sensitive to the value of *ns* chosen. The derived interfacial shear stress distributions are shown in Figure 4.11(b) and the value of interfacial shear stress at the flake ends is also very sensitive to the values of *ns* chosen. The best fit to the experimental data is for an *ns* value of 20, giving a maximum interfacial shear stress of around 2 MPa, well below the value of 50 MPa found for the carbon fibres (Montes-Morán and Young, 2002). The graphene has an inert atomically-smooth surface such that any interactions with the polymers will be through van der Waals bonding. The T50-O carbon fibres used by Montes-Morán and Young (2002) on the other had been plasma oxidized and had rough surfaces, leading to much stronger bonding with the polymer matrix. In the case of fibres that had not received the plasma oxidation treatment, lower levels of interfacial shear stress, approaching those found in similar investigations upon graphene, were obtained (Montes-Morán and Young, 2002).

Young et al (2011) showed in a further study, that the strain distribution in a single graphene atomic layer sandwiched between two thin layers of polymer on the surface of a PMMA beam (Figure 4.9) could be mapped in two dimensions with a high degree of precision from Raman band shifts as shown in Figure 4.12. The distribution of strain across the graphene monolayer was found to be relatively uniform at levels of matrix strain up to ~0.6% strain but that it became highly non-uniform above this strain. This change in strain distribution was shown (Young et al, 2011) to be due to a fragmentation process as a result of the development of cracks, most likely in the polymer coating layers, with the graphene appearing to remain intact. Between the cracks, the strain distributions in the graphene were approximately triangular in shape and the interfacial shear stress, τ_i, in the fragments was found to be only about 0.25 MPa. This is an order of magnitude lower than the interfacial shear stress before fragmentation (Gong et al, 2010). This relatively poor level of adhesion between the graphene and polymer layers again has important implications for the use of graphene in nanocomposites.

Although these investigations upon monolayer graphene have produced interesting an important insight into the reinforcement of polymers by graphene, large-scale graphene production invariably produces few-layer material. The behaviour of this material will be considered next.

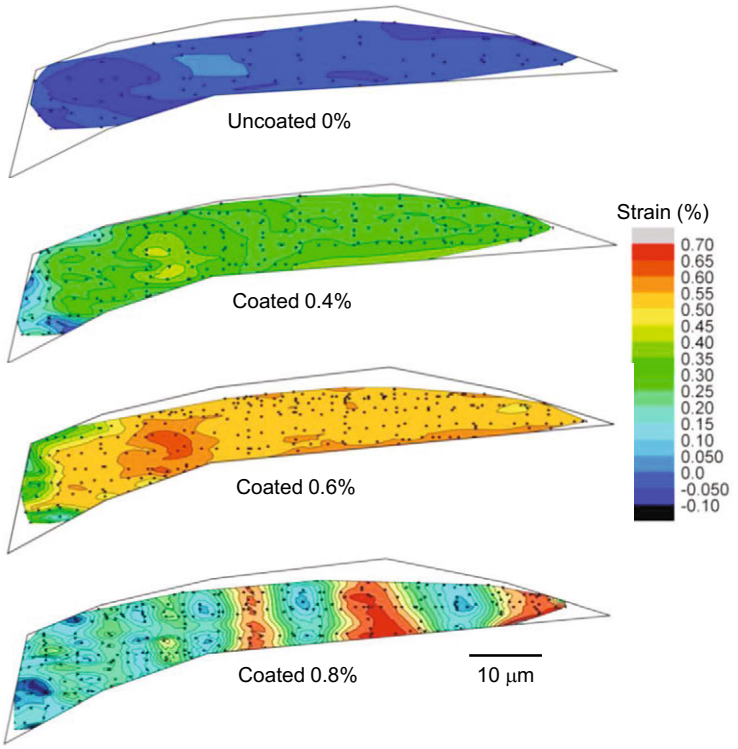

Figure 4.12. Contour maps of strain mapped over the graphene monolayer in a model composite. Maps are shown for the original flake before coating with the top polymer layer and then after coating with the top polymer layer at different levels of matrix strain indicated. (Adapted from Young et al, 2011 with permission from the American Chemical Society).

4.4.2. Few-layer Graphene

The deformation micromechanics of few-layer graphene in composites has also been investigated using Raman spectroscopy as shown in Figure 4.13 (Gong et al, 2012). The distribution of strain across a graphene flake containing both monolayer and bilayer regions is shown in Figure 4.13(a). This shows two important findings. Firstly the data can again be fitted well to the shear-lag model (Equation (4.11)). Secondly it can be seen that the strain in the bilayer regions is identical to that in adjacent monolayer regions. Figure 4.13(b) shows the strain distribution across a bilayer flake that has fragmented due probably to cracking in the polymer coating

(Gong et al, 2012). In this case triangular strain distributions are obtained, indicating damage to the interface and stress transfer by frictional sliding.

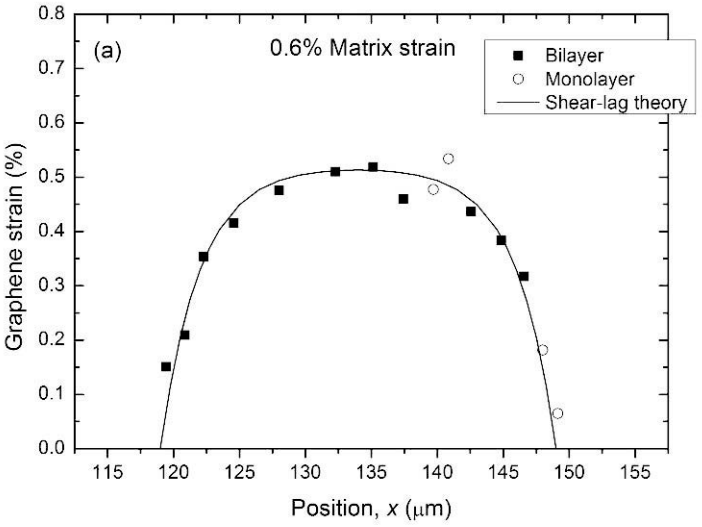

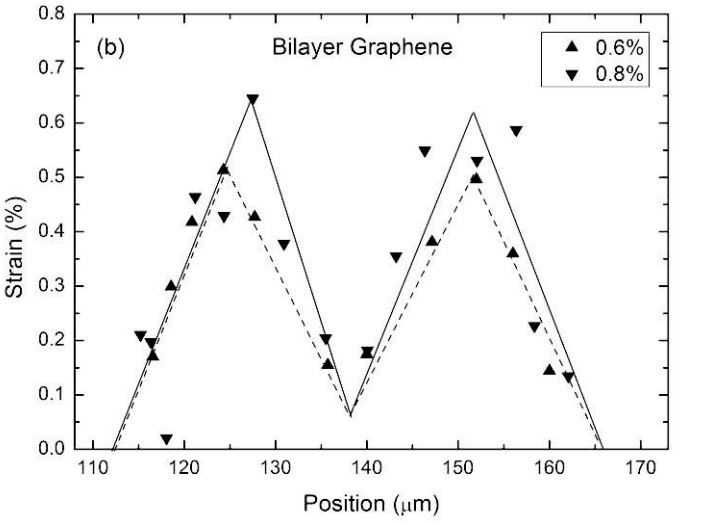

Figure 4.13. Distributions of strain at different matrix strain levels in the direction of the tensile axis across a graphene nanoplatelet. (a) Region with both monolayer and bilayer graphene at 0.6% matrix strain. (b) Bilayer region showing the effect fragmentation at 0.6% and 0.8% strains. (Adapted from Gong et al, 2012 with permission from the American Chemical Society).

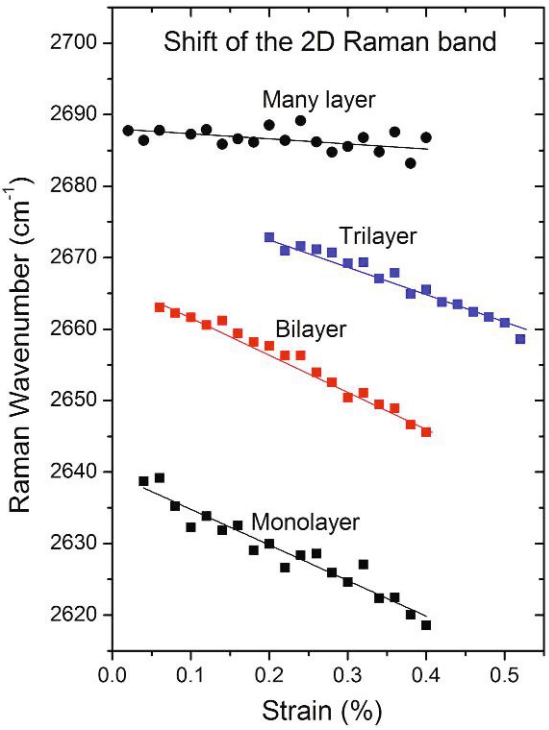

Figure 4.14. Shifts with strain of the 2D band for adjacent monolayer, bilayer and trilayer regions along with the shift with strain for the same band of a multilayer flake on the same specimen. (Adapted from Gong et al, 2012 with permission from the American Chemical Society).

Gong et al (2012) also undertook a systematic study of the deformation of bilayer, trilayer and many-layer graphene with a view to determining the optimum number of layers for the reinforcement of nanocomposites with graphene. The rate of 2D band shift per unit strain for uncoated bilayer graphene on a PMMA beam was found lower

to be than that for a monolayer, implying relatively poor stress transfer between the two layers in the bilayer material. In a subsequent paper Gong et al (2013) demonstrated clearly that the poor stress transfer between the layers in few-layer graphene is due to the reversible loss of Bernal stacking that takes place during shear deformation of the material.

The effect of coating the graphene was also investigated (Gong et al, 2012) and it was found that in this case the shift rate of the monolayer and bilayer material was the same. Measurements were also undertaken in the middle of adjacent monolayer, bilayer and trilayer regions of the same coated graphene flake up to 0.4% strain. The 2D band shifts with strain of these four different coated graphene structures are given in Figure 4.15. The slopes of the plots are similar for the monolayer and bilayer material but somewhat lower for the trilayer. In contrast, the slope for the many-layer graphene is significantly lower at only around -8 cm^{-1}/% strain. These findings were interpreted Gong et al (2012) as indicating that there was good stress transfer at the polymer-graphene interface but there were poorer levels of stress transfer between the graphene layers.

Gong et al (2012) adapted the theory of Zalamea et al (2007) for multi-walled nanotubes to quantify the stress transfer efficiency between the individual layers within graphene and considered first of all the advantages of using bilayer graphene rather than the monolayer material. In the case of two monolayer flakes dispersed well in a polymer matrix, the closest separation they can have will be controlled by the dimensions of the polymer coil, i.e. at least several nm (Gong et al, 2012). The separation between the two atomic layers in bilayer graphene is, however, only around 0.34 nm. It will therefore be easier to achieve higher loadings of bilayer material in a polymer nanocomposite which will lead to an improvement in reinforcement ability by up to a factor of two over monolayer material.

The optimum number of layers needed in many-layer graphene flakes for the best levels of reinforcement in polymer-based nanocomposites was also determined (Gong et al, 2012) The effective Young's modulus of monolayer and bilayer graphene will be similar and it will decrease as the number of layers decreases. For high volume fraction nanocomposites it will be necessary to accommodate the polymer coils between the graphene flakes. The separation of the flakes will be limited by the dimensions of the polymer coils as shown in Figure 4.15 and their minimum separation will depend upon the type of polymer and its interaction with the graphene. This is unlikely to be less than 1 nm and more likely several nm whereas the separation of the layers in multilayer graphene is only around 0.34 nm. In an ideal case, therefore, the nanocomposite can be assumed to be made up of parallel graphene flakes that are separated by thin layers of polymer, as shown in Figure 4.15.

The Young's modulus, E_c, of such as nanocomposite can be estimated to a first approximation using the simple "rule-of-mixtures" (Young and Lovell, 2011; Gibson, 2012) such that

$$E_c = E_{eff} V_g + E_m V_m \tag{4.13}$$

where E_{eff} is the effective Young's modulus of the multilayer graphene, E_m is the Young's modulus of the matrix (~3 GPa), and V_g and V_m are the volume fractions of the graphene and matrix polymer respectively. The maximum nanocomposite Yo ung's modulus can be determined using this equation for different numbers of graphene layers, as a function of the polymer layer thickness. The modulus is found to peak for three-layer graphene for a 1 nm polymer layer thickness and then decrease. The maximum nanocomposite Young's modulus is found to be virtually constant for composites with more than four graphene layers.

In summary, it was suggested by Gong et al (2012) that monolayer material does not necessarily give the best reinforcement and that the optimum number of graphene layers for the best reinforcement will depend upon the polymer layer thickness and the efficiency of stress transfer between the graphene layers.

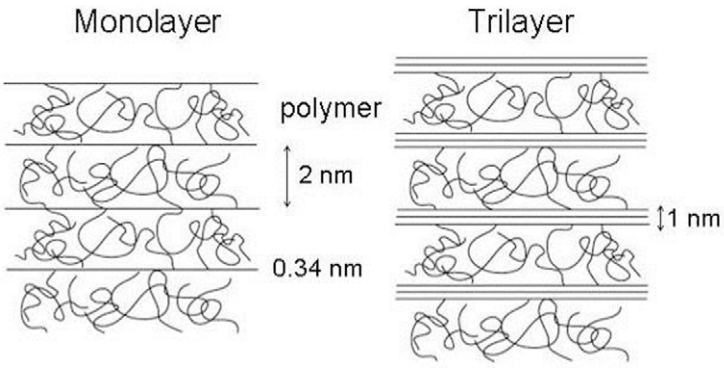

Fig. 8.15. Schematic diagram of the microstructure of graphene-based nanocomposites based upon either monolayer or trilayer reinforcements. The interlayer spacing of the graphene is 0.34 nm and the effective thickness of the polymer coils is assumed to be to be around 2 nm. (Adapted from Gong et al, 2012 with permission from the American Chemical Society).

4.5. Conclusions

A clear conclusion of this study is that the micromechanics of deformation of graphene nanoplatelets can be analyzed in terms of the shear-lag theory developed originally for fibre reinforcement. Although the analysis of fibre reinforcement has been taking place for over 50 years, it is still not yet fully understood. The study of

nanoplatelelet reinforcement in nanocomposites has been undertaken over a much a shorter period and so is far less well-developed. It has been shown that it appears that continuum mechanics is still applicable at the nanoscale and so much of the analysis undertaken for macroscopic composites can be employed and adapted. Nevertheless it remains to be seen how far it is possible, at the nanoscale, to use this analytical methodology and when it is necessary to employ numerical techniques such as the finite element method.

There are again a variety of different challenges that exist in developing micromechanics at the nanoscale that include:

- Axial compression. It is not clear how nanoplatelets respond to in-plane compression and what deformation modes lead to ultimate failure.
- Nanoplatelelet/nanoplatelelet interactions, including restacking. The effect of nanoplatelet separation and restacking upon mechanical properties is yet to be analysed.
- Nanoplatelelet /crack interactions. This is an area that has not yet been explored.
- Effect of nanoplatelelet orientation, waviness and wrinkling. It is thought that waviness and wrinkling may lead to inferior mechanical properties for nanoplatelelet-reinforced nanocomposites but this is yet to be put on a firm theoretical foundation.
- Effect of nanoplatelelet surface treatment and modification. It is highly likely that the chemical modification of nanoplatelelet surfaces will affect stress transfer in nanocomposites but no systematic studies have yet been undertaken.

Many of these problems and issues are similar at both the macroscopic and nanoscales. Some of them are different but the finding outlined in the present chapter that continuum mechanics is still applicable for the understanding of nanomechanics gives us confidence that there are good prospects that further rapid progress will be made in the years to come.

References

Avouris P. (2010). Graphene: Electronic and photonic properties and devices. *Nano Letters*, 10:4285-4294.

Bae S., Kim H. K., Lee Y. B., Xu X. F., Park J.-S., Zheng Y., Balakrishnan J., Lei T., Kim H. R., Song Y. I., Kim Y.-J., Kim K. S., Özyilmaz B., Ahn J.-H., Hong B. H., and Iijima S. (2010). Roll-to-roll production of 30-inch graphene films for transparent electrodes. *Nature Nanotechnology*, 5:574-578.

Bangert U., Gass M. H., Bleloch A. L., Nair R. R., and Geim A. K. (2009). Manifestation of ripples in free-standing graphene in lattice images obtained in an aberration-corrected scanning transmission electron microscope. *Physics Status Solidi A*, 206:1117–1122.

Booth T. J., Blake P., Nair R. R., Jiang D., Hill E. W., Bangert U., Bleloch A., Gass M., Novoselov K. S., Katsnelson M. I., and Geim A. K. (2008), Macroscopic graphene membranes and their extraordinary stiffness. *Nano Letters*, 8:2442-2446.

Cooper C. A., Young R. J., and Halsall M. (2001). Investigation into the deformation of carbon nanotubes and their composites through the use of Raman spectroscopy. *Composites A: Applied Science and Manufacturing*, 32:401-411.

Cox H. L. (1952). The elasticity and strength of paper and other fibrous materials. *British Journal of Applied Physics*, 3:72-79.

Ferrari A. C., Meyer J. C., Scardaci V., Casiraghi C., Lazzeri M., Mauri F., Piscanec S., Jiang D., Novoselov K. S., Roth S., and Geim A. K. (2006). Raman spectrum of graphene and graphene layers. *Physical Review Letters*, 97:187401.

Geim A. K., and Novoselov K. S. (2007). The rise of graphene. *Nature Materials*, 6:183-190.

Geim A. K. (2011). Nobel Lecture: Random walk to graphene. *Reviews of Modern Physics*, 83:851-862.

Gibson R. F. (2012). *Principles of Composite Material Mechanics*, 3rd Edition, CRC Press, Boca Raton.

Gong L., Kinloch I. A., Young R. J., Riaz I., Jalil R., and Novoselov K. S. (2010). Interfacial stress transfer in a graphene monolayer nanocomposite. *Advanced Materials*, 22:2694-2697.

Gong L., Young R. J., Kinloch I. A., Riaz I., Jalil R., and Novoselov K. S., Optimizing the reinforcement of polymer-based nanocomposites by graphene. *ACS Nano*, 2012, 6:2086-2095.

Gong L., Young R. J., Kinloch I. A., Haigh S. J., Warner J. H., Hinks J. A., Xu Z. W., Li L., Ding F., Riaz I., Jalil R., and Novoselov K. S. (2013). Reversible loss of Bernal stacking during the deformation of few-layer graphene in nanocomposites. *ACS Nano*, 7:7287-7294.

Hernandez Y., Nicolosi V., Lotya M., Blighe .F M., Sun Z. Y., De S., McGovern I. T., Holland B., Byrne M., Gun'ko Y. K., Boland J. J., Niraj P., Duesberg G., Krishnamurthy S., Goodhue R., Hutchison J., Scardaci V., Ferrari A. C., and Coleman J. N. (2008). High-yield production of graphene by liquid-phase exfoliation of graphite, *Nature Nanotechnology*, 3:563-568.

Kalaitzidou K., Fukushima H., Drzal L. T. (2007). A new compounding method for exfoliated graphite–polypropylene nanocomposites with enhanced flexural properties and lower percolation threshold. *Composites Science and Technology*, 67:2045–2051.

Kelly A. (1966). *Strong Solids*, Clarendon Press, Oxford.

Kelly A., and Macmillan N. H. (1986). *Strong Solids*, 3rd Edition, Clarendon Press, Oxford.

Lee C., Wei X. D., Kysar J. W., and Hone J. (2008). Measurement of the elastic properties and intrinsic strength of monolayer graphene. *Science*, 321:385-388.

Liu F., Ming P. B. and Li J. (2007). *Ab initio* calculation of ideal strength and phonon instability of graphene under tension. *Physical Review B*, 76:064120.

Malard L. M., Pimenta M. A., Dresselhaus G., and Dresselhaus M. S. (2009). *Physics Reports-Review Section of Physics Letters*. 473:51-87.

Meyer J. C., Geim A. K., Katsnelson M. I., Novoselov K. S., Booth T. J., and Roth S. (2007). The structure of suspended graphene sheets. *Nature*, 446:60-63.

Montes-Morán M. A., and Young R. J. (2002). Raman spectroscopy study of HM carbon fibres: effect of plasma treatment on the interfacial properties of single fibre/epoxy composites, Part II: Characterisation of the fibre/matrix interface. *Carbon*, 40:857-875.

Nair R. R., Blake P., Grigorenko A. N., Novoselov K. S., Booth T. J., Stauber T., Peres N. M. R., and Geim A. K. (2008). Fine structure constant defines visual transparency of graphene. *Science*, 320:1308.

Novoselov K. S., Geim A. K., Morozov S. V., Jiang D., Zhang Y., Dubonos S. V., Grigorieva I. V., and Firsov A. A. (2004). Electric field effect in atomically thin carbon films. *Science*, 306:666-669

Novoselov K. S. (2011). Nobel Lecture: Graphene: Materials in the flatland. *Reviews of Modern Physics*. 83:837-849.

Rao C. N. R., Biswas K., Subrahmanyam K. S., and Govindaraj A. (2009), Graphene, the new carbon. *Journal of Materials Chemistry*, 19:2457-2469.

Suk J. W., Kitt A., Magnuson C. W., Hao Y., Ahmed S., An J., Swan A. K., Goldberg B. B., and Ruoff R. S. (2011). Transfer of CVD-grown monolayer graphene onto arbitrary substrates. *ACS Nano*, 5:6916-6924

Young R. J. (1995). Monitoring deformation processes in high-performance fibres using Raman spectroscopy. *Journal of the Textile Institute*, 86:360-381.

Young R. J., Gong L., Kinloch I. A., Riaz I., Jalil R., and Novoselov K. S. (2011). Strain mapping in a graphene monolayer nanocomposite. *ACS Nano*, 5:3079-3084.

Young R. J., Kinloch I. A., Gong L., and Novoselov K. S. (2012). The mechanics of graphene nanocomposites: A review. *Composites Science and Technology*, 72:1459–1476.

Young R. J., and Lovell P. A. (2011). *Introduction to Polymers*, CRC Press, Boca Raton, Chapter 24.

Zalamea L., Kim H., and Pipes R. B. (2007). Stress transfer in multi-walled carbon nanotubes. *Composites Science and Technology*, 67:3425-3433.

5 Carbon Nanotubes Under Pressure

Yiwei Sun* and David J Dunstan *

* School of Physics and Astronomy, Queen Mary University of London, London, United Kingdom

5.1 Introduction

Carbon nanotubes (CNTs) have extraordinary mechanical properties due to the stiff sp^2 bond resulting in the exceptionally high Young's moduli in the tera-pascal range, together with their tube structure (Treacy et al., 1996). They have unique electronic properties; they can be either metallic or semiconducting depending on the chirality — the direction along which a tube is rolled up (Odom et al., 1998). Pressure modifies these properties. The sp^2 bond stiffens further, and the band gap in semiconducting CNTs changes with pressure (Yang and Han, 2000). To characterize and understand the behaviour of CNTs under pressure, the shift rates of the phonon frequencies with pressure are very interesting, as they directly reflect the mechanics and are closely related to the electronic properties. They can also be used as strain sensors.

In this chapter, we will focus on the shift with pressure of the graphite mode (GM) and the radial breathing mode (RBM). The GM is an in-plane vibrational mode, coming from graphite and characteristic of sp^2-hybridized carbon (Tuinstra and Koenig, 1970). The study of the GM pressure coefficients of CNTs thus provides a direct approach to understand the sp^2 bond. It links closely to the high pressure study of other sp^2-bonded materials such as graphene and fullerene. The RBM, though related to the GM, is a unique signature of CNTs (Rao et al., 1997). Its vibrational frequency is diameter-dependent and therefore of critical importance to the study of features, which are related to the tube structure, including the GM pressure coefficients. We will briefly mention other modes, such as the 2D-mode, the second order D-mode from defects, which reflects the change in the electron bands, essential to characterizing graphene (Ferrari et al., 2006).

O. Paris (Ed.), *Structure and Multiscale Mechanics of Carbon Nanomaterials*,
CISM International Centre for Mechanical Sciences
DOI 10.1007/ 978-3-7091-1887-0_5

5.2 The Graphite Mode

5.2.1 The Graphite Mode Phonons in Graphite

The GM is the Raman-active $E_{2g}^{(2)}$ optical mode of graphite at 1582 cm^{-1}, illustrated in Figure 5.1 by Reich and Thomsen (2004). It is a two-fold (longitudinal and transverse) degenerate mode, first reported by Tuinstra and Koenig (1970). The degeneracy is removed if the symmetry is broken by an external perturbation, such as strain. Mohiuddin et al. (2009) demonstrate this in the case of graphene under uniaxial tensile strain, where the G^+ (+ for higher energy) and G^- denote the two perpendicular modes (see Figure 5.2).

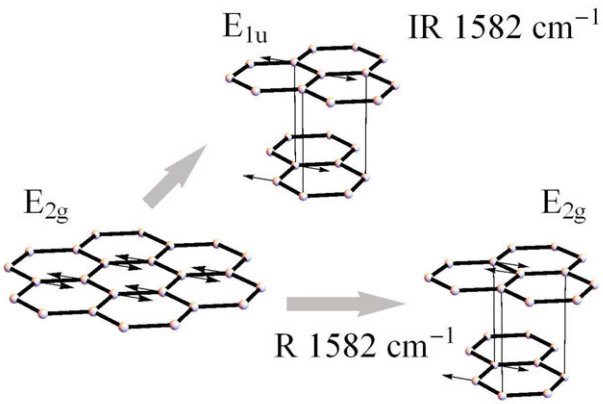

Figure 5.1. "Phonon eigenvectors of graphene and graphite. Every phonon eigenvector of graphene gives rise to two vibrations of graphite. For example, the in-phase combination of the two layers for the E_{2g} optical mode of graphene yields $E_{2g} \otimes A_{1g} = E_{2g}$ and the out-of-phase combination $E_{2g} \otimes B_{1u} = E_{1u}$. Next to the graphite modes it is indicated whether they are Raman (R) or infrared (IR) active and the experimentally observed phonon frequencies. The translations of graphite are omitted from the figure." After Figure 2 of Reich and Thomsen (2004).

Hanfland et al. (1989) record the first Raman spectrum of graphite under high pressure. Figure 5.3 shows the GM ($E_{2g}^{(2)}$) frequencies with the pressure

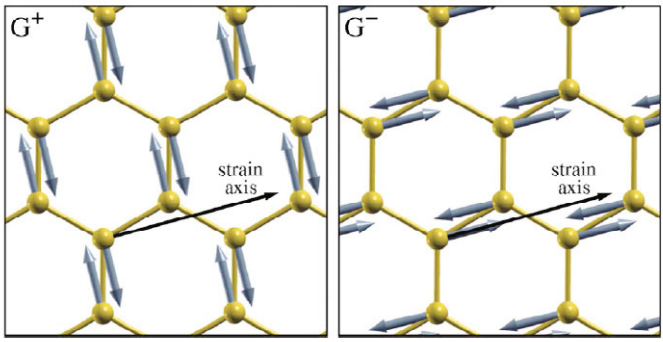

Figure 5.2. "Eigenvectors of G^+ and G^- modes determined by density-functional perturbation theory. These are perpendicular to each other, with G^- polarized along the tensile strain axis, as expected." Reprinted figure with permission from [T. M. G. Mohiuddin et al., Phys. Rev. B 79, 205433 (2009)] Copyright (2009) by the American Physical Society.

under which they are obtained. The pressure dependence of the frequency

$$\omega(P)/\omega_0 = [(\delta_0/\delta')P + 1]^{\delta'} \tag{1}$$

where δ_0 is the logarithmic pressure derivative $(dln\omega/dP)_{P=0}$ and δ' is the pressure derivative of $dln\omega/dP$, is least-square fitted to the experimental data. The frequency of the GM increases sublinearly under pressure with an initial pressure coefficient of 4.7 $cm^{-1}GPa^{-1}$.

The GM is an in-line anti-phase motion (see Figure 5.1) and therefore the shift of its frequency with pressure (4.7 $cm^{-1}GPa^{-1}$) should be determined by the shortening of the $C-C$ bond. The sublinearity observed in graphite is considered (Sun et al., 2013) to be the result of the combination of the very soft C_{33}, 39 GPa in graphite (Bosak and Krisch, 2007) together with its relatively large pressure coefficient C'_{33} ~10 (Green et al., 1972).

Experimental and theoretical efforts have been made to explain the value of 4.7 $cm^{-1}GPa^{-1}$. The natural approach is, as we mentioned, to relate the GM frequency to the sp^2 bond length. Huang et al. (2009) give the dynamic equations of the graphene GM as

$$\sum_{\beta} K_{\alpha\beta}u_{\beta} = \omega^2 u_a \tag{2}$$

where $\mathbf{u}=(u_1, u_2)$ is the relative displacement of the two carbon atoms in the unit cell, ω is the phonon frequency and K is the force constant tensor,

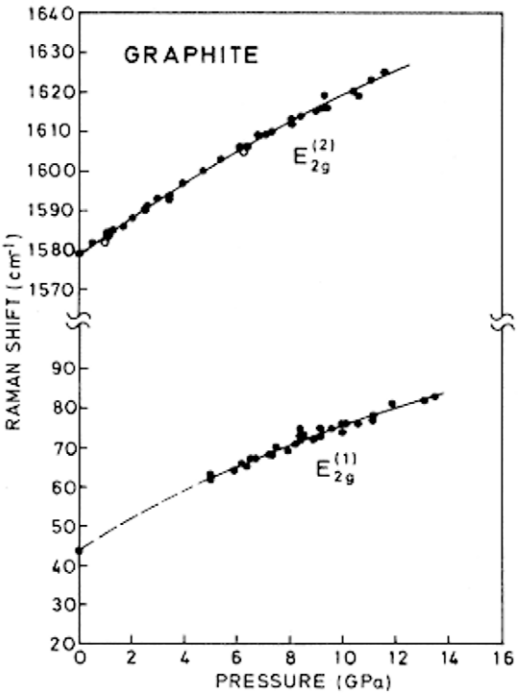

Figure 5.3. Raman shifts of the two E_{2g} modes of graphite. Lines are for the results of a least-squares fit of Eq. (1) to the experimental data. Open circles are for decreasing pressure. Reprinted figure with permission from [M. Hanfland, H. Beister, and K. Syassen, Phys. Rev. B 39, 12598 (1989)] Copyright (1989) by the American Physical Society.

which can be expanded in powers of strain as

$$K_{\alpha\beta} = K^0_{\alpha\beta} + \sum_{lm} K^{\varepsilon}_{\alpha\beta lm}\varepsilon_{lm} \tag{3}$$

The secular equation for Eq. 2, where $K^{\varepsilon}_{\alpha\beta lm}$ has only two independent elements because of the hexagonal lattice, gives the solutions of phonon frequencies in terms of strain. Thomsen et al. (2002) express the solutions with the Grüneisen parameter and shear deformation potential (SDP) as

$$\frac{\Delta\omega}{\omega_0} = \gamma(\varepsilon_{xx} + \varepsilon_{yy}) \pm \frac{1}{2}SDP(\varepsilon_{xx} - \varepsilon_{yy}) \tag{4}$$

where ω_0 is the unperturbed frequency. Eq. 4 makes explicit the two-dimensional nature of the analysis. The Grüneisen parameter γ and the SDP are the two key parameters and a number of experimental (Mohiuddin et al., 2009; Huang et al., 2009; Ni et al., 2008; Proctor et al., 2009; Soldatov et al., 2012) and theoretical (Mohiuddin et al., 2009; Mohr et al., 2009; Thomsen et al., 2002) papers report work on graphene under strain to define their accurate values. The results are shown in Table 5.1. It is worth noticing that Ghandour et al. (2013) point out that the transverse strain ε_T=0 rather than ε_T=-$\nu\varepsilon_L$, where ν is in-plane Poisson's ratio and ε_L is longitudinal strain, in the case that uniaxial strain is applied by flexure of a wide beam or sheet to which a graphene flake adheres.

Table 5.1. The Grüneisen parameter and SDP obtained from various experiments and calculations of graphene. The values in square brackets are the corrections by Ghandour et al. (2013)

Experiments	γ	SDP
uniaxial strain (beam flexure) (Huang et al., 2009)	0.69[0.58]	0.38[0.435]
uniaxial strain (beam flexure) (Mohiuddin et al., 2009)	1.99[1.34]	0.99[1.31]
uniaxial strain (substrate stretch) (Ni et al., 2008)	1.5	
hydrostatic pressure (Proctor et al., 2009)	1.99	
hydrostatic pressure (Soldatov et al., 2012)	2.3	
Calculations		
uniaxial strain (Mohiuddin et al., 2009)	1.87	0.92
uniaxial strain (Mohiuddin et al., 2009)	1.83	1.18
biaxial strain (Mohiuddin et al., 2009)	1.8	
hydrostatic and shear strain (Thomsen et al., 2002)	2.0	0.66

For graphite, the pressure coefficient of 4.7 $cm^{-1}GPa^{-1}$ is equivalent to the Grüneisen parameter of 2.0. A good agreement has been achieved from calculations. The discrepancy from the experiments is not understood, and is currently attributed to the effect of the substrate (Nicolle et al., 2011).

This leads to a very important problem for sp^2-hybridized carbon material, that is, why and by how much the environment (e.g., substrate, solvent, bundles) can affect the $C-C$ bond stiffening with pressure.

5.2.2 What We Expect in Single-Wall Carbon Nanotubes

Graphene sheets are stacked to make graphite and rolled up to make single-wall carbon nanotubes (SWCNTs). It is reasonable to assume that the GM pressure coefficient of SWCNTs is also determined by the shortening of $C-C$ bond and therefore the shift rate of a solvent-filled tube is expected to be 4.7 $\mathrm{cm}^{-1}\mathrm{GPa}^{-1}$.

Now we consider an empty tube under hydrostatic pressure. Taking a finite wall thickness into account (the thick-wall-tube model), the tangential stress is

$$\sigma_t = \frac{r_o}{r_o - r_i} P \tag{5}$$

and the axial stress is

$$\sigma_a = \frac{r_o^2}{r_o^2 - r_i^2} P \tag{6}$$

where r_o is the outer radius of the wall and r_i is the inner radius. Setting, for example, the diameter at a typical value of 1.3 nm and the wall thickness at 0.36 nm (the interlayer distance a_{33} of graphite), we expect the pressure coefficients of the 'tangential' mode to be 8.5 and the 'axial' to be 5.9 $\mathrm{cm}^{-1}\mathrm{GPa}^{-1}$. Jorio et al. (2002) assigned the lower energy G^- to the tangential mode, the frequency of which is sensitive to the tube wall curvature and the higher energy G^+ to the axial mode which is independent of the curvature. A caveat here is the significant electron-phonon coupling due to a Kohn anomaly, which softens only the axial mode of metallic tubes and hereby makes it G^-. This has been predicted (Dubay et al., 2002) and confirmed (Farhat et al., 2007), while its effect on the GM pressure coefficients, however, is still unclear.

If we keep compressing an empty tube, there is a critical point, beyond which it will collapse. Therefore we expect the GM to shift with pressure as illustrated in Figure 5.4 — the shift rate is at the value of a thick-wall hollow tube initially and the frequency and its shift rate should both decrease to the values of graphite when the tube collapses (Caillier et al., 2008). In this chapter, we will focus on the behaviour of CNTs below the critical pressure and the problem of the collapse will be discussed in details in Chapter 7.

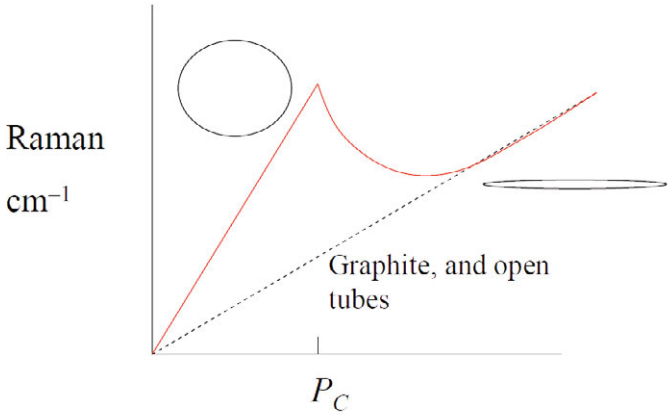

Figure 5.4. The solid line is for the GM shift with pressure of a hollow SWCNT and the dash line is for graphite. This illustration is based on the results reported by Caillier et al. (2008).

5.2.3 What We Find (Not What We Expect)

First, we introduce early published results of the GM pressure coefficients which were not assigned to a specific tube diameter. Venkateswaran et al. (1999) perform the first high pressure experiment on SWCNTs. They loaded samples into a diamond anvil cell (DAC) and recorded their Raman spectra at various pressures (see Figure 5.5). They plot the frequencies of the G^+ (T3) and the wall-curvature (tube diameter) dependent G^- band (T1 and T2) with pressure (see Figure 5.6 (b)), and obtain the initial linear shift rates at 7.1, 10 and 8 $cm^{-1}GPa^{-1}$ for T3, T2 and T1, respectively.

Since then, many high pressure studies on the GM of SWCNTs have been published, using various laser excitation wavelength and different pressure transmit media (PTM). Only recently were the GM pressure coefficients assigned to a specific diameter; we return to this point later. Meanwhile, no consensus on the value of the pressure coefficient was achieved, as shown in Figure 5.7 (Venkateswaran et al., 1999; Christofilos et al., 2007, 2005; Ghandour et al., 2011; Venkateswaran et al., 2001; Proctor et al., 2006; Thomsen et al., 1999; Lebedkin et al., 2006; Sood et al., 1999; Sandler et al., 2003; Merlen et al., 2005; Yao et al., 2008), which gives a summary of some early work on the shift rates of the dominant G^+ band (the signal is clear enough to extract accurate frequencies despite to the weaker signals from inside diamond-anvil high-pressure cells). Nevertheless, what can be

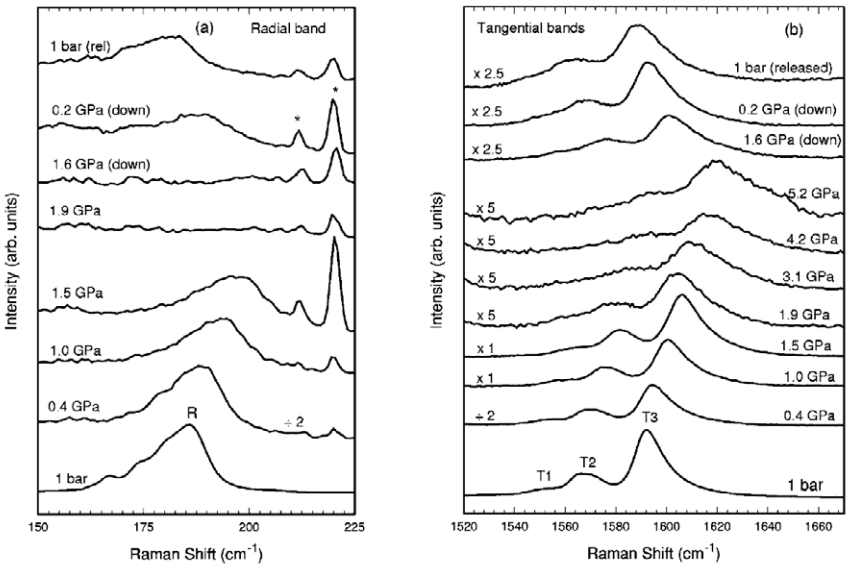

Figure 5.5. The pressure dependence of the room-temperature Raman spectra of SWCNTs bundles for the RBM (a) and the GM (b). The GM intensity drops significantly above 1.5 GPa. The spectra were recorded using 514.5 nm excitation. The observed laser plasma lines are labelled by $\star$ in panel (a). Reprinted figure with permission from [U. D. Venkateswaran et al., Phys. Rev. B 59, 10928 (1999)] Copyright (1999) by the American Physical Society.

seen from Figure 5.7 is that effects such as PTM, laser excitation energy and bundling/surfactant can all affect the GM pressure coefficients observed.

Although we cannot yet give a clear answer what the GM pressure coefficients are, some facts are worth noticing before considering the assignment of data to particular diameters. First, the evolution of the GM shift with pressure is reported to indicate tube collapsing as expected. Yao et al. (2008) and Caillier et al. (2008) present a representative GM shift with pressure (see Figure 5.8), clearly showing that the GM frequency of empty tubes shifts faster than graphite (4.7 $\mathrm{cm^{-1}GPa^{-1}}$) initially and both the frequency and its shift rate drop to about the values of graphite after the tubes collapse. Second, the GM pressure coefficient of solvent-filled tubes, against expectation, is not 4.7 $\mathrm{cm^{-1}GPa^{-1}}$. Merlen et al. (2006) report the GM pressure coefficients of open-ended tubes as 6.5 $\mathrm{cm^{-1}GPa^{-1}}$ in argon

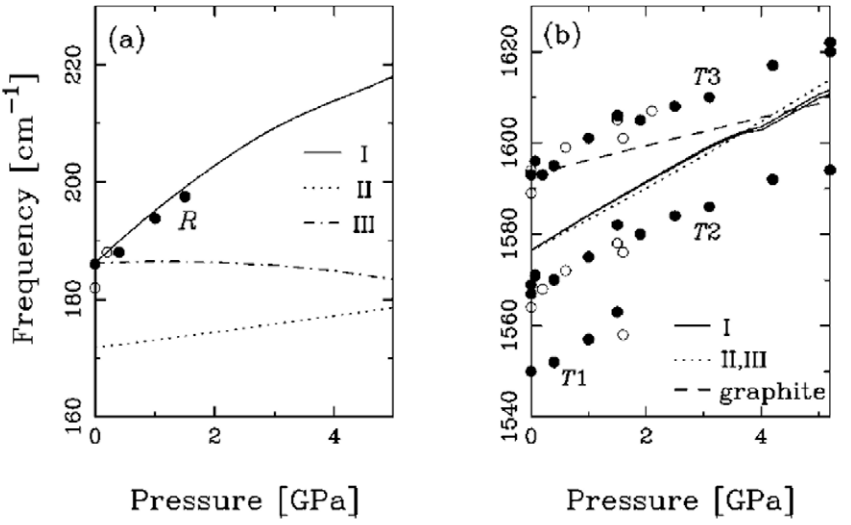

Figure 5.6. Pressure dependence of the RBM (a) and the GM (b) frequencies of SWCNTs bundles. The results of the calculations using different models are indicated by solid and dotted lines. Experimental data (T1, T2, and T3) measured during the upward and downward cycles of pressure are plotted as solid and open circles, correspondingly. Dashed line in (b) corresponds to generalized tight-binding molecular dynamics result for the $E_{2g}^{(2)}$ mode frequency in graphite. Reprinted figure with permission from [U. D. Venkateswaran et al., Phys. Rev. B 59, 10928 (1999)] Copyright (1999) by the American Physical Society.

and in 4:1 methanol-ethanol, and as 10 cm^{-1}GPa^{-1} in paraffin oil. This raises another issue: what molecules can enter, and how much they can enter, into a SWCNT through an open end. Third, doping shifts the GM frequencies. Skakalova et al. (2005) report the doping effects on the GM frequency (see Figure 5.9), which indicate that the charge transfer shifts the GM frequency, but whether it changes the GM pressure coefficient is unclear — an increase in charge transfer with pressure is plausible, and this would impact on the pressure coefficient.

Recent reported experimental work enables the assignment of the observed GM pressure coefficients to a specific tube diameter. This can be done in two ways: using resonance-enhanced Raman spectroscopy (RRS), which generally requires a Raman system equipped with a wavelength-

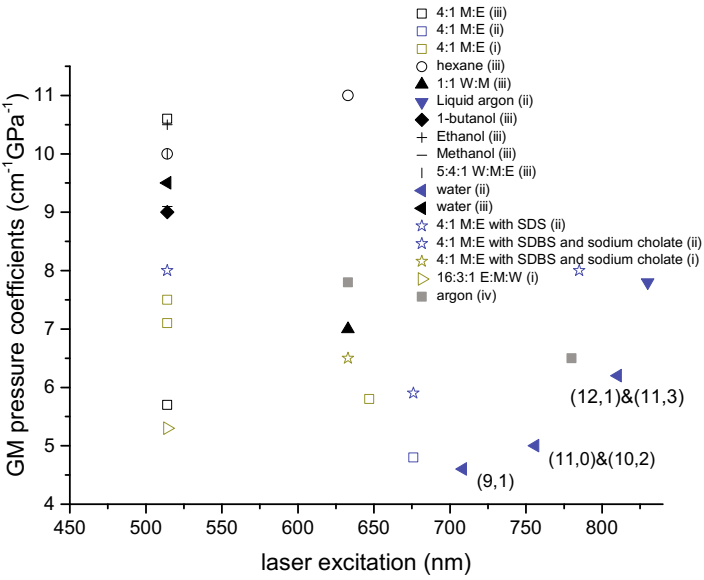

Figure 5.7. The GM pressure coefficients of SWCNTs reported in previous literature are plotted against the laser excitation wavelengths, at which they were obtained. Symbols identify the PTM used. The stars are for the individual tubes dispersed by surfactants. Three points are labelled with specific chiralities, to which they are assigned. M:Methanol; E:Ethanol; W:Water; SDS:Sodium dodecyl sulfate; SDBS:Sodium dodecylbenzene sulfonate. i: samples produced by pulsed-laser vaporization process, with a diameter range of 1.22–1.36 nm; ii: high pressure catalytic decomposition of carbon monoxide, 0.8–1.2 nm; iii: arc discharge method, 1.2–1.6 nm; iv: synthesis method not specified, 1.3±0.2 nm, labelled as dark green, blue, black and grey, respectively.

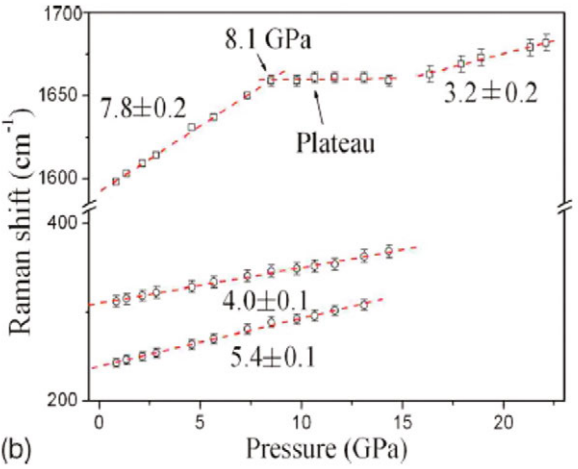

Figure 5.8. The frequencies of two RBMs (circles) and the most intense G^+ peak (squares) are plotted with pressure. Reprinted figure with permission from [Mingguang Yao et al., Phys. Rev. B 78, 205411 (2008)] Copyright (2008) by the American Physical Society.

tunable laser, or using SWCNTs samples of a single diameter. Liu et al. (2011) successfully synthesised SWCNTs of a single chirality (and therefore diameter) but these tubes are not yet commercially available and no high pressure study of them has been reported. Hence, here we focus on the other method, picking out tubes of a specific diameter by RRS.

RRS depends on the electronic structure of SWCNTs. As one-dimensional materials, they have the feature that their density of states (DOS) is not a continuous function of energy, but descends gradually and increases in a spike. The sharp peaks are called Van Hove singularities and the gaps between them are found to be related to the tube diameters. This is presented by Kataura et al. (1999) in the famous Kataura Plot (Figure 5.10).

For Raman scattering, the resonance condition is given by Martin and Falicov (1975) as

$$I(E_{laser}) \propto |\frac{1}{(E_{laser} - E_{ii} - i\Gamma)(E_{laser} \pm E_{ph} - E_{ii} - i\Gamma)}|^2 \qquad (7)$$

where I is the intensity of Raman scattering, E_{laser} is the laser energy, E_{ii} is the transition energy (gap between Van Hove singularities), E_{ph} is the energy of a specific phonon mode, and Γ is the broadening factor deriving

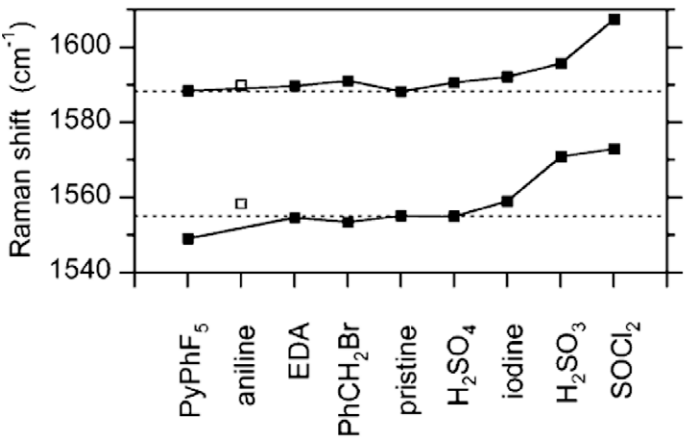

Figure 5.9. Raman shifts of the GM for SWCNTs chemically treated with different molecules as labelled are compared to the values for the pristine sample (dotted lines). The order of samples along the horizontal axis is of increasing conductivity. Aniline data (open squares) are not included in the trend lines. Adapted with permission from (V. Skkalov, A. B. Kaiser, U. Dettlaff-Weglikowska, et al, J. Phys. Chem. B, 2005, 109 (15), pp 71747181). Copyright (2005) American Chemical Society.

from the life time of the resonant states. Because Γ is usually tiny compared to other terms, the Raman intensity will increase significantly when either the incident photon at E_{laser} or the outgoing photon at $E_{laser} \pm E_{ph}$ (+ for anti-Stokes and – for Stokes scattering) matches the transition energy E_{ii} (resonance). Practically, the amount of such increase can easily reach up to 10^6. Therefore, at selected laser excitation wavelength, we can obtain a Raman spectrum dominated by the SWCNTs of a specific diameter, which are in resonance. A 3D plot by Fantini et al. (2004) gives a clear demonstration for RBM (see Figure 5.11). The GM behaves similarly, as long as we pay attention to the E_{ph}, which is about 200 meV for the GM and about 50 meV for the RBM.

A specific tube diameter corresponds to a unique chirality. In principle, the GM pressure coefficient can be assigned to a specific chirality, while the practical difficulty rises as lots of chiralities may correspond to very similar diameters. The uncertainty of the chirality assignment can be decreased by a further analysis of the Katuara plot — the branches in Figure 5.10

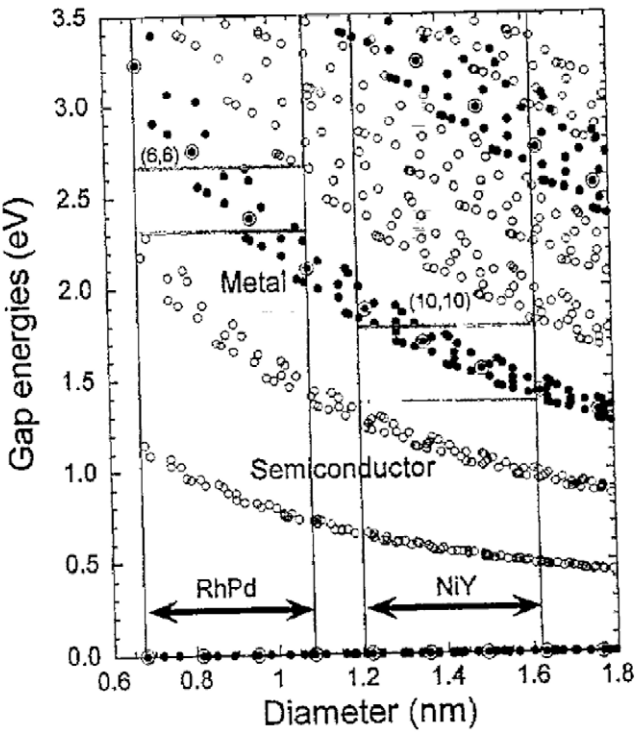

Figure 5.10. "Calculated gap energies between mirror-image spikes in density of states for $\gamma = 2.75$ eV. Solid circles indicate the metallic SWNTs and open circles the semiconducting ones. Double circles indicate the armchair-type SWNTs. Gap energies for all the chiral indexes with larger diameter than (5, 5) are plotted as a function of diameter. Arrows show diameter distributions for the each catalyst. Two horizontal lines in each catalyst area show metallic window in which the optical transitions only by the metallic tubes would be observed." Reprinted figure with permission from [H. Kataura,Y. Kumazawa,Y. Maniwa,I. Umezu,S. Suzuki,Y. Ohtsuka,Y. Achiba, Synthetic Metals 103, 2555–2558 (1999)] Copyright (1999) by the Elsevier.

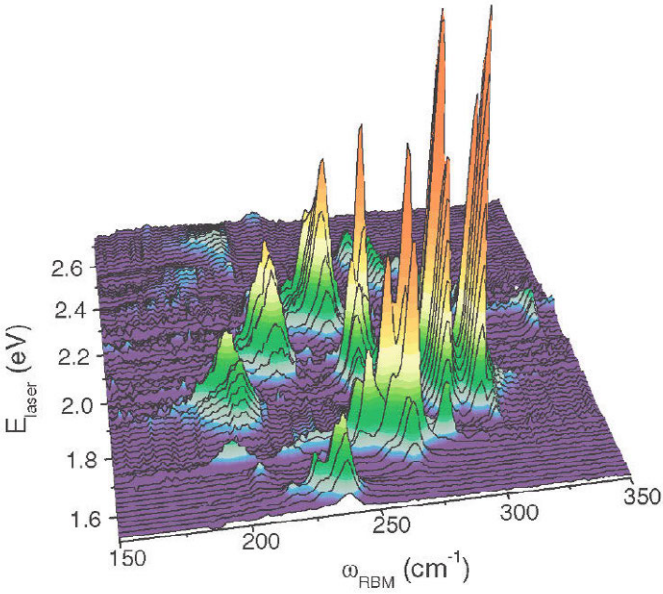

Figure 5.11. The RBM Raman measurements of SWCNTs dispersed in SDS aqueous solution (O'Connell et al., 2002), measured with 76 different laser lines. The non-resonance Raman spectrum from a separated CCl_4 solution is obtained after each of the RBM measurement, and is used to calibrate the intensities of the spectra and to check the frequency calibration. Reprinted figure with permission from [C. Fantini et al., Phys. Rev. Lett. 93, 147406 (2004)] Copyright (2004) by the American Physical Society.

refer to semiconducting or metallic tubes, which is determined by the chirality (Odom et al., 1998), and the order of transitions (E_{11} for the nearest van Hove singularities and so on). It says that chiralities corresponding to similar tube diameters but belonging to different branches will not contribute to the ambiguity in chirality assignment. Further refinement of the Kataura plot has been carried out by detailed comparison of experiment and theory. Figure 5.12 by Maultzsch et al. (2005) is a good reference for chirality assignment in RRS experiments of SWCNTS under high pressure, with the caveat that we do not know exactly how the whole diagram shifts with pressure.

Ghandour et al. (2013) give an experimental example of achieving the

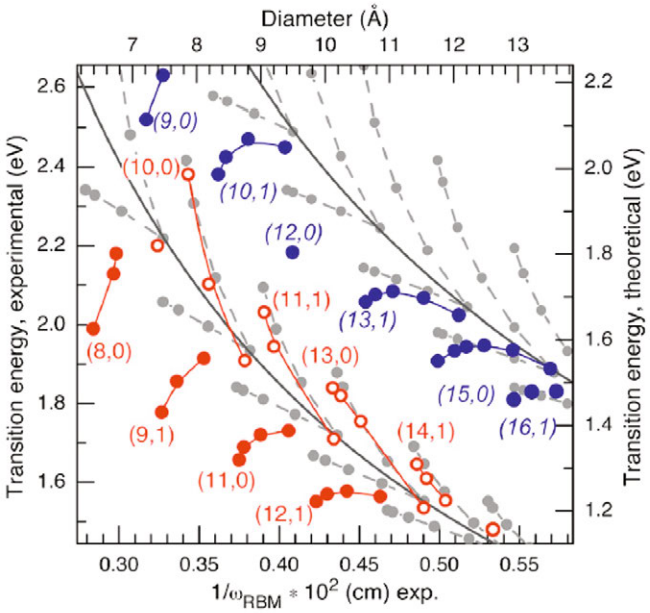

Figure 5.12. "Experimental (large open and closed circles, left and bottom axes) and theoretical (small gray circles, right and top axes) Kataura plot. The second transitions of semiconducting tubes E_{22}^S and the first transitions E_{11}^M of metallic tubes are shown. The solid lines give the approximate 1/d dependence of the transition energies. The dashed lines indicate the 'V'-shaped branches, where the chirality of a tube is related to its left neighbour (n_1, n_2) by $(n_1', n_2')=(n_1-1, n_2+2)$. In the experimental data, the assignment is given for the first tube in each branch, where upright numbers indicate semiconducting and italic numbers indicate metallic tubes. The semiconducting tubes are divided into two families with $\nu=(n_1-n_2) \bmod 3= -1$ (full circles, lower branches) and with $\nu= +1$ (open circles, upper branches)." Reprinted figure with permission from [J. Maultzsch et al., Phys. Rev. B 72, 205438 (2005)] Copyright (2005) by the American Physical Society.

GM pressure coefficient of a specific chirality. They applied high pressure to SWCNTs at selected laser excitation wavelength and recorded the Raman spectra as shown in Figure 5.13. We see only one dominant and identifiable RBM peak at each of these particular excitation energies and therefore the GM peak at that excitation energy is known to be acquired from tubes of the same chirality (after some analysis of the E_{ph}). The pressure coefficients are presented in Figure 5.7, marked with the tube chiralities to which they belong.

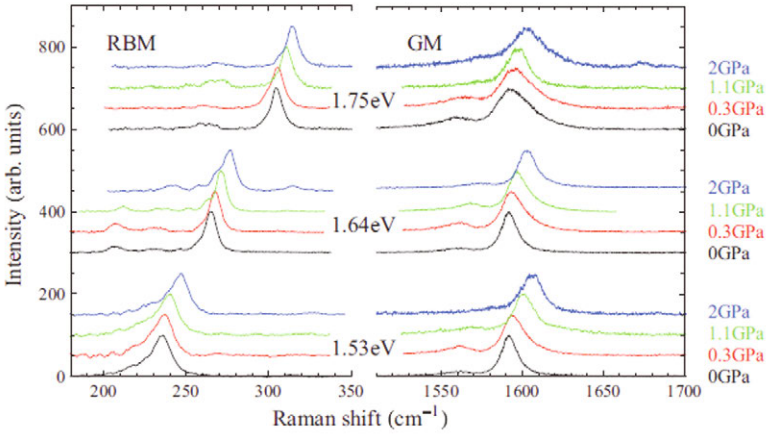

Figure 5.13. "RBM and G-mode spectra for the excitation energies and pressures marked, offset vertically for clarity. The spectra under 1.75-eV excitation (upper group) are assigned to the (9, 1) chirality, the spectra under 1.64-eV excitation (middle group) to the (11, 0) and (10, 2) chiralities, and the spectra under 1.53 eV (lower group) to the (12, 1) and (11, 3) chiralities." Reprinted figure with permission from [A. J. Ghandour et al., Phys. Rev. B 87, 085416 (2013)] Copyright (2013) by the American Physical Society.

Experimental data for more chiralities is required in order to reliably establish a relationship between the GM pressure coefficients and the tube chiralites. Sun et al. (2014) report the GM pressure coefficient of (6, 5) tubes, which are of similar diameter to the (9, 1) tubes reported by Ghandour et al. (2013) (Figure 5.7). Unexpectedly, the result is very different from the (9, 1) tubes and from the value predicted by the thick-wall-tube model (see Figure 5.14). Though the ovalization of tubes before collapsing may be responsible for abnormal shifts of the GM (Aguiar et al., 2012), no

evidence shows that it can increase the pressure coefficient of the G^+, not mentioning by the amount about twice as much.

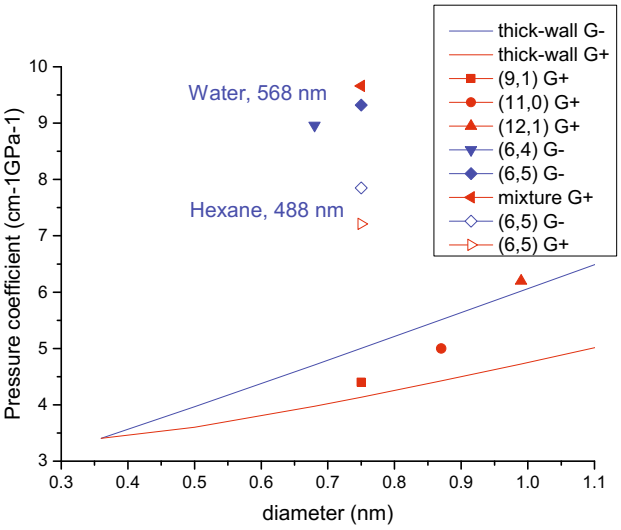

Figure 5.14. The pressure coefficients of carbon nanotubes are plotted against their diameters. The solid lines are for the values predicted by the thick-wall-tube model. The colour red is for the G^+ and the blue is for the G^-. The experimental data is presented as labelled. The data of (9, 1), (11, 0) and (12, 1) tubes are from Ghandour et al. (2013) and the others are from Sun et al. (2014), with the corresponding laser excitation wavelength labelled. Solid symbols are for the data obtained in water and open symbols are for in hexane. The 'mixture G^+' refers to the mixture of (6, 5) and (6, 4) tubes. After Figure 3 of Sun et al. (2014).

In conclusion, we cannot yet give a clear answer to what the GM pressure coefficient is, but we may expect to be able to, after obtaining sufficient chirality-assigned data. At the same time, we need to quantify and understand the exogenous effects, such as the laser energy, PTM, doping and bundling on the shift rates, based on variable controlled and of course chirality assignable experiments. The summary of the current understanding of these effects is as follows. First, the laser energy dependence of the GM pressure coefficient shown in Figure 5.7 can be explained that tubes of different chiralities are picked out at different excitation energy. Therefore it is in fact the intrinsic tube chirality dependence. This is thereby under-

standable as we do not expect the laser energy to have any effect (only what affects the $C-C$ bond shortening with pressure is expected to have an effect) on the pressure coefficients. This however needs to be confirmed by measurements on samples of a single chirality in the same conditions except the excitation energy. Second, it is reported that PTM shift the transition energy (Ghandour et al., 2012) and therefore the PTM effect in Figure 5.7 can be again interpreted as the chirality dependence, as tubes of different chiralities are picked out in different PTM, even at the same excitation energy. The PTM should not affect the GM pressure coefficient. But the results of the (6, 5) tubes in Figure 5.14 contradict such expectation and hence cannot be understood yet. Third, doping shifts the GM frequency at ambient pressure but no evidence shows whether it affects the shift rates with pressure. And fourth, bundling effects are more complicated than all the above. CNTs tend to form bundles (Bandow et al., 1998), which means that, if not otherwise specified, all the reported results of the GM pressure coefficients are of CNTs bundles. Moreover, bundling effects on the GM pressure coefficient of the tube picked out by RRS may vary with parameters such as the diameters of the surrounding tubes, the bundling configuration (tangled, etc) and the degree of bundling, which is affected by the sample concentration but cannot be precisely controlled. On the other hand, surfactants stably disperse CNTs, which allow to exclude the bundling effects and their uncertainties, while possibly introduce surfactant effects (via interactions between tubes and surfactants molecules). Early work compared the GM shift rates of individual tubes dispersed by surfactants to the shift rates of bundles (see Figure 5.7) (Christofilos et al., 2007; Lebedkin et al., 2006), but they were not assigned to a specific chirality.

5.2.4 Double-Wall Carbon Nanotubes

We briefly discuss the GM pressure coefficients of double-wall carbon nanotubes (DWCNTs). We expect the outer tube to behave similarly to a SWCNT and the inner tube to be protected by the outer tube from external pressure, because the strong sp^2 bonds, compared with the soft C_{33} of graphite, leads to only a small shrinkage of the outer tube under pressures in the gigapascal range. However, Puech et al. (2006) report the GM pressure coefficients of the inner tube at 3.3, 4.1 and 5.1 $\mathrm{cm}^{-1}\mathrm{GPa}^{-1}$ in methanol-ethanol, oxygen and argon, respectively, about 2/3 of the corresponding values of the outer tube. These values vary with the PTM, even there is no contact at all between the inner tube and the PTM. A possible explanation is that the π-electrons compressed through the sp^2 network of the outer wall may act as a PTM and this might be the link.

To summarize, we expect the GM pressure coefficients of DWCNTs to be consistent with the predicted value from the thick-wall-tube model. They do not appear to be, and more data from tubes assigned to a specific chirality is required.

5.3 The Radial Breathing Mode

5.3.1 Experimental Pressure Coefficients

The RBM is a unique signature of CNTs, derived from tube structure, first reported by Rao et al. (1997). The frequency of the RBM is proportional to the inverse tube diameter (Reich et al., 2004), which is refined as

$$\omega_{RBM} = \frac{c_1}{d} + c_2 \tag{8}$$

where c_1=215 cm^{-1}nm and c_2 is introduced to account for external forces from environment (Maultzsch et al., 2005). So if individual RBM peaks are resolved, the pressure coefficients of RBM obtained in a high pressure measurement can be assigned to tubes of specific chiralities without finely tuning the excitation wavelength to make tubes of only one specific chirality in resonance, thereby dominating the spectrum. In the first high pressure experiment on SWCNTs, Venkateswaran et al. (1999) report a pressure coefficient of the observed RBM band of about 7 $\mathrm{cm}^{-1}\mathrm{GPa}^{-1}$ (see Figure 5.6 (a)). Figure 5.5 (a) presents their RBM spectra recorded under various pressures. It is typical to observe decreasing intensities of RBM peaks with increasing pressure leading to the peaks disappearing beyond a certain pressure (1.5 GPa here). This decrease of the intensities is not fully understood (a possible interpretation is the ovalization of tubes under pressure) and the disappearance may be correspond to the collapse of tubes.

With the aid of the Kataura plot and Eq. 8, Lebedkin et al. (2006) assign each of the RBM peaks in their spectrum to specific chiralities (see Figure 5.15). They track these peaks under pressure and obtain the shift rates shown in Table 5.2.

5.3.2 Theoretical Pressure Coefficients

Now we try to explain the experimental pressure coefficients of the RBM. There is a direct relation between the GM and RBM. Gerber et al. (2009) first consider Newton's equation for a linear chain of atoms with spring constant k and the out of phase stretching motion of neighbouring atoms

Table 5.2. "Pressure coefficient of the RBM frequency, ω_{RBM}, versus the nanotube helicity index (n, m). Data are for HiPco nanotubes dispersed in water-sodium cholate under low pressure conditions ($\leqslant$1 GPa). Three groups of metallic and semiconducting (n, m) nanotubes were probed at laser excitation wavelengths of 514, 633, and 785 nm (from top to bottom). Italic (n, m) indices denote metallic nanotubes." Reprinted table with permission from [Sergei Lebedkin et al., Phys. Rev. B 73, 094109 (2006)] Copyright (2006) by the American Physical Society.

n,*m*	ω_{RBM},[a] cm^{-1}	Pressure derivative, cm^{-1}/GPa	Tube diameter,[b] nm
8,5	266	7.4±0.5	0.89
9,3	273	7.6±0.5	0.85
11,8	184	7.7±0.8	1.29
12,6	191	8.2±1.0	1.24
13,4 (14,2)[c]	197	7.4±0.8	1.20 (1.18)
10, 3	253	5.9±0.3	0.92
7, 6	265	5.2±0.5	0.88
7, 5	284	5.6±0.3	0.82
8, 3	299	5.2±0.4	0.77
9, 7	215	6.4±0.3	1.09
10, 5	225	6.2±0.4	1.04
11, 3	233	5.9±0.3	1.00
12, 1	237	6.0±0.3	0.98

[a]Accuracy ±1 cm^{-1}.
[b]Calculated using carbon-carbon bond length of 0.142 nm.
[c]RBM band can be assigned to both (*n*,*m*) species.

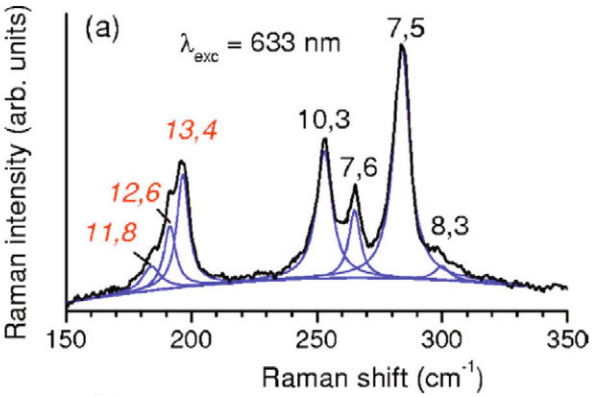

Figure 5.15. "The RBM Raman spectrum of water-1wt.% sodium cholate dispersion of HiPco nanotubes at ambient pressure as excited at 633 nm (black). Also shown are Lorentzian fits of contributing bands as well as their assignment to (n, m) nanotubes. Italic n, m indices denote metallic nanotubes." Reprinted figure with permission from [Sergei Lebedkin et al., Phys. Rev. B 73, 094109 (2006)] Copyright (2006) by the American Physical Society.

(GM) with mass m_C. The frequency of the GM is

$$\omega_G^2 = \frac{4k}{m_C} \tag{9}$$

For a closed linear chain in circumferential direction,

$$\frac{1}{K_{tube}} = \sum_i \frac{1}{k} \Rightarrow K_{tube} = \frac{ka}{\pi d} \tag{10}$$

where a is the bond length and d is the diameter. The mass is

$$M_{tube} = m_C \frac{\pi d}{a} \tag{11}$$

Then they introduce a spring constant along the radial direction and the Lagrangian $\mathcal{L}$ for a tube section is

$$\mathcal{L} = \frac{1}{2}M_{tube}\dot{r}^2 - \frac{1}{2}K_{tube}\Delta l^2 \tag{12}$$

$$\mathcal{L} = \frac{1}{2}M_{tube}\dot{r}^2 - \frac{1}{2}K_{tube}(2\pi\Delta r)^2 \tag{13}$$

$$\mathcal{L} = \frac{1}{2}M_{tube}\dot{r}^2 - \frac{1}{2}K_{tube}^{radial}(\Delta r)^2 \tag{14}$$

where $\dot{r}$ is the speed in radial direction and Δl is the change in the circumference. Using the Euler-Lagrange equation, they obtain

$$\omega_{RBM}^2 = \frac{K_{tube}^{radial}}{M_{tube}} = 4\pi^2\frac{ka}{\pi d}\frac{a}{m_C\pi d} = \omega_G^2\frac{a^2}{d^2} \tag{15}$$

Given that ω_G=1581 cm^{-1} and a=1.42 $\mathring{A}$,

$$\omega_{RBM}(cm^{-1}) = \omega_G\frac{a}{d} = \frac{225}{d}(nm^{-1}) \tag{16}$$

This shows the relationship between the frequency of the RBM and GM.

The frequency of the GM and RBM can be calculated separately in the framework of appropriately-handled continuum models. We start by supposing the tube wall to consist of a two-dimensional sheet of continuum material with the two-dimensional graphene elastic constants $k_{11} = C_{11}h_G =$ 372 Nm^{-1} and $k_{12} = C_{12}h_G = 47$ Nm^{-1} (Bosak and Krisch, 2007), where we use the value of graphite interlayer distance for h_G, $h_G = a_{33} = 3.35$ $\mathring{A}$. In the RBM motion, the wall has tangential strain but no axial strain, so the relevant elastic stiffness constant is k_{11}. The potential energy per unit length of tube at the extreme of a radial sinusoidal motion $r = Acos\omega$t is

$$U_{max} = \frac{1}{2}k_{11}\varepsilon^2 \times 2\pi R_C = \pi R_C k_{11}\frac{A^2}{R_C^2} \tag{17}$$

while the kinetic energy at the centre of the motion is

$$E_{max} = \frac{1}{2}mA^2\omega^2 = \frac{1}{2}A^2\omega^2 \times 2\pi R_C N m_0 \tag{18}$$

where $N = 3.8\times10^{19}$ is the number of carbon atoms of mass m$_0$ in a unit area of graphene and R_C is the tube radius measured at the carbon nuclei. Equating U_{max} and E_{max}, and rearranging, we have

$$\omega_{RBM} = \frac{1}{R_C}\sqrt{\frac{k_{11}}{Nm_0}} = \frac{235}{d(nm)}cm^{-1} \tag{19}$$

where the diameter $d = 2R_C$. Eq. 19 is in excellent agreement with one of the recent experimental values of the numerator at 227 (Araujo et al., 2008). Not surprisingly, the continuum model works very well for this large-scale deformation of the nanotube.

To relate the frequency of the RBM to GM, it is necessary to discretise the continuous mechanics model, by concentrating the mass into lines or points representing atoms. We take n mass concentrations equispaced around the circumference of the tube, connected by springs of length a_0 and an *ad-hoc* effective spring constant k between adjacent atoms, and an effective mass m – these account for the hexagonal lattice with sp^2 bonds at various orientations. In the GM alternate atoms move in anti-phase, with a tangential displacement $x = Acos\omega_G t$, we have:

$$U_{max} = \frac{1}{2}nk(2A\cos\frac{\pi}{n})^2 \approx 2nkA^2 \tag{20}$$

$$E_{max} = \frac{1}{2}nm\omega_G^2 A^2 \tag{21}$$

$$\omega_{GM} = 2\sqrt{\frac{k}{m}} \tag{22}$$

The cosine term in Eq. 20 comes from the angle between the spring and the motion; it is approximated to unity here. For the RBM mode,

$$U_{max} = \frac{1}{2}nk(2A\sin\frac{\pi}{n})^2 \approx 2nkA^2\frac{^2}{n^2} \tag{23}$$

$$E_{max} = \frac{1}{2}nm\omega_{RBM}^2 A^2 \tag{24}$$

$$\omega_{RBM} = \frac{2\pi}{n}\sqrt{\frac{k}{m}} \tag{25}$$

Approximating the diameter d to na_0/π with a_0 equal to the sp^2 bond length of 1.42Å, Eq. 20 to Eq. 25 lead directly to Eq. 16 by Gerber et al. (2009):

$$\omega_{RBM} = \frac{a_0}{d}\omega_G = \frac{0.142nm \times 1590cm^{-1}}{d(nm)} = \frac{226}{d(nm)}cm^{-1} \tag{26}$$

and in excellent agreement with Eq. 19. It is remarkable that the GM frequency is thus directly related to the continuum properties without needing any details of the hexagonal structure, the bond potentials, or even the carbon atomic mass. It would be interesting to derive k and m from bond potentials or from *ab initio* theory — this would be a good test of these

models. Meanwhile, this gives confidence that the continuum approach is good even to the atomic scale in graphene and CNTs.

The consequence of this is that the pressure coefficients of the GM and the RBM should be in proportion to their frequencies, i. e. the pressure coefficient of the RBM is predicted to be 0.8 $cm^{-1}GPa^{-1}$, according to the data of Venkateswaran et al. (1999) — $\omega_{GM} = 1590cm^{-1}$, $\omega_{RBM} = 185cm^{-1}$ and the pressure coefficient of the GM is 7 $cm^{-1}GPa^{-1}$. But it equals 7 $cm^{-1}GPa^{-1}$. There have to be other major effects responsible for the ∼90% unexplained part of the observed shift rates of RBM. See the next section.

5.3.3 Interaction With The Environment

A simulation work performed by Longhurst and Quirke (2007) shows that the RBM is coupled with an absorbed fluid shell (highlighted in Figure 5.16) via the van der Waals interaction. The pressure coefficient of the RBM is thereby mainly induced by the decrease of the interlayer spacing between the tube and the absorbed fluid shell, rather than the shortening of $C - C$ bonds which is related to the shift of the GM. This indicates that, unlike the GM, the shift of the RBM with pressure could be strongly affected by environment, such as the nature of the PTM and the bundling status of the CNTs samples. A caveat, however, is that under compression it is the repulsive part of the interaction which becomes more important, and the repulsive part (Pauli exclusion) would not vary so much with these variables.

Ghandour et al. (2013) compare the experimental pressure coefficients of Venkateswaran et al. (2003), Lebedkin et al. (2006), and their own, to this model and find reasonably good agreement (see Figure 5.17), confirming its validity.

5.3.4 Resonance and Effects of Solvents

In this section, we introduce how the RBM is used to study the effects of solvents on the CNTs resonance condition. A preferable way to present the results is to plot the RBM peak intensity with the excitation energy and the RBM frequency. It has to be mentioned that when making the chirality assignment of the RBM peaks according to the Kataura plot, we need to consider both the first and second optical transition (E_{11} and E_{22}). Telg et al. (2007) give an example as shown in Figure 5.18. According to the study by Cambré et al. (2010), solvent-filling effect shifts not only excitation energy, but also the RBM frequency, as clearly shown in Figure 5.19. Maultzsch et al. (2005) find small shifts in excitation energy peaks for metal-

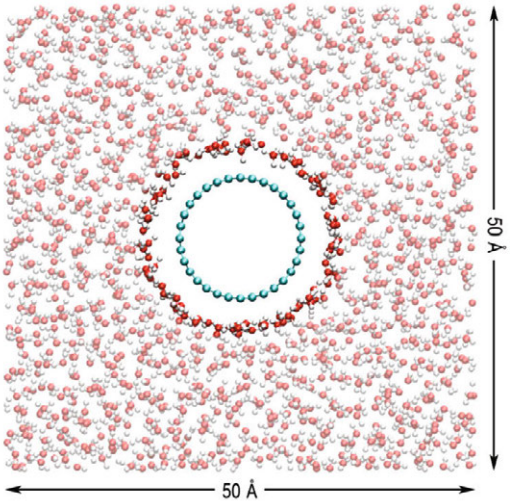

Figure 5.16. "Representation of the simulation cell for a (16, 0) carbon nanotube immersed in water. The adsorbed shell of water is highlighted for clarity." Reprinted figure with permission from [M. J. Longhurst and N. Quirke, Phys. Rev. Lett. 98, 145503 (2007)] Copyright (2007) by the American Physical Society.

lic and semiconducting tubes, but in opposite directions, when comparing the tubes in two different surfactants. The Figure 5.20 by Ghandour et al. (2012) shows that the effects of solvents and pressure on tubes of a specific chirality are roughly orthogonal to each other — solvents shift the resonance energy without shifting the RBM frequency (with exception of air) and pressure shifts the frequency with only a slight shift in energy.

5.3.5 Double-Wall Carbon Nanotubes

To study the RBM of DWCNTs, we need to assign the Raman peak not only to a specific chirality, as we do for SWCNTs, but also to the inner or the outer tube. We do not know whether the excitation energy of an inner or outer tube is the same as for a SWCNT of the same chirality, whereas the RBM frequency is different due to the coupling between the inner and outer tube (Dobardzic et al., 2003). Aguiar et al. (2011) and Alencar et al. (2014) report that the RBM frequencies of inner tubes, with few exceptions, shift little under pressure, as a result of the small shrinkage of the outer

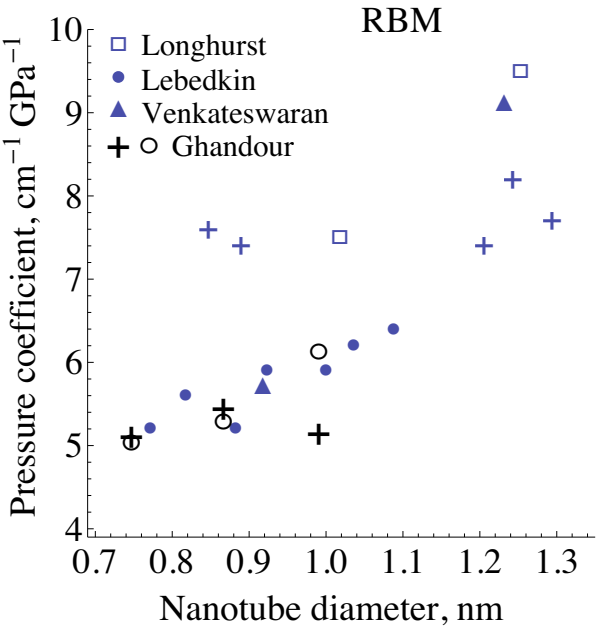

Figure 5.17. Pressure coefficients are plotted against the tube diameters. Open circles and crosses are for SWCNTs bundles in water (Ghandour et al., 2013). Triangles are for bundled semiconducting tubes in ethanol/methanol (Venkateswaran et al., 2003). Small solid circles are for unbundled semiconducting tubes in water/surfactant (Lebedkin et al., 2006). And open squares are for MD simulation results of unbundled semiconducting tubes in water (Longhurst and Quirke, 2007). After Figure 4 (a) of Ghandour et al. (2013).

tube and hence little change of the coupling. For further study on both the excitation energy and RBM frequency under pressure, a wavelength-tunable laser is highly desirable. We acknowledge that C. Rice from University of Manchester provides an unpublished figure, as a very good example (see Figure 5.21).

5.4 The 2D-mode

Here we only briefly mention the 2D-mode of SWCNTs under pressure, by showing the results of Wood et al. (1999) (see Figure 5.22). Compared to pressure, the frequency of the 2D-mode is more sensitive to solvent, which

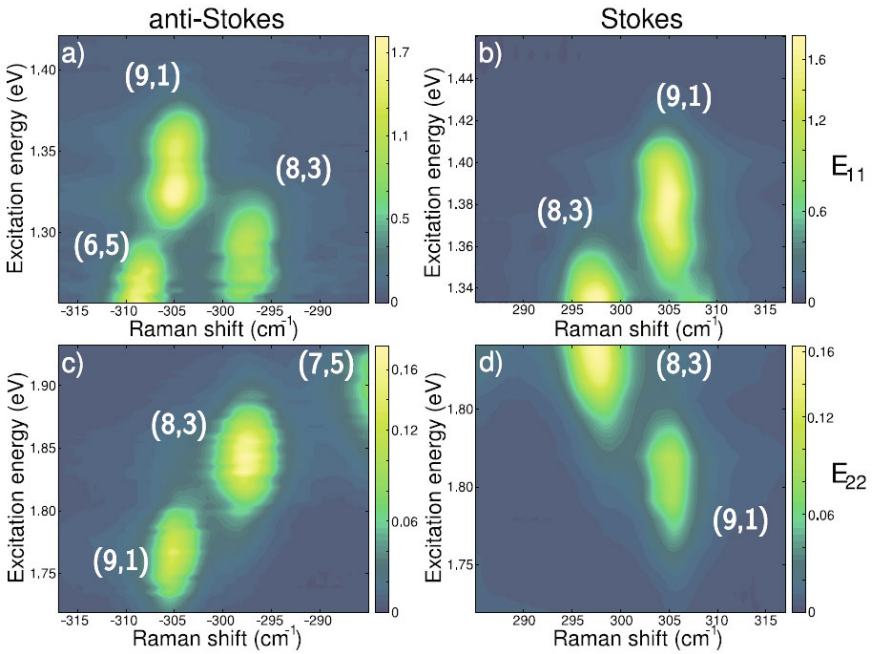

Figure 5.18. "The plotted intensities are proportional to the Raman susceptibility. Upper plots contain anti-Stokes(a) and Stokes(b) Raman spectra excited resonantly via E_{11}. Lower plots show anti-Stokes(c) and Stokes(d) spectra in resonance with E_{22}." Reprinted figure with permission from [H. Telg, J. Maultzsch, S. Reich, C. Thomsen, Phys. Status Solidi (b) 244, 4006–4010 (2007)] Copyright (2007) by John Wiley and Sons.

is linked to the study of graphene.

5.5 Conclusion

In this chapter, we discuss the GM and the RBM of SWCNTs under pressure and briefly mention DWCNTs and the 2D-mode of SWCNTs. For the GM, we give expectations for the pressure coefficients from its origin in graphite (the shift of frequency with pressure is induced by the shortening of $C-C$ bond) and the tube structure. We review early studies but find no consensus on the value of the pressure coefficient. This emphasizes the importance of chirality assignment in high pressure studies of the GM. From recent results,

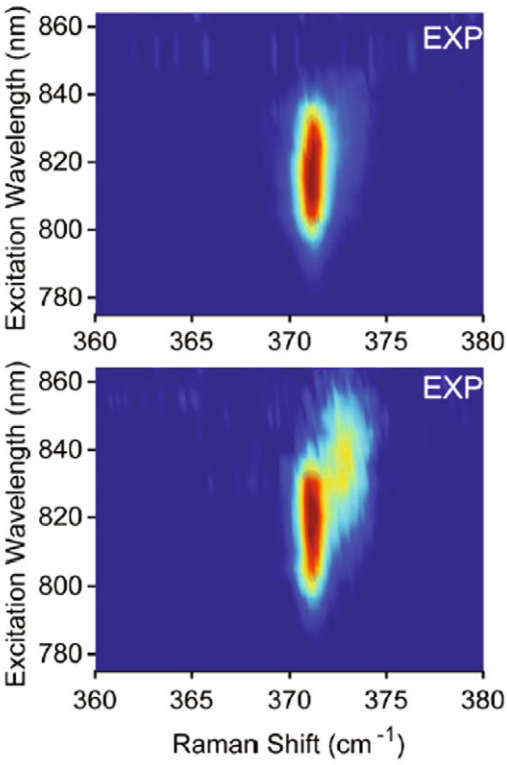

Figure 5.19. The Raman-excitation maps of the first electronic transition of the (5, 4) tubes. The sample used for the upper panes contains less open (solvent-filled) tubes than the sample used for the lower ones. Reprinted figure with permission from [Sofie Cambré et al., Phys. Rev. Lett. 104, 207401 (2010)] Copyright (2010) by the American Physical Society.

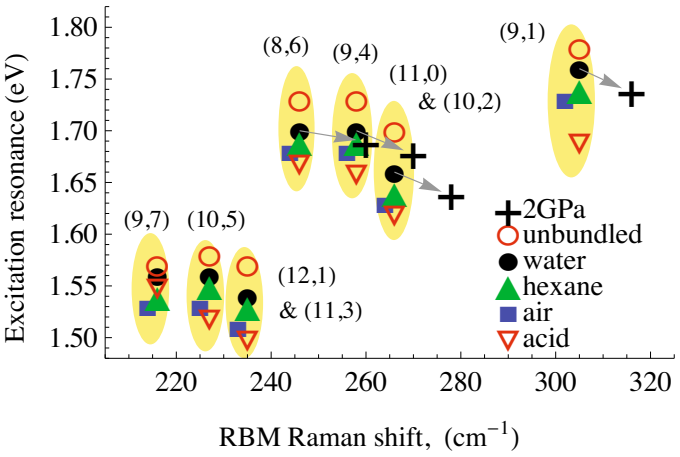

Figure 5.20. Data points corresponding to the RBM frequency and the excitation resonance energy for HiPCO semiconducting nanotubes with the chiral indices (m, n) labelled. The squares are for dry nanotubes in air; the down triangles for sulphuric acid; the up triangles for hexane. The solid circles are for bundled tubes in water and the open circles for unbundled in water with surfactant. Data taken under the pressure of 2GPa is shown by the crosses (+) for bundled nanotubes in water. The arrows show the shifts due to pressure. After Figure 2 of Ghandour et al. (2012).

we find the effects of chirality, solvent and bundling, which are unexpected and lack full understanding. In contrast, the pressure dependence of the RBM is well-explained. It is mainly determined by the decrease of the interlayer spacing between the absorbed fluid shell and the tube. The $C-C$ bond shortening with pressure, related to the GM, contributes only about 10% of the experimental shift of the RBM. The high pressure study of DWCNTs is similar to SWCNTs in the need for chirality assignment, but differs in having the extra complexity of inner and outer tubes, the behaviour of which are not fully understood. The frequency of the 2D-mode, being intensively studied for graphene, is much more sensitive to solvents than pressure. For the future work, we think the study of CNTs under pressure relies on high resolution Raman spectroscopy equipped with a tunable laser or the manufacturing of CNTs samples of specified chiralities.

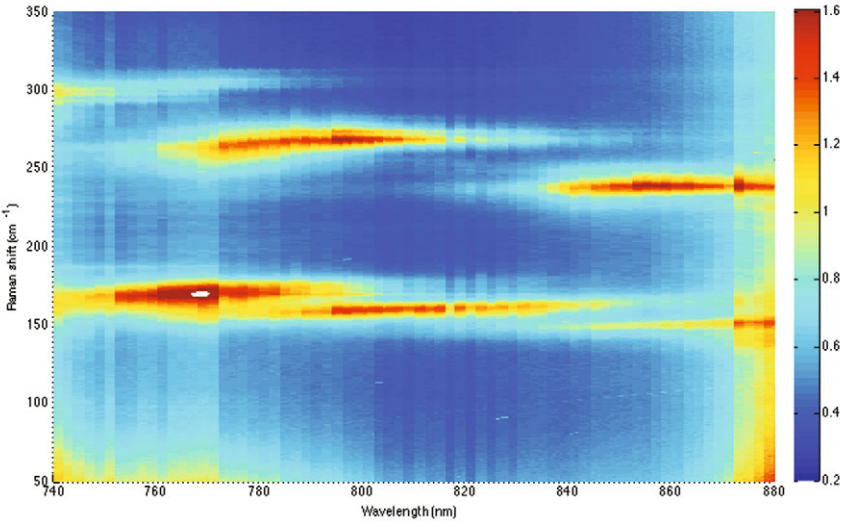

Figure 5.21. The RBM frequencies of both inner and outer tubes of DWCNTs are plotted against the laser excitation wavelength, with the colour coding for Raman intensity. From C. Rice, University of Manchester, unpublished.

References

A. L. Aguiar, E. B. Barros, R. B. Capaz, A. G. Souza Filho, P. T. C. Freire, J. Mendes Filho, D. Machon, Ch. Caillier, Y. A. Kim, H. Muramatsu, M. Endo, and A. San-Miguel. Pressure-induced collapse in double-walled carbon nanotubes: Chemical and mechanical screening effects. *J. Phys. Chem. C*, 115:53785384, 2011.

A. L. Aguiar, R. B. Capaz, A. G. Souza Filho, and A. San-Miguel. Structural and phonon properties of bundled single- and double-wall carbon nanotubes under pressure. *J. Phys. Chem. C*, 116:22637–22645, 2012.

R. S. Alencar, A. L. Aguiar, A. R. Paschoal, P. T. C. Freire, Y. A. Kim, H. Muramatsu, M. Endo, H. Terrones, M. Terrones, A. San-Miguel, M. S. Dresselhaus, and A. G. Souza Filho. Pressure-induced selectivity for probing inner tubes in double- and triple-walled carbon nanotubes: A resonance raman study. *J. Phys. Chem. C*, 118:81538158, 2014.

P. T. Araujo, I. O. Maciel, P. B. C. Pesce, M. A. Pimenta, S. K. Doorn, H. Qian, A. Hartschuh, M. Steiner, L. Grigorian, K. Hata, and A. Jorio. Nature of the constant factor in the relation between radial breathing

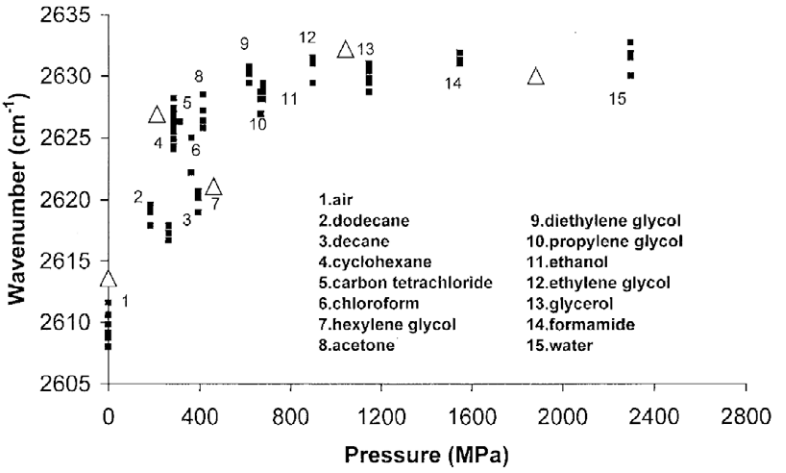

Figure 5.22. Raman shift of the 2D band in the Raman spectrum of SWCNTs aggregates in solvents of various cohesive energy densities. The triangles show the data from the high pressure experiments performed in condensed argon. Reprinted with permission from (Jonathan R. Wood, Mark D. Frogley, Erwin R. Meurs, et al, J. Phys. Chem. B, 1999, 103 (47), pp 1038810392). Copyright (1999) American Chemical Society.

mode frequency and tube diameter for single-wall carbon nanotubes. *Phys. Rev. B*, 77:241403, 2008.

S. Bandow, S. Asaka, Y. Saito, A. M. Rao, L. Grigorian, E. Richter, and P. C. Eklund. Effect of the growth temperature on the diameter distribution and chirality of single-wall carbon nanotubes. *Phys. Rev. Lett.*, 80:3779, 1998.

A. Bosak and M. Krisch. Elasticity of single-crystalline graphite: Inelastic x-ray scattering study. *Phys. Rev. B*, 75:153408, 2007.

Ch. Caillier, D. Machon, A. San-Miguel, R. Arenal, G. Montagnac, H. Cardon, M. Kalbac, M. Zukalova, and L. Kavan. Probing high-pressure properties of single-wall carbon nanotubes through fullerene encapsulation. *Phys. Rev. B*, 77:125418, 2008.

S. Cambré, B. Schoeters, S. Luyckx, E. Goovaerts, and W. Wenseleers. Experimental observation of single-file water filling of thin single-wall carbon nanotubes down to chiral index (5,3). *Phys. Rev. Lett.*, 104: 207401, 2010.

D. Christofilos, J. Arvanitidis, C. Tzampazis, K. Papagelis, T. Takenobu, Y. Iwasa, H. Kataura, C. Lioutas, S. Ves, and G.A. Kourouklis. Raman

study of metallic carbon nanotubes at elevated pressure. *Diamond Relat. Mater*, 15:1075–1079, 2005.

D. Christofilos, J. Arvanitidis, K. S. Andrikopoulos, G. A. Kourouklis, S. Ves, T. Takenobu, and Y. Iwasa. Comparative high pressure raman study of individual and bundled single-wall carbon nanotubes. *phys. stat. sol. (b)*, 244:100–104, 2007.

E. Dobardzic, J. Maultzsch, I. Milosevic, C. Thomsen, and M. Damnjanovic. The radial breathing mode frequency in double-walled carbon nanotubes: an analytical approximation. *phys. stat. sol. (b)*, 237:R7–R10, 2003.

O. Dubay, G. Kresse, and H. Kuzmany. Phonon softening in metallic nanotubes by a peierls-like mechanism. *Phys. Rev. Lett.*, 88:235506, 2002.

C. Fantini, A. Jorio, M. Souza, M. S. Strano, M. S. Dresselhaus, and M. A. Pimenta. Optical transition energies for carbon nanotubes from resonant raman spectroscopy: Environment and temperature effects. *Phys. Rev. Lett*, 93:147406, 2004.

H. Farhat, H. Son, Ge. G Samsonidze, S. Reich, M. S. Dresselhaus, and J. Kong. Phonon softening in individual metallic carbon nanotubes due to the kohn anomaly. *Phys. Rev. Lett.*, 99:145506, 2007.

A. C. Ferrari, J. C. Meyer, V. Scardaci, C. Casiraghi, M. Lazzeri, F. Mauri, S. Piscanec, D. Jiang, K. S. Novoselov, S. Roth, and A. K. Geim. Raman spectrum of graphene and graphene layers. *Phys. Rev. Lett.*, 97:187401, 2006.

I. C. Gerber, P. Puech, A. Gannouni, and W. Bacsa. Influence of nitrogen doping on the radial breathing mode in carbon nanotubes. *Phys. Rev. B*, 79:075423, 2009.

A. J. Ghandour, D. J. Dunstan, and A. Sapelkin. Raman g-mode of single-wall carbon nanotube bundles under pressure. *J. Raman Spectrosc.*, 42: 1611–1613, 2011.

A. J. Ghandour, A. Sapelkin, I. Hernandez, D. J. Dunstan, I. F. Crowe, and M. P. Halsall. Raman excitation spectroscopy of carbon nanotubes: effects of pressure medium and pressure. *High Pressure Res.*, 32:67–71, 2012.

A. J. Ghandour, I. F. Crowe, J. E. Proctor, Y. W. Sun, M. P. Halsall, I. Hernandez, A. Sapelkin, and D. J. Dunstan. Pressure coefficients of raman modes of carbon nanotubes resolved by chirality: Environmental effect on graphene sheet. *Phys. Rev. B*, 87:085416, 2013.

J. F. Green, P. Bolsaitis, and I. L. Spain. Pressure dependence of c-axis elastic parameters of oriented graphite. *J. Phys. Chem. Solids*, 34:1927–1937, 1972.

M. Hanfland, H. Beister, and K. Syassen. Graphite under pressure: Equation of state and first-order raman modes. *Phys. Rev. B*, 39:12598, 1989.

M. Huang, H. Yan, C. Chen, D. Song, T. F. Heinz, and J. Hone. Phonon softening and crystallographic orientation of strained graphene studied by raman spectroscopy. *PNAS*, 106:7304–7308, 2009.

A. Jorio, A. G. Souza Filho, G. Dresselhaus, M. S. Dresselhaus, A. K. Swan, M. S. Unlu, B. B. Goldberg, M. A. Pimenta, J. H. Hafner, C. M. Lieber, and R. Saito. G-band resonant raman study of 62 isolated single-wall carbon nanotubes. *Phys. Rev. B*, 65:155412, 2002.

H. Kataura, Y. Kumazawa, Y. Maniwa, I. Umezu, S. Suzuki, Y. Ohtsuka, and Y. Achiba. Optical properties of single-wall carbon nanotubes. *Synt. Met.*, 103:2555–2558, 1999.

S. Lebedkin, K. Arnold, O. Kiowski, F. Hennrich, and M. M. Kappes. Raman study of individually dispersed single-walled carbon nanotubes under pressure. *Phys. Rev. B*, 73:094109, 2006.

H. Liu, D. Nishide, T. Tanaka, and H. Kataura. Large-scale single-chirality separation of single-wall carbon nanotubes by simple gel chromatography. *Nat. Commun.*, 2:309, 2011.

M. J. Longhurst and N. Quirke. Pressure dependence of the radial breathing mode of carbon nanotubes: The effect of fluid adsorption. *Phys. Rev. Lett*, 98:145503, 2007.

R. M. Martin and L. M. Falicov. Light scattering in solids. In Manuel Cardona, editor, *Topics in Applied Physics*. Springer, 1975.

J. Maultzsch, H. Telg, S. Reich, and C. Thomsen. Radial breathing mode of single-walled carbon nanotubes: Optical transition energies and chiral-index assignment. *Phys. Rev. B*, 72:205438, 2005.

A. Merlen, N. Bendiab, P. Toulemonde, A. Aouizerat, A. San Miguel, J. L. Sauvajol, G. Montagnac, H. Cardon, and P. Petit. Resonant raman spectroscopy of single-wall carbon nanotubes under pressure. *Phys. Rev. B*, 72:035409, 2005.

A. Merlen, P. Toulemonde, N. Bendiab, A. Aouizerat, J. L. Sauvajol, G. Montagnac, H. Cardon, P. Petit, and A. San Miguel. Raman spectroscopy of open-ended single wall carbon nanotubes under pressure: effect of the pressure transmitting medium. *phys. stat. sol. (b)*, 243: 690–699, 2006.

T. M. G. Mohiuddin, A. Lombardo, R. R. Nair, A. Bonetti, G. Savini, R. Jalil, N. Bonini, D. M. Basko, C. Galiotis, N. Marzari, K. S. Novoselov, A. K. Geim, and A. C. Ferrari. Uniaxial strain in graphene by raman spectroscopy: G peak splitting, grneisen parameters, and sample orientation. *Phys. Rev. B*, 79:205433, 2009.

M. Mohr, K. Papagelis, J. Maultzsch, and C. Thomsen. Two-dimensional electronic and vibrational band structure of uniaxially strained graphene from ab initio calculations. *Phys. Rev. B*, 80:205410, 2009.

Z. H. Ni, T. Yu, Y. H. Lu, Y. Y. Wang, Y. P. Feng, and Z. X. Shen. Uniaxial strain on graphene: Raman spectroscopy study and band-gap opening. *ACSNANO*, 2:2301–2305, 2008.

J. Nicolle, D. Machon, P. Poncharal, O. Pierre-Louis, and A. San-Miguel. Pressure-mediated doping in graphene. *Nano Lett.*, 11:3564–3568, 2011.

M. J. O'Connell, S. M. Bachilo, C. B. Huffman, V. C. Moore, M. S. Strano, E. H. Haroz, K. L. Rialon, P. J. Boul, W. H. Noon, C. Kittrell, J. Ma, R. H. Hauge, R. B. Weisman, and R. E. Smalley. Band gap fluorescence from individual single-walled carbon nanotubes. *Science*, 297:593, 2002.

T. W. Odom, J. Huang, P. Kim, and C. M. Lieber. Atomic structure and electronic properties of single-walled carbon nanotubes. *Nature*, 391: 62–64, 1998.

J. E. Proctor, M. P. Halsall, A. Ghandour, and D. J. Dunstan. High pressure raman spectroscopy of single-walled carbon nanotubes:effect of chemical environment on individual nanotubes and the nanotube bundle. *J. Phys. Chem. Solids*, 67:2468–2472, 2006.

J. E. Proctor, E. Gregoryanz, K. S. Novoselov, M. Lotya, J. N. Coleman, and M. P. Halsall. High-pressure raman spectroscopy of graphene. *Phys. Rev. B*, 80:073408, 2009.

P. Puech, E. Flahaut, A. Sapelkin, H. Hubel, D. J. Dunstan, G. Landa, and W. S. Bacsa. Nanoscale pressure effects in individual double-wall carbon nanotubes. *Phys. Rev. B*, 73:233408, 2006.

A. M. Rao, E. Richter, S. Bandow, B. Chase, P. C. Eklund, K. A. Williams, S. Fang, K. R. Subbaswamy, M. Menon, A. Thess, R. E. Smalley, G. Dresselhaus, and M. S. Dresselhaus. Diameter-selective raman scattering from vibrational modes in carbon nanotubes. *Science*, 275:187–191, 1997.

S. Reich and C. Thomsen. Raman spectroscopy of graphite. *Phil. Trans. R. Soc. Lond. A*, 362:2271–2288, 2004.

S. Reich, C. Thomsen, and J. Maultzsch. *Carbon Nanotubes: Basic Concepts and Physical Properties*. Wiley-VCH, 2004.

J. Sandler, M. S. P. Shaffer, A. H. Windle, M. P. Halsall, M. A. Montes-Moran, C. A. Cooper, and R. J. Young. Variations in the raman peak shift as a function of hydrostatic pressure for various carbon nanostructures: A simple geometric effect. *Phys. Rev. B*, 67:035417, 2003.

V. Skakalova, A. B. Kaiser, U. Dettlaff-Weglikowska, K. Hrncarikova, and S. Roth. Effect of chemical treatment on electrical conductivity, infrared absorption, and raman spectra of single-walled carbon nanotubes. *J. Phys. Chem. B*, 109:7174–7181, 2005.

A. V. Soldatov, S. You, M. Mases, and K. S. Novoselov. Free standing graphene monolayer at high hydrostatic pressure. In *Graphene 2012, Abstract Book of the Conference*, page 172, 2012.

A. K. Sood, P. V. Teresdesai, D. V. S. Muthu, R. Sen, A. Govindara, and C. N. R. Rao. Pressure behaviour of single wall carbon nanotube bundles and fullerenes: A raman study. *phys. stat. sol. (b)*, 215:393, 1999.

Y. W. Sun, D. J. Dunstan, M. A. Hartmann, and D. Holec. Nanomechanics of carbon nanotubes. *Proc. Appl. Math. Mech.*, 13:7–10, 2013.

Y. W. Sun, I. Hernandez, A.J. Ghandour, C. Rice, I.F. Crowe, M.P. Halsall, A. Sapelkin, J. Gonzalez, F. Rodriguez, and D.J. Dunstan. Resonance raman spectroscopy of carbon nanotubes: pressure effects on g-mode. *High Pressure Res.*, 34:191–197, 2014.

H. Telg, J. Maultzsch, S. Reich, and C. Thomsen. First and second optical transitions in single-walled carbon nanotubes: a resonant raman study. *phys. stat. sol. (b)*, 244:4006–4010, 2007.

C. Thomsen, S. Reich, H. Jantoljak, I. Loa, K. Syassen, M. Burghard, G.S. Duesberg, and S. Roth. Raman spectroscopy on single- and multi-walled nanotubes under high pressure. *Appl. Phys. A*, 69:309, 1999.

C. Thomsen, S. Reich, and P. Ordejon. Ab initio determination of the phonon deformation potentials of graphene. *Phys. Rev. B*, 65:073403, 2002.

M. M. J. Treacy, T. W. Ebbesen, and J. M. Gibson. Exceptionally high young's modulus observed for individual carbon nanotubes. *Nature*, 381: 678–680, 1996.

F. Tuinstra and J. L. Koenig. Raman spectrum of graphite. *J. Chem. Phys.*, 53:1126, 1970.

U. D. Venkateswaran, A. M. Rao, E. Richter, M. Menon, A. Rinzler, R. E. Smalley, and P. C. Eklund. Probing the single-wall carbon nanotube bundle: Raman scattering under high pressure. *Phys. Rev. B*, 59:10928, 1999.

U. D. Venkateswaran, E. A. Brandsen, U. Schlecht, A. M. Rao, E. Richter, I. Loa, K. Syassen, and P. C. Eklund. High pressure studies of the raman-active phonons in carbon nanotubes. *phys. stat. sol. (b)*, 223:225–236, 2001.

U. D. Venkateswaran, D. L. Masica, G. U. Sumanasekera, C. A. Furtado, U. J. Kim, and P. C. Eklund. Diameter dependent wall deformations during the compression of a carbon nanotube bundle. *Phys. Rev. B*, 68: 241406, 2003.

J. R. Wood, M. D. Frogley, E. R. Meurs, A. D. Prins, T. Peijs, D. J. Dunstan, and H. D. Wagner. Mechanical response of carbon nanotubes under molecular and macroscopic pressures. *J. Phys. Chem. B*, 103: 10388–10392, 1999.

L. Yang and J. Han. Electronic structure of deformed carbon nanotubes. *Phys. Rev. Lett.*, 85:154–157, 2000.

M. Yao, Z. Wang, B. Liu, Y. Zou, S. Yu, W. Lin, Y. Hou, S. Pan, M. Jin, B. Zou, T. Cui, G. Zou, and B. Sundqvist. Raman signature to identify the structural transition of single-wall carbon nanotubes under high pressure. *Phys. Rev. B*, 78:205411, 2008.

6 Atomistic and continuum modelling of graphene and graphene-derived carbon nanostructures

Markus A. Hartmann * and Melanie Todt † and F.G. Rammerstorfer †

* Institute of Physics, Montanuniversität Leoben, Franz-Josef Strasse 18, 8700 Leoben, Austria

† Institute of Lightweight Design and Structural Biomechanics, Vienna University of Technology, Getreidemarkt 9, 1060 Vienna, Austria

6.1 Introduction

Nanometer sized particles formed by carbon atoms mainly arranged in a hexagonal atomic structure are called carbon nanostructures (CNS). In this chapter we focus exclusively on *sp*2-bonded CNS that include graphene (Geim, 2009; Geim and Novoselov, 2007), single- and multi-walled carbon nanotubes (Iijima, 1991; Pantano et al., 2004), fullerenes (Kroto et al., 1985), and carbon onions (Banhart and Ajayan, 1996; Kroto, 1992; Ugarte, 1992, 1995). Especially graphene has drawn a lot of attention within the last years, because it possesses exceptional mechanical and electrical properties (Geim, 2009; Novoselov et al., 2004) and a high thermal conductivity (Lau et al., 2012). It is the main building block of all other CNS based on *sp*2-bonded carbon, which therefore should inherit its exceptional properties making them promising candidates for applications in the field of structural mechanics and the electronics industry, as fillers in nanocomposites (Choi and Lee, 2012; Baughman et al., 2002; Stankovich et al., 2006) and as solid lubricants (Hirata et al., 2004). This chapter will focus on the amazing mechanical properties of CNS only. Information regarding the extraordinary electronic and thermal properties can be found elsewhere (Novoselov et al., 2004; Castro Neto et al., 2009; Balandin, 2011).

For an expedient and reliable application of CNS their (mechanical) properties have to be well understood. Besides experimental characterization (Banhart and Ajayan, 1996; Iijima, 1991; Kroto et al., 1985) different computational simulation techniques have shown to be powerful tools for investigating the formation and properties of CNS (Chuvilin et al., 2010;

O. Paris (Ed.), *Structure and Multiscale Mechanics of Carbon Nanomaterials*,
CISM International Centre for Mechanical Sciences
DOI 10.1007/ 978-3-7091-1887-0_6

Pantano et al., 2004; Yakobson et al., 1996). The different simulation techniques that can be used range from *ab initio* (first principle) studies to continuum mechanical methods. The choice of the appropriate method mainly depends on the size, i.e., the number of atoms forming the CNS and the property to be investigated.

Ab initio simulations require the solution of the many-body Schrödinger equation, which is a computational expensive task. Therefore, the applicability of this technique is limited to small CNS consisting of a few hundred to thousand atoms. The biggest advantage of this method is that only the atomic number (i.e., the number of electrons) of the involved atoms is required as input. *Ab initio* methods are used, e.g., in (Lier et al., 2000) and (Dumlich and Reich, 2011) to investigate the mechanical properties of CNS and the binding energy and intertube distance of bundles of carbon nanotubes, respectively. In (Dumlich and Reich, 2011) van der Waals (vdW) interactions are considered in the model, which is not a straight forward task in *ab initio* simulations. Workarounds are presented, e.g., in (Dion et al., 2004; Grimme, 2004). *Ab initio* techniques are not further discussed in this chapter, but more details can be found, e.g., in (Dreizler and Gross, 1990; Rafii-Tabar, 2008).

Classical atomistic simulation methods like Monte Carlo or molecular dynamics give the possibility of investigating larger systems than can be done using *ab initio* techniques. But the quality of the results of these classical methods crucially depends on the quality of the used potentials or force fields. These methods will be discussed in detail in section 6.2.

Compared to the previously described atomistic simulation techniques the computational requirements of continuum mechanical methods are rather low. This allows the investigation of single and multi-layered CNS consisting of many million atoms. CM methods have shown – within some limits – to be appropriate to investigate the mechanical properties of CNS, see e.g., (Li and Chou, 2003a; Yakobson et al., 1996; Xin et al., 2000) and allow the treatment of vdW interactions in multi-layered CNS (Kelly, 1981; Lu et al., 2009b; Todt et al., 2011). The required input parameters are derived from atomistic simulations (Li and Chou, 2003a; Yakobson et al., 1996; Pantano et al., 2004) and are the subject of intense discussion in the scientific community, see e.g., (Hartmann et al., 2013; Lu et al., 2009a; Pantano et al., 2004; Wu et al., 2008a; Yakobson et al., 1996). Continuum modeling techniques and the determination of appropriate input parameters are discussed in more detail in Section 6.3.

For the sake of completeness also multi-scale methods are mentioned but not discussed in detail. An exhaustive review of these methods can be found, e.g., in (Liew and Sun, 2010; Liu et al., 2004). Multi-scale methods take

advantage of both, atomistic and continuum mechanical approaches. Thus, they can be used to investigate the mechanical behavior of large CNS, where at specific positions the local atomic configurations are of importance. The main issue of multi-scale approaches lies on the smooth bridging between the atomistic and continuum length scale. A multi-scale approach is, e.g., used in (Xu et al., 2012b) to investigate the crack propagation in a graphene sheet.

6.2 Monte Carlo Simulations and Molecular Dynamics

In classical physics the state of a many-body system is described by specification of the momenta and positions of all N particles in the system. This information is summarized in a vector r which is an element of the $6N$-dimensional phase space Γ

$$\Gamma \ni r(t) = \begin{pmatrix} x_1 \\ y_1 \\ z_1 \\ \vdots \\ p_N^x \\ p_N^y \\ p_N^z \end{pmatrix}. \tag{1}$$

Here $x_1,\ y_1,\ z_1 \cdots x_N,\ y_N,\ z_N$ and $p_1^x,\ p_1^y,\ p_1^z \cdots p_N^x,\ p_N^y,\ p_N^z$ describe the three components of the position and the momentum vectors of particles 1 to N and the time dependency of the vector r is explicitly indicated. $r(t)$ describes a one-dimensional curve in phase space. This curve is given by Hamilton's equations of motion (that are equivalent to Newton's equations of motion)

$$\begin{aligned} \frac{dp_k}{dt} &= -\frac{\partial H}{\partial x_k} \\ \frac{dx_k}{dt} &= \frac{\partial H}{\partial p_k}, \end{aligned} \tag{2}$$

with the Hamilton function

$$H(p,x) = \sum_{k=1}^{3N} \frac{p_k^2}{2m} + \sum_{i=1}^{N} U_i(x_j). \tag{3}$$

The Hamilton function gives nothing else than the total energy of the system. The first sum gives the kinetic energy of the system, while the second

sum corresponds to the potential energy. While the kinetic energy depends solely on the momenta (velocities) of the particles, the potential energy depends on the positions of the particles in the system. This is why this part is also called the configurational part of the energy. It is the quality of the potential used that largely determines the reliability of the results obtained from a molecular dynamics or Monte Carlo simulation. The different types of potentials used for the simulation of CNS will be discussed in Chapter 6.2.3

In principle, when the interactions between the particles are defined, then Equations (2) to (3) suffice to calculate the time evolution of the system and, thus, to know the system in every detail, i.e. to calculate the positions and the momenta of the particles at all times starting from an initial configuration. This route taken is what classical molecular dynamics is doing: macroscopic variables like energy, pressure or density are obtained by performing a time average over the microscopic trajectories. In contrast, Monte Carlo simulations produce a sequence of states of the system, where in equilibrium each state occurs with its proper Boltzmann weight. Macroscopic parameters are then determined by an ensemble average. It should be noted that while molecular dynamics also gives the time evolution of a system (in particular, the route the system takes to equilibrium), the results of Monte Carlo simulations are strictly valid only when the system has reached equilibrium.

This chapter can only very briefly introduce the two methods. For more detailed information the interested reader is referred to textbooks on this topic, e.g., the excellent treatise (Landau and Binder, 2009) or (Frenkel and Smit, 2002).

6.2.1 Molecular dynamics simulations

Molecular dynamics starts from Equations 2. The equations of motion are then numerically integrated. This means that the result of a MD simulation is the vector $r(t)$ as given in Equation (1). When this trajectory is known, then any desired quantity can be obtained by performing an average over the obtained configurations. This kind of average corresponds to a time average. Many different algorithms exist that allow an efficient integration of the equations. The most famous is probably the Verlet Algorithm (Verlet, 1967). Here the positions a time step Δt ahead can be calculated via

$$x_i(t + \Delta t) = 2x_i(t) - x_i(t - \Delta t) + \frac{F_i(t)}{m_i}\Delta t^2 + O(\Delta t^4), \tag{4}$$

with $F_i(t)$ the total force exerted on particle i from all other particles and external forces. The forces can be calculated from the potential by building the negative gradient

$$F_i(t) = -\nabla V(x_1, \cdots x_{3N}). \tag{5}$$

Note, that to calculate the new positions the positions of the particles at time step t and $t - \Delta t$ are needed.

One of the most common variants of the MD method is to change from the microcanonical ensemble of constant energy as desribed above to the canonical ensemble of constant temperature. Here the Andersen or the Nosé-Hoover thermostat are two of the most common methods to switch between the ensembles (Frenkel and Smit, 2002).

6.2.2 Monte Carlo simulations

Another approach taken is the Monte Carlo method. Here one considers a system in contact with a heat bath at temperature T. The probability of finding the system with an energy U is given by

$$p(U) = \frac{1}{Z} \exp\left(-\frac{U}{k_B T}\right), \tag{6}$$

with the normalization

$$Z = \sum_r \exp\left(-\frac{U_r}{k_B T}\right), \tag{7}$$

where the sum runs over all possible configurations of the system. $Z(V, T, N)$ is called the *canonical partition sum* of the system and contains all thermodynamic information of the system. In particular Z is connected to the free energy $F(V, T, N)$ of the system via

$$F(T, V, N) = -k_B T \ln Z(V, T, N). \tag{8}$$

Only for very simple systems it is possible to calculate the partition sum analytically. These special cases include non-interacting particles like the ideal gas or non-interacting spins in an external field.

Direct estimation of the partition sum via numerical integration in a computer simulation is often not possible. The problem is twofold. First, already for a small number of particles the number of grid points, where the function has to be evaluated, becomes astronomically large. A regular grid of P points per phase space dimension results in P^{3N} grid points. Thus, for $N = 100$ particles and only 10 points per dimension the sum in

Equation (7) has to be evaluated at 10^{300} points. Second, the partition function is sharply peaked and non-zero only in a limited region in phase space. This is a direct consequence of the central limit theorem and the law of large numbers. Consequently, the mesh has to be very fine to resolve these details of the partition sum.

Monte Carlo simulations give a possibility to circumvent these problems. The idea is not to sample all regions of phase space with equal probability, but to sample regions of phase space in which the partition sum is not negligible small with higher weight. This concept is called Importance Sampling. Of course there is also a drawback. It is not possible to calculate the partition sum itself, but observables of the kind

$$\langle A \rangle = \frac{\sum_r A_r \exp\left(-\frac{U_r}{k_B T}\right)}{\sum_r \exp\left(-\frac{U_r}{k_B T}\right)}. \tag{9}$$

The idea is to generate a so-called Markov chain. This is a successive chain of states of the system in which the single states occur with their proper Boltzmann weight. Thus, the averaging procedure simplifies to a standard mean

$$\langle A \rangle = \frac{1}{n} \sum_{i=1}^{n} A_i, \tag{10}$$

with A_i the value of the observable in the i-th configuration of the system.

Generating a Markov chain with these properties can be done in several ways. Most importantly the algorithm has to fulfill detailed balance. This means that the algorithm must not destroy equilibrium once it is reached. This is achieved when on average all jumps out of a special configuration are exactly canceled by the jumps in this configuration from all other configurations. Detailed balance now poses an even stronger condition that is more easily implemented in a computer code. The jumps out of a configuration o into a new configuration n have to be exactly canceled by the jumps from n to o. One of the most prominent algorithms fulfilling detailed balance is the Metropolis Algorithm (Metropolis and Ulam, 1949; Metropolis et al., 1953). Here one chooses a new configuration, mostly by a small perturbation of the current configuration. Then the energy of the current and the new configuration is evaluated. The new configuration is accepted with probability

$$p = \min\left\{1, \exp\left(-\frac{\Delta U}{k_B T}\right)\right\}. \tag{11}$$

6.2.3 Potentials for carbon

As stated before the quality of the results of atomistic simulations crucially depends on the quality of the potentials/force fields used in the simulations to describe the interactions of the particles. In the following some of the most prominent examples of potentials used for the description of CNS will be introduced. These potentials can be roughly classified in two groups: non-reactive force fields that do not allow for changes in bond coordination and reactive force fields that do so. The free parameters of these force fields can be obtained by *ab initio* calculations or semi-empirically by fitting the potential functions to known experimental data like elastic constants or phonon frequencies.

Non-reactive force fields One way to derive a classical potential for carbon (and other covalently bonded structures) is to start from a Taylor expansion of the full potential

$$\begin{aligned} U &= \sum_i U_1(x_i) + \sum_{j<i} U_2(x_i, x_j) + \sum_{k<j<i} U_3(x_i, x_j, x_k) + \\ &\quad + \sum_{l<k<j<i} U_4(x_i, x_j, x_k, x_l) + \cdots . \end{aligned} \tag{12}$$

Here the first, i.e. single-body term U_1 corresponds to an external potential. The second, i.e. two-body term U_2 is corresponding to a pair potential describing bond stretching. The three coordinates involved in the three-body term U_3 define an angle and, thus, correspond to changes in energy due to changes of the bond angle. The four-body term U_4 corresponds to the torsion angle that is defined as the angle between the planes containing atoms (x_i, x_j, x_k) and atoms (x_j, x_k, x_l). The functional form of these potentials are normally given by a Morse potential for the stretching term, a harmonic bending term and a dihedral torsion term

$$U_2(r) = E_0 \left[\left(1 - e^{-\beta(r-r_0)} \right)^2 - 1 \right] \tag{13}$$

$$U_3(\theta_{ijk}) = \frac{1}{2} k_\theta \left(\cos\theta_{ijk} - \cos\theta_0 \right)^2 \tag{14}$$

$$U_4(\phi_{ijkl}) = \frac{1}{2} k_\phi \left(1 - \cos 2\phi_{ijkl} \right), \tag{15}$$

here E_0 is the binding energy of the structure, r and r_0 are the actual and the equilibrium bond distance, respectively, and β is a measure for the width of the stretching potential. k_θ is the bending constant and θ_{ijk} and

θ_0 the actual and equilibrium bond angle, respectively. k_ϕ and ϕ_{ijkl} are the torsion constant and the torsion angle, respectively.

The parameters needed in this potential can be obtained by performing *ab initio* calculations on the structures and fits to these results. An example for this strategy can be found in (Maple et al., 1994; Holec et al., 2010). Another possibility is to fit these expressions to experimental data like lattice constants, elastic constants and phonon frequencies, respectively. Famous examples include the DREIDING (Mayo et al., 1990; Guo et al., 1991), CHARMM (Brooks et al., 1983) and AMBER (Weiner et al., 1984; Cornell et al., 1995) force fields. The major advantage of such potentials is that they are easy to implement and relatively low in computational cost. One disadvantage is that they do not allow for changes in bond coordination of the atoms involved. One possibility to circumvent this problem is discussed in the next section.

Reactive Empirical Bond Order (REBO) Potentials These potentials were developed starting from the 80ies to take also into account changes in the bond coordination. Pure pair potentials always lead to closed packed structures. It was Abell who made the observation that the strength of individual bonds decreases when the coordination of an atom increases (Abell, 1985). Thus, there is a trade-off of having either few strong or many weak bonds. If there is a weak dependence of bond strength on coordination then closed packed structures, i.e. structures with a maximum number of neighbors, are favored, while a strong dependence of bond strength on coordination favors dimers, i.e. having only one neighbor. This is the principal idea of the family of so called reactive empirical bond order (REBO) potentials that were first introduced by Tersoff (Tersoff, 1988b,a).

The proposed form of the potential is given by

$$U_{REBO} = \sum_{<ij>} f_c \left[f_R(r_{ij}) + b_{ij} f_A(r_{ij}) \right], \tag{16}$$

where the sum runs over all pairs of atoms i and j that have a distance of r_{ij}. f_c is a smooth cutoff function taking into account the short range character of covalent bonds. In molecular dynamics, where the derivative of the potential functions (the force) enters in the main equations (see Equations (4) and (5)) it is beneficial to use a smooth (differentiable) cutoff instead of a simple step function to keep the forces finite. Tersoff proposes the

following form of the cutoff (Tersoff, 1988b)

$$f_c(r_{ij}) = \begin{cases} 1 & r_{ij} < R \\ \frac{1}{2}\left(1 + \cos\left[\pi \frac{r_{ij}-R}{S-R}\right]\right) & R < r_{ij} < S \\ 0 & r_{ij} > S \end{cases}, \tag{17}$$

with R and S being two constants (see Table 6.1). This cutoff ensures that two atoms that are closer than R together interact completely, while particles a distance larger than S apart do not have any interaction. f_c is interpolating smoothly between these two regimes.

The two functions f_R and f_A correspond to the repulsive and attractive part of the potential, respectively. Motivated by the general exponential distance dependence of atomic orbitals they are chosen as Morse like functions

$$f_R(r_{ij}) = A\exp(-\lambda r_{ij}) \tag{18}$$

$$f_A(r_{ij}) = -B\exp(-\mu r_{ij}), \tag{19}$$

with A, B, λ and μ being constants (see Table 6.1).

Finally, b_{ij} is the term that takes into account bond order. b_{ij} is chosen such that it effectively reduces the attractive part of the potential when the number of neighbors of a given atom increases

$$b_{ij} = \left(1 + \beta^n \zeta_{ij}^n\right)^{-1/2n} \tag{20}$$

$$\zeta_{ij} = \sum_{k \neq i,j} f_c(r_{ik}) g(\theta_{ijk}) \tag{21}$$

$$g(\theta_{ijk}) = 1 + \frac{c^2}{d^2} - \frac{c^2}{d^2 + (h - \cos\theta_{ijk})^2}. \tag{22}$$

Here β, n, c, d and h are constants (see Table 6.1). For any pair of atom $< ij >$ the sum runs over all atoms k (excluding the atoms i and j) inside the cutoff region of atom i and θ_{ijk} is the angle defined by the three atoms.

One of the advantages of the REBO potential is that the bond order may change in the course of the simulation. This means also that bonds may open and reform and that the covalent network may evolve.

More recent refinements of the original potential given by Tersoff is the Tersoff-Brenner potential that corrects for overbinding of radicals (Brenner, 1990), the 2nd Generation REBO, where improved analytical functions are used (Brenner et al., 2002) and the AIREBO (Adaptive Intermolecular REBO) potential that includes also non-bonded and dihedral interactions (Stuart et al., 2000).

Table 6.1. Parameters of the Tersoff potential for carbon.

A	1393.6 eV
B	346.74 eV
λ	3.4879 Å
μ	2.2119 Å
β	1.572×10^{-7}
n	0.72751
c	38049
d	4.3484
h	-0.57058
R	1.8 Å
S	2.1 Å

6.3 Continuum Mechanics

If continuum mechanics is used for modeling CNS, the atomic layers are represented using continuum structures. These continuum structures can be either beams and/or trusses (Meo and Rossi, 2006; Li and Chou, 2003a; Sakhaee-Pour, 2009) representing the interatomic bonds or continuum shells (Pantano et al., 2004; Yakobson et al., 1996) describing the overall layer behavior. Both concepts are briefly described in the following sections, where the focus of this review is on continuum shell models of CNS.

In general the resulting boundary value problem is solved using the finite element (FE) method. For continuum shell models an analytical treatment of the mechanical behavior of single and multi-layer CNS is possible within certain limits regarding geometry and nonlinearities see, e.g., (Hartmann et al., 2013; Baowan et al., 2007; He et al., 2005). These analytical relations can become rather complex for multi-layer CNS, such that a closed-form analytical solution is not possible. In this case the set of equations has to be solved numerically (Baowan et al., 2007; He et al., 2005).

6.3.1 Space Frame Models

Space frame models are closely related to MD simulations. Instead of interatomic potentials structural elements like beams, trusses and/or springs are used to describe the interatomic bonds. Truss/spring models are not further considered within this section but are discussed in more detail, e.g., in (Meo and Rossi, 2006; Xu et al., 2013).

In the following, a short overview about beam models is given. Further details can be found, e.g., in (Li and Chou, 2003a). In literature the

continuum beam modeling of atomistic structures is often denoted as lattice structure method (Arghavan and Singh, 2011) or molecular structural mechanics approach (Sakhaee-Pour, 2009). Within this approach each interatomic bond is modeled using a single beam element which usually is assumed to have a circular cross section (Li and Chou, 2003a; Sakhaee-Pour, 2009). The structural properties of the beams are derived from corresponding interatomic potentials used in MC or MD simulations. According to Equation (12) the total potential energy of an atomic system can be split into a bond-stretching, bond bending, and a dihedral torsion term, which are explicitly stated in, e.g., Equations (13) to (15). If small strains are assumed the potentials can be described by simple harmonic forms (Li and Chou, 2003a) reading

$$U_2 = \frac{1}{2}\tilde{k}_S(\Delta r)^2, \quad U_3 = \frac{1}{2}\tilde{k}_\theta(\Delta\theta)^2, \quad U_4 = \frac{1}{2}\tilde{k}_\phi(\Delta\phi)^2 \ . \tag{23}$$

The parameters $\tilde{k}_S$, $\tilde{k}_\theta$, and $\tilde{k}_\phi$ denote the bond stretching, bond angle bending, and bond torsional resistance, respectively. The changes in bond length, bond angle and the twisting increment are described by Δr, $\Delta\theta$, and $\Delta\phi$, respectively. Note that $\tilde{k}_\theta$ and $\tilde{k}_\phi$ are the limiting values for small deformations of k_ϕ and k_θ used in Equations (14) and (15), respectively.

Under the assumption of small strains the strain energy contributions of a beam subjected to pure tension, pure bending, and pure torsion take a similar form given as

$$U^{\mathrm{S}} = \frac{1}{2}k^{\mathrm{S}}(\Delta L)^2, \quad U^{\mathrm{B}} = \frac{1}{2}k^{\mathrm{B}}(2\Delta\alpha)^2, \quad U^{\mathrm{T}} = \frac{1}{2}k^{\mathrm{T}}(\Delta\beta)^2, \tag{24}$$

where k_{S}, k_{S}, and k_{T} are the axial, bending, and torsional stiffness of the beam elements, respectively. The quantities ΔL, $\Delta\alpha$, and $\Delta\beta$ denote the change in beam length, the beam bending angle, and the torsional angle of the beam, respectively. More details on the definition of ΔL, $\Delta\alpha$, and $\Delta\beta$ can be found in (Li and Chou, 2003a). Under the assumption of analogous beam and bond deformations, i.e., $\Delta L = \Delta r$, $2\Delta\alpha = \Delta\theta$, and $\Delta\beta = \Delta\phi$, the stiffness properties of the beam are directly obtained by comparing Equations (23) with (24) reading

$$k^{\mathrm{S}} = \tilde{k}_S, \quad k^{\mathrm{B}} = \tilde{k}_\theta, \quad k^{\mathrm{T}} = \tilde{k}_\phi \ . \tag{25}$$

In contrast to using the stiffness parameters k, as proposed in (Li and Chou, 2003a), a corresponding parameter set consisting of diameter d, Youngs modulus E, and shear modulus G can be obtained leading to (Tserpes and Papanikos, 2005)

$$d = 4\sqrt{\frac{k^{\mathrm{B}}}{k^{\mathrm{S}}}}, \quad E = \frac{(k^{\mathrm{S}})^2 l}{4\pi k^{\mathrm{B}}}, \quad G = \frac{(k^{\mathrm{S}})^2 k^{\mathrm{T}} l}{8\pi (k^{\mathrm{B}})^2}, \tag{26}$$

where l is the length of the beam and therefore, equal to the carbon-carbon bond length. This parameter set has the advantage of a straight forward use in standard FE programs. The force field parameters $k_S = 6.52 \cdot 10^{-7}\,\mathrm{N/nm}$, $k_B = 8.76 \cdot 10^{-10}\,\mathrm{N\,nm\,rad^{-2}}$, and $k_T = 2.78 \cdot 10^{-10}\,\mathrm{N\,nm\,rad^{-2}}$ used in most of the space frame models are usually those used in (Li and Chou, 2003a) and stem originally from (Cornell et al., 1995) and (Jorgensen and Severance, 1990) and were derived for benzene molecules. In (Li and Chou, 2003a) the influence of the choice of k_S and k_B is investigated showing that small deviations of these values are only of minor influence on the overall elastic properties. Furthermore, it is found that k_T has almost no influence on the obtained overall Young's moduli of carbon nanotubes.

The model proposed by Li and Chou (2003a) and the forcefield parameters therein have widely been applied to investigate the mechanical behavior of graphene (Arghavan and Singh, 2011; Li and Chou, 2003a; Sakhaee-Pour, 2009; Kordkheili and Moshrefzadeh-Sani, 2013) or carbon nanotubes (Arghavan and Singh, 2011; Li and Chou, 2003a,b; Domínguez-Rodríguez et al., 2014) and to derive the homogenized elastic properties of the atomic layers see, e.g., (Sakhaee-Pour, 2009; Kordkheili and Moshrefzadeh-Sani, 2013). The overall elastic parameters derived with the space frame models can be used as input for continuum shell models.

6.3.2 Shell Models

Continuum shell models for investigating the mechanical behavior of CNS have first been proposed by (Yakobson et al., 1996). The shell properties are expressed in terms of the membrane stiffness C, the bending stiffness D, and the Poisson's ratio ν and have been derived from MD simulations. The considerations made in (Yakobson et al., 1996) are briefly reviewed in the following.

The parameters C and D are derived from energy considerations in which the total energy obtained by MD simulations is assumed to be equal to the strain energy introduced into a continuum model of a carbon nanotube for the same deformation state. For a carbon nanotube subjected to axial compression the induced energy change per atom ΔU_A in a MD simulation can be expressed as

$$\Delta U_\mathrm{A} = \frac{1}{2}(\Delta U_\mathrm{A})''\epsilon_x^2. \tag{27}$$

The quantity $(\Delta U_\mathrm{A})''$ denotes the second derivative of ΔU_A with respect to the axial strain ϵ_x where a value of $59\,\mathrm{eV/atom}$ is found for $\Delta U_\mathrm{A}''$ in (Yakobson et al., 1996). For the whole nanotube the change in total energy

is obtained as

$$\Delta U = \int_S \rho \Delta U_{\mathrm{A}} \mathrm{d}S = \int_S \rho \frac{1}{2} (\Delta U_{\mathrm{A}})'' \epsilon_x^2 \mathrm{d}S, \tag{28}$$

with ρ and S being the atom density per unit area and the surface area of the nanotube, respectively.

For the same loading case the strain energy V_{A} reads

$$V = \frac{1}{2} \int_S \frac{C}{1-\nu^2} [(\epsilon_x + \epsilon_y)^2 - 2(1-\nu)(\epsilon_x \epsilon_y)] \mathrm{d}S, \tag{29}$$

where it is assumed that the nanotube is a thin-walled cylindrical shell. In this case V depends only on the axial strain ϵ_x and the circumferential strain ϵ_y. If further the strains are assumed to be small, ϵ_y can be expressed as

$$\epsilon_y = -\nu \epsilon_x \ , \tag{30}$$

and Equation (29) simplifies to

$$V = \frac{1}{2} \int_S C \epsilon_x^2 \mathrm{d}S \ . \tag{31}$$

A comparison between Equations (28) and (31) leads to (Yakobson et al., 1996)

$$C = \rho (\Delta U_{\mathrm{A}})'' = 360 \, \mathrm{N/m} \ . \tag{32}$$

The bending stiffness D is estimated under the assumption that a carbon nanotube with radius R is a rolled graphene sheet. The change in total energy $|U_{\mathrm{NT}} - U_{\mathrm{G}}|$, i.e. the difference between the total energy of a carbon nanotube U_{NT} and a planar graphene sheet U_{G} is than equal to the strain energy U_{R} introduced by rolling a graphene sheet. If thin shells are assumed U_{R} can be expressed as

$$U_{\mathrm{R}} = \frac{1}{2} \frac{D}{R^2}, \tag{33}$$

leading finally to a bending stiffness $D = 0.16 \, \mathrm{nN \ nm}$ (Yakobson et al., 1996). The Poisson's ratio $\nu = 0.19$ is evaluated from the change in tube diameter due to axial deformation (Yakobson et al., 1996).

Using the relations

$$C = Eh, \quad D = \frac{Eh^3}{12(1-\nu^2)}, \tag{34}$$

one obtains a Young's modulus $E = 5500 \, \mathrm{N/mm^2}$ and a thickness $h = 0.066 \, \mathrm{nm}$. Note that E and h should not be interpreted as quantities with

a real physical meaning but as effective parameters describing the overall mechanical properties of a single carbon layer. In (Xin et al., 2000) it is confirmed that modeling the atomic layer with continuum shells is consistent with atomistic modeling techniques and that the values derived in (Yakobson et al., 1996) are in the correct order of magnitude. In the following the model is denoted as Yakobson-model.

For the Yakobson-model the layers are assumed to possess isotropic linear elastic material behavior, i.e. the model does not account for the chirality of carbon nanotubes. Further, the type of loading seems to have an influence on the elastic parameters (Huang et al., 2006) being also not considered within the Yakobson-model. A more advanced continuum shell model accounting also for the anisotropy and chirality of the nanotubes is proposed, e.g., in (Wu et al., 2008a; Chang, 2010). Inelastic effects are considered in the nonlocal shell model derived in (Ansari and Rouhi, 2012). This analytical model gives a very good representation of the fundamental frequencies of nanotubes if appropriate nonlocal parameters are used (Ansari and Rouhi, 2012). An exhaustive review on nonlocal shell models of carbon nanotubes is given, e.g., in (Arash and Wang, 2012). Such advanced models allow to capture effects not considered in the Yakobson-model, but are in general more complex. For example, the nonlocal shell parameter used in (Arash and Wang, 2012) depends on the size of the nanotube, the boundary conditions, and on the number of layers in a multi-walled carbon nanotube. Therefore, this parameter has to be derived from atomistic models for each tube configuration leading to high computational costs. Further, in (Chang, 2010) it is shown that the influence of chirality on the elastic properties vanishes fast with increasing tube radius. For nanotubes with their diameter being larger than 1 nm this effect is already negligible. Additionally, the assumption of isotropic layers used in the Yakobson-model is admissible as long as small strains (deformations) are considered (Wu et al., 2008b).

Overall, the Yakobson-model seems to give a good representation of the mechanical behavior of CNS as long as the CNS are large enough and if small strains are considered. Continuum shell models have widely been used to investigate the mechanical behavior of CNS like carbon nanotubes (Yakobson et al., 1996; Pantano et al., 2004), graphene (Hartmann et al., 2013), carbon crystallites (Todt et al., 2010), and carbon onions (Todt et al., 2014a).

The elastic parameters of the shells in terms of E, ν, and h derived by various authors differ significantly, see Table 6.2. This phenomenon is also known as the Yakobson paradox (Shenderova et al., 2002). Good agreement can only be found for the membrane stiffness C, whereas the bending stiffness also seems to be a topic of ongoing discussion. To resolve this paradox,

different solutions were discussed: in (Huang et al., 2006) it was argued that the effective thickness of nanotubes is not constant but depends on the size of the nanotube, its chirality and the loading type. In (Zhang et al., 2011) it was suggested that the Yakobson paradox can be understood by the breakdown of plate theory for a single layer of graphene. It should be noted that the Young's modulus of graphene or carbon nanotubes is often calculated from the membrane stiffness C under the assumption that the thickness of a carbon layer is equal to the interlayer spacing in graphite and, therefore, reads $h = 0.34\,\text{nm}$ (Arghavan and Singh, 2011; Lier et al., 2000; Xu et al., 2012a). This layer thickness leads in combination with the corresponding values of E and ν to a strong overestimation of the bending stiffness obtained, e.g., in (Lu et al., 2009a; Lu and Huang, 2009). However, in (Xu et al., 2012a) it was possible to reproduce nanoindentation experiments conducted in (Lee et al., 2008) with an assumed layer thickness of $h = 0.34\,\text{nm}$. In the nanoindentation experiments the contribution of the bending deformation to the total strain energy is found to be three orders of magnitude smaller than the contribution due to membrane strains. From this outcome it is concluded that graphene has no intrinsic bending stiffness (Lee et al., 2008). Zero bending stiffness of graphene is also proposed in (Zhang et al., 2011), as bending of a single layer graphene sheet does not lead to a change in the atom-atom distances. However, zero bending stiffness of graphene is in clear contradiction with results obtained in (Cadelano et al., 2010; Lu et al., 2009a; Lu and Huang, 2009). In (Lu et al., 2009a) it is shown that further effects like three-atom bending or four-atom out-of-plane torsion contribute to the total potential energy of the system. In (Nikiforov et al., 2014) the π-orbital axis vector scheme is used to show that graphene has a non-vanishing bending stiffness resulting from the torsional misalignment of the π hybrid orbitals. This contribution can be considered using an additional dihedral-angle term in the 2nd-generation Brenner potential as is done, e.g., in (Lu et al., 2009a). However, this term has to be parameterized appropriately (Nikiforov et al., 2014). Further, in (Nikiforov et al., 2014) it is shown that although continuum plate/shell theory does not correspond to the physical molecular orbital description, it can be used to reproduce the bending behavior of graphene, at least for small strains. In (Xu et al., 2013) the non-zero bending stiffness of graphene is attributed to residual internal moments and not to changes in bond-lengths and used to investigate self-buckling of free standing graphene sheets. This discussion shows that whether or not continuum shell models can be used to describe the mechanical behavior of CNS is far from being clarified. Especially the question which combination of E, h, and ν gives the best description of CNS needs further investigation. Examples for the application of contin-

uum models for investigating the mechanical behavior of CNS and further concepts for obtaining the elastic shell parameters are given in Section 6.4.

Table 6.2. Values for C, D, E, h and ν taken from literature.

Method/Structure/Ref.	C [J/m^2]	D [nNnm]	E [GPa]	h [nm]	ν [-]
(Arghavan and Singh, 2011) molecular structural mechanics					
graphene, in-plane	-	-	~ 1000	0.34[1]	0.16[1]
graphene, out-of-plane	-	-	~ 110	0.34[1]	0.16[1]
(Lee et al., 2008) nanoindentation experiments					
graphene	342 ± 30	0	-	-	-
(Lier et al., 2000) *ab initio*					
graphene	-	-	1110	0.34[1]	-
nanotube $r = 0.344\,\text{nm}$	-	-	1060	0.34[1]	0.125
nanotube $r = 0.369\,\text{nm}$	-	-	940	0.34[1]	0.047
(Lu et al., 2009a) analytically, graphene					
1st gen. Brenner pot.	-	0.133	-	-	-
2nd gen. Brenner pot	-	0.110	-	-	-
incl. dihedral angle effect	-	0.225	-	-	-
(Lu and Huang, 2009) analytically, graphene	340 ± 50	0.255			0.398
(Pantano et al., 2004) finite element method, nanotubes	363	0.176	4840	0.075	0.19[1]
(Sears and Batra, 2004) molecular mechanics, nanotubes					
MM3 ((Allinger et al., 1989))	-	-	2520	0.134	0.21
Tersoff-Brenner	-	-	3100	0.098	0.26
(Wu et al., 2008b) atomistic-based shell theory					
graphene[2]	$\sim$470	$\sim$0.22	-	-	-
nanotubes[2]	$\sim$480	$\sim$0.225	-	-	-
(Xin et al., 2000) electronic band theory, nanotubes	377.4 (357.7)	0.183 (0.176)	5100	0.074	0.24
(Xu et al., 2012a) *ab initio*, graphene	-	-	1030	0.34[1]	0.22
(Yakobson et al., 1996) molecular dynamics, nanotubes	363	0.137	5500	0.066	0.19
(Zhang et al., 2011) molecular dynamics, graphite	-	0	1240	0.34[1]	0.24
(Hartmann et al., 2013)	324	0.476	2400	0.132	0.1844

[1] Values are assumed in the cited papers.
[2] Values obtained for the unstrained CNS.

6.3.3 Further aspects

Besides the layer properties, further aspects have to be considered in continuum mechanical modeling of CNS. In multi-layered CNS vdW interactions play an important role, and in curved CNS like carbon nanotubes and carbon onions the curvature induced surface stress has to be considered. Furthermore, the carbon layers are not perfect but contain defects like vacancies or interstitial atoms. In multi-layer CNS these defects may also lead to covalent interlayer bonds which cross-link adjacent layers. All of these aspects are briefly discussed in the following.

Van der Waals interactions In multi-layer CNS the van der Waals (vdW) interactions between adjacent layers result form the vdW interactions between individual atoms making up the layers. vdW interactions are relatively week compared to the covalent interlayer bonds and result from induced dipole interactions between uncharged atoms. vdW interactions between individual atoms can be described as a function of the atom-atom distance r using a pair potential, e.g., the Lennard-Jones potential (Kelly, 1981)

$$U_{12} = 4\epsilon \left[\left(\frac{\sigma}{r}\right)^{12} - \left(\frac{\sigma}{r}\right)^{6} \right], \tag{35}$$

where ϵ and σ are Lennard-Jones parameters describing the depth of the potential well and the atom-atom distance at $U_{12} = 0$, respectively. The first derivative of Equation (35) with respect to r describes the force $F_{12} = -\frac{d\ U_{12}}{dr}$ between the interacting atoms. If $F_{12} = 0$, i.e., the potential U_{12} posseses a minimum and the two atoms have reached their equilibrium distance $r_0 = 2^{1/6}\ \sigma$.

In continuum mechanical modeling of CNS, vdW interactions can be either considered using linear or nonlinear springs or trusses or using a nonlinear pressure-distance relation. Truss/spring elements are applicable for space frame models and continuum shell models, whereas pressure-distance relations are only applicable in continuum shell models.

The first attempt is used, e.g., in (Li and Chou, 2003b) and (Kordkheili and Moshrefzadeh-Sani, 2013) where two interacting atoms represented by finite element nodes are connected with a truss/spring element. The stiffness of these elements is derived as the second derivative of the Lennard-Jones potential given by Equation (35) with respect to r. Theoretically, one atom of a layer interacts with all atoms of the adjacent layers meaning that each atom has to be connected with all other atoms by truss or spring elements. As the vdW interactions vanish fast with increasing atom-atom distance usually only interactions between nearest neighboring layers are considered.

Further, only atoms with a maximum distance of approximately 4 to 8 times the equilibrium distance r_0 are taken into account.

For deriving a pressure distance relation the vdW interactions between atoms of adjacent layers can be summed up and related to the surface area of the layers leading, e.g., to

$$p(\alpha) = \frac{C_{33}}{6} \left[\left(\frac{\sigma}{\alpha}\right)^{10} - \left(\frac{\sigma}{\alpha}\right)^{4} \right], \tag{36}$$

for graphite, where $C_{33} = 36.5\,\mathrm{GPa}$ is the compressive constant (Kelly, 1981; Zhao and Spain, 1989) and α is the current interlayer distance. If the condition $p(\alpha = \alpha_{\mathrm{eq}}) = 0$ is satisfied two adjacent layers have reached their equilibrium distance. This leads to

$$\alpha_{\mathrm{eq}} = \sigma, \tag{37}$$

being by factor of $2^{1/6}$ smaller than the atom-atom equilibrium distance r_0. Another possible way of obtaining a pressure-distance relation for planar CNS is to replace the discrete sum by a surface integral and use the atom density per unit area, ρ_∞, to describe the number of atoms in an infinitesimally small area of the layers, see e.g. (Hamaker, 1937; Lu et al., 2009b; Todt et al., 2011). This approach leads to a different result for graphite as obtained in Equation (36) reading

$$p(\alpha) = C_0 \left[\left(\frac{\sigma}{\alpha}\right)^{11} - \left(\frac{\sigma}{\alpha}\right)^{5} \right], \tag{38}$$

with

$$C_0 = 8\ \epsilon\ (\rho_\infty)^2\ \sigma\ \pi\ . \tag{39}$$

In this approach the compressive constant C_0 depends on the Lennard-Jones parameters and the exponents are different than those in Equation (36). The influence of the differences between Equations (36) and (38) are investigated in more detail in Section 6.4.3. It should be noted that Equations (38) and (36) lead to the same α_{eq}. The pressure distance relations given by Equations (38) and (36) are both derived for graphite under the assumption that neighboring layers consist of the same number of atoms. In carbon nanotubes or carbon onions the number of atoms is different in adjacent layers. This difference has to be considered in the pressure distance relations. In (He et al., 2005; Ru, 2000; Wang et al., 2003) the curvature effect in carbon nanotubes is considered by assuming that the vdW pressure on opposing faces of adjacent layers is inversely proportional to their radii, leading to $p_{\mathrm{in}} R_{\mathrm{in}} = p_{\mathrm{out}} R_{\mathrm{out}}$. In more advanced approaches like in (Lu

et al., 2009b) for carbon nanotubes or in (Hamaker, 1937; Iglesias-Groth et al., 1997; Todt et al., 2011) for spherical CNS the curvature effect is already considered in the derivation of the pressure-distance relations. In (Lu et al., 2009b) it is shown that the critical pressure of carbon nanotubes is overestimated by 25% or 75% if $p_{\text{in}}R_{\text{in}} = p_{\text{out}}R_{\text{out}}$ or $p_{\text{in}} = p_{\text{out}}$ (graphite relation) are used, respectively, instead of the relation directly considering the different number of atoms in the layers. In (Todt et al., 2011) the influence of the vdW formulation on the equilibrium interlayer distances and on the layer deformation in two-layered carbon onions is investigated. It is shown that although the simplified models lead to the same equilibrium interlayer distance as the model considering the curvature effect, substantial differences could be observed for the layer deformations. In the advanced model the outer layer undergoes larger deformations than the inner layer especially for large fullerenes. This leads also to larger membrane forces in the outer layer, which become of major interest if the structural stability of carbon onions is considered. Concluding it can be said that accounting for the different number of atoms in adjacent layers in the formulation of the vdW model is of great importance, especially if the stability of multi-layer CNS is investigated.

Comparing the nonlinear truss/spring approach with the pressure-distance approach one can say that the truss/spring models are cumbersome from a modeling point of view if large CNS are considered. Nevertheless, truss/spring models offer some advantages. If an atom of one layer is connected by springs/trusses to all other atoms of the adjacent layers the curvature effect is naturally taken into account. Furthermore, the interlayer shear stiffness of the vdW interactions is considered, which is usually neglected when pressure distance relations are used, see e.g., (Pantano et al., 2004; Yao et al., 2008; Todt et al., 2014a). The interlayer shear modulus is in the range of $4 - 5\,\text{GPa}$ (Kelly, 1981). Compared to the inplane stiffness of the carbon layers and the vdW stiffness perpendicular to the layers the interlayer shear stiffness is small and becomes only of importance if sliding between adjacent layers occurs, e.g., in (Byrne et al., 2010).

Intra- and interlayer defects CNS are not defect-free. Defects can occur within a single layer or lead to covalent cross linking between the layers. Defects within a single layer can occur as point defects and one dimensional line defects. Point defects are Stone-Wales (SW) defects, single and multiple vacancies, carbon or foreign add atoms, and substitutional impurities. Some of these defects are experimentally observed, e.g., in (Hashimoto et al., 2004; Meyer et al., 2008). The one dimensional line defects comprise dislocation like defects separating two graphene domains with different lattice orien-

tations, see e.g., (Huang et al., 2011; Kim et al., 2011) and defects at the edges of graphene layers involving dangling bonds and the saturation of free atoms with, e.g., hydrogen atoms. Detailed reviews on the different defect types, their structure, their formation, and their influence on the chemical, magnetic, electronic, and mechanical properties can be found, e.g., in (Banhart et al., 2011; Terrones et al., 2012). Methods for the experimental characterization of defects in graphene and graphene based materials are reviewed in (Araujo et al., 2012).

To study the influence of defects on the mechanical properties mainly MD simulations, e.g., (Ansari et al., 2011; Wang et al., 2012; Sharma et al., 2014) or space frame continuum models (Tapia et al., 2012; Tserpes, 2012; Georgantzinos et al., 2012) are used. In (Tapia et al., 2012) a structural mechanics approach is used to show that already a single vacancy defect significantly reduces the fracture strength of graphene but has only minor influence on the Young's modulus. This is in good agreement with the results obtained in (Ansari et al., 2011) using MD simulations and results of (Georgantzinos et al., 2012; Tserpes, 2012) using space frame models. The influence of SW defects on the fracture strength seems to be only of minor importance due to the fact that SW defects annihilate by inverse bond rotation under mechanical loading (Sun et al., 2012). The findings of (Sun et al., 2012) are in contradiction to the results obtained in (Wang et al., 2012) where a significant reduction of the fracture strength due to SW defects is observed. With increasing number of defects also the Young's modulus decreases as shown in (Sharma et al., 2014) for carbon nanotubes. Similar results have been obtained in (Tapia et al., 2012; Tserpes, 2012). Vacancy and SW defects also reduce the axial buckling load of carbon nanotubes, but seem to have only minor influence on the compressive modulus (Eftekhari et al., 2013). In general, SW defects show a stronger influence on the buckling load and the elastic properties than vacancies (Eftekhari et al., 2013). SW defects locally reduce the load carrying capacity of CNTs and lead to a stress and strain concentration around the defect (Chandra et al., 2004). To investigate the local influence of SW defects, atomic scale stress and strain measures are employed in (Chandra et al., 2004), where the strains are formulated in a - from a continuum mechanics point of view - unusual form. It is shown that the stress concentration decreases for higher overall strains, whereas the strain concentration increases. Structures containing defects show a lower overall energy than defect free structures when subjected to mechanical loading (Chandra et al., 2004), which may explain spontaneous defect formation at higher strains. The formation of defects in pristine graphene under mechanical loading is investigated, e.g., in (Wang et al., 2012), revealing that vacancy defects are easier generated than SW

defects. Dewapriya et al. (2014) studied the fracture behavior of graphene in more detail and also investigated the capability of different continuum mechanics based fracture criteria to predict the fracture strength. It turned out that the quantized fracture mechanics approach (Pugno and Ruoff, 2004) captures the fracture strength of graphene quite well (Dewapriya et al., 2014).

In contrast to MD simulations or space frame approaches continuum shell models are less frequently used to investigate the influence of defects in CNS. This is because considering the structure and local influences of the defects is not as straight forward in continuum shell models as in space frame models. In (Zhang et al., 2014) a generalized von Karman equation for flexible solid membranes is utilized to account for topological defects, like heptagonal-pentagonal pairs, via corresponding eigenstrains. The arising set of differential equations is solved using FEM and allows to predict the stress field and the out-of-plane deformations in a graphene sheet under uniaxial and biaxial strains, respectively. (Chen and Chrzan, 2011) use a similar approach where the arising set of differential equations is solved in the Fourier Space. The defects are modeled via topological constraints. The received in-plane strains and out-of-plane deformations due to the defects are in good agreement with results of atomistic simulations. Pentagonal rings increase the local curvature of carbon structures (Cataldo, 2002) and are required to form closed caged structures like fullerenes or carbon onions. SW defects – as combination of two pentagonal and two heptagonal atomic rings – can also increase the sphericity of fullerenes (Terrones and Terrones, 1997). Further, a combination of pentagonal-heptagonal rings might be utilized to design curved graphene structures, such as graphene funnels (Zhang et al., 2014). In (Todt et al., 2014b) a continuum shell model of a C_{240} fullerene is used to investigate the influence of the required 12 pentagonal atomic rings on the membrane stiffness of fullerenes. It is shown that the pentagonal rings lead to a local stiffening of the fullerene structure, which is also observed in MD simulations (Todt et al., 2014b).

Intra-layer defects, such as vacancies or interstitial atoms and dangling bonds at the edges of the graphene layers, can be the source for a formation of covalent interlayer bonds (Telling et al., 2003; Vollath, 2008). Further, nanoindentation of multi-walled nanotubes and multi-layer graphene can give rise to the formation of such bonds (Guo et al., 2004). Interlayer bonds influence the mechanical properties of CNS, like multi-walled carbon nanotubes (Byrne et al., 2010; Huang et al., 2010; Peng et al., 2012) and carbon nanotube bundles (Kis et al., 2004). Cross links constrain sliding between nanotube walls (Byrne et al., 2010) and adjacent nanotubes (Kis et al., 2004), the load transfer between the tubes being best if the bonds

are uniformly distributed (Byrne et al., 2010). However, for covalent bonds formed by Frenkel pair defects (Telling et al., 2003) a decrease in the axial buckling load of double-walled nanotubes is observed, as the Frenkel pair defect weakens the layers and stresses are concentrated around these defects (Peng et al., 2012). Furthermore, the increased interlayer shear stiffness of carbon crystallites forming carbon fibers (Loidl et al., 2003; Sauder and Lamon, 2005) is attributed to the formation of covalent interlayer bonds (Loidl et al., 2003). Interlayer bonds may also play a role in the formation of nanodiamonds due to the irradiation induced self-compression of carbon onions (Banhart et al., 1997).

The examples above show that interlayer defects should be considered in a continuum mechanical analysis of CNS. As a first attempt a continuum truss model is used in (Todt et al., 2010) to represent such covalent interlayer bonds in carbon crystallites. Therein, the defects are assumed to correspond to a fourfold coordinated interstitial atom (Telling et al., 2003) locally reducing the interlayer distance from 0.34 nm to approximately 0.258 nm. Each defect is represented by a single truss element (Todt et al., 2010), and hence, the actual structure of the defects is ignored. The axial stiffness of the trusses is assumed to be high enough, so that the conflating effect of the interlayer bonds is not significantly influenced by the membrane stiffness of the layers. With this model it is shown that the amount and the distribution of interlayer defects has an influence on the occurrence of buckling in carbon crystallites, see Section 6.4.4.

Curvature induced excess surface energy In curved CNS a curvature induced excess surface energy is present (Holec et al., 2010) being defined as the curvature induced increase in total energy with respect to planar graphene. Due to the excess surface energy a surface stress develops in curved carbon layers leading to a non-zero membrane stress state in the absence of external loading (Fischer et al., 2008). In a continuum mechanical model this surface stress can be taken into account by applying a corresponding inwards oriented mechanical pressure, see e.g., (Todt et al., 2014a). The excess surface energy being present in carbon fullerenes is discussed in more detail in Section 6.4.3 and (Holec et al., 2010).

6.4 Applications

In the following sections we discuss some examples on how the concepts introduced in the preceding chapters can be used to study the mechanical behavior of CNS. Starting from planar graphene it is explained how atomistic simulations were used to extract effective mechanical properties for this

fascinating material. Then nanotubes are discussed. These cylindrically shaped objects are obtained when graphene is rolled up in one direction. Nanotubes are typically characterized by a very large aspect ratio, i.e., the ratio of length to diameter is very large. Typical questions concern the stability of nanotubes during uniaxial compression, bending or hydrostatic loading, thermal buckling and the influence of defects. When graphene is not only curved in one but in two dimensions then spherical fullerenes are obtained. In contrast to plane graphene and nanotubes, fullerenes intrinsically contain structural defects, because it is not possible to close a structure consisting of three fold coordinated particles and hexagons only. At least 12 pentagons have to be included. When many of such fullerenes of different size are "stacked" into each other then so called carbon onions form. In these multilayered structures the non-covalent vdW interactions are of utmost importance. Special care has to be taken in the description of vdW interactions in the framework of continuum mechanics when these forces act between curved surfaces. In carbon onions it is most likely that vdW forces define the maximum number of layers that an onion can consist of. Finally, the mechanics of carbon fibers is discussed. It is shown that the mechanical properties of these fibers strongly depend on the concentration and distribution of defects in the carbon nano-crystallites the fibers are consisting of.

6.4.1 Graphene

Graphene is a single layer of graphite, i.e., a truly 2-dimensional material. Graphene consists of sp^2 bonded carbon, i.e., each atom has exactly 3 neighbors. Note, that graphene is not a bravais lattice. The smallest unit cell of graphene consists of 2 atoms. Although graphene seems to be a simple structure, some tricky questions may arise. One of these is: What is the thickness of a two-dimensional material? Even if on first sight this question may seem academical it has important implications. Graphene is the elementary building block of all other CNS, like nanotubes, fullerenes, carbon onions, and carbon crystallites in carbon fibers. Thus, a thorough understanding of graphene is essential to understand also the larger structures. Because of the small size of graphene experiments on these structures are scarce. One of the few examples is presented in (Lee et al., 2008). Consequently, computer simulations are of utmost importance to gain additional insight into these structures. Nevertheless, studying the mechanical properties of these structures using a full atomistic description is often not feasible due to the large number of atoms in graphene layers being sufficiently large. A possible solution is to use methods from continuum mechanics to inves-

tigate such structures. A natural way describing these structures is as thin elastic shells. This demands the input of three macroscopic parameters: the Young's modulus E, the Poisson's ratio ν and the thickness h of the shell. In other words, the goal is to find *effective* elastic parameters of a hypothetical shell that shall show the same elastic behavior as a sheet of graphene. While the determination of a membrane stiffness $Y = Eh$ can easily be done in a simulation and partly also in experiments, the bending stiffness and, thus, the effective thickness explicitly is harder to grasp as already discussed in Section 6.3.2. Using potentials obtained in (Holec et al., 2010) in (Hartmann et al., 2013) computational loading tests were performed on graphene using the Monte Carlo method. The membrane stiffness, Poisson's ratio and the strength of graphene were obtained by computational tension tests, while the bending stiffness (and, thus, the effective thickness) were derived by compression tests, in which buckling was enforced. It was shown that the continuum approximation breaks down for systems composed of too few atoms, but that a constant effective thickness of $h = 1.32$ Å is reached for graphene longer than 50 Å (see also Figure 6.1).

6.4.2 Nanotubes

An infinite sheet of planar graphene is the lowest energy conformation of sp^2 bonded carbon. The edges of any finite sheet of graphene increase the energy of this structure. Thus bending and closure of the sheet may become energetically favorable, and structures like nanotubes (Baughman et al., 2002) may form. Nanotubes are of cylindrical symmetry and may be single or multi-walled. Besides inheriting the amazing mechanical properties from graphene, nanotubes also show remarkable electronic properties. Depending on its chirality the tube may either be metallic or semiconducting (Dai, 2002).

One convenient procedure of testing nanotubes (either in a pressure cell using Raman spectroscopy or in a computer experiment) is to apply hydrostatic pressure from the outside (Sun et al., 2013). The deformation of the nanotubes is first given by a reduction in radius without a change in shape for low pressure and an ovalization of the cross section of the tube that is accompanied by a subsequent softening of the tube for high pressure. This behavior, which corresponds to typical buckling of thin tubes under external pressure (Windenburg and Trilling, 1934), was predicted in computer simulations (Sun et al., 2004) using molecular dynamics and also found in experiments (Sun et al., 2014). Monte Carlo simulations of nanotubes under hydroststic pressure show similar results as the molecular dynamics calculations (see Figure 6.2) (Sun et al., 2013). Details on the continuum

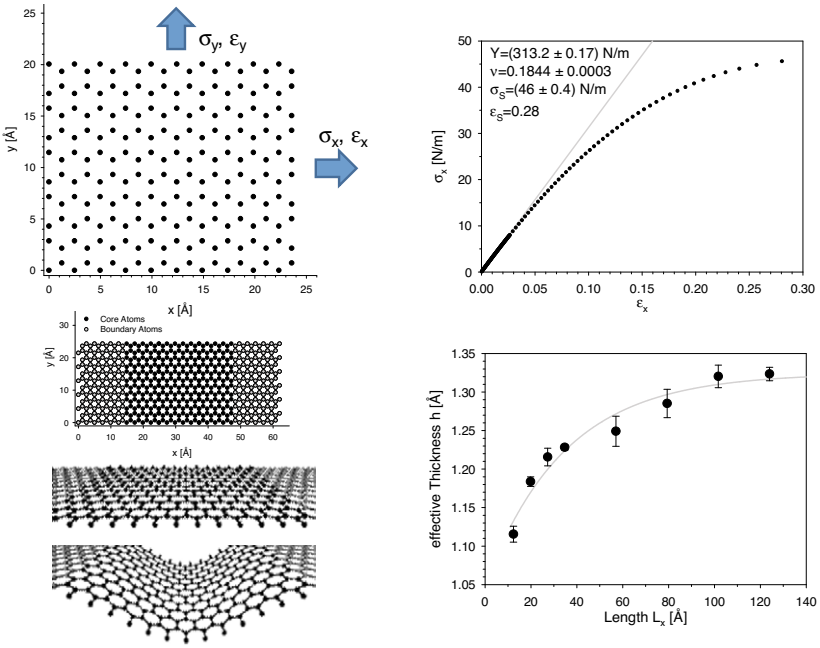

Figure 6.1. Determination of the effective elastic properties of graphene. Top row: The membrane stiffness Y, Poisson's ratio ν, the strength σ_S, and the ultimate strain ϵ_S of graphene is obtained by loading a sheet of graphene in uni-axial tension (left) and recording the corresponding strains in x and y-directions. Bottom row: Compression tests on graphene to obtain the effective thickness h. On the left the used geometry and two snapshots of the graphene layer before and after buckling are shown. On the right the effective thickness obtained for different lengths of the graphene patch is shown. For a length smaller than approximately 50 Å the effective thickness of graphene decreases due to the breakdown of the continuum approximation, but attains a constant value of ≈ 1.32 Å for longer patches. (Figure reproduced with permission and adapted from (Hartmann et al., 2013)).

mechanical modeling of the behavior of nanotubes under external pressure can be found in Chapter 7.

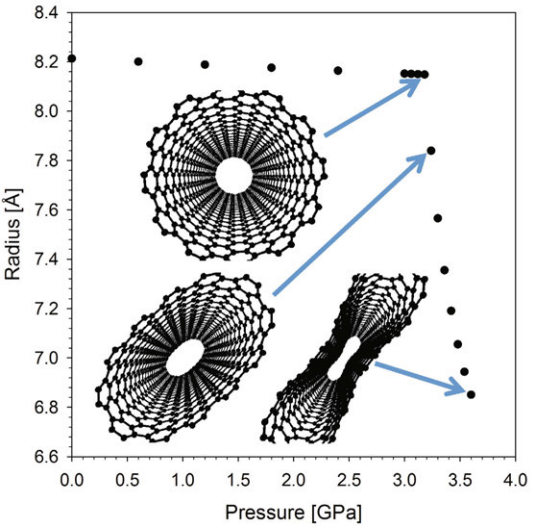

Figure 6.2. The behavior of nanotubes under radial compression (hydrostatic pressure). The figure shows the radius of the tube as a function of the applied load as obtained by Monte Carlo simulations. The radius is defined as the mean normal distance of all atoms with respect to the tube axis. For low loads the radius of the tubes shrinks homogeneously. After a certain critical pressure is exceeded the cross section of the tubes ovalizes and loses its circular shape. (Figure adapted from (Sun et al., 2013). Copyright Wiley-VCH Verlag GmbH & Co. KGaA. Reproduced with permission).

Using molecular dynamics methods in (Wang et al., 2005) the behavior of nanotubes under axial load was investigated. Here it was shown that depending on the length of the tube it fails either via local buckling or global bending. In (Hao et al., 2008) the influence of defects (vacancies) on the mechanical properties of nanotubes was modeled, while in (Walther et al., 2001) the interaction of water and nanotubes was modeled to investigate the radial-breathing-mode (RBM) vibration of nanotubes that shows a pronounced signal in Raman spectra. Also the buckling of double-walled nanotubes can be monitored in a simulation, where it was shown that the vdW interactions between the layers have a large influence on the buckling load (Zhang et al., 2007).

6.4.3 Fullerenes and Onions

In contrast to cylindrical nanotubes, spherical CNS can not be formed solely by hexagons. According to Euler's theorem at least 12 pentagons are necessary to close the structure. Fulfilling Eulers theorem is a neccesarry but not a sufficient condition for fullerenes to be thermodynamically stable. Additionally, the so called isolated pentagon rule (IPR) (Kroto, 1987) must be fulfilled and the fullerene must consist of an even number of atoms (Kroto, 1987). The IPR is an implication of the fact that the local stability – in terms of the position of the atoms – of a fullerene increases if the local curvature decreases (Klein et al., 1986). It states that only such fullerenes are thermodynamically stable for which the pentagons are not in direct contact with each other. These pentagons can be regarded as intrinsic intra-layer defects that result in a lower bond angle than the perfect hexagons. Due to the pentagons fullerenes have the shape of truncated icosahedrons, where the pentagons are located at the vertices of the icosahedrons. The thermodynamic stability of fullerenes up to C_{240} is investigated in (Klein et al., 1986) considering only fullerenes with their number of atoms being equal to $n = 20(m^2+mk+k^2), \quad 0 \leq k \leq m$, with m and k being integers. C_{60}, C_{180}, and C_{240} fullerenes are thermodynamically quite stable. The fullerenes C_{80} and C_{140} show a lower thermodynamic stability and therefore, are less likely to form than, e.g., a C_{60} fullerene. Thermodynamic stability considerations on larger fullerenes (Tang and Huang, 1995) show that all fullerenes with $k = m$ form a closed-cage structure, which is not necessarily the case for $k = 0$. Therefore, the number of atoms forming a fullerene - in terms of a closed-cage icosahedron – can be calculated as $n = 60k^2$.

As mentioned in Section 6.3.3 curved CNS possess an intrinsic curvature excess surface energy. In (Holec et al., 2010) the excess surface energy of fullerenes of different size is investigated in detail. First, classical potentials are obtained using *ab initio* calculations. In a second step the excess surface energy is calculated with *ab initio* for small fullerenes up to C_{240} and with Monte Carlo simulations for larger fullerenes up to C_{5120}. It is shown that Monte Carlo simulations over estimate the total amount of the surface energy by a constant factor of approximately 1.6. Nevertheless, the Monte Carlo method as well as the *ab initio* calculations lead to the same exponent $\beta = 1.4$ for the decay of the surface energy E_S as a function of radius $E_S \propto R^{-\beta}$. The results show that the excess surface energy is only of importance for small fullerenes, as it vanishes fast with increasing fullerene radius. For fullerenes the resulting surface stress σ_S (here in terms of a membrane force per unit area) corresponds to a plane hydrostatic stress state and can be related to the excess surface energy by the Shuttleworth

equation (Fischer et al., 2008) reading $\sigma_S = E_S + \frac{\mathrm{d}E_S}{\mathrm{d}\epsilon_S}$. The parameter ϵ_S denotes the strain in each circumferential direction of the sphere in a small strain setting (Fischer et al., 2008). For a first estimate, usually the second term of the right hand side of the Shuttleworth Equation is neglected.

Large fullerenes with $k = m$ tend to form multi-layer arrangements as they are more stable (Tang and Huang, 1995). Multi-layered particles were first observed by Iijima in 1980 (Iijima, 1980). These particles were called carbon onions (Kroto, 1992) and form from soot when subjected to intense electron irradiation (Ugarte, 1992). They show a rather polyhedral shape or are almost perfectly spherical. In a strict sense only the spherical particles should be denoted as carbon onions. Today, various methods are avialable to produce carbon onions, such as electron irradiation of graphite at elevated temperatures ($\geq 300°$C) (Banhart and Ajayan, 1996; Banhart et al., 1997), high temperature annealing of nanodiamonds (Tomita et al., 2002), synthesis by decomposition of phenolic resin (Zhao et al., 2007), high pressure transformation of graphite, or thermo-mechanical processing of graphite powders (Güler and Evin, 2014). Onions produced by high-pressure transformation of single crystal graphite seem to grow from the inside to the outside (Blank et al., 2007; Du et al., 2007; Füller and Banhart, 1996). This corresponds to the presumption (Kroto, 1992) that carbon onions grow by the spiraling network mechanism (Kroto and McKay, 1988; Zhang et al., 1986). If high-temperature annealing of nanodiamonds is used to produce carbon onions, the particles grow from the outer boundaries of the nanodiamond towards the center (Tomita et al., 2002). Due to their multi-layer spherical structure carbon onions posses a high local electron density leading to a high ability for absorbing electromagnetic radiation. This makes them promising candiates as fillers in nanocomposites for electromagnetic shielding (Macutkevic et al., 2009). They have also potential application as additives in lubricants (Joly-Pottuz et al., 2008), as solid lubricants (Hirata et al., 2004), or as nanoscopic pressure cells for the production of nanodiamonds (Banhart and Ajayan, 1996).

In all of these applications the mechanical properties of carbon onions under external pressure and the size of these particles play a role. In (Peón-Escalante et al., 2014) the "bulk modulus" B – as applied pressure per relative change of the enclosed volume – of a C_{60} fullerene is predicted with *ab initio* and the space frame modeling appraoch discussed in Section 6.3.1. The obtained values of B are between 750 GPa and approximately 900 GPa and are in good agreement with references given in (Peón-Escalante et al., 2014). In (Peón-Escalante et al., 2014) the use of shell models for estimating B of fullerenes is considered as problematic with allusion to the definition of an appropriate shell thickness. This is in clear contradiction to

the results presented in (Todt et al., 2014b), where the applicability of shell models to describe the mechanical properties of fullerenes is investigated in detail. In (Todt et al., 2014b) icosahedral fullerenes up to a size of C_{1280} are modeled using continuum shells where different parameter sets of E, h, and ν are used. The fullerenes are subjected to an external pressure and a circumferential ring load allowing to obtain their hydrostatic and ringload stiffness, respectively. The results are compared to results obtained by MC simulations. Although larger fullerenes are not perfectly spherical the hydrostatic stiffness of the fullerenes could be well predicted by the continuum shell model and is almost the same for all parameter sets for E, h, and ν. This result is not surprising as hydrostatic pressure leads to a pure membrane stress state. As can be seen from Table 6.2 all parameter sets lead to comparable values of the membrane stiffness and therefore, to similar values of the hydrostatic stiffness. Further, it is shown that parameter sets for which h is choosen to be around 0.34 nm strongly overestimate the ring load stiffness of the fullerenes. Parameter sets with $h \approx 0.07$ nm and a thereof resulting E of around 5000 GPa gave the best prediction of the ring load stiffness. It is also shown that the loading conditions in the MC simulations and in the continuum model have to be similar to lead to comparable results.

For investigating the mechanical properties of spherical CNS consisting of a large number of atoms, such as carbon onions, atomistic methods become computationally expensive. In this case, continuum mechanical methods can be used to investigate their mechanical behavior. For example, in (Todt et al., 2014a) continuum mechanical shell models are applied to investigate a possible growth limit of carbon onions. There, the model used assumes that carbon onions grow from the inside to the outside and considers the excess surface energy as well as the vdW interactions between the layers. The arising boundary value problem is solved using the FEM method. The vdW interactions are described using the pressure-distance relations given in (Kelly, 1981) and (Todt et al., 2011) for graphite/graphene. These relations allow a straight forward implementation into the FEM model but neglect the curvature effect within the vdW interactions. The question regarding the growth limit of carbon onions is formulated as a buckling eigenvalue problem

$$\left(\underset{\approx}{\boldsymbol{K}}_N + \lambda_N \Delta \underset{\approx}{\boldsymbol{K}}_N\right) \underset{\sim}{\boldsymbol{\Phi}}_N = \underset{\sim}{\boldsymbol{0}} \tag{40}$$

with $\underset{\approx}{\boldsymbol{K}}_N$ being the stiffness matrix of a N-layered onion in its equilibrium state. The matrix $\Delta \underset{\approx}{\boldsymbol{K}}_N$ represents the change in the stiffness of the onion due to an externally applied fictitious pressure. Hence, an eigenvalue $\lambda_N = 0$ means that no external pressure is required for the onion to loose its

structural stability, and therefore, indicates the growth limit of the onion. The vector $\underset{\sim}{\mathbf{\Phi}}_N$ is the corresponding buckling mode to the eigenvalue λ_N. With this formulation it has been shown that the size of carbon onions is most likely limited by the occurence of a structural instability. The loss of stability is caused by a self-equilibrating stress state emerging from the accommodation of misfitting carbon layers during the growing process. The self-equilibrating stresses in the layers are mainly introduced by the vdW interactions between the layers, whereas the excess surface energy is of importance for the innermost layers only, for details see (Todt et al., 2014a). Figure 6.3 a) shows the results of the eigenvalue problem, revealing that the use of different exponents in the pressure distance relations for the vdW interactions (see Section 6.3.3) are only of minor importance, whereas the choice of the Lennard-Jones parameters has a strong influence on the results. From the obtained buckling mode – depicted in Figure 6.3 (b) it can be concluded that the outermost layers start to buckle, and the innermost layers remain almost unaffected. This is because only the outermost layers of the onion are under compression, see Figure 6.3 (c), where the number of layers under compression increases during the growth of the onion. The largest onion obtained in the analysis has about 72 layers, which is close to experimental observations, e.g, in (Banhart, 1997; Banhart et al., 1997). In conclusion, it can be said that due to uncertainities in the parameters describing the layer properties and the high sensitivity on the vdW parameters, the results rather have a qualitative than a quantitative character. However, the model clearly indicates a growth limit of carbon onions and can act as basis for further research.

6.4.4 Carbon Fibers

Carbon fiber reinforced plastics (CFRP) are – due to their high stiffness and strength at low mass density – used in many lightweight applications. Although many different parameters, like the fiber content or the bonding between fibers and matrix influence the properties of CFRP, it is necessary to have detailed knowledge about the mechanical properties of the fibers. Hence, these properties are subject of intense research activities, see, e.g., (Gao et al., 2011; Hawthorne, 1993; Loidl et al., 2005; Naito et al., 2008; Sauder et al., 2004). Due to the small diameters of the fibers they show a tendency towards buckling when subjected to compressive loading, making it difficult to assess their compressive behavior experimentally. Methods to overcome these problems are, e.g., the loop test (Sinclair, 1950) or the tensile recoil method (Allen, 1987). For a more detailed review of experimental methods, see, e.g., (Oya and Johnson, 1999). Such experiments revealed

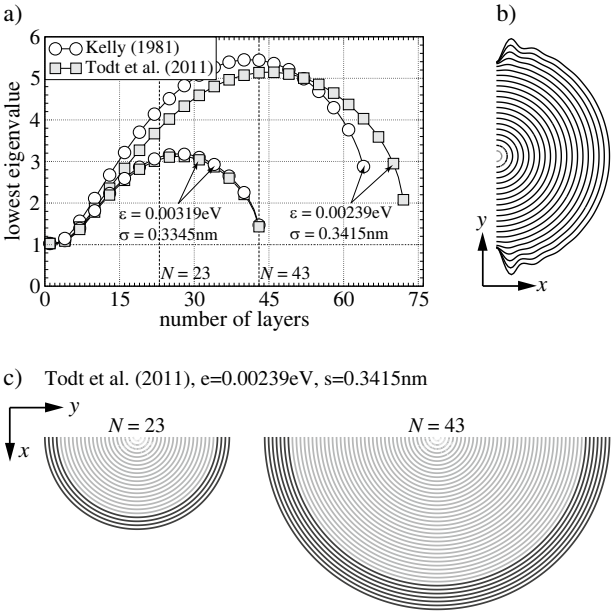

Figure 6.3. a) Results of the buckling eigenvalue analysis during the growth of carbon onions obtained with different vdW models and Lennard-Jones parameters. The loss of structural stability is indicated by the approach of the lowest eigenvalue to 0. b) Buckling mode of a carbon onion, where only every second layer is shown, see (Todt et al., 2014a) (Figure appearing with the permission of Elsevier). c) Layers under compression (black) and tension (gray) of onions grown to different sizes.

that the nanostructure of the fibers has a strong influence on their compressive behavior (Dobb et al., 1995; Oya and Johnson, 2001; Nakatani et al., 1999; Loidl et al., 2005). For example, polyacrylonitrile (PAN) based carbon fibers show a skin-core structure (Paris and Peterlik, 2009), where the outer surface of the fibers is formed by a skin-like layer, and randomly distributed so called carbon crystallites form the inner region, see Figure 6.4. In fibers subjected to compressive loading, crystallite buckling was supposed to occur (Oya and Johnson, 2001; Nakatani et al., 1999) and was at first directly observed in (Loidl et al., 2005) using microbeam X-ray diffraction. Crystallite buckling is related to fiber failure (Dobb et al., 1995) and the non-Hookean behavior of fibers observed in loop tests (Hawthorne, 1993). Thus, it has a strong influence on the mechanical behavior of carbon fibers.

Besides experimental methods continuum mechanical modeling can help to gain further insight into the dependency of the fibers properties on their nanostructure, see, e.g., (Sauder and Lamon, 2005; Todt et al., 2010). In (Sauder and Lamon, 2005) the tensile properties of the fibers are determined using the theory of elasticity for anisotropic solids. It is shown that an aritificially high interlayer shear stiffness is required to obtain a good representation of the Young's modulus of the fibers confirming observations made in (Loidl et al., 2003) for PAN based fibers. This model is also applicable to investigate the compressive and bending behavior of carbon fibers as long as crystallite buckling has not occurred. Crystallite buckling is inves-

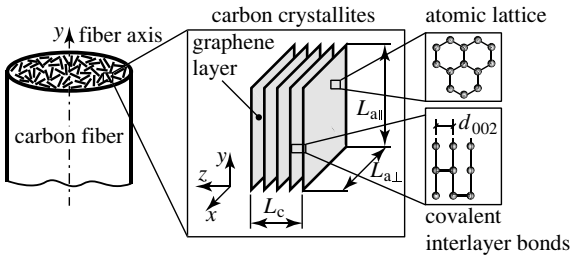

Figure 6.4. Nanostructure of PAN-based carbon fibers. (Figure taken from (Todt et al., 2010) and appearing with kind permission from Springer Science+Business Media.)

tigated in (Todt et al., 2010) using a detailed continuum mechanical model of a single crystallite. In (Todt et al., 2010) the layers of the crystallite depicted in Figure 6.4 are modeled using continuum shells. In the model the crystallite is assumed to consist of eight layers with in-plane dimensions of $L_{a\parallel} \times L_{a\perp} = 4.32\,\text{nm} \times 3.87\,\text{nm}$, with the graphene planes being oriented parallel to the fiber axis. The vdW interactions between the individual layers are described using the pressure-distance relation given in Equation (36) and the interlayer defects are modeled using the defect model briefly discussed in Section 6.3.3. Defects randomly distributed within the whole crystallite lead to local dimples in the graphene layers, whereas defects located along the edges only cause an overall bending of the crystallite. This difference in the pre-deformation has a substantial influence on the mechanical behavior of carbon crystallites subjected to compressive loading along the fiber axis. In the pre-buckling state the apparent secant modulus of the crystallites is almost constant and independent of the amount of interlayer defects if the defects are distributed within the whole crystallite, see Figure 6.5 (left). After the occurrence of crystallite buckling the secant modulus

decreases significantly, where the axial load leading to the onset of buckling substantially increases with the amount of defects. If the defects are distributed along the edges only, the crystallite possesses a much lower initial secant modulus which strongly decreases already for small deformations and is almost independent of the amount of interlayer defects, Figure 6.5 (right). This behavior can be attributed to the pre-bending deformation introduced by the formation of the defects along the edges. Comparison with literature (Loidl et al., 2003) reveals that it is more likely that the defects are distributed within the whole crystallite, as in this case the obtained overall Young's modulus of the crystallites corresponds well with the experimentally obtained value (Loidl et al., 2003). The reduction of the secant modulus after the onset of buckling explains the observed shift in the neutral axis during loop-testing of fibers (Loidl et al., 2005). Although this continuum model contains some simplifications, especially regarding the sturcture of the defects and their properties, it provides some insight to mechanisms determining the compressive behavior of carbon fibers on a nanostructural level.

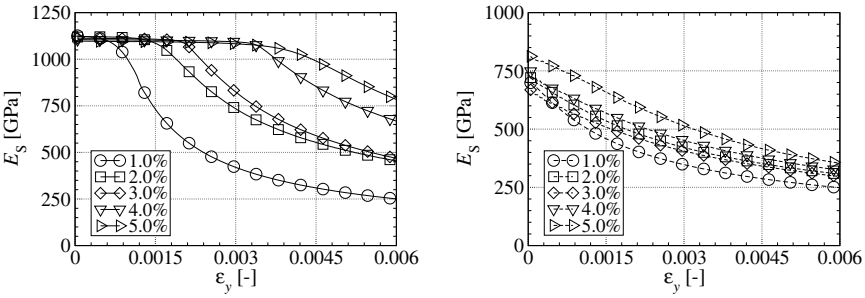

Figure 6.5. Deformation dependent apparent secant modulus of carbon crystallites with their interlayer defects being distributed within the whole crystallite (left) or along the edges only (right). The amount of interlayer defects is varied from 1% to 5% of the maximum number of possible interlayer defects.

6.5 Conclusion

Computational methods, such as molecular dynamics, Monte Carlo methods, and continuum mechanical approaches can be used to investigate the mechanical properties of carbon nanostructures. These methods should be

seen as complementary to experimental methods, allowing to investigate phenomena which are difficult to observe in experiments. The choice of the method depends on the length scale on which a specific phenomena occurs and the size of the carbon nanostructures to be investigated. Molecular dynamics and Monte Carlo methods allow to access the position of the individual atoms within a carbon nanostructure and phenomena like bond breaking and bond formation can directly be investigated. However, for carbon nanostructures consisting of a large number of atoms these methods can become computationally expensive. For such large nanostructures continuum mechanical methods can provide insight the overall mechanical behavior with relatively low computational costs. Overall it can be said, that an interplay between experimental, atomistic, and continuum mechanical methods is required to get a fundamental understanding of the mechanical behavior of carbon nanostructures.

References

G.C. Abell. Empirical chemical pseudopotential theory of molecular and metallic bonding. *Physical Review B*, 31:6184, May 1985.

S.R. Allen. Tensile recoil measurement of compressive strength for polymeric high performance fibres. *Journal of Materials Science*, 22:853–859, 1987.

N.L. Allinger, Y.H. Yuh, and J.H. Lii. Molecular mechanics. The MM3 force field for hydrocarbons. *Journal of the American Chemical Society*, 111: 8551–8566, 1989.

R. Ansari and H. Rouhi. Analytical treatment of the free vibration of single-walled carbon nanotubes based on the nonlocal flugge shell theory. *Journal of Engin eering Materials and Technology*, 134:011008, 2012.

R. Ansari, B. Motevalli, A. Montazeri, and S. Ajori. Fracture analysis of monolayer graphene sheets with double vacancy defects via MD simulation. *Solid State Communications*, 151:1141 – 1146, 2011.

B. Arash and Q. Wang. A review on the application of nonlocal elastic models in modeling of carbon nanotubes and graphenes. *Computational Materials Science*, 51:303–313, 2012.

P.T. Araujo, M. Terrones, and M.S. Dresselhaus. Defects and impurities in graphene-like materials. *Materials Today*, 15:98–109, 2012.

S. Arghavan and A.V. Singh. Atomic lattice structure and continuum plate theories for the vibrational characteristics of graphenes. *Journal of Applied Physics*, 110:084308, 2011.

A.A. Balandin. Thermal properties of graphene and nanostructured carbon materials. *Nat Mater*, 10:569–581, 2011.

F. Banhart. The transformation of graphitic onions to diamond under electron irradiation. *Journal of Applied Physics*, 81:3440–3445, 1997.

F. Banhart and P.M. Ajayan. Carbon onions as nanoscopic pressure cells for diamond formation. *Nature*, 382:433–435, 1996.

F. Banhart, T. Füller, Ph. Redlich, and P.M. Ajayan. The formation, annealing and self-compression of carbon onions under electron irradiation. *Chemical Physics Letters*, 269:349–355, 1997.

F. Banhart, J. Kotakoski, and A.V. Krasheninnikov. Structural defects in graphene. *ACS Nano*, 5:26–41, 2011.

D. Baowan, N. Thamwattana, and J.M. Hill. Continuum modelling of spherical and spheroidal carbon onions. *European Physical Journal D*, 44: 117–123, 2007.

R.H. Baughman, A.A Zakhidov, and W.A. de Heer. Carbon nanotubes – the route toward applications. *Science*, 297:787–792, 2002.

V.D. Blank, V.N. Denisov, A.N. Kirichenko, B.A. Kulnitskiy, S. Yu Martushov, and B.N. Mavrin et al. High pressure transformation of single-crystal graphite to form molecular carbon onions. *Nanotechnology*, 18: 345601, 2007.

D.W. Brenner. Empirical potential for hydrocarbons for use in simulating the chemical vapor deposition of diamond films. *Physical Review B*, 42: 9458, 1990.

D.W. Brenner, O.A. Shenderova, J.A. Harrison, S.J. Stuart, B. Ni, and S.B. Sinnott. A second-generation reactive empirical bond order (REBO) potential energy expression for hydrocarbons. *Journal of Physics: Condensed Matter*, 14:783, 2002.

B.R. Brooks, R.E. Bruccoleri, B.D. Olafson, D.J. States, S. Swaminathan, and M. Karplus. Charmm: A program for macromolecular energy, minimization, and dynamics calculations. *Journal of Computational Chemistry*, 4(2):187, 1983.

E.M. Byrne, A. Letertre, M.A. McCarthy, W.A. Curtin, and Z. Xia. Optimizing load transfer in multiwall nanotubes through interwall coupling: Theory and simulation. *Acta Materialia*, 58:6324–6333, 2010.

E. Cadelano, S. Giordano, and L. Colombo. Interplay between bending and stretching in carbon nanoribbons. *Physical Review B*, 81:144105, 2010.

A.H. Castro Neto, F. Guinea, N.M. R. Peres, K.S. Novoselov, and A.K. Geim. The electronic properties of graphene. *Rev. Mod. Phys.*, 81:109–162, 2009.

F. Cataldo. The impact of a fullerene-like concept in carbon black science. *Carbon*, 40:157–162, 2002.

N. Chandra, S. Namilae, and C. Shet. Local elastic properties of carbon nanotubes in the presence of stone-wales defects. *Physical Review B*, 69: 094101, 2004.

T. Chang. A molecular based anisotropic shell model for single-walled carbon nanotubes. *Journal of the Mechanics and Physics of Solids*, 58: 1422–1433, 2010.

S. Chen and D.C. Chrzan. Continuum theory of dislocations and buckling in graphene. *Physical Review B*, 84:214103, 2011.

W. Choi and J.W. Lee, editors. *Graphene Synthesis and Applications*. CRC Press, New York, 2012.

A. Chuvilin, U. Kaiser, E. Bichoutskaia, N.A. Besley, and A.N. Khlobystov. Direct transformation of graphene to fullerene. *Nature Chemistry*, 2: 450–453, 2010.

Wendy D. Cornell, Piotr Cieplak, Christopher I. Bayly, Ian R. Gould, Kenneth M. Merz, David M. Ferguson, David C. Spellmeyer, Thomas Fox, James W. Caldwell, and Peter A. Kollman. A second generation force field for the simulation of proteins, nucleic acids, and organic molecules. *Journal of the American Chemical Society*, 117(19):5179, 1995.

H. Dai. Carbon nanotubes: opportunities and challenges. *Surface Science*, 500:218 – 241, 2002.

M.A.N. Dewapriya, R.K.N.D. Rajapakse, and A.S. Phani. Atomistic and continuum modelling of temperature-dependent fracture of graphene. *International Journal of Fracture*, 187:199–212, 2014.

M. Dion, H. Rydberg, E. Schröder, D.C. Langreth, and B.I. Lundqvist. Van der Waals density functional for general geometries. *Physical Review Letters*, 92:246401, 2004.

M.G. Dobb, H. Guo, D.J. Johnson, and C.R. Park. Structure-compressional property relations in carbon fibres. *Carbon*, 33:1553–1559, 1995.

G. Domínguez-Rodríguez, A. Tapia, and F. Avilés. An assesment of finite element analysis to predict the elastic modulus and poisson's ratio of singlewall carbon nanotubes. *Computationa Material Science*, 82:257–263, 2014.

R.M. Dreizler and E.K.U. Gross. *Density Functional Theory: An Approach to the Quantum Many-Body Problem*. Springer-Verlag, 1990.

A.B. Du, X.G. Liu, D.J. Fu, P.D. Han, and B.S. Xu. Onion-like fullerenes synthesis from coal. *Fuel*, 86:294–298, 2007.

H. Dumlich and S. Reich. Nanotube bundles and tube-tube orientation: A van der Waals density functional study. *Physical Review B*, 84:064121, 2011.

M. Eftekhari, S. Mohammadi, and A.R. Khoei. Effect of defects on the local shell buckling and post-buckling behavior of single and multi-walled carbon nanotubes. *Computational Materials Science*, 79:736 – 744, 2013.

F.D. Fischer, T. Waitz, D. Vollath, and N.K. Simha. On the role of surface energy and surface stress in phase-transforming nanoparticles. *Progress in Materials Science*, 53:481–527, 2008.

D. Frenkel and B. Smit. *Understanding Molecular Simulation*. Academic Press, 2002.

T. Füller and F. Banhart. In situ observation of the formation and stability of single fullerene molecules under electron irradiation. *Chemical Physics Letters*, 254:372–378, 1996.

A. Gao, C. Zhao, S. Luo, Y. Tong, and L. Xu. Correlation between graphite crystallite distribution morphology and the mechanical properties of carbon fiber during heat treatment. *Materials Letters*, 65:3444 – 3446, 2011.

A.K. Geim. Graphene: Status and prospects. *Science*, 324:1530–1534, 2009.

A.K. Geim and K.S. Novoselov. The rise of graphene. *Nature Materials*, 6: 183–191, 2007.

S.K. Georgantzinos, D.E. Katsareas, and N.K. Anifantis. Limit load analysis of graphene with pinhole defects: A nonlinear structural mechanics approach. *International Journal of Mechanical Sciences*, 55:85–94, 2012.

S. Grimme. Accurate description of van der Waals complexes by density functional theory including emprical conditions. *Computational Chemistry*, 25:1463–1473, 2004.

Ö. Güler and E. Evin. Formation of carbon nano onions by thermomechanical processing of graphite powders. *Materials Testing*, 56:241–244, 2014.

W. Guo, C.Z. Zhu, T.X. Yu, C.H. Woo, B. Zhang, and Y.T. Dai. Formation of sp^3 bonding in nanoindented carbon nanotubes and graphite. *Physical Review Letters*, 93:245502, 2004.

Y. Guo, N. Karasawa, and W.A. Goddard III. Prediction of fullerene packing in C60 and C70 crystals. *Nature*, 351:464, 1991.

H.C. Hamaker. The London–van der Waals attraction between spherical particles. *Physica IV*, 10:1058–1072, 1937.

X. Hao, H. Qiang, and Y. Xiaohu. Buckling of defective single-walled and double-walled carbon nanotubes under axial compression by molecular dynamics simulation. *Composites Science and Technology*, 68:1809, 2008.

M.A. Hartmann, M. Todt, F.G. Rammerstorfer, F.D. Fischer, and O. Paris. Elastic properties of graphene obtained by computational mechanical tests. *Europhysics Letters*, 103:68004, 2013.

A. Hashimoto, K. Suenaga, A. Gloter, K. Urita, and S. Iijima. Direct evidence for atomic defects in graphene layers. *Nature*, 430:870–873, 2004.

H.M. Hawthorne. On non-Hookean behavior of carbon fibers in bending. *Journal of Material Science*, 28:2531–2535, 1993.

X.Q. He, S. Kitipornchai, and K.M. Liew. Buckling analysis of multi-walled carbon nanotubes: a continuum model accounting for van der Waals interaction. *Journal of the Mechanics and Physics of Solids*, 53:303–326, 2005.

A. Hirata, M. Igarashi, and T. Kaito. Study on solid lubricant properties of carbon onions produced by heat treatment of diamond clusters or particles. *Tribology International*, 37:899–905, 2004.

D. Holec, M.A. Hartmann, F.D. Fischer, F.G. Rammerstorfer, P.H. Mayrhofer, and O. Paris. Curvature-induced excess surface energy of fullerenes: Density functional theory and Monte Carlo simulations. *Physical Review B*, 81:235403, 2010.

P.Y. Huang, C.S. Ruiz-Vargas, A.M. van der Zande, W.S. Whitney, M.P. Levendorf, J.W. Kevek, S. Garg, J.S. Alden, C.J. Hustedt, Y. Zhu, J. Park, P.L. McEuen, and D.A. Muller. Grains and grain boundaries in single-layer graphene atomic patchwork quilts. *Nature*, 469:389–392, 2011.

X. Huang, H. Yuan, W. Liang, and S. Zhang. Mechanical properties and deformation morphologies of covalently bridged multi-walled carbon nanotubes: Multiscale modeling. *Journal of the Mechanics and Physics of Solids*, 58:1847–1862, 2010.

Y. Huang, J. Wu, and K. C. Hwang. Thickness of graphene and single-wall carbon nanotubes. *Physical Review B*, 74:245413, 2006.

S. Iglesias-Groth, J. Breton, and C. Girardet. An analytical approach for the interlayer interaction in spherical buckyonions. *Chemical Physics Letters*, 264:351–358, 1997.

S. Iijima. Direct observation of the tetrahedral bonding in graphitized carbon black by high resolution electron microscopy. *Journal of Crystal Growth*, 50:675–683, 1980.

S. Iijima. Helical microtubules of graphitic carbon. *Nature*, 354:56–58, 1991.

L. Joly-Pottuz, N. Matsumoto, H. Kinoshita, B. Vacher, M. Belin, and G. Montagnac et al. Diamond-derived carbon onions as lubricant additives. *Tribology International*, 41:69–78, 2008.

W.L. Jorgensen and D.L. Severance. Aromatic aromatic interactions–free-energy profiles for the benzene dimer in water, chloroform, and liquid benzene. *Journal of American Chemical Society*, 112:4768 – 4774, 1990.

B. Kelly. *Physics of Graphite*, pages 79–80. Advanced Science Publishers, 1981.

K. Kim, Z. Lee, W. Regan, C. Kisielowski, M.F. Crommie, and A. Zettl. Grain boundary mapping in polycrystalline graphene. *ACS Nano*, 5: 2142–2146, 2011.

A. Kis, C. Csányi, J.P. Salvetat, T.N. Lee, E. Couteau, A.J. Kulik, W. Benoit, J. Brugger, and L. Forró. Reinforcement of single-walled carbon nanotube bundles by intertube bridging. *Nature Materials*, 3: 153–157, 2004.

D.J. Klein, W.A. Seitz, and T.G. Schmalz. Icosahedral symmetry carbon cage molecules. *Nature*, 323:703–706, 1986.

S.A. Hosseini Kordkheili and M. Moshrefzadeh-Sani. Mechanical properties of double-layered graphene sheets. *Computationa Material Science*, 69: 335 – 343, 2013.

H.W. Kroto. The stability of the fullerenes C_n, with $n = 24$, 28, 32, 36, 50, 60, and 70. *Nature*, 329:529–531, 1987.

H.W. Kroto. Carbon onions introduce new flavour to fullerene studies. *Nature*, 359:670–671, 1992.

H.W. Kroto and K. McKay. The formation of quasi-icosahedral spiral shell carbon particles. *Nature*, 331:328–331, 1988.

H.W. Kroto, J.R. Heath, S.C. O'Brien, R.F. Curl, and R.E. Smalley. C60: Buckminsterfullerene. *Nature*, 318:162–163, 1985.

D.P. Landau and K. Binder. *A Guide to Monte-Carlo Simulations in Statistical Physics*. Cambridge University Press, 2009.

C.N. Lau, W. Bao, and J. Velasco Jr. Properties of suspended graphene membranes. *Materials Today*, 15:238–245, 2012.

C. Lee, X. Wei, J.W. Kysar, and J. Hone. Measurement of the elastic properties and intrinsic strength of monolayer graphene. *Science*, 321: 385–388, 2008.

C. Li and T.W. Chou. A structural mechanics approach for the analysis of carbon nanotubes. *International Journal of Solids and Structures*, 40: 2487–2499, 2003a.

C. Li and T.W. Chou. Elastic moduli of multi-walled carbon nanotubes and the effect of van der Waals forces. *Composite Science and Technology*, 63:1517–1524, 2003b.

G. Van Lier, C. Van Alsenoy, V. Van Doren, and P. Geerlings. *Ab initio* study of the elastic properties of single-walled carbon nanotubes and graphene. *Chemical Physics Letters*, 326:181–185, 2000.

K.M. Liew and Y.Z. Sun. Computational modelling and simulation of carbon nanotubes. In B.H.V Topping, J.M. Adam, F.J. Pallarés, R. Bru, and M.L. Romeo, editors, *Development and Applications in Engineering Computational Technology*, pages 201–217. Saxe-Coburg Publications, Stirlingshire, Scotland, 2010.

W.K. Liu, E.G. Karpov, S. Zhang, and H.S. Park. An introduction to computational nanomechanics and materials. *Computer Methods in Applied Mechanics and Engineering*, 193:1529–1578, 2004.

D. Loidl, H. Peterlik, M. Müller, Ch. Riekel, and O. Paris. Elastic moduli of nanocrystallites in carbon fibers measured by in-situ X-ray microbeam diffraction. *Carbon*, 41:563–570, 2003.

D. Loidl, O. Paris, M. Burghammer, C. Riekel, and H. Peterlik. Direct observation of nanocrystallite buckling in carbon fibers under bending load. *Physical Review Letters*, 95:225501, 2005.

Q. Lu and R. Huang. Nonlinear mechanics of single-atomic-layer graphene sheets. *International Journal of Applied Mechanics*, 1:443–467, 2009.

Q. Lu, M. Arroyo, and R. Huang. Elastic bending modulus of monolayer graphene. *Journal of Physics D*, 42:102002, 2009a.

W.B. Lu, B. Liu, J. Wu, J. Xiao, K.C. Hwang, and S.Y. Fu et al. Continuum modeling of van der Waals interactions between carbon nanotube walls. *Applied Physics Letters*, 94:101917, 2009b.

J. Macutkevic, D. Seliuta, G. Valusis, J. Banys, P. Kuzhir, and S. Maksimenko et al. Dielectric properties of onion-like carbon based polymer films: Experiment and modeling. *Solid State Sciences*, 11:1828–1832, 2009.

J.R. Maple, M.-J. Hwang, T.P. Stockfisch, U. Dinur, M. Waldman, C.S. Ewig, and A.T. Hagler. Derivation of Class II Force Fields. I. Methodology and Quantum Force Field for the Alkyl Functional Group and Alkane Molecules. *Journal of Computational Chemistry*, 15:162, 1994.

S.L. Mayo, B.D. Olafson, and W.A. Goddard III. DREIDING: A Generic Force Field for Molecular Simulations. *Journal of Physics and Chemistry*, 94:8897, 1990.

M. Meo and M. Rossi. Prediction of Young's modulus of single wall carbon nanotubes by molecular-mechanics based finite element modelling. *Composites Science and Technology*, 66:1597–1605, 2006.

N. Metropolis and S. Ulam. The Monte Carlo Method. *Journal of the American Statistical Association*, 44:335, 1949.

N. Metropolis, A.W. Rosenbluth, M.N. Rosenbluth, A.H. Teller, and E. Teller. Equation of State Calculations by Fast Computing Machines. *Journal of Chemical Physics*, 21:1087–1092, 1953.

J.C. Meyer, C. Kisielowski, R. Erni, M.D. Rossell, M.F. Crommie, and A. Zettl. Direct imaging of lattice atoms and topological defects in graphene membranes. *Nano Letters*, 8:3582–3586, 2008.

K. Naito, Y. Tanaka, J.M. Yang, and Y. Kagawa. Tensile properties of ultrahigh strength PAN-based, ultrahigh modulus pitch-based and high ductility pitch-based carbon fibers. *Carbon*, 46:189–195, 2008.

M. Nakatani, M. Shioya, and J. Yamashita. Axial compressive fracture of carbon fibers. *Carbon*, 37:601–608, 1999.

I. Nikiforov, E. Dontsova, R.D. James, and T. Dumitrică. Tight-binding theory of graphene bending. *Physical Review B*, 89:155437, 2014.

K.S. Novoselov, A.K. Geim, S.V. Morozov, D. Jiang, Y. Zhang, and S.V. Dubonos et al. Electric field effect in atomically thin carbon films. *Science*, 306:666–669, 2004.

N. Oya and D.J. Johnson. Direct measurement of longitudinal compressive strength in carbon fibres. *Carbon*, 37:1539–1544, 1999.

N. Oya and D.J. Johnson. Longitudinal compressive behaviour and microstructure of PAN-based carbon fibres. *Carbon*, 39:635–645, 2001.

A. Pantano, D.M. Parks, and M.C. Boyce. Mechanics of deformation of single- and multi-wall carbon nanotubes. *Journal of the Mechanics and Physics of Solids*, 52:789–821, 2004.

O. Paris and H. Peterlik. The structure of carbon fibres. In S. Eichhorn, J.W.S Hearle, M. Jaffe, and T. Kikutani, editors, *Handbook of textile fibre structure*, volume 2. Woodhead Publishing Limited, Cambridge, UK, 2009.

B. Peng, Y. Li, S. Liu, Z. Guo, and L. Ding. The roles of crosslinks in the buckling behaviors and load transferring mechanisms of double-walled nanotubes under compression. *Computational Materials Science*, 55:95–99, 2012.

R. Peón-Escalante, C. Villanueva, R. Quintal, F. Avilés, and A. Tapia. The bond force constant and bulk modulus of C60. *Computational Materials Science*, 83:120 – 126, 2014.

N.M. Pugno and R.S. Ruoff. Quantized fracture mechanics. *Philosophical Magazine*, 84:2829–2845, 2004.

H. Rafii-Tabar. *Computational physics of carbon nanotubes*. Cambridge University Press, Cambridge, 2008.

C.Q. Ru. Effect of van der Waals forces on axial buckling of a double-walled carbon nanotube. *Journal of Applied Physics*, 87:7227–7231, 2000.

A. Sakhaee-Pour. Elastic properties of single-layered graphene sheet. *Solid State Communications*, 149:91–95, 2009.

C. Sauder and J. Lamon. Prediction of elastic properties of carbon fibers and CVI matrices. *Carbon*, 43:2044–2053, 2005.

C. Sauder, J. Lamon, and R. Pailler. The tensile behavior of carbon fibers at high temperatures up to 2400°C. *Carbon*, 42:715–725, 2004.

A. Sears and R.C. Batra. Macroscopic properties of carbon nanotubes from molecular-mechanics simulations. *Physical Review B*, 69:235406, 2004.

S. Sharma, R. Chandra, P. Kumar, and N. Kumar. Effect of stone-wales and vacancy defects on elastic moduli of carbon nanotubes and their composites using molecular dynamics simulation. *Computational Materials Science*, 86:1 – 8, 2014.

O.A. Shenderova, V.V. Zhirnov, and D.W. Brenner. Carbon Nanostructures. *Critical Reviews in Solid State and Materials Sciences*, 27:227, 2002.

D. Sinclair. A bending method for measurement of the tensile strength and Young's modulus of glass fiber. *Journal of Applied Physics*, 21:380–386, 1950.

S. Stankovich, D.A. Dikin, G.H.B. Dommett, K.M. Kohlhaas, E.J. Zimney, and E.A. Stach et al. Graphene-based composite materials. *Nature*, 442: 282–286, 2006.

S.J. Stuart, A.B. Tutein, and J.A. Harrison. A reactive potential for hydrocarbons with intermolecular interactions. *Journal of Chemical Physics*, 112:6472, 2000.

D.Y. Sun, D.J. Shu, M. Ji, F. Liu, M. Wang, and X.G. Gong. Pressure-induced hard-to-soft transition of a single carbon nanotube. *Physical Review B*, 70:165417, 2004.

Y.J. Sun, F. Ma, D.Y. Ma, K.W. Xu, and P.K Chu. Stress-induced annihilation of Stone-Wales defects in graphene nanoribbons. *Journal of Physics D*, 45:305303, 2012.

Y.W. Sun, D.J. Dunstan, M.A. Hartmann, and D. Holec. Nanomechanics of carbon nanotubes. *Proceedings in Applied Mathematics and Mechanics*, 7:13, 2013.

Y.W. Sun, I. Hernández, A.J. Ghandour, C. Rice, I.F. Crowe, M.P. Halsall, A. Sapelkin, J. Gonzalez, F. Rodriguez, and D.J. Dunstan. Resonance Raman spectroscopy of carbon nanotubes: pressure effects on G-mode. *High Pressure Research*, 34(2):191–197, 2014.

A.C. Tang and F.Q. Huang. Stability rules of icosahedral (Ih or I) fullerenes. *Chemical Physics Letters*, 247:494–501, 1995.

A. Tapia, R. Peón-Escalante, C. Villanueva, and F. Avilés. Influence of vacancies on the elastic properties of a graphene sheet. *Computational Materials Science*, 55:255–262, 2012.

R.H. Telling, C.P. Ewels, A.A. El-Barbary, and M.I. Heggie. Wigner defects bridge the graphite gap. *Nature Materials*, 2:333–337, 2003.

H. Terrones and M. Terrones. The transformation of polyhedral particles into graphitic onions. *Journal of the Physics and Chemistry of Solids*, 58:1789–1796, 1997.

H. Terrones, R. Lv, M. Terrones, and M.S. Dresselhaus. The role of defects and doping in 2d graphene sheets and 1d nanoribbons. *Reports on Progress in Physics*, 75:062501, 2012.

J. Tersoff. Empirical Interatomic Potential for Carbon, with Applications to Amorphous Carbon. *Physical Review Letters*, 61:2879, 1988a.

J. Tersoff. New Empirical approach for the structure and energy of covalent systems. *Physical Review B*, 37:6991, 1988b.

M. Todt, F.G. Rammerstorfer, O. Paris, and F.D. Fischer. Nanomechanical studies of the compressive behavior of carbon fibers. *Journal of Material Science*, 45:6845–6848, 2010.

M. Todt, F.G. Rammerstorfer, F.D. Fischer, P.H. Mayrhofer, D. Holec, and M.A. Hartmann. Continuum modeling of van der Waals interactions between carbon onion layers. *Carbon*, 49:1620–1627, 2011.

M. Todt, R.D. Bitsche, M.A. Hartmann, F.D. Fischer, and F.G. Rammerstorfer. Growth limit of carbon onions - a continuum mechanical study. *International Journal of Solids Structures*, 51:706–715, 2014a.

M. Todt, F.G. Rammerstorfer, and M.A. Hartmann. Continuum shell models for closed cage carbon nanoparticles. In W. Pietraszkiewicz and J. Górski, editors, *Shell Structures: Theory and Applications*, pages 149–152. Taylor & Francis Group, London, UK, 2014b.

S. Tomita, A. Burian, J.C. Dore, D. LeBolloch, M. Fujii, and S. Hayashi. Diamond nanoparticles to carbon onions transformation: X-ray diffraction studies. *Carbon*, 40:1469–1474, 2002.

K.I. Tserpes. Strength of graphenes containing randomly dispersed vacancies. *Acta Mechanica*, 223:669–678, 2012.

K.I. Tserpes and P. Papanikos. Finite element modeling of single-walled carbon nanotubes. *Composites: Part B*, 36:468–477, 2005.

D. Ugarte. Curling and closure of graphitic networks under electron-beam irradiation. *Nature*, 359:707–709, 1992.

D. Ugarte. Onion-like graphitic particles. *Carbon*, 33:989–993, 1995.

L. Verlet. Computer "Experiments" on Classical Fluids. I. Thermodynamical Properties of Lennard-Jones Molecules. *Physical Review*, 159:98, 1967.

D. Vollath. *Nanomaterials*. Wiley-VCH, Weinheim, 2008.

J.H. Walther, R. Jaffe, T. Halicioglu, and P. Koumoutsakos. Carbon Nanotubes in Water: Structural Characteristics and Energetics. *Journal of Physical Chemistry B*, 105:9980, 2001.

C.Y. Wang, C.Q. Ru, and A. Mioduchowski. Axially compressed buckling of pressured multiwall carbon nanotubes. *International Journal of Solids and Structures*, 40:3893–3911, 2003.

M.C. Wang, C. Yan, L. Ma, N. Hu, and M.W. Chen. Effect of defects on fracture strength of graphene sheets. *Computational Materials Science*, 54:236 – 239, 2012.

Y. Wang, X. Wang, X. Ni, and H. Wu. Simulation of elastic response and the buckling modes of single-walled carbon nanotubes. *Computational Material Science*, 32:141, 2005.

S.J. Weiner, P.A. Kollman, D.A. Case, U.C. Singh, C. Ghio, G. Alagona, S. Profeta, and P. Weiner. A new force field for molecular mechanical simulation of nucleic acids and proteins. *Journal of the American Chemical Society*, 106(3):765, 1984.

D.F. Windenburg and C. Trilling. Collapse by instability of thin cylindrical shells under external pressure. *Transactions of the American Society of Mechanical Engineers*, 56(11):819, 1934.

J. Wu, K.C. Hwang, and Y. Huang. An atomistic-based finite-deformation shell theory for single-wall carbon nanotubes. *Journal of the Mechanics and Physics of Solids*, 56:279–292, 2008a.

J. Wu, J. Peng, K.C. Hwang, J. Song, and Y. Huang. The intrinsic stiffness of single-wall carbon nanotubes. *Mechanics Research Communications*, 35:2–9, 2008b.

Z. Xin, Z. Jianjun, and Q.Y. Zhong-can. Strain energy and Young's modulus of single-wall carbon nanotubes calculated from electronic energy-band theory. *Physical Review B*, 62:13692–13696, 2000.

M. Xu, J.T. Paci, J. Oswald, and T. Belytschko. A constitutive equation for graphene based on density functional theory. *International Journal of Solids and Structures*, 49:2582–2589, 2012a.

M. Xu, A. Tabarraei, J.T. Paci, J. Oswald, and T. Belytschko. A coupled quantum/continuum mechanics study of graphene fracture. *International Journal of Fracture*, 173:163–173, 2012b.

R. Xu, Y. Wang, B. Liu, and D. Fang. Mechanics interpretation on the bending stiffness and wrinkled pattern of graphene. *Journal of Applied Mechanics*, 80:040910–1–5, 2013.

B.I. Yakobson, C.J. Brabec, and J. Bernholc. Nanomechanics of carbon tubes: Instabilities beyond linear response. *Physical Review Letters*, 76: 2511–2514, 1996.

X. Yao, Q. Han, and H. Xin. Bending buckling behaviors of single- and multi-walled carbon nanotubes. *Computationa Material Science*, 43:579–590, 2008.

D.-B. Zhang, E. Akatyeva, and T. Dumitrica. Bending Ultrathin Graphene at the Margins of Continuum Mechanics. *Physical Review Letters*, 106: 255503, 2011.

H.W. Zhang, L. Wang, and J.B. Wang. Computer simulation of buckling behavior of double-walled carbon nanotubes with abnormal interlayer distances. *Computational Material Science*, 39:664, 2007.

Q.L. Zhang, S.C. O'Brien, J.R. Heath, Y. Liu, R.F. Curl, and H.W. Kroto et al. Reactivity of large carbon clusters: Spheroidal carbon shells and their possible relevance to the formation and morphology of soot. *Journal of Physical Chemistry*, 90:525–528, 1986.

T. Zhang, X. Li, and H. Gao. Defects controlled wrinkling and topological design in graphene. *Journal of the Mechanics and Physics of Solids*, 67: 2 – 13, 2014.

M. Zhao, H. Song, X. Chen, and W. Lian. Large-scale synthesis of onion-like carbon nanoparticles by carbonization of phenolic resin. *Acta Materialia*, 55:6144–6150, 2007.

Y.X. Zhao and I.L. Spain. X-ray diffraction data for graphite to 20 GPa. *Physical Review B*, 40:993–997, 1989.

7. Continuum Modelling of Nanotubes: Collapse Under Pressure

David J. Dunstan

School of Physics and Astronomy, Queen Mary University of London, London, United Kingdom

7.1. Introduction

The collapse of tubes under external pressure is a problem that has been studied since the early nineteenth century, because of its importance in, for example, multi-tubed steam boilers. Some early experimental studies (Figure 7.1) and theoretical results are reported by Carman (1905) and Carman and Carr (1906); for a recent discussion see Corradi *et al.* (2011). Experimentally, end-effects tended to dominate even for what seemed like long tubes, while theoretically, this example of Euler buckling was recognized to be one of the hardest problems in elasticity theory. Indeed, exact solutions have been found only recently.

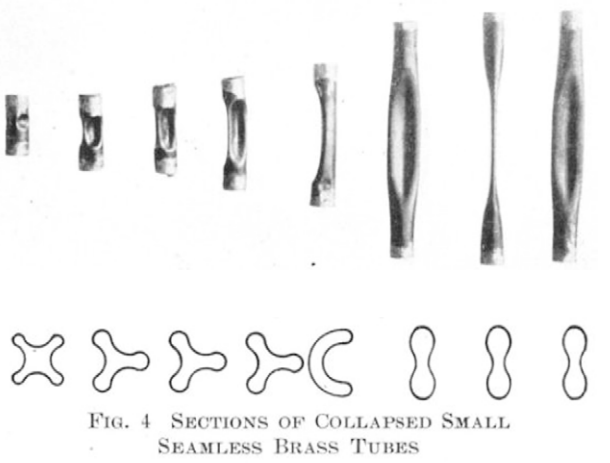

FIG. 4 SECTIONS OF COLLAPSED SMALL SEAMLESS BRASS TUBES

Figure 7.1. Taken from Figures 3 and 4 of Carman and Carr (1906) showing seamless drawn brass tubes after collapse induced by external pressure. It was recognized that the multi-lobed cross-sections were the result of end effects. Courtesy of www.ideals.illinois.edu /handle/2142/4114

O. Paris (Ed.), *Structure and Multiscale Mechanics of Carbon Nanomaterials*,
CISM International Centre for Mechanical Sciences
DOI 10.1007/ 978-3-7091-1887-0_7 © CISM Udine 2016

Continuum models include, at the extreme of simplification, the perfectly elastic ring defined solely by a bending modulus D and by the area A contained within it, under a pressure P. The criterion for the pressure of the onset of collapse, P_C, is then that the increase in the elastic bending energy $\frac{1}{2}D\,R^{-2}$ integrated round the ring just equals the decrease in the energy term PA, as the ring undergoes an infinitesimal ovalisation. This model is appropriate for thin-walled tubes; and may be made more complicated by taking the wall thickness into account. Such idealized continuum models may also be refined slightly by varying the distribution of bending compliance around the ring. On the other hand, atomistic models may be taken to the other extreme of direct density functional *ab-initio* theory to simulate carbon nanotubes, or molecular dynamics or Monte Carlo methods based on realistic interatomic potentials derived from DFT or from fitting to experiment (see chapter 6). Much may be learned from a comparison of the results of these very different approaches.

7.2. The Continuum Models

7.2.1. The Simple Elastic Ring

Zang *et al.* (2004) give the exact solution for the critical pressure for the onset of collapse of an elastic ring of radius R and bending modulus D,

$$P_C = 3DR^{-3} \tag{7.1}$$

and attribute the formula to Levy (1884). For the shape of the ring during collapse, as the pressure is increased, they use molecular dynamics simulations of armchair and zig-zag tubes. They find that the shapes are independent of the diameter and chirality. A mathematical analysis finishing with numerical solutions confirms that these shapes are just as predicted by the simple elastic ring model.

An analytic solution for the shapes of the ring as the pressure is increased above P_C has been given (Djondorov *et al.* 2011), and the shapes in Figure 7.2 are calculated using the resources (*Mathematica*® notebooks) available through their paper. It should be noted that, unlike typical Euler buckling in elastic-plastic engineering problems, there is no catastrophic collapse. At P_C there is a bifurcation (of major and minor axes) with infinite rate of change for infinitesimal deformation, but finite increases in pressure are required for finite deviations from circularity. The other key result relevant to nanotubes is that, while the collapse is very fast at first – the transition from entirely positive curvature to positive and negative curvature (the "peanut" shape) occurs at $P = 1.11\,P_C$, while completion of collapse (the two walls touching) requires a much higher pressure of $P = 1.55\,P_C$. For finite thickness walls, of course, touching will occur earlier.

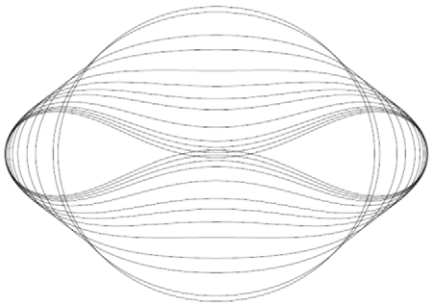

Figure 7.2. The shapes taken by the simple elastic ring, as the pressure is increased through P_C and up to about 1.6 P_C. For a real ring, after touching, a straight portion is formed at the centre.

7.2.2. The Thick-Walled Elastic Tube

This problem is of greater engineering importance than the simple elastic ring, but most of the difficulties arise only when plasticity is considered. For purely elastic deformation, the solution for a tube of outside diameter d and wall thickness h (Timoshenko and Gere, 1961; Corradi *et al.*, 2011) is similar to Eq.7.1,

$$P_C = \frac{2Yh^3}{(1-\nu^2)} \frac{1}{d(d-h)^2} \tag{7.2}$$

and may be recognized to have Eq.7.1 as its limit as h/d goes to zero and the usual expression for the bending stiffness D of an isotropic plate is considered. As h approaches R the critical pressure diverges to infinity as expected, and if h is taken to be 0.34 nm then the critical pressures of small nanotubes would be very high. However, the relevance of Eq.7.2 to the carbon nanotube may be questioned.

Graphite is not an isotropic material, and graphene should not be seen as a "plate" of isotropic graphite. Single-crystal graphite is highly anisotropic, with an in-plane Young's modulus of about 1 TPa due to the sp^2 hybridised σ-bonds, but a c-axis modulus (c_{33}) of only 33 GPa due to the π-orbitals. It is quite incorrect to relate the bending stiffness D of graphene in any way to its in-plane σ-bonds. Some authors describe the bending stiffness of graphene in terms of an effective Young's modulus Y_{eff} and an effective thickness h_{eff} such that the stiffness term of Eq.7.2 with these values – typically, 5TPa and 0.06 nm, but values vary widely (Huang *et al.* 2006) – becomes the experimentally or theoretically determined D of graphene. However, the point of expressing an uncertain but physical parameter D in terms of two non-physical and very uncertain parameters Y_{eff} and h_{eff} is not clear to the present

author. Certainly, neither h_{eff} nor the actual spacing of graphene planes in graphite, 0.34 nm, are suitable values for use in Eq.7.2.

In molecular dynamics and Monte Carlo simulations using interatomic bond potentials, the fact that two-atom and three-atom potentials cannot give any bending stiffness to a two-dimension lattice such as graphene is resolved by using suitable four-atom potentials to give the bending stiffness. These may be pyramidal or dihedral (torsional) – see Zhang *et al.* (2006) – but they still do not imply a thickness h appropriate for use in Eq.7.2.

Fundamentally, Eq.7.2 is inapplicable to nanotubes because the effect of h is to change the area that enters into the PA energy term. Consider, for example, the limit as h goes to d. The tube becomes solid, the area A goes to zero, and the collapse pressure goes to infinity. See Section 7.2.4 below for further discussion.

7.2.3 The Atomistic Refinement of the Elastic Ring

Considering the sp^2 bonds between the carbon atoms as straight links and the atoms themselves as hinges, the elastic ring is slightly modified – discretised – by moving the continuously-distributed compliance to the vertices of an inscribed polygon. Treating the vertices as hinges with Hooke's Law angular springs and the polygon sides as rigid, the angles and energies may be calculated explicitly as the pressure is increased (Fig.7.3). This was done by Sun *et al.* (2013). For larger tubes, polygons of the order of the dodecagon and larger, excellent agreement was found for the collapse pressure both with Eq.7.1 and with Monte Carlo simulations using DFT-derived interatomic potentials (see chapter 6). For the smaller polygons, P_C fell systematically below the values from Eq.7.1, as did the Monte Carlo simulations. The advantage of this kind of simulation is that the behaviour may be – indeed can only be – understood in terms as simple as the model itself.

The reason for the small polygons showing a smaller critical pressure is just that the discretisation moves the compliance from the four places of the circle that have little or no change in curvature at the onset of collapse, towards the four places that have maximum change in curvature. In the simplest example, the square, with four hinges, compliance has been moved from the parts of the circle corresponding to the centres of the sides of the square, towards the four corners of the square. Putting the compliance where the bending is greatest reduces the elastic energy of bending, and so decreases the collapse pressure. In the case of the square, this reduction is about a factor of two.

This model also makes it explicit that Eq.7.1 should apply (to large polygons or continuous circles) rather than seeking a thickness appropriate for use in Eq.7.2. The area change under deformation is entirely that of the polygon defined by the atomic centres. The compliance of the σ-bonds is irrelevant. It is so high that the area change due to compression of the C—C bonds as the system goes through the transition from

circular to oval is completely insignificant. In contrast, in the thick-walled model discussed above, the tangential compliance of the material is intimately linked with its bending compliance, and the neutral plane moves inwards and outwards with changes of curvature, bringing h into Eq.7.2.

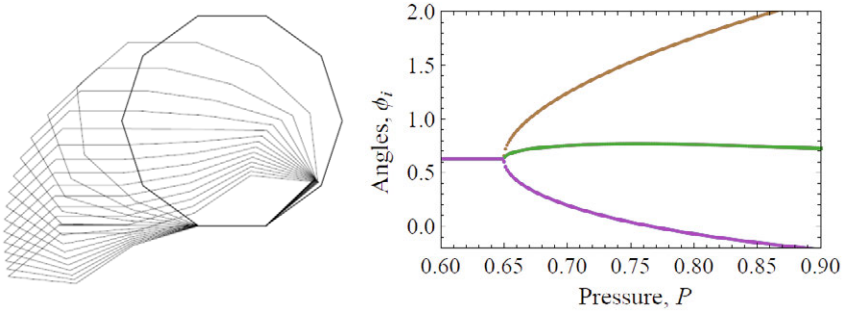

Figure 7.3. The shapes adopted by a decagon as the pressure is increased are shown in (a). The angles are plotted against pressure in (b).

In this model, what lies outside (and inside) the polygon defined by the atom centres and the sp^2 σ-bonds is the p electrons and π-bonds. This is what gives the 0.34 nm thickness – spacing – of graphene in graphite. The mechanical properties of this layer have not been studied except as they are known from the values of c_{33} and c_{13} of graphite. These stiffnesses are so low compared with the in-plane stiffnesses that we may consider what lies outside to do no more than provide the bending stiffness and transmit the pressure to the σ-bonded polygon. Accordingly, in what follows, we shall assume that the nanotube collapse is correctly described by Eq.7.1 except for the polygonal effects at small diameters.

7.2.4 Continuum Structural Model

The foregoing discussion leads to the proposal of a continuum *structure* rather than a continuum *material* model for graphene and the nanotube (Puech and Dunstan, 2015). We contrast the isotropic plate model of Figure 7.4a with the structural model of Figure 7.4b, in which a very thin central layer (the atomic centres and the σ-bonds) has a large in-plane stiffness but no bending stiffness, while a soft surrounding material (the π-bonds), with isotropic elastic moduli similar to the c_{33} of graphite and a thickness of 0.34 nm, is what provides the bending stiffness. Remarkably, taking the value of c_{11} of this material to be equal to c_{33} of graphite, 39 GPa, and making other reasonable assumptions, gives a bending stiffness of about 1 eV, within a factor

of two or three of any reasonable values coming from theory or experiment (see Section 7.3.1).

Figure 7.4. The isotropic solid model of graphene (a) contrasts with a structural model (b) in which all the in-plane stiffness comes from the thin central layer (black) and all the bending stiffness comes from the surrounding (grey) material.

This structural model of graphene makes various predictions about nanotubes which are largely borne out by, or at least consistent with, the theoretical and experimental knowledge that we do have (Puech and Dunstan, 2015). Relevant here is that this model is explicitly in accord with the discussion of Section 7.2.2 on the relevant radius. In this model, the area that changes upon ovalisation is the area described by the thin central layer. To first order, the area of the grey layer outside does not change. Whatever the Poisson's ratio of this material, the changes in thickness due to compression and tension around the ring cancel out.

7.3. Comparison with Experiment and Simulation

7.3.1. Simulation using Molecular Dynamics and *Ab Initio*

Many simulations have been reported, which show the expected behaviour. The main issue is the choice of or the value of the bending modulus D in the simulations. Lucas *et al*. (1993) give a value of $D \sim 4.2$ eV from tight-binding calculations. In molecular dynamics, the two-atom and three-atom potentials are well-characterised from work on graphite, but these potentials alone give a bending stiffness of zero. Zhang *et al.* (2011) describe the pyramidal or dihedral four-atom potentials required to get a non-zero D. The classic Tersoff-Brenner potentials include four-atom terms which give D ~ 2 eV. But Huang *et al.* (2006) tabulate values used in or from a variety of theoretical methods, ranging from 0.124 eV to 4.1 eV, and Kang and Lee (2013) cite values over a still larger range.

A particularly interesting way to obtain D was reported by Sen et al. (2010). The tearing of a thin film from a substrate normally produces a tear that tapers down, as commonly observed with Scotch tape or while stripping wallpaper. The included angle of the tear derives from the bending stiffness of the film, and Sen *et al*. deduced $D = 2.3$ eV. They gave values for bilayers (130 eV) and thicker; these values derive

directly from the in-plane elastic constants of graphite when the graphene sheets do not slide over each other; if they do slide freely, of course, an *n*-layer just has the bending stiffness of *nD*.

Ab initio DFT calculations of the collapse of tubes are limited because of the number of atoms required for a unit cell of a tube, particularly of larger diameter tubes. As mentioned above, DFT of graphite or graphene is used to obtain potentials for use in molecular dynamics or in Monte Carlo methods (see, e.g., Holec *et al.*, 2010 and Sun *et al.*, 2014, for collapse calculated with Monte Carlo methods from potentials from DFT). A value for *D* can be deduced from the mechanical behaviour; Hartmann *et al.* (2013) gave $D = 2.94$ eV. Alternatively, methods such as DFT- tight-binding can be used (see, e.g. Cerqueiro *et al.*, 2014), but here the value of *D* cannot be extracted from the calculation but only be deduced from the collapse pressures observed. Authors do not generally do this.

7.3.2. Experiment

Recognition of collapse in experiment has not been easy. As discussed in chapter 5, it is expected that hollow tubes are under greater stress than the external applied pressure, so that pressure coefficients of, for example, the vibrational frequencies (Raman shifts) will be greater than in graphite. After collapse, the nanotube is not unlike bilayer graphite, and a nanotube bundle not unlike multilayer graphite, and so the pressure dependence of a Raman shift is expected to fall back to the graphite line (Figure 5.4). For many years, that was not observed. Venkateswaran *et al.* (2003) and many other authors observed a breakpoints with reductions in gradient, often to values close to the graphite value, as discussed in chapter 5. Most often, this breakpoint in the gradient coincides with a large or total loss of Raman signal intensity. The breakpoint is then readily identified with the collapse. However, no consensus was reached about the collapse pressure for any given diameter of nanotube. Different authors observed breakpoints at pressures as much as an order of magnitude apart. The variety of breakpoints and plateaux which could be observed (see chapter 5) prevented any certainty on the collapse pressure – diameter relationship.

Recently, the situation has greatly improved. Yao *et al.* (2008) reported a plateau that extended to the graphite line (see Figure 5.8) and then continued in approximate agreement with it. Caillier *et al.* (2008), and later Aguiar *et al.* (2011), in a few datasets, report behaviour very like the expected behaviour of Figure 5.4 with a clear drop to the graphite line. Figure 7.5 reproduces the key result from Aguiar *et al.* (2011).

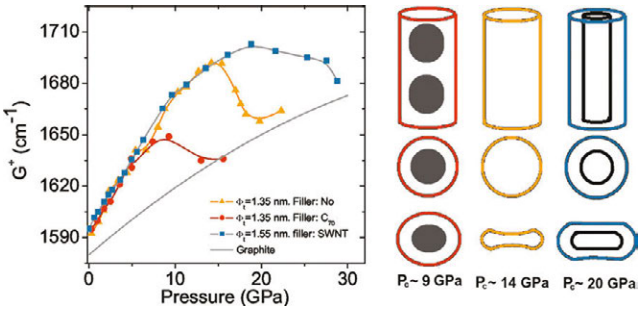

Figure 7.5. The shifts of the G-band with pressure are plotted against pressure for SWCNTs and for similar nanotubes filled with C_{60} or with internal tubes (constituting DWCNTs). At collapse, the shift falls back to the graphite line. Reprinted with permission from Aguiar *et al.*, J. Phys. Chem. C**115**, 5378–5384, 2011. Copyright 2011 American Chemical Society.

It is not entirely clear why these results are closer to what is expected from theory than earlier work. High-purity samples and a narrow range of diameters selected by resonance with the 514.5 nm laser excitation and observed in the RBM spectra are probably key points. Several puzzles remain; in particular a dependence of the collapse pressure on the pressure-transmitting medium. Also, while stabilization was obtained in DWCNTs as expected, the presence of buckyballs inside reduced the collapse pressure – which is not expected.

7.4. Conclusions

The collapse of carbon nanotubes presents few subtleties theoretically. The continuum mechanics of simple elastic rings provides a good description, as expected, with atomistic effects for only the smallest tubes. Experimentally, major complications arise through bundling, through the pressure medium, and through filling. However, there is now the prospect that a systematic study, of individualized tubes of known chirality, well-distinguished by their RBM spectra, will clarify these complications.

References

Aguiar, A.L., Barros, E.B., Capaz, R.B., Souza Filho, A.G., Freire, P.T.C., Mendes Filho, J., Machon, D., Caillier, C., Kim, Y.A., Muramatsu, H., Endo, M., and San-Miguel A. (2011). Pressure-induced collapse in double-walled carbon nanotubes: Chemical and mechanical screening effects. *J. Phys. Chem. C* 115:5378–5384.

Caillier, C., Machon, D., San-Miguel, A., Arenal, R., Montagnac, G., Cardon, H., Kalbac, M., Zukalova, M., and Kavan, L. (2008). Probing high-pressure properties of single-wall carbon nanotubes through fullerene encapsulation. *Phys. Rev. B* 77, 125418.

Carman, A.P. (1905). Resistance of Tubes to Collapse, *Physical Review* 21:381–387.

Carman, A.P., and Carr, M.L. (1906). Resistance of Tubes to Collapse. *University of Illinois Bulletin* vol. III no. 17 – Bulletin No.5 of the University of Illinois Engineering Experiment Station. Urbana, IL: University of Illinois.

Cerqueira, T.F.T., Botti, S., San-Miguel, A., and Marques, M.A.L. (2014). Density-functional tight-binding study of the collapse of carbon nanotubes under hydrostatic pressure. *Carbon* 69:355–360.

Corradi, L., Cammi, A., and Luzzi, L. (2011). Collapse behaviour of moderately thick tubes pressurised from outside. In Tsvetkov, P., ed., *Nuclear Power - Control, Reliability and Human Factors*. USA: InTech. 260.

Djondjorov, P.A., Vassilev, V.M., and Mladenov, I.M. (2011). Analytic description and explicit parametrisation of the equilibrium shapes of elastic rings and tubes under uniform hydrostatic pressure. *Int. J. Mech. Sci.* 53:355–384.

Hartmann, M.A., Todt, M., Rammerstorfer, F.G., Fischer, F.D., and Paris, O. (2013). Elastic properties of graphene obtained by computational mechanical tests. *Euro. Phys. Lett.* 103:68004.

Holec, D., Hartmann, M.A., Fischer, F.D., Rammerstorfer, F.G., Mayrhofer, P.H., and Paris, O. (2010). Curvature-induced excess surface energy of fullerenes: Density functional theory and Monte Carlo simulations. *Phys. Rev. B* 81:235403.

Huang, Y., Wu, J., and Hwang, K.C. (2006). Thickness of graphene and single-wall nanotubes. *Phys. Rev. B* 74:245413.

Kang, J.W., and Lee, S. (2013). Molecular dynamics study on the bending rigidity of graphene nanoribbons. *Comp. Mater. Sci.* 74:107–113.

Levy, M. (1884). Memoire sur un nouveau cas intégrable du problème de l'élastique et l'une de ses applications," *J. Math. Pur Appl.*, Ser. 3, 7.

Lucas, A.A., Lambin, P.H., and Smalley, R.E. (1993). On the energetics of tubular fullerenes. *J. Phys. Chem. Sol.* 54:587–593.

Puech, P., and Dunstan, D.J. (2015), Thickness of graphene and single-wall carbon nanotubes: high pressure effects. *To be published*, 2015.

Sen, D., Novoselov, K.S., Reis, P.M., and Buehler, M.J. (2010). Tearing graphene sheets from adhesive substrates produces tapered nanoribbons. *Small* 6:1108–1116.

Sun, Y.W., Dunstan, D.J., Hartmann, M.A., and Holec, D. (2013) Nanomechanics of carbon nanotubes. *Proc. Appl. Math. Mech.* 13:7–10.

Timoshenko, S.P., and Gere, J.M. (1961). *Theory of Elastic Stability*. New York: McGraw-Hill 2nd edition.

Venkateswaran, U. D., Masica, D. L., Sumanasekera, G. U. Furtado, C. A., Kim, U. J., and Eklund, P. C. (2003). Diameter dependent wall deformations during the compression of a carbon nanotube bundle. *Phys. Rev. B* 68:241406, 2003.

Yao, M., Wang, Z., Liu, B., Zou, Y., Yu, S., Lin, W., Hou, Y., Pan, S., Jin, M., Zou, B., Cui, T., Zou, G., and Sundqvist, B. (2008). Raman signature to identify the structural

transition of single-wall carbon nanotubes under high pressure. *Phys. Rev. B* 78:205411.

Zang, J., Treibergs, A., Han, Y., and Liu, F. (2004). Geometric constant defining shape transitions of carbon nanotubes under pressure. *Phys. Rev. Lett.* 92:105501.

Zhang, D.B., Akatyeva, E., and Dumitrica, T. (2011). Bending ultrathin graphene at the margins of continuum mechanics. *Phys. Rev. Lett.* 106:255503.

8 Collective Behaviour of Vertically Aligned Carbon Nanotubes: from a Single Tube towards Complex Networks

Siddhartha Pathak

Center for Integrated Nanotechnologies, Los Alamos National Laboratory, Los Alamos, NM 87545, USA

8.1. Definition

In this chapter we discuss the mechanical behaviour of vertically aligned carbon nanotubes (VACNTs) also known as carbon nanotube (CNT) arrays, bundles, brushes, foams, forests, mats, and turfs. VACNTs are complex, hierarchical structures of intertwined tubes arrayed in a nominally vertical alignment due to their perpendicular growth from a stiff substrate. They are a unique class of materials having many of the desirable thermal, electrical, and mechanical properties of individual carbon nanotubes, while exhibiting these properties through the collective interaction of thousands of tubes on a macroscopic scale.

8.2. Introduction

While individual CNTs have been announced as the strongest material known (Treacy et al. 1996) and have shown extremely high strength and Young's modulus in tensile tests on individual tubes (Treacy et al. 1996, Min-Feng et al. 2000), VACNTs are more likely to find use in applications requiring large compliance and deformability (Cao et al. 2005, Gogotsi 2006). Examples of these include microelectromechanical systems (MEMS) and impact mitigation/energy absorption, where they are promising candidates for their multifunctional nature, wide ranging thermal stability, well-defined large surface area, and relative ease of manufacture (Cao et al. 2005). A proper understanding of the collective mechanical behaviour of these structures, especially instabilities leading to buckling and inhomogeneity's which weaken mechanical performance, is thus of great importance for their design and success in these and other future applications.

VACNTs are distinct from other CNT structures (Salvetat et al. 2006) in that the tubes that make up the material grow perpendicularly to the support substrate, making them *nominally* vertically aligned. An important characteristic all VACNTs share is that the tubes themselves are long enough to become intertwined with each other during the growth process, leading to a highly complex and hierarchical

O. Paris (Ed.), *Structure and Multiscale Mechanics of Carbon Nanomaterials*,
CISM International Centre for Mechanical Sciences
DOI 10.1007/ 978-3-7091-1887-0_8

microstructure with distinct organizational details at different magnification levels. This is in contrast to arrays of vertically aligned CNTs that are short and/or sparse enough that each CNT stands alone (Waters et al. 2004, Waters et al. 2005). Figure 8.1 show the complex hierarchical nature of the VACNT microstructure with their

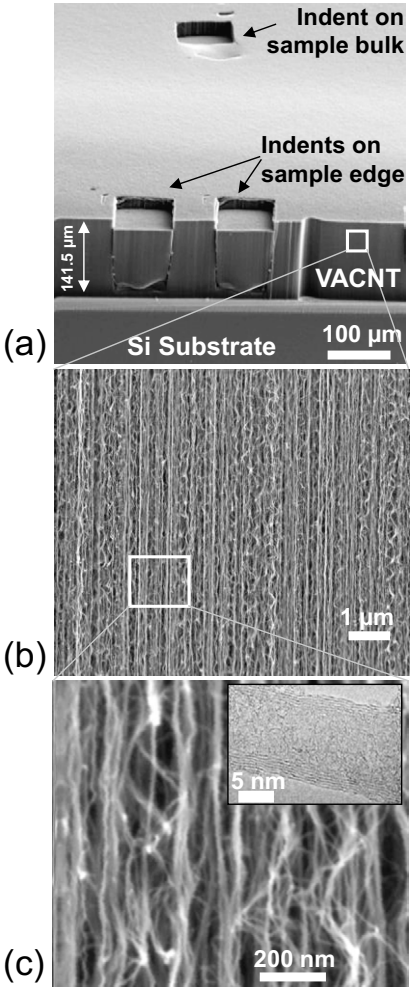

Figure 8.1. SEM images reveal the hierarchical morphology of the **(a)** 141.5 µm thick VACNT films (magnification 260X), which consist of **(b)** nominally vertical aligned CNTs visible at a lower magnification of 30kX, and **(c)** a complex intertwined network seen at higher magnifications of 240kX. SEM pictures are taken at a 60 deg tilt angle. (c inset) Individual multiwalled CNTs of outer diameter 8.8±2.1 nm (average ± standard deviation) are visible in the TEM image. (Pathak et al. 2013) reproduced with permission.

distinct organizational details across multiple length scales. Thus, while the VACNT appears as a continuous film at lower magnifications of 260X (Fig. 8.1a), the nominally vertical alignment of CNTs growing perpendicularly to the support substrate in the VACNT bundle becomes visible at a higher magnification of 30,000X (Fig. 8.1b). Increased magnification of 240,000X reveals significant intertwining in the long, curved lengths of individual CNTs, revealing the isotropic CNT network (Deshpande et al. 2000, Hutchens et al. 2010, Hutchens et al. 2011). As a result, in their as-grown states certain segments of the CNT forest appear to be pre-buckled/pre-bent, and the favourable contact energy between the tubes (van der Waals) is thought to balance the bending strain energy of their arrangement, resulting in a stable low energy configuration (Mesarovic et al. 2007). At still higher magnifications (nanometre length scales, see TEM image in Fig. 8.1c inset) – individual, discrete CNTs dominate the mechanical performance with details like CNT diameter, number of walls *etc*. governing their deformation. Such hierarchy in the VACNT microstructure governs its overall mechanical behaviour, which is a result of not only the properties of individual CNTs, but also of their complex mutual interactions and distribution throughout the array.

The method by which these structures are synthesized is the primary factor affecting their complex, hierarchical morphology. This microstructure, in turn, affects their mechanical behaviour, in particular the modulus, buckling strength, and recoverability. Synthesis techniques for VACNTs can be divided into two main categories: the Chemical Vapour Deposition (CVD) synthesis method, and the Carbide-Derived Carbon (CDC) synthesis method – which relate to the top-down vs. bottom-up growth processes respectively. In the CVD process, the VACNT film is coated onto an existing substrate. This is accomplished by depositing a thin layer of catalyst (e.g., Fe) on the substrate (typically Si or Quartz) and flowing a carbon source (e.g., ethylene) over the substrate at atmospheric pressure and temperatures typically around 750ºC. In the CDC method (Presser et al. 2011), on the other hand, carbon is formed by selective extraction of the metal or metalloid atoms in the carbide (e.g., silicon carbide) at high temperatures (>1600ºC), transforming the carbide structure into pure carbon. Since the CNT layer is formed by inward growth, this usually retains the original shape and volume of the precursor.

VACNTs grown by these different techniques demonstrate very different structure and mechanical properties. Even within materials grown via CVD, control of the growth conditions, such as the atmosphere, catalyst activity, and pressure, are known to significantly affect the repeatability of the VACNT's morphology and hence the consistency of mechanical properties (McCarter et al. 2006). For example, using 'floating' *vs.* 'fixed' catalysts Yaglioglu et al. (2012) in the CVD syntheses (Kumar et al. 2010) have been shown to result in vastly different VACNT morphologies. Differences in the growth processes used are revealed in the widely varying VACNT information reported in literature, as seen in the large range in

properties in Table 8.1. This is not to mention variations in tube diameter (from 2-3 nm (Pathak et al. 2009), to 20-50 nm (Hutchens et al. 2010), to greater than 100 nm (Qi et al. 2003)), number of walls in the CNT structure, and degree of tube alignment; properties which are sometimes neither measured nor reported. Further, the different stages of the CNT growth process can result in a height dependent inhomogeneity (Bedewy et al. 2009). This manifests as a gradient in both the density and the alignment of the tubes within the same VACNT structure. As discussed later in this entry, such a structure gradient may lead to a corresponding strength and stiffness gradient along the VACNT height. As an extreme example of the microstructure-property relationship, CDC-VACNTs are known to have a considerably higher average density (roughly 10 times higher than typical VACNTs), due to the conformal transformation of the carbide into carbon. This in turn leads to significantly larger values for the elastic modulus and yield stress in CDC-VACNTs (Pathak et al. 2009) (see Table 8.1). These promising characteristics, however, are unavailable for applications requiring macroscopic films as currently only VACNTs grown via CVD can reach macroscopic heights (~mm). Growth of CDC-VACNTs remains limited to only a few micrometres in height. Only CVD-VACNTs when used in combination with conformal coating methods, where the CNTs are coated with nanoscale coatings of ceramics like Al_2O_3 (Brieland-Shoultz et al. 2014), amorphous SiC (Poelma et al. 2014), etc. (Table 8.1) are able to reach a similar level of mechanical performances as compared to the CDC-VACNTs.

Table 8.1: Summary of Reported VACNT Elastic Modulus and Yield Strength Values. White rows denote values for CVD synthesized VACNTs, while grey rows are for CDC-VACNTs.

VACNT details (Density, porosity etc.)	Measurement Method	Modulus	Yield/ Buckling Strength	Reference
CVD-VACNTs				
87% porosity	compression	50 MPa	12 MPa	(Cao et al. 2005)
/	compression	< 2 MPa	/	(Suhr et al. 2007)
10^{10} tubes/cm^2 [a]	compression	0.22-0.25 MPa	/	(Tong et al. 2008)
97% porosity	compression	818 MPa	14.1 MPa	(Deck et al. 2007)
0.08 g/cm^3	compression	177±11 MPa	2.69±0.12 MPa	(Pathak et al. 2012)
/	compression	9-31 MPa	0.15 – 0.3 MPa	(Pathak et al. 2013)

Table 8.1 continued on next page

Table 8.1 continued from previous page

0.008 g/cm^3 (fixed catalyst, argon anneal) 0.015 g/cm^3 (fixed catalyst, hydrogen anneal) 0.2 g/cm^3 (floating catalyst)	compression	1.86 MPa (range 1.3-3.26) 7.44 MPa (range 5.2-13.04) 138.5 MPa	0.021 MPa 0.117 MPa 9.997 MPa	(Yaglioglu et al. 2012)
0.018 g/cm^3 0.114 g/cm^3 (After post-growth CVD treatment)	compression	/	0.12 MPa 5.5 MPa (After post-growth CVD treatment)	(Bradford et al. 2011)
0.12 g/cm^3	compression	0.55 MPa (parallel to the nanotube axis) 1.09 MPa (normal to CNT axis)	/	(Ci et al. 2008)
3×10^{10} / cm^2 (number density) 1 g/cm^3 (after Al_2O_3 coating)	compression	14 MPa 20 GPa (after Al_2O_3 coating)	compressive strength (0.8 MPa to 0.16 GPa)	(Brieland-Shoultz et al. 2014)
10^{10} / cm^2 (number density)	compression	200 MPa 125 GPa (after amorphous SiC coating)	compressive strength <1 MPa (uncoated VACNTs) 1.8 GPa (after amorphous SiC coating)	(Poelma et al. 2014)
/	nanoindentation – Berkovich uniaxial compression	15 MPa	0.2-4.3 MPa	(Zbib et al. 2008)

Table 8.1 continued on next page

Table 8.1 continued from previous page

0.08 g/cm^3	Flat punch indentation	120-175 MPa	1.49-1.75 MPa	(Pathak et al. 2013)
0.13 gm/cm^3 0.06 gm/cm^3	Flat punch indentation	7-33 MPa 100-350 MPa	0.44±0.04 MPa 0.9 MPa	(Pathak et al. 2013)
/	nanoindentation – Berkovich	58 MPa	/	(Zhang et al. 2010)
/	nanoindentation - Berkovich	50±25 MPa	/	(Qiu et al. 2011)
/	DMA(Dynamic Mechanical Analysis)	~ 50 MPa	/	(Mesarovic et al. 2007)
0.009 g/cm^3	DMA	~ 1 MPa	/	(Xu et al. 2010)
CDC-VACNTs				
0.95 g/cm^3	compression	30 GPa	800 MPa	(Pathak et al. 2015)
0.95 g/cm^3	nanoindentation – Spherical	18-20 GPa	90-590 MPa	(Pathak et al. 2009)

Figure 8.2 highlights four literature examples of the differences in the mechanical response of various CVD-VACNT micro-pillars subjected to compression. Note in particular the higher stiffness and strength of the VACNTs grown using the floating catalyst technique in Fig 8.2a, (Cao et al. 2005) as compared to the ones grown using the fixed catalyst method (Figs. 8.2b, (Yaglioglu et al. 2012) 8.2c (Pathak et al. 2012) and 8.2d (Hutchens et al. 2010)). Other differences between these nominally identical VACNT samples are the ability of some of them to recover almost completely after large compressions (Figs. 8.2a and c) (Cao et al. 2005, Pathak et al. 2012) while others deform permanently even at modest strains (Figs. 8.2b and d) (Yaglioglu 2007, Zbib et al. 2008, Hutchens et al. 2010, Zhang et al. 2010, Cao et al. 2011).

Figure 8.2 also demonstrates the similarities in the deformation characteristics of the various VACNT systems. All of the four VACNT systems show 3 distinct regimes in their stress-strain response – elastic, plateau and densification – similar to open-cell foams. Unlike foams however, the plateau region in the VACNTs generally has a positive slope, which can vary significantly between VACNT samples. The slopes of the plateau region were calculated to be 11, 5 and 0.6 MPa for Figs. 8.2a, c, and d, respectively. Note also that all VACNT systems shown in Fig. 8.2

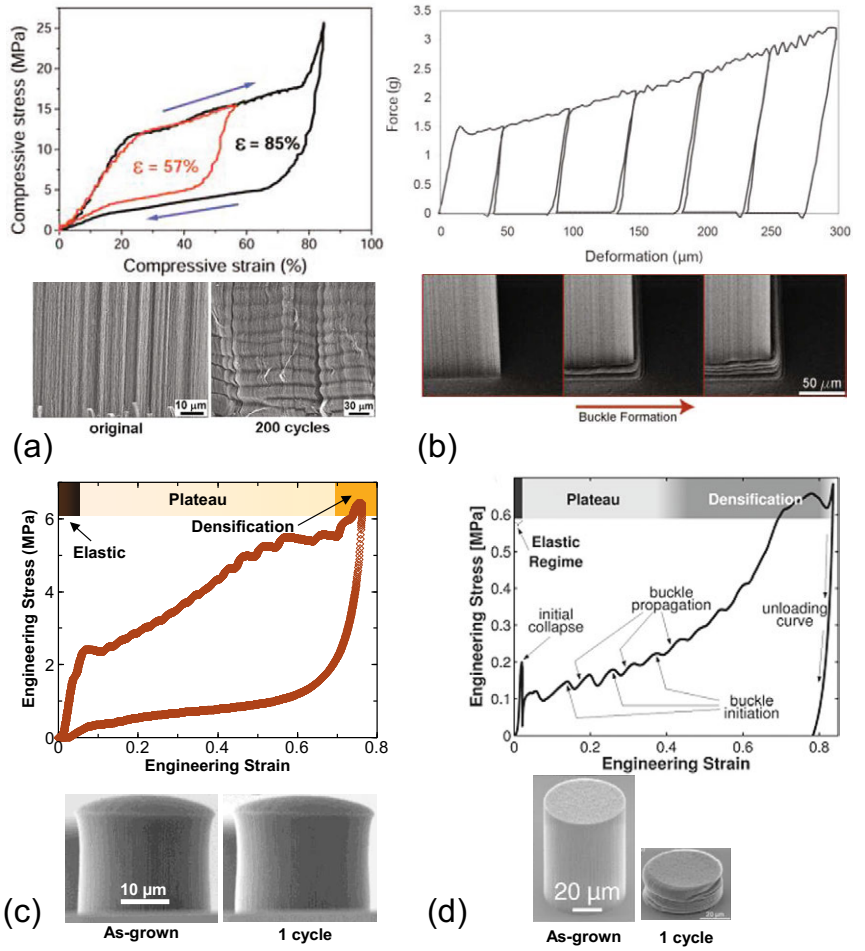

Figure 8.2. VACNT behaviour under compression for **(a)** 860 μm thick VACNT array, (reprinted from (Cao et al. 2005) with permission from AAAS), **(b)** 400 μm diameter CNT column (Yaglioglu et al. 2012) (Copyright Wiley-VCH Verlag GmbH & Co. KGaA. Reproduced with permission) **(c)** 30 μm × 30 μm (diameter × height) VACNT micro-pillar (Adapted with permission from (Pathak et al. 2012) Copyright 2012 American Chemical Society) and **(d)** 50 μm × 60 μm (diameter × height) VACNT micro-pillar (Hutchens et al. 2010) (Copyright Wiley-VCH Verlag GmbH & Co. KGaA. Reproduced with permission). All of these VACNT systems show 3 distinct regimes in their stress-strain response – elastic, plateau and densification – similar to open-cell foams. Unlike foams, the plateau region in the VACNTs generally has a strong positive slope. All VACNT systems shown here also exhibit a bottom-first sequence of buckling.

These VACNT systems differ widely in their ability to recover from large deformations. Thus while both VACNT systems in (a) and (c) show an almost complete recovery, even after multiple cycles, the VACNT systems in (b) and (d) do not exhibit any appreciable recovery.

exhibit a bottom-to-top sequence of buckling. Here the first buckle generally nucleates close to the substrate, and each subsequent lateral collapse event initiates only after the preceding one was completed, thus sequentially collapsing the entire structure. (Cao et al. 2005, Hutchens et al. 2010, Pathak et al. 2012, Yaglioglu et al. 2012) A recent report by Pathak et al. (2013) has suggested that such sequential bottom-to-top buckling and hardening in stress-strain response are observed in samples with smaller relative density at the bottom. When the density gradient was insubstantial or reversed, a different buckling sequence was observed where the bottom regions were always found to buckle last, and a flat stress plateau was obtained.

8.3. Experimental Techniques for Studying VACNT Mechanics

Instrumented indentation, using a variety of tip geometries such as flat punch, spherical, Berkovich, and cube corner, has been the most common method for studying mechanical properties of VACNTs (Qi et al. 2003). Each geometry has its own strengths and weaknesses. While maintaining parallel contact between the indenter and the sample is a major concern for flat punch indentation, it does allow for more uniaxial-like, compressive loading. The sharper Berkovich or cube corner geometries can cause the CNTs to bend away from the indenter, testing a slightly different mode of behaviour (Qi et al. 2003, Waters et al. 2004, Waters et al. 2005). In both cases, modulus and hardness are measured from the unloading portion of the test. On the other hand, spherical indentation is advantageous in that it allows indentation stress-strain curves to be extracted from the raw load-displacement data, which enables resolution of the evolution of the mechanical response in the VACNT array: from initial elasticity, to the initiation of buckling, to post-buckling behaviour at finite strains (Pathak et al. 2009). Though indentation is a relatively simple test to perform, analyses of the results, especially non-linear elastic behaviour is difficult due to their highly localized stress fields. It is also limited in total strain.

Another testing geometry, that of uniaxial compression, eliminates these localized, applied stress fields and help reveal the existence of a localized deformation mechanism in VACNTs. In these tests, the samples are either large (~1 mm tall) bulk films and compressed between two platens (Cao et al. 2005) or microscale (up to tens of microns in height) cylinders and compressed using a flat punch indenter (Hutchens et al. 2010, Yaglioglu et al. 2012).

Both indentation and compression tests can be performed *in situ*, where the load-displacement data is gathered simultaneously with micrographs in an optical or electron microscope (SEM). These tests can offer valuable insights on the morphological evolution in the VACNTs during deformation and are discussed in detail in the next sections.

8.4. Compression Response under Large Strain

The deformation of VACNTs is governed by their hierarchical microstructure, collective inter-tube interactions, and inherent property gradient. Taken as a whole, their highly porous nature gives them an overall foam-like response. The idealized stress-strain response of traditional foams under compression is characterized by three distinct loading regimes: an initial elastic loading at low strain, followed by a plateau in the stress during which the struts bend and buckle, and finally a densification regime in which the space between struts has been nearly eliminated and the material begins to approach behaviour intrinsic to the struts themselves. For such a response, it is the intermediate plateau regime that is responsible for the bulk of energy absorption in the material, since the area under this region of the stress-strain curve, corresponding to the work done on the material, is largest. This foam-like response of a bulk VACNT film is apparent in the three distinctly differently sloped regions of the stress-strain responses shown in Fig 8.2. Locally, however, the response of VACNTs is quite unlike that of traditional foams. In VACNTs, the accommodation of strain during uniaxial compression is accomplished entirely through the formation of folds or buckles of small regions of the structure while the remaining portion remains nearly undeformed. This is in contrast to traditional foams, where cell-edge bending and cell collapse are primarily responsible for the elastic-plastic foam response (Gibson et al. 1999, Gibson 2000).The superposition of an overall foam-like response with localized strain accommodation is the key characteristic of VACNT deformation.

Experimental characterization of this buckle formation yields several interesting qualitative results. In their early study, Cao et al. (2005) compressed relatively large structures (area: 0.5-2 cm^2, height: 860 μm – 1.2 mm) and observed that the buckles formed near the bottom of the structure (the end from which the CNTs grow perpendicularly to the substrate) are more deformed that those that formed near the top (Fig. 8.2a). Motivated by this observation, they hypothesized that the bottom buckles form first. A reversal of the loading direction, by flipping the sample upside down, resulted in the same deformed morphology, with the tightest buckles forming at what was the end of the sample attached to the growth substrate. These observations point to the idea of an inherent, axial property gradient being responsible for the sequential nature of the buckling. Note that each individual buckle is on the order of 12-25 μm in size (depending on sample height) so that several tens of buckles form during deformation. The sequential, localized buckling phenomenon was later observed in much smaller samples by other researchers (Figs. 8.2 b-d) illustrating the universality of this response in VACNTs. Buckles in these microscopic studies were 12 μm (Zbib et al. 2008) and 7 μm (Hutchens et al. 2010) in wavelength (measured from the unbuckled conformation) for cylindrical samples with diameters of 30-300 μm (Zbib et al. 2008) and 50 μm (Hutchens et al. 2010),

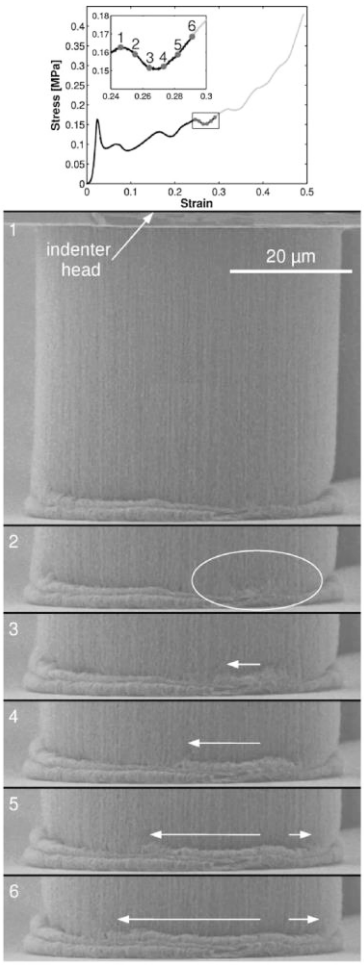

Figure 8.3. *In situ* video micrographs and accompanying nominal stress-strain data illustrating bottom-first buckling and buckle initiation and propagation events. (Hutchens et al. 2010) (Copyright Wiley-VCH Verlag GmbH & Co. KGaA. Reproduced with permission).

respectively. The bottom-first buckling mechanism was visually verified by Hutchens et al. (2010) through *in situ* experiments that further revealed the mechanism by which a single, localized buckle evolves. As shown in their study, each individual buckle does not form all at once, but rather nucleates at one point and then propagates laterally across the cylindrical sample until completion (Hutchens et al. 2010). In addition, each subsequent buckle begins only after the previous buckle has completely formed, i.e., the crease had spread across the entire cylinder (Cao et

al. 2005, Hutchens et al. 2010, Pathak et al. 2012, Yaglioglu et al. 2012). Figure 8.3 illustrates the evolution and localization of deformation for a uniaxially loaded VACNT cylinder. Cross correlation of the *in situ* images with the accompanying stress-strain data reveals that the localized buckle formation and propagation cor respond to undulations in the nominal stress-strain curve. Specifically, softening corresponds to the first appearance of the buckle and the subsequent hardening coincides with the lateral propagation of the buckle. This localized response overlays the aforementioned overall foam-like behaviour seen in these materials.

Notable differences between the classic foam-like stress-strain behaviour and the overall response of VACNTs in uniaxial compression studies of VACNT structures have also been observed in both macroscopic (Cao et al. 2005, Suhr et al. 2007, Tong et al. 2008) and microscopic (Zbib et al. 2008, Hutchens et al. 2010) samples. First, the plateau regime is highly sloped. In typical foams, a sloped plateau indicates some homogeneous variation in strut buckling stress due either to random strut alignment, a distribution of strut sizes (aspect ratio, diameter, etc.), or both. While both kinds of inhomogeneity's exist in VACNTs, the plateau regime is too highly sloped to be explained by these small fluctuations. Moreover the non-local nature of the buckling points to an alternate cause. In fact, the sloped plateau regime is suggestive of the presence of an axial property gradient in VACNTs. As discussed previously, a gradient in tube density arises in VACNTs as a result of the CVD growth process. This gradient can be such that there is a lower tube density at the bottom of the structure (i.e., the point at which the substrate attaches) than the top. It follows that such a tube density gradient would result in a corresponding strength and stiffness gradient. This property gradient is evident in the stress-strain responses seen in Figs. 8.2 and 8.3 in the progressive increase in peak stress values for undulations in the plateau region. Throughout this plateau, buckles are known to form sequentially, bottom-to-top, and therefore each subsequent buckle forms at a higher (and more dense) location within the cylinder than the previous buckle, requiring a larger stress in order to form a new fold.

A recent study by Pathak et al. (2013) has reported a different buckling sequence in VACNTs. In addition to the commonly reported bottom-to-top buckling pattern (where the bottom buckle forms first), these authors also observed VACNT samples where the bottom buckle was instead the *last* buckle to form (Fig. 8.4c). These experiments were performed on two sets of VACNT micropillars, both grown by the same chemical vapour deposition (CVD) synthesis on the same Si substrate but located on different regions of the substrate. *In-situ* uniaxial compression experiments conveyed that the sequence in the localized folds formation was unique for each sample type (Figs. 8.4 b and c). In the first set (Fig. 8.4b) the first buckling-like instability, which corresponded to the transition from elastic loading to plateau in the stress-strain data, always formed at the bottom of the sample. After initiation, the fold propagated laterally until it fully spanned the pillar width. Bottom-to-top

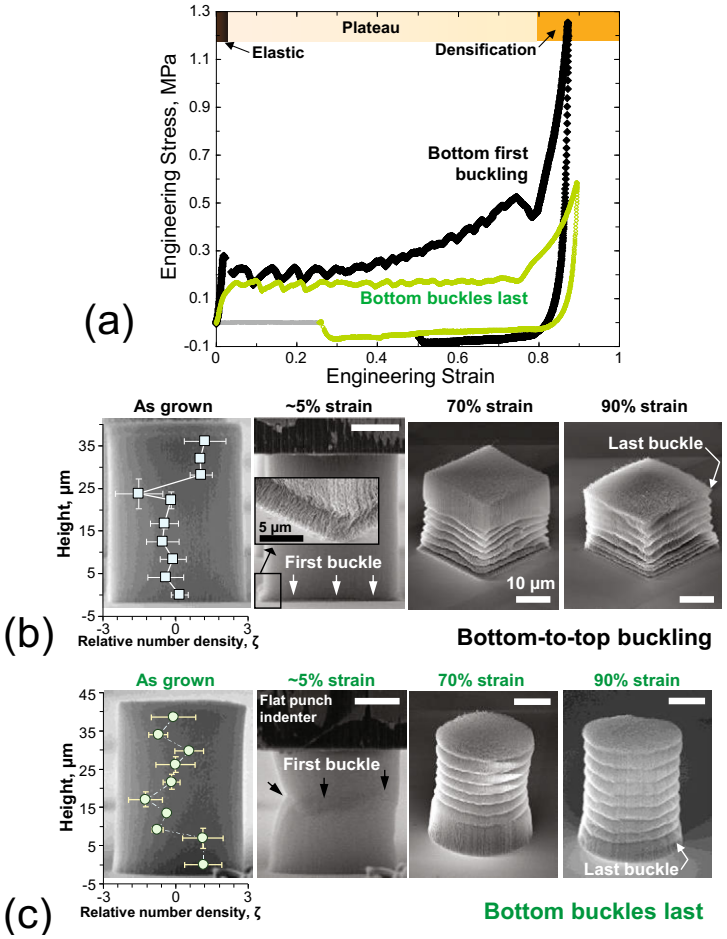

Figure 8.4. (a) Comparison of the stress-strain responses of two VACNT pillar systems grown on the same substrate; one showing the commonly reported bottom-to-top buckling sequence where the bottom buckle is the first one to form **(b)**, vs. the ones where the bottom buckle is the last buckle to form **(c)**. (b) and (c) also show the relationship between the relative tube number density ζ and the sequence of buckle-formation in these pillars. (Adapted with permission from (Pathak et al. 2013) Copyright 2013 American Chemical Society)

buckling occurred in succession, with each subsequent buckle initiating only after the previous one, located below it, had completed, similar to the observations in Cao et al. (2005), Hutchens et al. (2010). Unloading from maximum compression of ~70% strain left the top third of the pillar relatively undeformed (Fig. 8.4b, third panel from left), and the buckle closest to the top always formed last (Fig. 8.4b,

right-most panel). In contrast, post-compression SEM images of the second set of VACNT pillars, unloaded from the same maximum strain of 70%, showed that it was the *bottom* third of the pillar that remained relatively undeformed (Fig. 8.4c, third panel from left). The first instability in these pillars always formed somewhere at their mid-height (Fig. 8.4c, second panel from left), and the buckle closest to the substrate always formed last (Fig. 8.4c right-most panel).

The authors in Pathak et al. (2013) have suggested that the substantial differences in the deformation responses between the two pillar types shown in Fig. 8.4 were likely caused by their differing microstructural features and density gradients (the shapes of VACNT pillar cross-sections – square *vs*. circular – did not appear to influence their deformation characteristics). In order to capture the density gradients in these two pillar types the authors used edge detection analysis of systematically obtained SEM images to calculate the average relative number density, ζ, of tubes in each SEM image. Image analysis revealed that the two types of pillars exhibited opposite trends in relative density, which can be used to predict the location of initial buckling instability in a VACNT matrix (Figs. 8.4b and c). For example, it is reasonable to expect the first folding/buckling event during compressions of VACNTs to originate close to the substrate because of its rigid constraint (Zbib et al. 2008). Pillars showing a bottom-to-top buckling sequence corroborated this notion (Fig. 8.4b). These VACNT pillars had highest ζ in the top 10 μm, and their density profiles resembled a step function, where $\zeta \approx 1$ for all locations above the height of ~23 μm, and $\zeta \leq 0$ at all locales below. In contrast, the incipient instability in pillars where the bottom buckles formed last occurred somewhere in the middle of pillar height, at the locales with the lowest relative CNT density (Fig. 8.4c). Maximum ζ in these pillars was located in the bottom ~10 μm, close to the substrate, while the minimum ζ was in the midsection of the pillars. It appears that the lower relative density trumps the constraining effects of the substrate in driving the location of the buckling instability in these pillars. The last buckles in both sets of pillars occurred in the regions with the highest relative CNT densities: near the top in the samples showing bottom-to-top buckling sequence and at the base in the ones where the bottom buckles formed last.

In addition these two pillar types also show some key differences in their stress-strain response (Fig. 8.4a). The stress plateau in the pillars showing bottom-to-top buckling had two separate slopes: a relatively flat section up to 30% strain and a steeper region, with the slope of 0.65 MPa up to unloading at 75% strain. In contrast the pillar set where the bottom buckles formed last had a nearly flat plateau (slope ~ 0.02 MPa) up to a strain of 75%. There was also a noticeable difference in the amount of recovery between the two sample types when unloaded from post-densification regime: pillars showing bottom-to-top buckling ($R \approx 57.9 \pm 0.9$ %) showed an almost 45% higher recovery than those where the bottom buckles formed last ($R \approx 39.8 \pm 3.9$ %).

It has been suggested that such differences in the compressive responses of VACNTs can be predicted based on their local variations in density along the VACNT sample heights. Such property dependence was initially modelled by Hutchens et al. (2010) in a viscoplastic finite element framework which showed a direct correspondence between the presence and extent of an applied property gradient and the amount of hardening within the plateau. Details of this and other efforts to capture VACNT deformation mechanisms through modelling are summarized in the next section.

8.5. Modelling of VACNT Deformation

Only a few preliminary models exist to describe the mechanical deformation of VACNTs. Motivated by both the morphology of the VACNTs (a series of nominally vertical struts) as well as the observed buckling behaviour, many researchers utilize an Euler buckling framework to mechanistically describe their findings. In Euler buckling, an ideal column (perfectly straight, homogeneous, and free from initial stress) is determined to buckle when the applied load reaches some critical value that causes the column to be in a state of unstable equilibrium. Up to the point of buckling, the column is assumed to be perfectly elastic. Scaling calculations by Cao et al. (2005) utilize this critical stress to estimate the transition stress value for departure from linear elastic behaviour, i.e., the buckling stress, given a reasonable estimate of the tube number density. Similarly, Mesarovic et al. (2007) included an additional intertube contact energy to account for favourable van der Waals interactions between tubes in their energetic treatment of VACNTs. Another Euler based model by Zbib et al. (2008), motivated by the formation of buckles they observed, proposes piece-wise buckling that assumes the top of the pillar deforms via simple shear while the bottom undergoes collapse. Using this framework, they predict the buckling stress increases asymptotically with decreasing pillar height (for similar aspect ratio pillars). Notably, however, none of these models make predictions concerning the length-scale of the buckles formed or their dependence on material parameters such as density, stiffness, tube alignment, or size as the parameter space is difficult to grow in these materials.

Another subset of mechanical analyses utilizes an alternating hardening-softening-hardening local constitutive relation, and are the only theories that attempt to capture material response beyond the initial buckling event. The first, a hierarchical bi-stable spring model, captures the *quantitative* stress-strain response of VACNTs in compression (Fraternali et al. 2011). A subsequent finite element viscoplastic solid with a positive-negative-positive sloped flow strength captures the *qualitative* sequential periodic buckle morphology. The bi-stable spring model consists of mesoscale elements characterized by elastic-plateau-densification and, most importantly, hysteresis in the unloading curve. These mesoscale elements were

shown to be the limiting case of infinitely many bi-stable spring elements in series. Briefly, a bi-stable spring consists of two thermodynamically stable elastic loading sections separated by an unstable, negative stiffness region of the stress-strain curve across which the material snaps, similarly to a phase transition. When placed in series, these mesoscale elements capture the hysteretic unloading response seen by Cao et al. (2005) very closely. Thus, this model can be utilized to characterize the energy dissipation in VACNTs. In a similar vein, Hutchens et al. (2011) postulate a

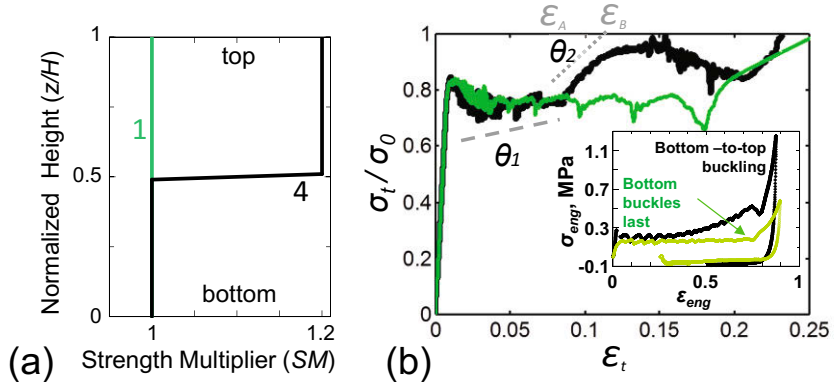

Figure 8.5. (a) Two variations of the *SM* (strength multiplier) function used for simulations: Case 1: constant *SM* function (green curve) vs. Case 4 (step variation of the *SM* function over the pillar height, black curve). **(b)** Corresponding normalized stress-strain curves for these two cases. Note that the plateau region in Case 4 can be further subdivided by two distinct slopes, *θ1* and *θ2*. (b Inset) Experimental uniaxial stress-strain responses of the two VACNT pillars shown earlier in Fig. 8.4 showing the similarity in their responses as compared to the two simulation cases in (a). (Adapted with permission from (Pathak et al. 2013) Copyright 2013 American Chemical Society)

positive-negative-positive stress-strain relation reminiscent of a bi-stable spring, but rather than being elastic, it is used as a plastic flow-strength function governing the local deformation of an element post-elastic loading. The latter analyses find that this constitutive relation is capable of producing sequential, periodic buckles in an axisymmetric, circular cylindrical mesh with fixed boundary conditions at the base, identical to those in VACNTs. In addition, an axial gradient in the strength is not necessary to initiate bottom-first buckling, as seen in experiments; rather, the fixed boundary conditions are sufficient. However, a reversal of buckle initiation, top-to-bottom, can be achieved for a sufficient inverse axial gradient (having lower strength at the top of the pillar than the bottom). Both of these analyses capture essential elements of VACNT deformation, but do so for two very different sets of experimental observations: recoverable deformation, and plastic deformation.

An example of the approach proposed by Hutchens et al. (2011) is shown in Fig. 8.5. Here the same model was utilized to predict the stress and strain responses of the two VACNT pillar types shown earlier in Fig. 8.4, assuming the stiffness of VACNTs to be linearly related to its density, $E \sim \zeta$. The mechanical property gradient was represented by a strength multiplier, *SM*, which is a multiplier giving the spatial variations of E (Young's modulus) and σ_0 where $SM=E/E_{\text{bottom}}$ and similarly for σ_0. Two particular cases are of interest (which matches the experiments most closely): Case 1 – *SM* is constant throughout the pillar height, and Case 4 – *SM* has a step-increase at the midpoint of the pillar height *i.e.* at $z/H=0.5$, where z is the coordinate along the pillar height. Strength gradients over the height in terms of *SM* for the two cases considered are shown in Fig. 8.5a, and normalized stress-strain data are shown in Fig. 8.5b. Of special note is the similarity between the experimental and simulated stress *vs*. strain relationships (Fig. 8.5b inset) in these two cases – such as the flat plateau region for a constant *SM* function (Case 1), similar to the experimental case where the bottom buckles form last, as compared to the two different hardening slopes observed for the step function in *SM* (Case 4), similar to the experimental case of bottom-to-top buckling.

8.6. Large Displacement Indentations in VACNTs

In addition to uniaxial compression, large displacement (in the range of tens of micrometres) indentations using flat punch indenters (which offer a constant contact area with the sample) offers an alternative approach to analysing VACNT deformation under a different loading and boundary condition. These tests, conducted by a variety of researchers (Lu et al. 2012, Pour Shahid Saeed Abadi et al. 2012, Pathak et al. 2013, Pathak et al. 2013), help in comparing the influence of the boundary conditions posed by the presence or absence of the external matrix.

A comparison between the indentation responses at the sample-edge vs. the one in the sample interior was provided by Pathak et al. (2013) for flat punch indentations of a ~142-μm thick VACNT film on a Si substrate grown using an atmospheric pressure CVD synthesis technique (Fig. 8.6). The following salient points are of note from this figure. Firstly this plot indicates that while the curves are similar in shape, the on-edge regions deform at significantly lower loads than in-bulk locations at equivalent indentation depths. This result is not surprising due to the less restrictive boundary conditions in the on-edge setup. Secondly, in both cases the load first increases steeply up to an instability manifested by a large displacement burst of ~20 μm, after which the indenter tip is unloaded (Fig. 8.6a). SEM images obtained immediately after this burst reveal that a portion of VACNT film sheared off nearly perfectly vertically along the edges of the indenter tip (Fig. 8.6c). In the sheared off region the deformation appears to be highly localized, occurring only at the shear offset regions and at the buckles formed at the bottom of the sample. The remaining

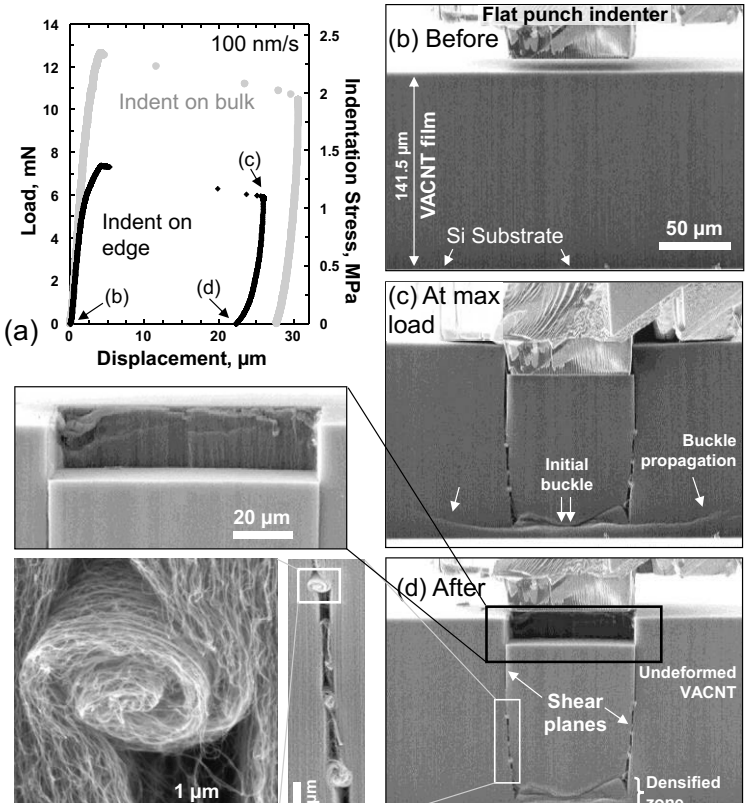

Figure 8.6. Large displacement indentations in VACNTs. **(a)** Comparative indentation load (and stress)-displacement curves at 100nm/s loading rate of *in-situ* SEM indentation tests conducted on the sample edge vs. in the interior of the sample using a 60 µm × 80 µm rectangular flat punch indenter . **(b, c and d)** For the indent on edge, the indentation process was recorded as a video file from which individual picture frames were extracted corresponding to a particular event during the loading/unloading cycle (as indicated on the load–displacement graph).

The double arrows in (c) mark the initiation of the first buckle at a load of around 6 mN. The wide lateral buckle marked by single arrows are formed after the first buckle, and increase in size with loading. (d) Upon unloading these lateral buckles disappear. **(d inset top)** The large displacement burst results in a vertical shear of the VACNT structure along the indenter edges. Note the clean edge of the shear wall. **(d bottom insets)** The shear appears to have been carried by a series of CNT 'micro-rollers' which act as effective lubricants protecting the rest of the VACNT structure from further damage. (Pathak et al. 2013) reproduced with permission.

portions of the VACNT film appear completely unaffected (Fig. 8.6d top inset). Thirdly, the shear appears to have been carried by a series of tangled CNTs, or 'micro-rollers' seen in the magnified inset images in Fig. 8.6d, whereby originally-vertical strands of several entangled CNT collectively coiled themselves into helical structures. The authors have speculated that these micro-rollers provide a low-friction path during the shear process. Finally unloading the indenter tip results in minimal recovery.

The shear event and the formation of the CNT micro-rollers are unique characteristics seen only in the intertwined VACNT systems. Neither foams (Sudheer Kumar et al. 2003, Flores-Johnson et al. 2010), where the deformation is confined only to regions directly beneath the indenter, nor non-interacting VACNTs (Pantano et al. 2004), where such shear would propagate without any micro-roller formation, show the unique features seen in Fig. 8.6.

Some of these phenomena can be understood in terms of the differences in boundary conditions between the two loading configurations – indentation (Pathak et al. 2013) vs. compression (Pathak et al. 2012) (Fig. 8.7), in combination with the overall similarity of the VACNT deformation to that of open-cell foam materials (Gibson et al. 1999). The characteristics of flat-punch indentations into VACNT films closely resembles those reported for metallic (Andrews et al. 1999, Sudheer Kumar et al. 2003) and polymeric foams (Flores-Johnson et al. 2010) (Gibson et al. 1999). In the spirit of foam-like deformation, the indentation zone for VACNTs is confined to the region directly beneath the indenter, while the surrounding regions are unaffected (see Fig. 8.6). The lack of lateral spread in the deformed region is typical for foams, whereby it can be attributed to the non-existent Poisson's ratio (Gibson et al. 1999, Sudheer Kumar et al. 2003, Zbib et al. 2008). This is diametrically opposite to monolithic materials, where the plastic zone underneath the indenter tip is typically represented by a continuous hemispherical plastic zone (Fleck et al. 1992). Another common characteristic between indentation into conventional foams and VACNTs is the appearance of a so-called 'tear line' (Sudheer Kumar et al. 2003, Flores-Johnson et al. 2010) along the corner of the flat punch indenter where the shear force is largest. The depth of this shear line in a foam generally depends on its strength (Sudheer Kumar et al. 2003, Flores-Johnson et al. 2010). Unlike foams, however, the constituents of the VACNT system – the individual CNTs themselves – are nominally vertically aligned with respect to the indenter tip (Fig. 8.1), and thus the vertical plane is expected to be the plane of lowest shear strength in the VACNT matrix. Once the critical shear stress is attained during loading, the shear-off proceeds catastrophically along this vertical plane through the thickness of the VACNT film down to the underlying substrate. This results in highly localized deformation along the shear plane, with no notable perturbation in other regions. Subsequent loading initiates folding or buckling of the material close to the substrate but not in the sheared-off block.

On the contrary, under uniaxial compression the shear stresses acting on the VACNT matrix are negligible. Instead, the applied compressive strain is accommodated entirely via the formation of lateral folds or buckles along the length of the bundle, while the remaining portion remains virtually unscathed (Hutchens et al. 2010, Pathak et al. 2012). Thus, the first instability shown in the compression stress-strain response in Fig. 8.7a is related to the onset of the first buckle formation in the VACNT matrix. Further loading beyond yield results in the compression of the collapsed buckles.

A comparison of the instability stresses between compression (buckling, 2.69±0.1 MPa) and indentation (shear, 1.75±0.3 MPa) on the CVD VACNT samples indicate

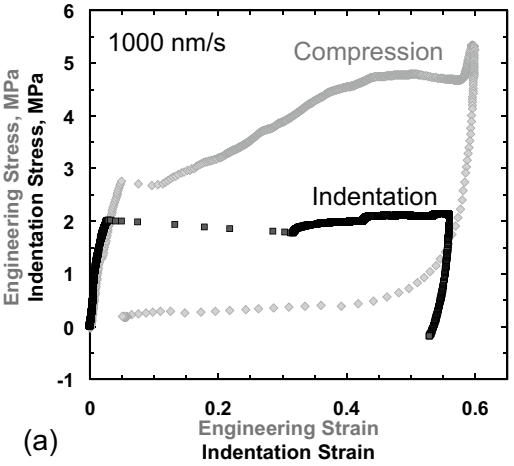

(a)

(b)

1000nm/s	Indentation	Compression
Instability stress	1.75±0.3 MPa (shear)	2.69±0.1 MPa (buckling)
Recovery @ ε=0.5	4.3±0.3 %	95.7±2.8 %
Loss Coefficient @ ε=0.5	0.005±0.001	0.05±0.01
Modulus @ ε=0.5	173.7±2 MPa	176.9±11 MPa

Figure 8.7. (a) Comparative stress-strain curves of VACNT in indentation and compression **(b)** Table comparing the measured values from indentation (Pathak et al. 2013) vs. compression (Pathak et al. 2012). (Pathak et al. 2013) reproduced with permission.

that the instability stress in indentation is 40% lower than that of compression (Fig. 8.7b). Interestingly, this observation is opposite to that of traditional indentation tests into monolithic materials, where yield in indentation typically requires 1-3

times higher stresses than for the uniaxial case for most solid (Johnson 1987) and porous (Fleck et al. 1992) as well as foam (Gibson et al. 1999, Andrews et al. 2001, Sudheer Kumar et al. 2003) materials. The two distinct modes of deformation in VACNTs – shear under indentation, and buckling in compression – are likely responsible for this apparent reversal in their instability stress values, i.e. during indentation the APCVD VACNT film reaches its critical shear stress before it can buckle.

8.7. Recoverability from Large Strains

A marked difference in material behaviour among different VACNT arrays is the ability (or lack thereof) to recover from large deformations; with some exhibiting superior creep recovery, seeing less than 15% deformation after thousands of cycles of strain to 85% (Cao et al. 2005, Suhr et al. 2007, Xu et al. 2010, Xu et al. 2011, Pathak et al. 2012), while others deform permanently even at modest strains (Yaglioglu 2007, Zbib et al. 2008, Hutchens et al. 2010, Zhang et al. 2010, Cao et al. 2011) (see Fig. 8.2). Energy can be dissipated in the former as they behave like viscoelastic rubbers, discussed in a later section. Energy can be absorbed in the latter. Both appear to deform via the same structural mechanism intrinsic to the complex microstructure of these systems. It is still largely unclear what is responsible for a VACNT material displaying plastic versus viscoelastic behaviour.

A number of experimental studies have identified a list of potential candidates that affect the recoverability of VACNTs. Pathak et al. (2013) have shown that both the experimental loading and boundary conditions as well the VACNT morphology have a marked effect on VACNT recoverability (Fig. 8.7). These authors have reported a large difference in recoverability of the VACNT matrix in indentation (4.3±0.3 %) vs. compression (95.7±2.8 %) conditions. This has been attributed to the different deformation modes and boundary conditions under the two loading modes. The almost complete recovery of the VACNT structure under compression in (Pathak et al. 2012) is related to the elastic un-folding of the buckles created during loading. This recoverability has been explained by the inter-tube interactions of the CNTs where the zipping and unzipping of CNTs in contact has been proposed as the primary criteria for the superior viscoelasticity and creep recovery of VACNTs (Gogotsi 2010, Xu et al. 2010, Bradford et al. 2011, Xu et al. 2011). On the contrary, recovery in indentation (Pathak et al. 2013) is inhibited by the additional constraints of the surrounding VACNT material. Thus even at lower strains (before the large shear burst) the recovery under indentation is still lower (50-80%) than that in compression. Moreover indentation experiments cause large shear forces to develop along the corners of the flat punch indenter. This causes the VACNT films to deform by an instantaneous vertical shearing of the material directly underneath the indenter tip (since the vertical plane is the plane of lowest

shear strength in the vertically aligned CNT matrix). After the displacement burst, recovery of the VACNTs in indentation is further compromised by the permanent nature of the damage caused by the shearing of a large block of the material from the matrix (Lu et al. 2012, Pathak et al. 2013).

The recoverability of VACNTs has also been shown to depend on the VACNT microstructure and morphology. In general, researchers growing CVD-VACNTs made using the 'floating' catalyst route (Andrews et al. 1999, Raney et al. 2011) have reported substantial (>90%) recovery in their samples (Cao et al. 2005, Raney et al. 2011, Raney et al. 2011, Yaglioglu et al. 2012), while the recoverability of majority of VACNTs made using the 'fixed' catalyst technique (Yaglioglu 2007, Bedewy et al. 2009) has been poor (Zbib et al. 2008, Hutchens et al. 2010, Zhang et al. 2010, Cao et al. 2011) (note: Pathak et al. (2012) is a notable exception). This effect is thought to be correlated to the thicker (>40 nm) diameter of the tubes, and a correspondingly higher density for VACNTs made using the floating catalyst route. A systematic study by Bradford et al. (2011) analysed this effect further, where it was shown that VACNTs grown using a fixed catalyst technique and exhibiting low resilience changed to an almost complete recovery after a post growth CVD treatment (Fig. 8.8a). This was attributed to an increase in the individual CNT wall thickness, which also caused increased surface roughness of the CNTs, resulting in a decrease of the van der Waals interactions.

Other aspects of the VACNT microstructure are also known to influence their mechanical properties, such as their tortuosity (or waviness) and the number of inter-tube junctions in the matrix, both of which are expected to increase with increasing CNT wall thickness and/or density of the sample (Astrom et al. 2004, Berhan et al. 2004). The effect of tortuosity on VACNT recovery has been demonstrated by Pathak et al. (2013) (Fig. 8.8b). In their work the authors synthesized two VACNT samples using the same nominal CVD growth conditions, but for different reaction times. This resulted in a taller VACNT film (Sample A in Fig. 8.8b), which in addition to having a higher density and CNT wall thickness, also showed increased tortuosity/waviness in its top portions. During flat punch indentation, sample A showed almost full recovery, while sample B (in which the CNTs have negligible tortuosity and follow relatively straighter paths) showed a much lower (~49%) recovery (Fig. 8.8b).

As discussed earlier, VACNTs subjected to large displacement flat punch indentations often exhibit a catastrophic shear-off event, which limits their recoverability. Thus the very high recovery of sample A is quite unique for VACNTs, and can be linked to its tortuous nature. The tortuosity/waviness of the CNTs in sample A is expected to cause a higher number of inter-tube contacts in its as grown state, and such interconnections are instrumental in increasing the vertical shear strength of the matrix and hence prevent any catastrophic shear off under indentation. The recovery process is also aided by the larger CNT wall thickness of sample A and the resultant

increase in the bending stiffness of the tubes. On the other hand, the more vertical alignment of the constituent CNTs in sample B results in a lower shear strength in the vertical plane of this sample, resulting in the expected catastrophic shear-off event, and hence negligible recovery (Fig. 8.8b).

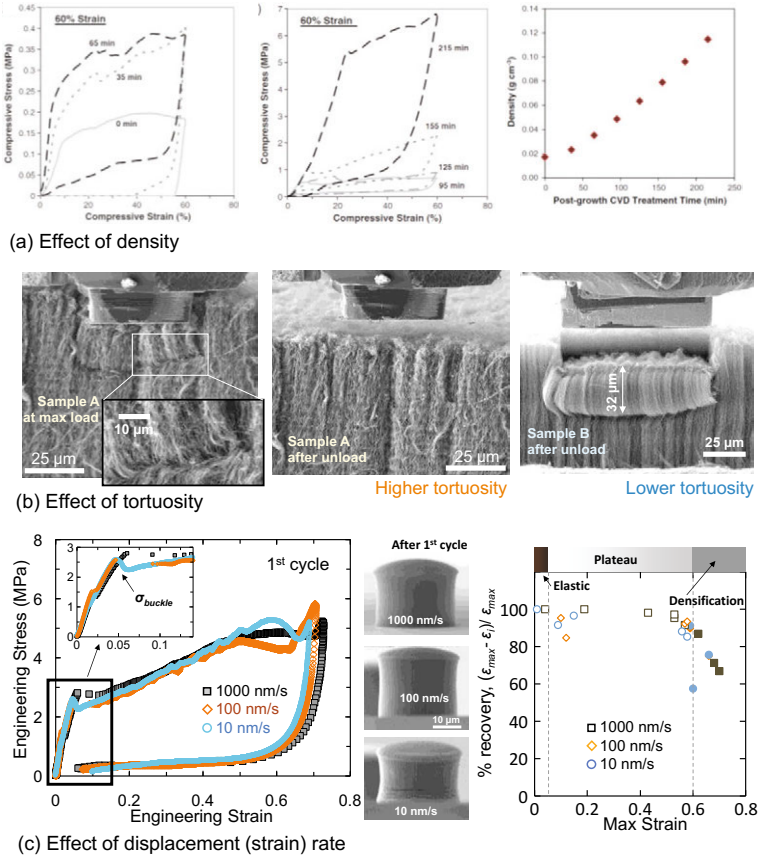

Figure 8.8. Factors affecting recoverability in VACNTs. % recovery in VACNTs increases with **(a)** increasing density (Reproduced from (Bradford et al. 2011) with permission from Elsevier) **(b)** increased tortuosity of VACNTs (Reproduced from (Pathak et al. 2013) with permission from Elsevier) and **(c)** higher displacement (strain) rates (Adapted with permission from (Pathak et al. 2012) Copyright 2012 American Chemical Society).

For VACNT bundles demonstrating nearly full recovery and energy dissipation, a further factor that affects the resilience of these systems is the displacement (strain) rates at which the compression tests were conducted (Pathak et al. 2012). This is shown in Fig. 8.8c for VACNT systems grown using 'fixed' catalyst techniques for three explored strain rates: 4×10^{-2}, 4×10^{-3} and 4×10^{-4} /sec (which correspond to

displacement rates of 1000, 100 and 10 nm/s respectively). These authors found that when compressed at the fastest strain rates of 4×10^{-2} /sec, the VACNT bundles recover virtually back to their original dimensions (> 95 % recovery) while at the slowest deformation rates of 4×10^{-4} /sec, they remain permanently deformed (< 86 % recovery), as evidenced by their post-mortem morphology containing localized buckles. The resilience of the VACNT samples is further compromised when they are loaded to beyond densification threshold strains of $\varepsilon\geq0.65$-0.7 for all strain rates.

All of this suggests a strong dependence of deformation commencement on strain rate, the basic phenomenological process for which may be understood as follows. When compressed at the lower deformation rates, the individual CNT struts re-arrange themselves by twisting, bending, *etc*., in response to the applied compressive load, thereby coming into close contact with one another. This type of individual strut re-configuration is not unreasonable in a high-entropy deformation process (*i.e.* many different configurations are available at each time step). In addition, CNTs are inherently "sticky," experiencing an adhesive driving force due to van der Waals interactions (Ruoff et al. 1993). Therefore, in the course of compression at the slower rates, an ever-increasing number of individual struts coalesce by coming into close proximity of one another, thereby forming localized densified regions (*i.e.* buckles). Importantly, the adhesion process appears to be largely irreversible, *i.e.* the adhesion driving force overrides the stored elastic energy upon unloading. This implies that after unloading the buckles remain even while undergoing elastic recovery. This all is in contrast to the deformation at higher rates, where the entire structure recovers completely, with no evidence of buckles' presence upon unloading (see Fig. 8.8c). This behaviour is believed to stem from an insufficient interaction time between individual tubes to come in contact with one another. This results in a significantly reduced contact inter-tubular area as compared with the slowly-deformed case, and hence leads to much lower adhesion. Compression at higher rates is likely a lower-entropy process since there are fewer configurations available during each time step, and therefore less inter-tubular contact occurs, leading to the lack of localized "zipped-up" densified buckles (Gogotsi 2010, Xu et al. 2010, Bradford et al. 2011, Xu et al. 2011).

A corollary to the above hypothesis is that if different VACNT micro-pillars were allowed similar amounts of time for the reconfiguration to occur, they should exhibit similar % recovery for all loading rates. This was demonstrated in Pathak et al. (2012) by conducting two tests: one at the slowest 4×10^{-4} /sec rate, and a second one at the fast rate of 4×10^{-2} /sec where the sample was held at the max load for a long time to ensure that it spends an equivalent amount of time before unload similar to the sample deformed at the slowest rate. Both pillars showed (equally reduced) recovery values of 86%. The above results suggest that it is the time spent by the VACNTs under high strains, rather than the loading history, that determines the permanence of their deformation.

8.8. Carbide Derived Carbons (CDC) VACNTs

While most of the previous sections in this chapter have focused on CVD-VACNTs, VACNTs prepared by the Carbide-Derived Carbon (CDC) synthesis method also deserve special mention. As discussed earlier, CDC-VACNTs refer to a bottom-up growth process, where carbon is formed by selective extraction of the metal or metalloid atoms in the carbide (e.g., silicon carbide) at high temperatures (>1600°C), transforming the carbide structure into pure carbon. It has been shown (Kusunoki et al. 1997) that high temperature decomposition of SiC by the reactions $SiC \rightarrow Si(g) + C$, $SiC + 1/2O_2\,(g) \rightarrow SiO\,(g) + C$, leads to the formation of CNTs growing normal to the carbon terminated $(000\bar{1})$ C-face of hexagonal SiC with primarily zigzag chirality (Kusunoki et al. 2002) and graphite growth on the Si terminated (0001) Si-face. These carbide-derived carbon (CDC) nanotube brushes have been shown to have a density close to 0.95 g/cm^3 (Cambaz et al. 2008), which is significantly (10 times or more) higher than in catalytic CVD growth of any kind of nanotubes. This higher density is generally thought be due to a conformal transformation of SiC into carbon. These dense CDC CNT brushes consist of small-diameter (1-3 nm outer diameter, 1-4 walled) non-catalytic CNTs with double walled CNTs being the most common, as determined from transmission electron microscopy (TEM), and a strong RBM mode in Raman spectra (Cambaz et al. 2008). Assuming an average outer diameter of 3 nm and 0.35 nm as the inter-tube distance, this would correspond to an aerial density of ~100,000 tubes per μm^{-2} for a hexagonal arrangement of CNTs, and ~89,000 tubes per μm^{-2} for a square arrangement. The actual aerial density of the CNTs packed randomly in a dense brush is likely to be somewhere in between.

The higher density of these CDC-VACNT brushes is evident in the SEM image in Fig. 8.9a inset of the CNT brush grown at 1700°C, where no apparent porosity is visible. Such dense VACNTs are ideal for indentation testing using smaller spherical indenters, something that is not possible for the wider spaced CVD-VACNTs (where the CNTs tend to simply bend away from the indenter). The use of spherical indenters is also advantageous in that, by using appropriate data analysis protocols (Kalidindi et al. 2008, Pathak et al. 2015), the extracted load-displacement data from these tests can be transformed into meaningful indentation stress-strain curves. The indentation stress-strain curves in turn enable one to follow the entire evolution of the mechanical response in the VACNT array, from initial elasticity to the initiation of buckling to post-buckling behaviour at finite plastic strains. In addition, the indentation stress-strain curves also allow one to estimate the Young's modulus and the stress at buckling in the indentation experiment. For example, using a 1 μm spherical indenter, the Young's modulus of 200 nm thick CDC-VACNT brushes was estimated to be ~17 GPa and the critical buckling stress was estimated as ~0.3 GPa at a load of 0.02 mN (Pathak et al. 2009).

The authors in Pathak et al. (2009) also used indentation stress-strain curves from different indenter radii to explore the effects of indentation zone sizes and the ma-

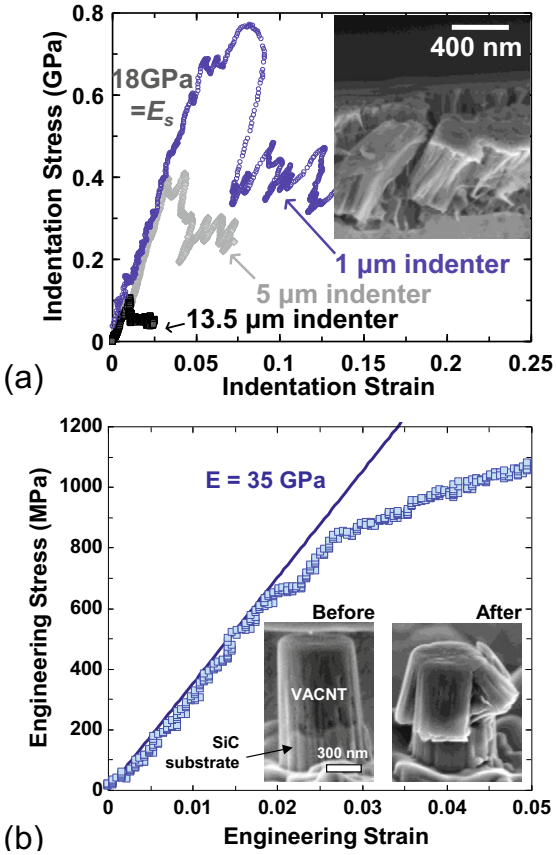

Figure 8.9. (a) Indentation stress-strain response on 1.3 μm thick CDC-VACNT brush as a function of indenter size (radius) showing an initial elastic behaviour followed by the buckling instability (Reproduced from (Pathak et al. 2009) with permission from Elsevier). **(b)** Uniaxial compression of a CDC-VACNT micro-pillar of diameter ~ 600 nm. The inset images show the VACNT micro-pillar before and after compression (Reproduced from (Pathak et al. 2015) with permission from Elsevier).

terial defect density on the VACNT buckling stress. This is shown in Fig. 8.9a where the indentation response on a thicker VACNT brush (thickness 1.2-1.4 μm, see Fig. 8.9a inset) is shown as a function of 3 different indenter radii. In general all three indenter sizes show a similar trend in the VACNT response: an initial elastic behaviour (Young's modulus ~18 GPa), followed by a sharp drop at a critical stress corresponding to CNT buckling. Note however that the values of buckling stresses

vary significantly between the three different indenters, where indentation with the smaller 1 μm indenter shows the highest buckling stress, followed by the 5 μm indenter, while buckling with the largest 13.5 μm indenter occurs at a significantly lower indentation stress.

Such differences in buckling stresses can be understood by a closer analysis of the indentation zones sizes between the 3 indenter radii used. The indentation zone sizes at buckling for the larger 13.5 μm indenter (~3.58 μm) extends well beyond the VACNT brush thickness (1.2-1.4 μm), while only a limited thickness of the VACNT brush (~ 0.39 μm) is exposed to indentation stress for the smaller 1 μm indenter. The corresponding differences in buckling stress are thus largely a consequence of the effective buckling length available in each case; with smaller indenters there is only a smaller buckling length and the material is able to withstand higher buckling stresses. Interestingly the authors in Pathak et al. (2009) also report a larger variation in the values of the buckling stress for the small 1 μm radii indenter as compared to the larger indenters. These values seem to indicate that defect density varies from one location to another in one VACNT brush. Thus the smaller volume sampled by the 1 μm indenter is more sensitive to the variation in defect density when different regions of the sample are probed, and causes a larger spread of the buckling stress values when using this indenter. The larger indenters, on the other hand, encounter a bigger volume, and hence they mostly register a combined VACNT-defect response leading to a lower buckling stress and a smaller spread in the buckling stress.

The above results have been validated by conducting compression tests on VACNT micro-pillars machined using a focused ion beam (FIB) on the same sample. This is shown in Fig. 8.9b which shows the uniaxial compression data for a ~600 nm diameter VACNT pillar. As seen from this figure, the values measured from indentation and compression tests are complementary to one another. The increase in the Young's modulus values in the micro-pillar compression tests (~30 GPa as compared to ~17-18 GPa in indentation) is due to ion-beam irradiation during the micro-machining process using FIB. This modifies the structure of the outer rim of CNTs in the VACNT pillar, which potentially results in intertube bridging between the densely packed CNTs and hence an increase in their Young's modulus (Kis et al. 2004).

These numbers suggest that these CDC-VACNT brushes perform significantly better and exhibit considerably higher mechanical properties compared to CVD VACNT turfs; CDC-VACNTs have values of Young's modulus 1-2 orders of magnitude higher (Mesarovic et al. 2007), and buckling strengths several orders of magnitude higher (Waters et al. 2004, Waters et al. 2005) compared to a CVD VACNT turf – a difference which is explained by the much higher density of the tubes per unit area in the CDC-VACNT resulting in considerably higher mechanical properties. These higher properties are of extreme importance for making selective

CNT membranes for gas or liquid filtration/separation or CNT coatings for tribological applications.

8.9. Viscoelasticity

In addition to their distinctive buckling behaviour and their ability to recover from large deformations, VACNTs have also been reported to demonstrate another case of extreme mechanical performance – a unique viscoelastic response that spans a truly wide temperature range from -196°C to 1000°C – something no other material has shown so far. Viscoelastic materials exhibit both viscous and elastic characteristics when subjected to load. Thus, a viscoelastic material is able to both dissipate energy through viscous behaviour (as in honey), while storing energy though elasticity (as in rubber band). The stress-strain response of viscoelastic materials is typified by hysteresis in the loading-unloading cycle.

Viscoelastic behaviour in a material is generally characterized in terms of its loss (E") or storage modulus (E') (or by the ratio, known as tan $\delta = E"/E'$, of these two moduli). E" relates to the amount energy dissipated while E' represents the stored energy in the material. The angle δ is the phase lag between the oscillatory load and displacement responses under a sine wave load. In a typical experiment, the material is loaded to a pre-determined strain and the mechanical probe is oscillated across a range of frequencies. By measuring the resultant load amplitude, displacement amplitude, and the phase lag during the test, the values of loss modulus, storage modulus, and tan δ are determined. Similarly, viscoelasticity can also be quantified by the memory or hysteresis effects during load-unload cycles under deformation, where the energy dissipated is given by the area of the hysteresis loop. These viscoelastic effects have recently been documented in the highly intertwined random networks of VACNTs. Viscoelasticity in CVD-VACNTs has been demonstrated by Hutchens et al. (2010), where both storage and loss stiffness's were studied in a frequency range from 1 to 45 Hz at different strain levels (Fig. 8.10a). Note that these stiffness values are proportional to moduli given a known Poisson's ratio which is lacking for VACNTs. The elastic response is clearly frequency independent, indicating the VACNT's elastic deformation is likely due to the same mechanism (likely tube bending) over the range of timescales tested. As shown in Fig. 8.10a, more energy is dissipated (higher values of loss stiffness's) at larger strain levels when a higher fraction of the VACNT pillar has buckled. Interestingly, for the more dense CDC-VACNTs the opposite seems to be true (Fig. 8.10b). For the highly dense CDC-VACNTs, Pathak et al. (2009) have shown a significant drop in the tan δ values of the CNTs after buckling, i.e., when the material was highly compacted. These observations indicate that while an increase in density can significantly increase the viscoelastic behaviour of CNTs, there appears to be a cut-off beyond which the contacting CNTs became increasingly bundled resulting in a

decrease in their ability to dissipate energy.

A recent report by Xu et al. (2010) also suggests a rubber like viscoelastic be-

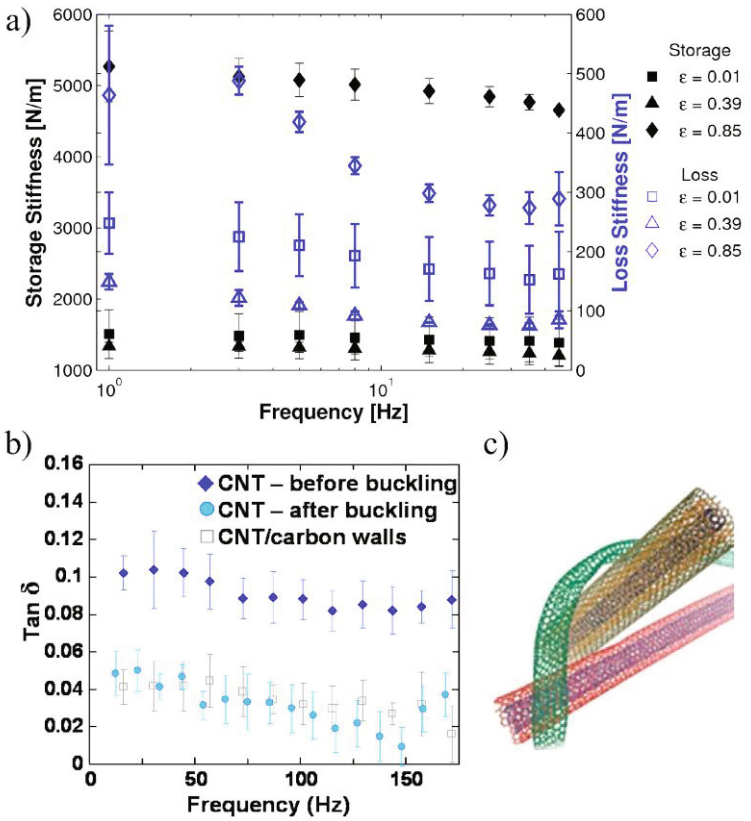

Figure 8.10. Visco-elastic behaviour as seen in: **(a)** CVD-VACNTs showing an increase in the loss stiffness with increasing strains (Hutchens et al. 2012) (Copyright Wiley-VCH Verlag GmbH & Co. KGaA. Reproduced with permission) **(b)** CDC-VACNTs showing a significantly decrease in values of tan δ after buckling Reproduced from (Pathak et al. 2009) with permission from Elsevier. **(c)** Atomistic modelling image of a possible entangled arrangement of single, double and triple-walled CNTs leading to their rubber-like viscoelastic behaviour. Reprinted from (Gogotsi 2010) with permission from AAAS.

haviour in a random network of long, interconnected and tangled CNTs, similar in many ways to VACNTs but significantly less aligned, over a very wide temperature range – from -196°C to 1000°C, with a possibility of extending this behaviour beyond 1500°C. While the oxidizing nature of carbon may limit the application of these materials to only vacuum or protective (reducing) environments, CNTs are nevertheless the only known solids to demonstrate such behaviour at extremely low

or very high temperatures. The authors attribute the reversible dissipation of energy in CNTs over this remarkable range to the zipping and unzipping of the CNTs upon contact (see Fig. 8.10c) caused by the van der Waals interactions. In this instance, 'reversible' means that beyond a critical strain the zipping/unzipping process was no longer possible everywhere as more and more tubes become permanently entangled at higher strain. This would lead to a loss in their viscoelasticity, similar to the observations in the highly dense CDC-VACNTs (Fig. 8.10b).

The unique combination of superior mechanical properties and the ability to dissipate energy during deformation is expected to have significant implications in damping applications utilizing VACNTs. These, combined with the wide temperature range of its viscoelastic behaviour, make VACNT based materials a promising choice for use in mechanical applications under extreme temperatures or temperature gradients. Possible environments range from the cold of interstellar space to down-to-earth viscoelastic applications, such as MEMS devices to high temperature vacuum furnaces.

8.10. Applications

Multiwall carbon nanotubes are well known for a variety of exceptional properties. These include a high tensile modulus, on the order of 1 TPa, high strength, on the order of tens of GPa, high thermal conductivity, recoverability after large bending angle deformation, and a range of electrical properties depending on the chirality of the graphene walls. For these reasons they are currently the subject of a wide range of research. In the form of VACNTs, these individual tube properties may be significantly altered by the collective interaction of thousands of tubes. Several applications of VACNT structures currently under study rely on the mechanical behaviour described earlier in this chapter. A remarkable, but incomplete list includes: components of highly compliant thermal contacts for micro-electro-mechanical-systems (MEMS) and microelectronics (McCarter et al. 2006, Zbib et al. 2008), dry adhesives, thermally robust energy dissipating rubber (Gogotsi 2010, Xu et al. 2010), and energy absorption or impact mitigation (Misra 2008). Other applications, such as optical coatings and cold cathode arrays, may rely less on the mechanical properties for optimization and design, but understanding is still necessary for evaluation of robustness and in-use lifetime analysis.

We go through each application briefly to highlight the VACNT specific mechanical behaviour of interest. First, thermal contacts for delicate electronics devices have two requirements. They must be highly thermally conductive and make conformal contact (to increase heat transfer) while avoiding damage to the components they are transferring heat to and from. CNT foams are ideal for this application due to the high compliance that comes from the reduced load capacity of the CNT struts as they buckle. Dry adhesive applications of VACNTs take advantage of the hier-

archical structure which can, as desired in MEMS switches, make conformal contact to surfaces at a variety of roughness length scales, thereby increasing the attractive interactions between the tubes and the surface. Third, energy dissipating and absorbing applications require more in-depth knowledge of the deformation mechanism. As mentioned in the previous section, energy dissipation is currently thought to be due to tube zipping/unzipping or tube-to-tube sliding and rearrangement (Mesarovic et al. 2007, Suhr et al. 2007, Pathak et al. 2009, Gogotsi 2010, Xu et al. 2010), while energy absorption is certainly maximized during buckle formation. Future applications may be able to take advantage of yet undiscovered traits of the incompletely characterized VACNTs.

8.11. Summary and Outlook

Although the mechanisms governing VACNTs collective mechanical behaviour are still largely uncharacterized, the special properties of multiwall carbon nanotubes combined with the complex interactions that arise between them in the hierarchical VACNT microstructure have generated significant research interest. Their wide range of properties, mechanical, electrical, and thermal, make them ideal candidates as multi-functional materials, particularly for applications in which soft materials (such as polymers) have traditionally dominated. Notably, VACNTs occupy a unique niche among engineering materials as shown in the Ashby property chart in Fig. 8.11 with the ability to span a wide range of properties given a tunable microstructure. There remains two major hurdles to rationally designing VACNTs for any application: control of the CNT growth process and understanding of the relationship between the microstructure and mechanical response. These hurdles are interrelated through the fact that the design space cannot be systematically probed until the microstructure can be systematically controlled. Mastery of these unknowns will not only further VACNTs place as novel materials in the current applications under study, but may reveal previously undiscovered behaviours in microstructures yet to be created or characterized.

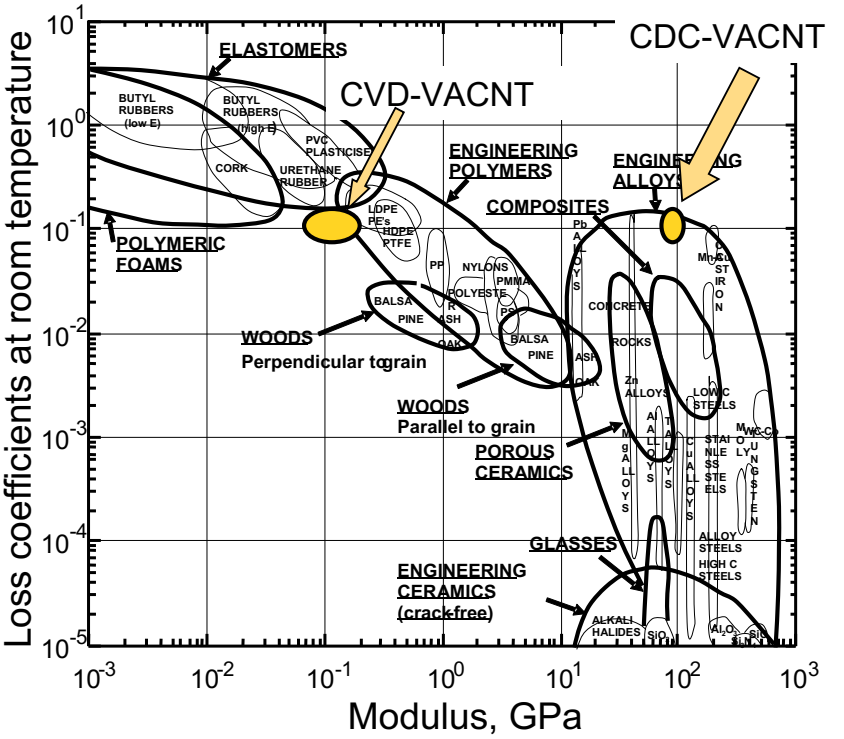

Figure 8.11. Ashby plot of Loss Coefficient vs. Modulus showing the performance of VACNTs.

Acknowledgements

This work was performed, in part, at the Center for Integrated Nanotechnologies, an Office of Science User Facility operated for the U.S. Department of Energy (DOE) Office of Science. Los Alamos National Laboratory, an affirmative action equal opportunity employer, is operated by Los Alamos National Security, LLC, for the National Nuclear Security Administration of the U.S. Department of Energy under contract DE-AC52-06NA25396. SP gratefully acknowledges funding from the Los Alamos National Laboratory Director's Postdoctoral Fellowship during the writing of this chapter.

References

Andrews, E. W., L. J. Gibson and M. F. Ashby (1999). "The creep of cellular solids." *Acta Materialia* 47(10): 2853-2863.

Andrews, E. W., G. Gioux, P. Onck and L. J. Gibson (2001). "Size effects in ductile cellular solids. Part II: Experimental results." *International Journal of Mechanical Sciences* 43(3): 701-713.

Andrews, R., D. Jacques, A. M. Rao, F. Derbyshire, D. Qian, X. Fan, E. C. Dickey and J. Chen (1999). "Continuous production of aligned carbon nanotubes: a step closer to commercial realization." *Chemical Physics Letters* 303(5-6): 467-474.

Astrom, J. A., A. V. Krasheninnikov and K. Nordlund (2004). "Carbon nanotube mats and fibers with irradiation-improved mechanical characteristics: A theoretical model." *Physical Review Letters* 93(21): 215503-215501-215503-215504.

Bedewy, M., E. R. Meshot, H. C. Guo, E. A. Verploegen, W. Lu and A. J. Hart (2009). "Collective Mechanism for the Evolution and Self-Termination of Vertically Aligned Carbon Nanotube Growth." *Journal of Physical Chemistry C* 113(48): 20576-20582.

Berhan, L., Y. B. Yi and A. M. Sastry (2004). "Effect of nanorope waviness on the effective moduli of nanotube sheets." *Journal of Applied Physics* 95(9): 5027-5034.

Bradford, P. D., X. Wang, H. Zhao and Y. T. Zhu (2011). "Tuning the Compressive Mechanical Properties of Carbon Nanotube Foam." *Carbon* 49(8): 2834-2841.

Brieland-Shoultz, A., S. Tawfick, S. J. Park, M. Bedewy, M. R. Maschmann, J. W. Baur and A. J. Hart (2014). "Scaling the Stiffness, Strength, and Toughness of Ceramic-Coated Nanotube Foams into the Structural Regime." *Advanced Functional Materials* 24(36): 5728-5735.

Cambaz, Z. G., G. Yushin, S. Osswald, V. Mochalin and Y. Gogotsi (2008). "Noncatalytic Synthesis of Carbon Nanotubes, Graphene and Graphite on SiC." *Carbon* 46(6): 841-849.

Cao, A., P. L. Dickrell, W. G. Sawyer, M. N. Ghasemi-Nejhad and P. M. Ajayan (2005). "Materials science: Super-compressible foamlike carbon nanotube films." *Science* 310(5752): 1307-1310.

Cao, C., A. Reiner, C. Chung, S.-H. Chang, I. Kao, R. V. Kukta and C. S. Korach (2011). "Buckling Initiation and Displacement Dependence in Compression of Vertically Aligned Carbon Nanotube Arrays." *Carbon* 49(10): 3190-3199.

Ci, L., J. Suhr, V. Pushparaj, X. Zhang and P. M. Ajayan (2008). "Continuous Carbon Nanotube Reinforced Composites." *Nano Letters* 8(9): 2762-2766.

Deck, C. P., J. Flowers, G. S. B. McKee and K. Vecchio (2007). "Mechanical Behavior of Ultralong Multiwalled Carbon Nanotube Mats." *Journal of Applied Physics* 101(2): 23512-23511-23519.

Deshpande, V. S. and N. A. Fleck (2000). "Isotropic constitutive models for metallic foams." *Journal of the Mechanics and Physics of Solids* 48(6-7): 1253-1283.

Fleck, N. A., H. Otoyo and A. Needleman (1992). "Indentation of porous solids." *International Journal of Solids and Structures* 29(13): 1613-1636.

Flores-Johnson, E. A. and Q. M. Li (2010). "Indentation into polymeric foams." *International Journal of Solids and Structures* 47(16): 1987-1995.

Fraternali, F., T. Blesgen, A. Amendola and C. Daraio (2011). "Multiscale mass-spring models of carbon nanotube foams." *Journal of the Mechanics and Physics of Solids* 59(1): 89-102.

Gibson, L. J. (2000). "Mechanical Behavior of Metallic Foams." *Annual Review of Materials Science* 30(Compendex): 191-227.

Gibson, L. J. and M. F. Ashby (1999). *Cellular Solids: Structure and Properties*. Cambridge, UK, Cambridge University Press.

Gogotsi, Y., Ed. (2006). *Nanotubes and Nanofibers*. Boca Raton, FL, CRC Press.

Gogotsi, Y. (2010). "High-Temperature Rubber Made from Carbon Nanotubes." *Science* 330(6009): 1332-1333.

Hutchens, S. and S. Pathak (2012). Vertically Aligned Carbon Nanotubes, Collective Mechanical Behavior. *Encyclopedia of Nanotechnology*, Springer. 22**:** 2809-2818.

Hutchens, S. B., L. J. Hall and J. R. Greer (2010). "In situ Mechanical Testing Reveals Periodic Buckle Nucleation and Propagation in Carbon Nanotube Bundles." *Advanced Functional Materials* 20(14): 2338-2346.

Hutchens, S. B., A. Needleman and J. R. Greer (2011). "Analysis of uniaxial compression of vertically aligned carbon nanotubes." *Journal of the Mechanics and Physics of Solids* 59(10): 2227-2237.

Johnson, K. L. (1987). *Contact Mechanics*, Cambridge University Press, Cambridge.

Kalidindi, S. R. and S. Pathak (2008). "Determination of the effective zero-point and the extraction of spherical nanoindentation stress–strain curves." *Acta Materialia* 56(14): 3523-3532.

Kis, A., G. Csanyi, J. P. Salvetat, T.-N. Lee, E. Couteau, A. J. Kulik, W. Benoit, J. Brugger and L. Forro (2004). "Reinforcement of single-walled carbon nanotube bundles by intertube bridging." *Nature Materials* 3(3): 153-157.

Kumar, M. and Y. Ando (2010). "Chemical vapor deposition of carbon nanotubes: A review on growth mechanism and mass production." *Journal of Nanoscience and Nanotechnology* 10(6): 3739-3758.

Kusunoki, M., M. Rokkaku and T. Suzuki (1997). "Epitaxial carbon nanotube film self-organized by sublimation decomposition of silicon carbide." *Applied Physics Letters* 71(18): 2620-2622.

Kusunoki, M., T. Suzuki, C. Honjo, T. Hirayama and N. Shibata (2002). "Selective synthesis of zigzag-type aligned carbon nanotubes on SiC (000-1) wafers." *Chemical Physics Letters* 366(5-6): 458-462.

Lu, Y. C., J. Joseph, Q. Zhang, M. R. Maschmann, L. Dai and J. Baur (2012). "Large-Displacement Indentation of Vertically Aligned Carbon Nanotube Arrays." *Experimental Mechanics* 52: 1551-1554.

McCarter, C. M., R. F. Richards, S. D. Mesarovic, C. D. Richards, D. F. Bahr, D. McClain and J. Jiao (2006). "Mechanical compliance of photolithographically defined vertically aligned carbon nanotube turf." *Journal of Materials Science* 41(23): 7872-7878.

Mesarovic, S. D., C. M. McCarter, D. F. Bahr, H. Radhakrishnan, R. F. Richards, C. D. Richards, D. McClain and J. Jiao (2007). "Mechanical Behavior of a Carbon Nanotube Turf." *Scripta Materialia* 56(2): 157-160.

Min-Feng, Y., O. Lourie, M. J. Dyer, K. Moloni, T. F. Kelly and R. S. Ruoff (2000). "Strength and breaking mechanism of multiwalled carbon nanotubes under tensile load." *Science* 287(5453): 637-640.

Misra, A. A. G., Julia R. AND Daraio, Chiara (2008). "Strain rate effects in the mechanical response of polymer-anchored carbon nanotube foams." *Advanced Materials* 20: 1-5.

Pantano, A., D. M. Parks and M. C. Boyce (2004). "Mechanics of deformation of single- and multi-wall carbon nanotubes." *Journal of the Mechanics and Physics of Solids* 52(4): 789-821.

Pathak, S., Z. G. Cambaz, S. R. Kalidindi, J. G. Swadener and Y. Gogotsi (2009). "Viscoelasticity and High Buckling Stress of Dense Carbon Nanotube Brushes." *Carbon* 47(8): 1969-1976.

Pathak, S. and S. R. Kalidindi (2015). "Spherical nanoindentation stress–strain curves." *Materials Science and Engineering: R: Reports* 91(0): 1-36.

Pathak, S., E. J. Lim, P. Pour Shahid Saeed Abadi, S. Graham, B. A. Cola and J. R. Greer (2012). "Higher Recovery and Better Energy Dissipation at Faster Strain Rates in Carbon Nanotube Bundles: An in-Situ Study." *ACS Nano* 6(3): 2189-2197.

Pathak, S., N. Mohan, E. Decolvenaere, A. Needleman, M. Bedewy, A. J. Hart and J. R. Greer (2013). "Local Relative Density Modulates Failure and Strength in Vertically Aligned Carbon Nanotubes." *ACS Nano* 7(10): 8593-8604.

Pathak, S., N. Mohan, P. Pour Shahid Saeed Abadi, S. Graham, B. A. Cola and J. R. Greer (2013). "Compressive Response of Vertically Aligned Carbon Nanotube Films gleaned from *In-Situ* Flat Punch Indentations." *Journal of*

Materials Research: Focus Issue on De Novo Carbon Nanomaterials 28(7): DOI: 10.1557/jmr.2012.1366.

Pathak, S., J. R. Raney and C. Daraio (2013). "Effect of morphology on the strain recovery of vertically aligned carbon nanotube arrays: An in situ study." *Carbon* 63: 303-316.

Poelma, R. H., B. Morana, S. Vollebregt, E. Schlangen, H. W. van Zeijl, X. Fan and G. Q. Zhang (2014). "Tailoring the Mechanical Properties of High-Aspect-Ratio Carbon Nanotube Arrays using Amorphous Silicon Carbide Coatings." *Advanced Functional Materials* 24(36): 5737-5744.

Pour Shahid Saeed Abadi, P., S. Hutchens, J. H. Taphouse, J. R. Greer, B. A. Cola and S. Graham (2012). "Effects of morphology on the micro-compression response of carbon nanotube forests." *Nanoscale* 4(11): 3373-3380.

Presser, V., M. Heon and Y. Gogotsi (2011). "Carbide-derived carbons - from porous networks to nanotubes and graphene." *Advanced Functional Materials* 21(5): 810-833.

Qi, H. J., K. B. K. Teo, K. K. S. Lau, M. C. Boyce, W. I. Milne, J. Robertson and K. K. Gleason (2003). "Determination of mechanical properties of carbon nanotubes and vertically aligned carbon nanotube forests using nanoindentation." *Journal of the Mechanics and Physics of Solids* 51: 2213-2237.

Qiu, A., D. F. Bahr, A. A. Zbib, A. Bellou, S. D. Mesarovic, D. McClain, W. Hudson, J. Jiao, D. Kiener and M. J. Cordill (2011). "Local and Non-Local Behavior and Coordinated Buckling of CNT Turfs." *Carbon* 49(4): 1430-1438.

Raney, J. R., F. Fraternali, A. Amendola and C. Daraio (2011). "Modeling and In Situ Identification of Material Parameters for Layered Structures Based on Carbon Nanotube Arrays." *Composite Structures* 93(11): 3013-3018.

Raney, J. R., A. Misra and C. Daraio (2011). "Tailoring the microstructure and mechanical properties of arrays of aligned multiwall carbon nanotubes by utilizing different hydrogen concentrations during synthesis." *Carbon* 49(Compendex): 3631-3638.

Ruoff, R. S., J. Tersoff, D. C. Lorents, S. Subramoney and B. Chan (1993). "Radial Deformation of Carbon Nanotubes by van der Waals Forces." *Nature* 364(6437): 514-516.

Salvetat, J.-P., S. Bhattacharyya and R. B. Pipes (2006). "Progress on Mechanics of Carbon Nanotubes and Derived Materials." *Journal of Nanoscience and Nanotechnology* 6(7): 1857-1882.

Sudheer Kumar, P., S. Ramchandra and U. Ramamurty (2003). "Effect of displacement-rate on the indentation behavior of an aluminum foam." *Materials Science and Engineering A* 347(1-2): 330-337.

Suhr, J., P. Victor, L. C. S. Sreekala, X. Zhang, O. Nalamasu and P. M. Ajayan (2007). "Fatigue Resistance of Aligned Carbon Nanotube Arrays under Cyclic Compression." *Nature Nanotechnology* 2(7): 417-421.

Tong, T., Y. Zhao, L. Delzeit, A. Kashani, M. Meyyappan and A. Majumdar (2008). "Height Independent Compressive Modulus of Vertically Aligned Carbon Nanotube Arrays." *Nano Letters* 8(2): 511-515.

Treacy, M. M. J., T. W. Ebbesen and J. M. Gibson (1996). "Exceptionally high Young's modulus observed for individual carbon nanotubes." *Nature* 381(6584): 678-680.

Waters, J. F., P. R. Guduru, M. Jouzi, J. M. Xu, T. Hanlon and S. Suresh (2005). "Shell buckling of individual multiwalled carbon nanotubes using nanoindentation." *Appl. Phys. Lett.* 87: 103109-103101-103103.

Waters, J. F., L. Riester, M. Jouzi, P. R. Guduru and J. M. Xu (2004). "Buckling Instabilities in Multiwalled Carbon Nanotubes under Uniaxial Compression." *Applied Physics Letters* 85(10): 1787-1789.

Xu, M., D. N. Futaba, T. Yamada, M. Yumura and K. Hata (2010). "Carbon Nanotubes with Temperature-Invariant Viscoelasticity from-196 degrees to 1000 degrees C." *Science* 330(6009): 1364-1368.

Xu, M., D. N. Futaba, M. Yumura and K. Hata (2011). "Carbon Nanotubes with Temperature-Invariant Creep and Creep-Recovery from −190 to 970 °C." *Advanced Materials* 23(32): 3686-3691.

Yaglioglu, O. (2007). *Carbon Nanotube Based Electromechanical Probes - PhD Thesis*. PhD, Massachusetts Institute of Technology.

Yaglioglu, O., A. Cao, A. J. Hart, R. Martens and A. H. Slocum (2012). "Wide Range Control of Microstructure and Mechanical Properties of Carbon Nanotube Forests: A Comparison Between Fixed and Floating Catalyst CVD Techniques." *Advanced Functional Materials* 22(23): 5028-5037.

Zbib, A. A., S. D. Mesarovic, E. T. Lilleodden, D. McClain, J. Jiao and D. F. Bahr (2008). "The Coordinated Buckling of Carbon Nanotube Turfs under Uniform Compression." *Nanotechnology* 19(17): 175704-175701-175707.

Zhang, Q., Y. C. Lu, F. Du, L. Dai, J. Baur and D. C. Foster (2010). "Viscoelastic Creep of Vertically Aligned Carbon Nanotubes." *Journal of Physics D-Applied Physics* 43(31): 315401-315401-315407.